Production and Oscillations of a Bose Einstein Condensate on an Atom Chip

Benjamin Yuen

Thesis submitted in partial fulfilment of the requirements for the degree of Doctor of Philosophy of Imperial College London and for the Diploma of the Imperial College.

Department of Physics

Imperial College London

December 2013

Declaration of Originality

I hereby declare that the work in this thesis is my own work, except where due acknowledgement is made.

Abstract

This thesis describes production of and experiments with a Bose-Einstein condensate of approximately 2×10^4 ^{87}Rb atoms, trapped at the surface of an atom chip. In the first half of this thesis I describe the process of trapping and cooling the atomic vapour close to the surface of an atom chip. This process, which cools the vapour by over 9 orders of magnitude, involves a highly complex sequence of events which I implemented and optimised over the first two years of my PhD. In the early stages of this process, the atomic vapour is laser cooled and magneto-optically trapped. The vapour is then transferred to a highly elongated magnetic trap produced by high field gradients a few hundred microns from the surface of the atom chip. Here the vapour is evaporatively cooled to below the transition temperature where a Bose-Einstein condensate emerges. A simple existing analytic model of evaporative cooling is extended in this work to account for the shape of our highly elongated trap. Predictions of this model are presented here along with experimental observations with which it has good agreement.

The second part of my thesis investigates some of the characteristics of the condensate, and dynamics of its low energy collective oscillations in the trap, based on experimental measurements taken in the final 18 months of my PhD. In particular, measurements taken of the centre of mass oscillations of the condensate along the long axis of the trap are presented. In the zero temperature limit the condensate is expected to behave as a perfect superfluid, and these low energy oscillations should go undamped. However, at finite temperature where not all atoms in the gas are condensed, damping is observed. In our experiment significant damping is found with an $1/e$ decay rate which varies between $2\,\mathrm{s}^{-1}$ and $8\,\mathrm{s}^{-1}$, depending on the fraction of non-condensed atoms in the gas. A finite temperature formalism is then used to describe the likely damping mechanism - Landau damping. We use a simple model of this formalism which estimates the temperature dependence of the damping rate $\gamma(T)$, but find this gives a significant overestimation of the rates we measure. However, we argue that a straightforward adaptation to this model reduces the predicted damping rate significantly, and suggests a functional form of $\gamma(T)$ that is in much better agreement with our experimental measurements.

Acknowledgements

I would like to start by thanking Professor Ed Hinds, who supervised my PhD and gave me the opportunity to work on a remarkable experiment in his group. He has offered great inspiration and insight along this journey, and I have very much enjoyed the discussions we have had on the physics we have learned over the final stages of my PhD.

It has also been humbling to work in his fantastic group, the Centre for Cold Matter (CCM) at Imperial. Within the group I have found much support from fellow students, post-docs and staff. In particular I would like to thank Joe Cotter, who has been there for almost my entire PhD, Isabel Llorente-Garcia, who was there at the beginning, but has offered me support and friendship throughout, and Iain Barr, who has been a dependable fellow PhD student in the laboratory towards the end of my PhD. Operation of the apparatus I have worked with now falls to Ian and Eoin Butler, to whom I wish much success.

Beyond CCM, I am deeply grateful for the support and encouragement of friends and family, a few of whom I would especially like to mention. Firstly, thanks to my mum for, besides the obvious of raising me, allowing me to explore whatever I ever wanted[1], and to my brother Michael, who's inquisitiveness has been inspirational[2]. Finally I thank Rachel, my wife, without who's support, guidance and ingenious approach to life, I would surely not have come this far.

[1] And allowing me to get away with it.

[2] And for leading me on such paths astray.

Contents

List of Tables

List of Figures

Chapter 1

Introduction

In 1938, London suggested that Bose-Einstein condensation occurred in liquid helium below the λ-temperature [1], in order to explain the 'superfluidity' observed by Allen and Misener [2]. Unlike the superfluid effects themselves, Bose-Einstein condensation is not directly observable in liquid Helium, and this idea was difficult to prove. Controversially, Landau omitted this idea in his quantitative explanation of superfluidity, summarised by the criterion that a minimum, non-zero amount of energy was needed in order to create excitations in the fluid which dissipate energy [3]. His dismissal of the idea was on the grounds that the energy of excitations of a condensate in a uniform ideal Bose gas could be arbitrarily small. In 1947 however, Bogoliubov showed that there existed just such an energy gap in the spectrum of a gas of weakly interacting condensed Bosons. Feynman later united the standpoints of London and Landau in his explanation of superfluid Helium, emphasising the role of Bose-Einstein statistics [4].

In 1995, Bose-Einstein condensates were observed for the first time in dilute atomic vapours [5, 6, 7]. In these experiments, vapours of neutral atoms under ultra high vacuum (10^{-11} mbar) were first laser cooled, then trapped magnetically where they were further cooled evaporatively to ultra-low temperatures ($\lesssim 10^{-7}$ K) where condensation occurs. Following this discovery, it was natural to ask whether these condensates had superfluid properties similar to liquid helium. Theoretically, this ground state ensemble of interacting bosons was governed by a non-linear Schrödinger equation, the Gross-Pitaevskii equation [8, 9, 10]. From this, a 'hydro-

dynamic' equation of its dynamics at low energy can be derived, which is almost identical to that of a viscous-free fluid (see [11] for example). The hydrodynamic equation predicted a spectrum of collective modes for the condensates confined in harmonic traps, analogous to low energy phonons in superfluid Helium. Thus, experimentalist began to search for low-energy collective modes in the laboratory.

The early experiments on these low energy collective modes were performed in systems with almost pure condensates, where the thermal cloud of the few remaining non-condensed atoms was negligible [12, 13]. The collective mode frequencies were measured from sequences of images of the oscillating condensate, and were found to be in excellent agreement with the zero temperature predictions from the hydrodynamic theory [14, 15]. Following these results, other collective excitations were measured in different experiments [16, 17, 18, 19]. Two results in particular are worth highlighting. Firstly, the measurement of the frequency of the 'scissors' mode showed conclusive evidence of dynamics exclusive to superfluids [20, 19]. Secondly, the propagation of sound predicted by the Bogoliubov theory was verified by measuring the velocity of localised excitations propagating through the condensate [16].

Experiments were also performed at higher temperatures where the interactions between the condensate and the thermal component of the gas play a role [21, 22, 23, 24]. For certain modes substantial temperature-dependent frequency shifts were measured [21, 22, 23]. The finite temperature theory of the condensate dynamics is considerable more complicated than at $T = 0$, and satisfactory theoretical explanations of the observed frequency shifts of the $m = 0$ mode in [21] for example, were not given until several years later [25].

In addition to frequency shifts, the damping rate of low energy collective modes were found to be highly temperature dependent [21, 22, 23, 24]. Theoretical explanation of these results was founded on a process called Landau damping, caused by collisions between particles in the condensate and particles in the thermal cloud [26, 27]. Through these collisions there is a net removal of energy from the collective mode of the condensate, which is absorbed and dissipated by the thermal cloud. To describe this process accurately on a microscopic level requires a complete theory of elementary excitations in terms of Bogoliubov quasi-particles which describe the low energy, small amplitude collective modes of the condensate, and the high energy ex-

citations which describe particles in the thermal cloud. Higher energy modes of this spectrum were measured experimentally in a series of experiments [28, 29, 30, 31], using pair of counter propagating laser beams to excite them [32].

Having built up a comprehensive picture of elementary excitations of the Bose gas, experiments turned to look at collective excitations in harmonically trapped gases in a reduced number of dimensions [33, 34]. In this regime, motion of the condensate and thermal cloud are 'frozen' out in a particular direction and the dynamics can be drastically altered e.g. [35, 36, 37, 38, 39]. The condition for regimes of reduced dimensions can be seen by comparing energy scales. The ground state energy of the interacting gas is given by the chemical potential of the condensate, μ, the thermal cloud is characterised by energy $k_{\mathrm{B}}T$, and in a harmonic trap the first excited state in the i^{th} direction has energy $\hbar\omega_i$. Motion in this direction is frozen out when $\mu, k_{\mathrm{B}}T \ll \hbar\omega_i$. To meet this criterion at measurable densities required the new types of trap to be created with tight confinement in one, two or three dimensions. Two trapping techniques emerged: optical lattices with confinement on the order of a wavelength ($< 1\,\mu$m), and magnetic micro-traps generated by atom chips.

Producing Bose-Einstein condensates in atomic vapours requires several stages of laser cooling and magneto-optical trapping, followed by evaporative cooling in either optical dipole traps or magnetic traps. This requires a complicated setup of optics and magnetic field coils. Atom chips are centimeter-sized wafers, incorporating on their surface a combination of optical components such as mirrors, gratings and waveguides, and magnetic components such as current carrying wires [40, 41]. The atoms can be first magneto-optically trapped close to the chip surface with a simple apparatus. Due to the close proximity of the atoms to the chip surface, they can then be magnetically trapped with high field gradients to create tight traps with only modest currents in the surface-mounted wires. This makes atom chips useful for studying Bose-Einstein condensates in reduced dimensions, particularly in narrow ($\sim 1\,\mu$m) highly elongated ($\gtrsim \mu$m) traps where they are close to being 1-dimensional in nature [36, 38, 39]. In our experiment we produce highly elongated Bose-Einstein condensates on an atom chip. We investigate the temperature dependence of collective mode dynamics in between the 3D and 1D regimes, where there is currently little experimental data. In particular, we focus on the temperature dependence of

Landau damping of longitudinal centre of mass oscillations of our condensate in this quasi-1D regime. We find the damping rate to be significantly weaker than expected for a 3D condensate, and derive an analytical model that explains why this is the case.

1.1 Experiment Overview

Our experiments are performed under ultra-high vacuum, where the atomic vapour exists in a meta-stable gaseous state that we can condense. We start by capturing atoms from a room temperature atomic vapour, and cooling them down to form a Bose-Einstein condensate. This involves laser cooling and magneto-optically trapping, followed by magnetic trapping and evaporative cooling to reach the critical temperature for condensation. We give a brief overview of this sequence of events below.

A vapour of rubidium atoms is produced by a small pulsed source inside a secondary vacuum chamber, where the vapour rapidly reaches equilibrium with the chamber walls at room temperature. ^{87}Rb atoms from the vapour are captured and cooled to $\sim 100\,\mu$K by the first of three magneto-optical traps (MOT). Atoms are pushed out of this MOT into the primary vacuum chamber, where a second MOT recaptures them a few millimeters above the surface of our atom chip. They are then smoothly transferred into the third and final atom chip-MOT, located a few hundred microns above the chip surface. From here they are loaded into the magnetic chip trap. Once in the magnetic trap they are evaporatively cooled through selective removal of the most energetic atoms by an rf field. Once cooled below the transition temperature $T_c \approx 350\,$nK, they start to condense. Further evaporation decreases the temperature of the remaining thermal atoms, and increases the number of condensed atoms.

We excite collective oscillations by resonantly shaking the magnetic trap. We study the oscillating condensate from absorption images of the cloud taken at a sequence of different times. To produce each image, we release the condensate from the magnetic trap and shine a laser beam at it, resonant with an atomic optical transition. The absorption of this light produces a shadow, which we image onto a

camera. From this image we obtain a 2D map of the column density of the cloud of atoms. This process destroys the condensate, so the entire sequence of events is repeated to obtained images of the oscillating condensate at subsequent times.

1.2 Organisation of this Thesis

This thesis falls into two parts: chapters 2-4 describe how we produce our condensates, while Ch.5-8 describe the experiments we perform on them and the theory we developed to understand our results. To understand the experiments presented in Ch.5-8, it is sufficient to follow the description of our experimental sequence in Ch.2, together with specific subsections we reference along the way.

Chapter 2 introduces the various stages of cooling and trapping that precede the formation of a Bose-Einstein condensate. In this chapter, we describe the function of each stage. In the second pat of Ch.2 we describe the apparatus used for this sequence.

Chapter 3 describes in detail how we reach the point of having magnetically trapped thermal atoms. We emphasise how we configured and optimised the sequence in the laboratory.

Chapter 4 describes in detail how we evaporatively cool the (magnetically trapped) atoms to form a condensate. A detailed theoretical treatment of evaporative cooling is given first, followed by a description of how we optimise this cooling stage experimentally. We then describe features of our trap which become important at ultra-cold temperatures ($T \lesssim 1\,\mu$K), and finish by describing the emergence of our condensates in the cloud of thermal atoms.

Chapter 5 begins by introducing the theory of the condensate at zero temperature. From this we calculate its density, which we compare to those we measure. We then describe the dynamics expected of our condensate at zero temperature, showing measurements of two low energy collective oscillations, and describe how the condensate density distribution evolves after it is released from the magnetic trap.

Chapter 6 describes techniques for manipulating the magnetically trapped atoms with an rf field. We show how these can be used to deform the trap potential, sensitively release atoms from the trap, and selectively remove atoms according their energy.

Chapter 7 introduces the theory of Bose-Einstein condensates at finite temperature. We use this theory to develop an accurate analytical model of the thermal density after the Bose gas is released from the trap. Our model describes the measured density profiles well, and provides an accurate method for determining the temperature and condensed fraction of the gas, improving on techniques currently in use.

Chapter 8 presents the primary results of this thesis; how the temperature of our quasi-1D Bose gas effects the damping rate of longitudinal centre of mass oscillations of the condensate. We describe our experimental method and the analysis of our data, for which we use the techniques of Ch.7. This produces a set of measurements of the damping rate versus temperature. We then introduce the microscopic theory of Landau damping, and modify the standard treatment to describe our trapped gas. We show that this modified theory is in good quantitative agreement with our experimental observations.

Chapter 9 summarises the main results of this thesis and gives an outlook on future research.

In this thesis we have explored in detail various experimental techniques and theoretical methods that apply to our experiment. Different readers will wish to gain different kinds of information from this thesis, and following all our arguments in detail is not necessary to understand the broader ideas of our results.

In particular, we have derived several detailed theoretical models in order to explain certain experimental observations. Some of these are on technical issues, namely the loading of the magnetic trap in sec.3.4 and evaporative cooling in sec.4.1. Our aim in deriving these models is to give new insights and explanations that will help guide the experimentalist faced with similar problems in the future. For the reader wishing to gain a more general overview of our experiment, following these sections in detail is not necessary to understand the work in later chapters.

Other theoretical models seek to explain more fundamental observations such as the density distribution of the thermal cloud in sec.7.2, and Landau damping in sec.8.4. These models have been derived from basic (although not always simple) principles, so that the interested reader may follow our arguments closely. Parts of our derivations that take a highly mathematical form without offering much new physical insight are presented in the appendices as referenced. Furthermore, in Ch.7 and Ch.8, where finite temperature effects of a Bose-Einstein condensate are discussed, we have also described the second quantised and mean field theories of the Bose gas in order to lay solid foundations on which our results are built.

It is not necessary to follow the derivations in detail to gain a broad understanding of our results. However, a basic understanding of the concepts in Ch.7 is useful for understanding the Landau mechanism which explains the results presented in Ch.8. The introductory theory in Ch.7 itself is at times quite abstract, but intuition can be gained by first reading Ch.5 in which the dynamics of the condensate are described by a semi-classical mean field.

Chapter 2

Experimental Sequence and Apparatus

This chapter introduces the various stages that make up the experimental sequence in section 2.1. Section 2.2 then details the experimental apparatus used to implement this sequence.

2.1 The BEC sequence

Figure 2.1 shows the 8 stages of the experimental sequence. The first 6 stages culminate in a magnetically-trapped BEC. The final stage consists of the experiment we wish to perform on the BEC. The duration of the stages range between 2 ms and 12 s long, and the whole sequence takes about 40 s to run. The sequence is computer controlled and runs at a repetition rate of once every 50 s.[1] At the end of each sequence, the BEC is released from the trap, and an absorption image taken. This process is destructive, so further tests cannot be made on the same BEC. To conduct our experiment on the time-dependent dynamics of a BEC, many sequences are run in a highly repeatable fashion, with the BEC imaged at different times in each cycle.

[1] The extra 10 s, allows software to be reconfigured for the next sequence to be run.

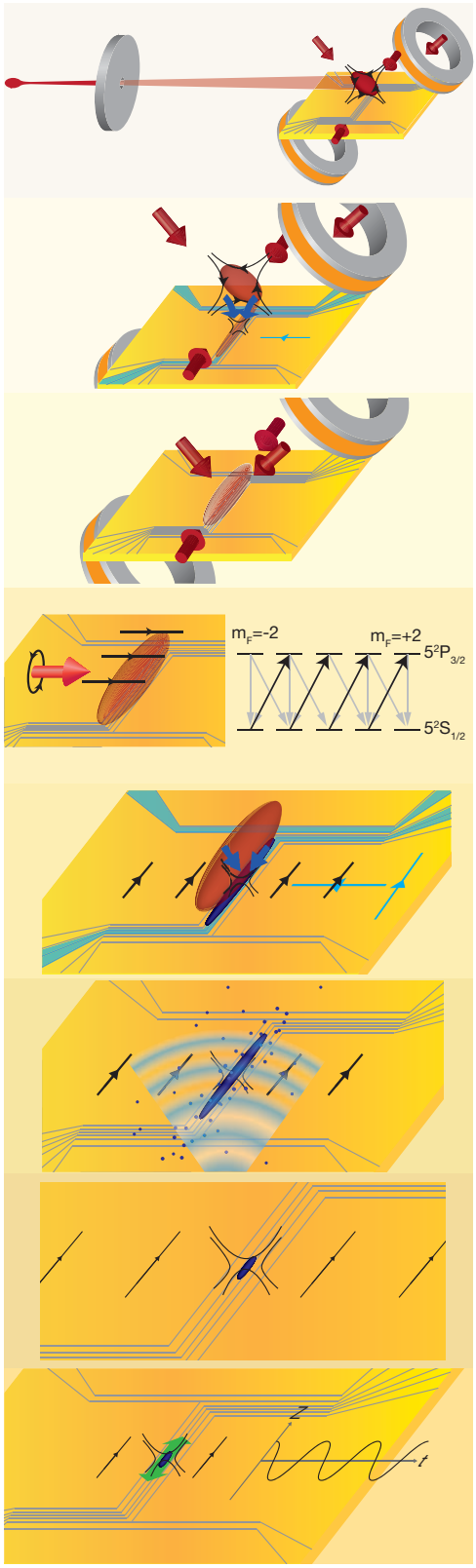

Stage 1 - Loading mirror MOT: The LVIS MOT (left) produces a cold stream of atoms that passes through the hole in the extraction mirror separating the LVIS chamber and science chamber. This beam loads the mirror MOT above the surface of the atom chip. Shown are the horizontal and diagonal MOT beams (cylindrical arrows), and the MOT coils that produce the quadrupole magnetic field (black lines with arrows).

Stage 2 - Atoms transferred from the MOT to the UMOT: The UMOT uses the same MOT beams, but a different quadrupole field, created by a U-shaped current distribution through the chip wires (shaded blue), together with the x bias field (blue line). The transfer is made by overlapping the two fields and smoothly changing it into just the UMOT quadrupole field.

Stage 3 - Optical Molasses: The atoms are released into an optical molasses by ramping off the UMOT quadrupole field. The trap light is detuned, and the cloud sub-doppler cooled.

Stage 4 - Optical Pumping: The trap light is switched off, and the cloud opticaly pumped into the m_F=2 zeeman sub-level. The optical pumping light is pulsed on with σ_+ polarisation relative to a 1 G field in the x direction. This leaves 60×10^6 atoms in the m_F=2, between 80 and 120 μK ready for magnetic trapping.

Stage 5 - Loading Magnetic Trap: The trap magnetic trap is loaded by gradually switching on the magnetic trapping field. The magnetic trap field is produced by running 2A through the small Z wires, together with bias fields in the x and z directions. The magnetic trap contains $\approx25\times10^3$ atoms at 120 μK after 600 ms.

Stage 6 - Evaporative Cooling to BEC: The atoms in the magentic trap are evaporatively cooled by selective removal of the hottest atoms using an RF field. The RF field is produced by running a RF current though thick copper bar centred 1.5 mm below the chip surface. As the atoms are cooled the size of the cloud in the harmonic trap potential also decreases.

BEC: A BEC is produced within a fragment at the bottom of the magnetic trap. The BEC contains between 10 and 40×10^3 atoms, and has radial and axial harmonic trap frequencies of 1.2 kHz and 8 Hz in the fragment that we perform experiments in. The BEC is in the 1-d to 3-d crossover regime.

Stage 7 - Experiments on Collective Excitaitons: Centre of mass and dipole (collective) oscillations are excited in the condensate by varying the x bias field and current in the end wires. The z bias field is also varied to alter the radial trap frequency and condensate aspect ratio. The dynamics of the condensate are measured from sequences of absorption images.

Figure 2.1: The stages of the experimental sequence that produce a BEC that we can then perform an experiment on. Further explanation of each stage is given in the following sub sections.

2.1.1 Loading the Mirror MOT

The first stage is to load the mirror-magneto-optical trap (mMOT) [42], a useful variant of the magneto-optical trap (MOT) for atoms chips. Magneto optical trapping techniques are nowadays commonplace in ultra-cold physics experiments. This section describes the setup in our experiment, noting the important technical specifications. Explanations of the theory behind magneto-optical trapping can be found in [43, 44], and with a setup almost identical to our present one in [45].

The mMOT allows us to cool and trap atoms 0.5 mm to 5 mm above the surface of our atom chip. It consists of a pair of counter-propagating horizontal beams, and two diagonal beams incident at 45° to the reflective gold chip surface. The two reflected diagonal beams form a pair counter-propagating to the incident diagonal beams. A set of coils in the anti-Helmholtz configuration produces a quadrupole field with an axial field gradient of $25\,\mathrm{G\,cm^{-1}}$, centred where the beams intersect.

The MOT beams contain trap light 12 MHz red detuned from the $5^2S_{1/2} \longrightarrow 5^2P_{3/2}$, $F = 2 \longrightarrow F' = 3$ 'trapping' transition. The natural line width is $\Gamma =$

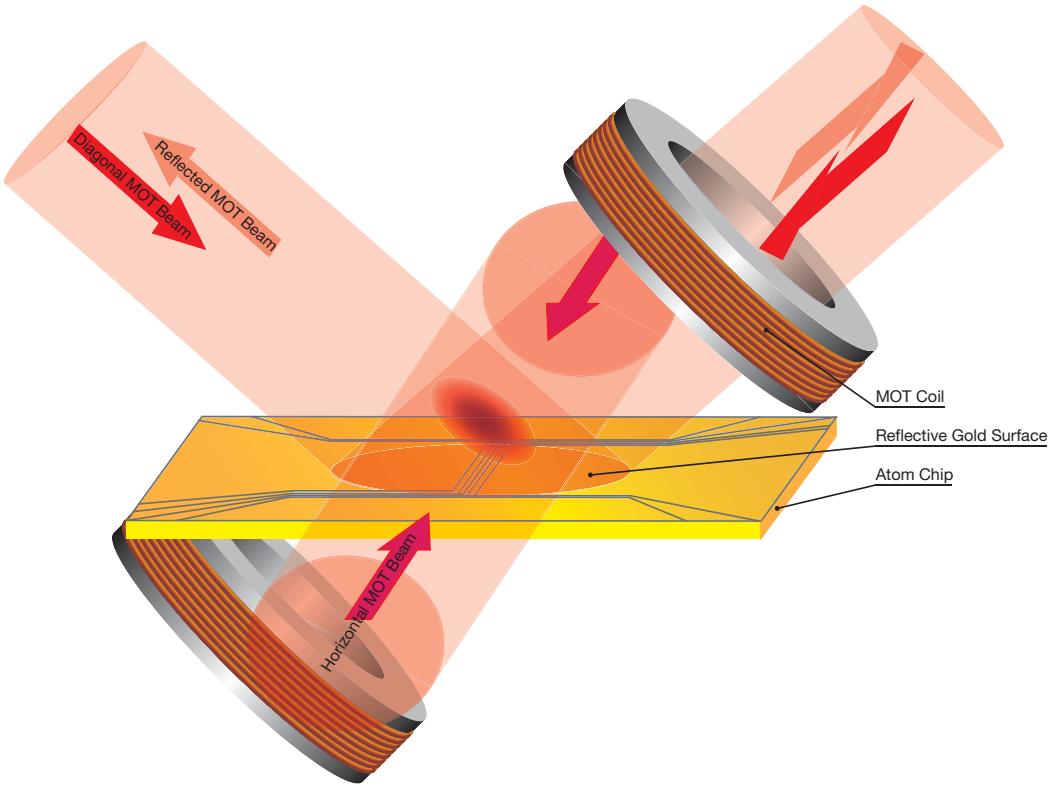

Figure 2.2: Mirror MOT.

$2\pi \times 6.07\,\mathrm{MHz}$ [46, 47, 48, 49]. The recoil of atoms as they scatter trap light from the MOT beams is responsible for the cooling and trapping of the atoms. The trap light also off-resonantly excites atoms into the $5^2\mathrm{P}_{3/2}$ $\mathrm{F}' = 2$ state. This transition is 266.650 (9) MHz red detuned from the trapping transition, so the trap light is approximately 245 MHz detuned from it [50]. From the $5^2\mathrm{P}_{3/2}$ $\mathrm{F}' = 2$ state they have high probability of decaying into the $5^2\mathrm{S}_{1/2}\mathrm{F} = 1$ ground state. This state being 6.8 GHz detuned from the trapping transition, is effectively dark to trap light. A second frequency - 'repump' light - is added to the MOT beams, resonant with the $5^2\mathrm{S}_{1/2} \longrightarrow 5^2\mathrm{P}_{3/2},\ \mathrm{F} = 1 \longrightarrow \mathrm{F}' = 2$ transition. This pumps atoms out of the $F = 1$ ground state back into the $F = 2$ ground state to maintain a high population cycling on the trapping transition.

The MOT beams are 25 mm in diameter. Their polarisation is σ_- relative to the direction of the magnetic field along the axis of the mMOT quadrupole as the incoming beams propagate towards the centre of the MOT (see fig. 2.1 in [45], for example). This ensures atoms preferentially scatter light from the beam propagating towards the centre of the MOT, providing confinement for the atoms [51, 43]. The intensity of trap light at the centre of each beam is above the saturation intensity for the trap transition, $I_{sat} = 3.577\,\mathrm{mW\,cm^{-2}}$ [46]. The total power in each of the horizontal MOT beams is 12 mW and is 20 mW in each diagonal beam. Once loaded, the power in the horizontal MOT beams is reduced, elongating the cloud along the direction of the horizontal beams. There is 2 mW of repump light in each beam.

The mMOT is centred 4 mm above the chip surface, and when fully loaded is $5-7$ mm long and 2 to 3 mm wide. The temperature is estimated to be $100\,\mu$K from its ballistic expansion after the MOT beams are switched off (see sec.3.2.2). The density in a MOT is limited by reabsorption of scattered photons and is typically between 10^{10} and $10^{11}\,\mathrm{cm^{-3}}$ [52, 53]. Between 10^8 and 10^9 atoms are loaded over 12 s into the mMOT from an intense beam of cold atoms from a low velocity intense source (LVIS) [54, 55]. The number and density of the mMOT is estimated from images of its fluorescence (see sec.2.1.8).

The LVIS is a 6 beam free space MOT in an adjoining vacuum chamber. It has a shadow along one of the retro-reflected beams formed by a 1 mm hole in the extraction mirror. This 6 mm thick mirror separates the LVIS chamber from the

science chamber. A cold, collimated beam of atoms is pushed along the shadow in this beam, away from the centre of the LVIS-MOT passing through the hole in the extraction mirror, and into the science chamber. The LVIS is aligned so the atomic beam is directed at the mMOT.

A rubidium dispenser is situated in the LVIS chamber. It is run continuously throughout the day, providing a steady source of rubidium vapour[2]. The LVIS allows us to load the MOT with a high flux of ^{87}Rb, with little increase in pressure in the science chamber from the dispensing of rubidium. This allows fast loading of the mMOT whilst maintaining the low pressure needed to make and hold BECs.

The mMOT loading time can be can be decreased from 12 s to about 5 s by increasing the rubidium vapour pressure in the LVIS chamber by running a higher current through the rubidium dispensers. This would increase the repetition rate of the experimental sequence by about 20%. The cost of running the dispensers at the required higher current is that they would need replacing every few months. Replacement of the three dispensers in the LVIS chamber is roughly a two week process, and runs a small risk of contamination of the UHV conditions in the science chamber. However, this is not the most cost effective way of increasing the repetition rate. Currently almost 50% of the experimental sequence time is taken by software processing and dead time which prevents software timing conflicts between multiple programs used to run the experimental hardware.

2.1.2 UMOT

The mMOT has a poor spatial overlap with the magnetic trap into which atoms are ultimately loaded. The atoms are therefore first loaded into an elongated narrow MOT, called the 'U'-MOT (UMOT), which is centred 500 μm from the chip surface. The same beams are used for the mMOT and UMOT, however the magnetic quadrupole field of the UMOT is produced by the 'U' shaped current distribution shown in figure 2.3 on the chip surface, and an external bias field. This creates a quadrupole field with high radial confinement ($\partial_r B \approx 150\,\mathrm{G\,cm^{-1}}$), stretching out over almost the entire 7 mm central section of the chip wires. The tight radial con-

[2]Both ^{85}Rb and ^{87}Rb. The LVIS-MOT and LVIS atomic beam contain only ^{87}Rb as ^{85}Rb requires a different set of frequencies for laser cooling and trapping

finement allows the UMOT to be brought close to the chip without losing atoms through collisions with the chip surface.

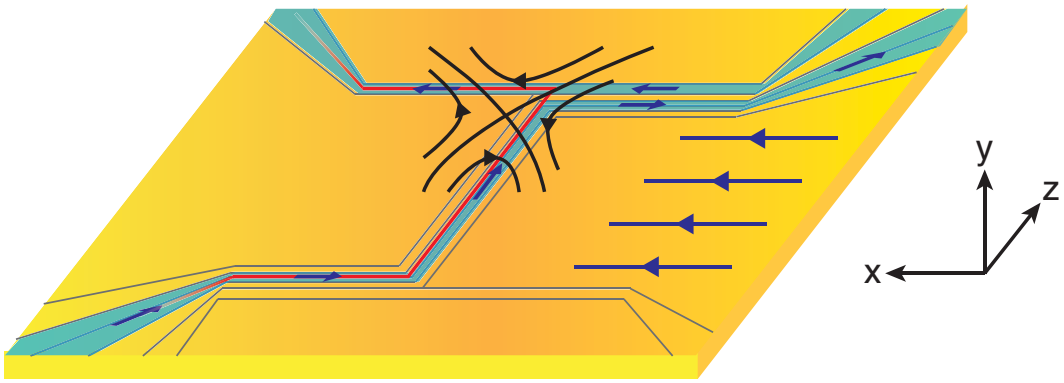

Figure 2.3: Current distribution (shaded blue and blue arrows) and magnetic bias fields (parallel blue arrows) used to produce the UMOT quadrupole field (black lines). 1 A is run through each of the small Z wires. 2 A are run through the end wire in so that the current opposes that in the end part of the small Z wires where they run parallel. The field along these anti parallel currents cancels, and we are left with the field from a 'U' shaped current distribution. The x bias field cancels the field circulating around the central section of the Z wires to form a quadrupole field in the $x-y$ plane. The field is asymmetric as the quadrupole centre is rotated outwards from the centre of the U by the field from the end sections of the U. The field from the ends of the U combine with that from the central section to complete the quadrupole in the $y-z$ plane (not shown here).

Atoms are transferred from the mMOT to the UMOT by overlapping the UMOT quadrupole field, then ramping up the UMOT current while ramping down the mMOT coils. A uniform bias field that controls the distance of the field minimum from the chip surface is simultaneously increased. This smoothly changes the magnetic field, and sweeps the atoms towards the chip surface, over a period of 100 ms. Over the last 30 ms, the trap light is detuned by a further 20 MHz, reducing the radiation pressure from scattered photons in centre of the UMOT, increasing the UMOT density. Previously [56], the transfer from mMOT to UMOT in our experiment was achieved by a sudden switch over from one quadrupole field to another. This method, new to our experiment, provides a more efficient and reliable way to transfer the atoms and is described in detail in section 3.1.

2.1.3 Optical Molasses

Atoms are then released from the UMOT into an optical molasses by switching off the UMOT current. The MOT beams are further red detuned by 36 MHz at the end of the UMOT so they are 76 MHz red detuned by the beginning of the optical

molasses stage. This reduces the scattering rate and therefore heating rate from photon recoil, lowering the temperature the atoms can reach through sub doppler cooling. The optical molasses also damps motion induced by field gradients as the quadrupole field is turned off.

Although still cooled, the atoms are no longer trapped and the cloud slowly expands. The optical molasses stage is kept short, between 2 and 3 ms, to prevent significant loss in phase space density. The trap light is then switched off, but the repump light remains on for optical pumping, described next.

2.1.4 Optical pumping

Once the trap light is off, almost all atoms decay to the $|5^2, \mathrm{S}_{1/2}, \mathrm{F} = 2\rangle$ ground state. A few decay to $|5^2, \mathrm{S}_{1/2}, \mathrm{F} = 1\rangle$, but they are rapidly pumped into the $|5^2, \mathrm{S}_{1/2}, \mathrm{F} = 2\rangle$ ground states while the repump light is left on. These atoms are distributed over all $2\mathrm{F}+1$ Zeeman sublevels, denoted by $\mathrm{m_F}$. Ultimately, the atoms are to be trapped magneticaly - as described in sec.2.1.5 below. To do so, they must be in either the $\mathrm{m_F} = 1$ or $\mathrm{m_F} = 2$ sublevel. In this stage, we therefore prepare the atoms in the correct sublevel for magnetic trapping by optically pumping them.

The optical pumping light is circularly polarised to drive σ^+ transitions which pump the atoms into the $\mathrm{m_F} = 2$ state. In this state the magnetic trap is strongest and deepest. To set the correct circular polarisation, a 1 G uniform magnetic field is applied along direction the beam propagates, and the beam is left-hand circularly polarised with respect to this direction. The atoms are pumped on the $5^2\mathrm{S}_{1/2} \longrightarrow 5^2\mathrm{P}_{3/2},\ \mathrm{F} = 2 \longrightarrow \mathrm{F}' = 2$ transition with a 500 μs pulse which has an intensity of a few $\mathrm{mW\,cm^{-2}}$. The $|\mathrm{m_F} = 2\rangle$ state is dark to this light. After optical pumping, we measure up to 6×10^7 atoms from absorption images, and temperatures of between 80 and 120 μK from the ballistic expansion of the gas.

2.1.5 Magnetic Trap

The magnetic trap field is produced by running 1 A through each of the two small Z wires on the atom chip, together with a uniform bias field in the $\hat{\mathbf{x}}$ direction. The

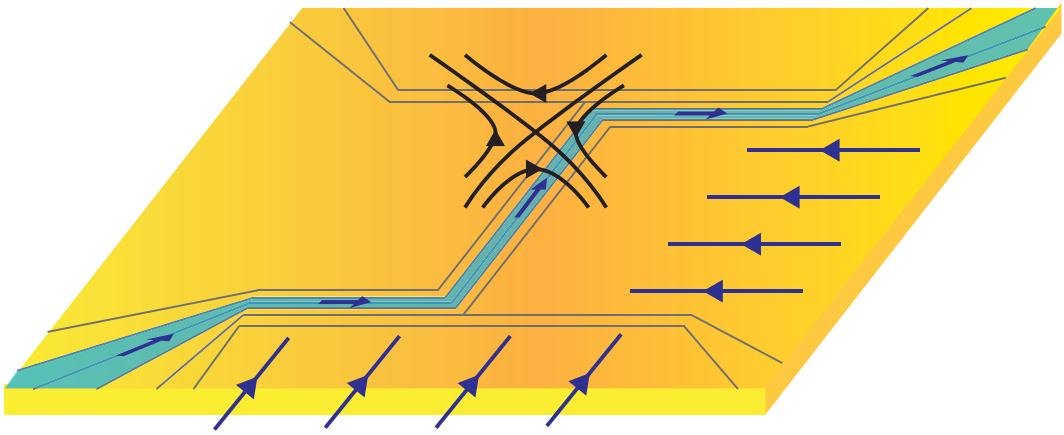

Figure 2.4: Current distribution (shaded blue and blue arrows) and magnetic bias fields (parallel blue lines) used to produce the magnetic trap potential. The 2-d quadrupole in the (black lines) $x - y$ plane is created by the central part of the small Z wires and the x bias field. The minimum occurs at the height that the x bias ≤ 35 G completely cancels the field from the Z wires (110 to 200 μm). This minimum is raised above zero by the z bias field (1 to 10 G). The field from the end sections of the Z wires provides axial confinement.

x bias and the field circulating around the central parts of the Z wires form a 2-d quadrupole field giving the tight radial confinement of the trap. The two end parts of the Z wires give axial confinement. As in the UMOT, the axial confinement is weak, rising strongly only over the last few hundred μm from the ends of the trap. To prevent spin flip loss [57] as atoms pass through the (2-d) quadrupole minimum [58], a z bias field is applied, raising the field minimum above zero, and smoothing the variation of the field direction. It also increases the Zeeman splitting between the spin states, reducing the probability of spin flip loss from oscillating stray fields.

The magnetic trap field is ramped up smoothly over 3 ms to capture atoms from the thermal cloud. Raising the trap potential increases the energy of atoms in the cloud. In turn this raises the temperature of the cloud as it thermalises through interatomic elastic collisions. After 20 ms there are typically between 3 and 3.5×10^7 atoms in the magnetic trap, and the hottest atoms can be seen escaping from the trap. The magnetic trap is compressed over the next 20 ms by increasing the x bias field to 35 G. This moves the trap closer to the chip (110 μm from its surface), increases the radial confinement, and increases the density and collision rate. A high collision rate is needed to permit fast evaporation in the next stage of cooling, as discussed in sec.4.1.3. After 600 ms the trapped cloud has thermalised, and we measure between between 2 and 3×10^7 atoms at a temperature of 120 μK.

2.1.6 Evaporative cooling to BEC

To cool the magnetically trapped cloud, the most energetic atoms are selectively removed from the trap. This is achieved using an rf field to flip the spin so that these atoms are ejected from the trap. The energy of the remaining atoms is redistributed as they thermalise through elastic collisions, and thus the temperature is lowered. The trap depth is gradually lowered by reducing the r.f. frequency, continuously forcing the cloud to cool. The maximum cooling rate is limited by how fast the energy can be redistributed, and therefore by the elastic collision rate.

Despite the forced loss of atoms, the density and elastic collision rate can increase because the size of the cloud decreases as the temperature drops. This depends on the geometry of the trap and how fast and how efficiency the cloud can be cooled and is discussed in section 4.1. When the elastic collision rate increases with time, the cooling becomes faster, leading to further increase in the collision rate. In this case the evaporation processes is described as 'runaway' [59]. Runaway evaporation ensures the process is sustainable and that the phase space density increases with time. It is important to be in this regime to cool to BEC.

As the temperature drops below the critical temperature T_c, which depends on number, a fraction of the cloud condenses into a Bose Einstein condensate. This usually occurs when the rf field is tuned to eject atoms having energy approximately 50 kHz above the trap bottom. As the rf frequency decreases further, the thermal cloud reduces, and the condensate fraction increases, until we have an almost pure Bose Einstein condensate.We produce a condensate after 8 s of evaporative cooling. When the initial atom number is particularly high, this can be done in under 5 s.

The currents in the Z wires meanders a little from side to side because of defects in the edges and the bulk of the wires [60, 61, 62, 63, 64]. The small transverse currents ($\lesssim 1\,\mu$A) cause small fluctuations in the axial magnetic field along the length of the trap close the trap bottom. This gives rise to roughness in the axial trap potential. At temperatures below $1\,\mu$K, this causes the cloud to fragment into several clouds at the various local minima in the rough potential along the axis of the trap. Our condensate forms in one or more of these minima, where the axial confinement of the condensate has a characteristic frequency between 5 Hz and 15 Hz. The radial

frequency of the trap is typically 2 kHz, and the number of atoms in a condensate is typically between 10^4 to 4×10^4.

2.1.7 Experiments with the BEC

With a computer interface controlling the laser light, the rf field, and the magnetic fields, the apparatus can be configured to perform a wide range of experiments.

Controlling the bias fields and currents through the chip wires we can precisely control the position and confinement of the trap in which the condensate sits. The x & y bias fields can be used to vary the distance of the trap from the chip wires and chip surface, at the same time changing the radial trap frequency. The z bias can be used to vary the radial trap frequency independently. The aspect ratio ω_r/ω_z can be tuned to adjust the dimensionality of the condensate from 3D to quasi-1D.

Finally, we can use the rf field to dress the potential [65, 66, 67]. This allows us to vary the ratio between ω_x and ω_y, and to smooth the roughness of the axial potential [68]. Such dressed potentials have previously been used in our experiment to split the condensate for matter wave interferometry [69, 56, 70].

Our current focus is on measuring the dynamics of the condensate. We can excite and measure centre of mass and dipole oscillations, both longitudinal and transverse. To excite longitudinal centre of mass oscillations, we use the end wires on our atom chip to move the centre of the trap without changing its curvature. We modulate this displacement at the axial trap frequency ω_z to resonantly drive centre of mass oscillations of the condensate. We explore the decay of this motion in the presence of a thermal cloud. By varying the trap depth with the rf field, we can control the number of atoms in the thermal fraction. We measure the effect this has on the decay rate. Our results are presented in chapter 8.

2.1.8 Imaging

We describe two imaging techniques we shall refer back to throughout this thesis, fluorescence imaging and absorption imaging, which we use to image cold atomic

clouds. During optical stages of the sequence given above we use fluorescence imaging, while for dark stages, such as when atoms are magnetically trapped, we use absorption image. The setup of the imaging apparatus is describe in the sec.2.2.4 further below.

Fluorescence Imaging

For optical stages, the atoms scatter the light of the MOT beams causing them to fluoresce. We image this fluorescence onto a camera from which we can see the shape, size and position of our MOT in real time. Additionally, we can obtain an order of magnitude estimate of how many atoms are in the MOT based on its fluorescence measured from processed images, as described below.

An accurate estimate of the number of atoms our MOT from its fluorescence is difficult to obtain due to its optical thickness, the re-scattering of photons in its centre, and the spatially dependent polarisation of MOT beams together with the Zeeman manifold of hyperfine states. However, for an order of magnitude estimate, we neglect such features by assuming each atom is equally illuminated, and behaves like a two-level atom. The fluorescence per atom can then be calculated from the scattering rate,

$$R = \frac{\Gamma}{2}\frac{I/I_{\mathrm{sat}}}{1 + I/I_{\mathrm{sat}} + 4\left(\Delta/\Gamma\right)^2}, \tag{2.1}$$

where I is the total intensity from all (six) MOT beams that illuminate the atoms, $\Gamma = 2\pi \times 6.07\,\mathrm{MHz}$ is the natural line width of the cooling transition $5^2\mathrm{S}_{1/2} \longrightarrow 5^2\mathrm{P}_{3/2}$, $\mathrm{F} = 2 \longrightarrow \mathrm{F}' = 3$ [46, 47, 48, 49], $\Delta/2\pi$ the detuning of the MOT beams from this transition which is typically 12 MHz, and I_{sat} is the saturation intensity. Since polarisation of the MOT beams varies with position, and the atoms, which are distributed over all m_{F} states, move rapidly around rapidly, we use the the saturation intensity for an isotropic polarisation, $I_{\mathrm{sat}} = 3.58\,\mathrm{mW\,cm^{-2}}$ [46, 47, 48, 49]. The total intensity is typically about $15\,\mathrm{mW\,cm^{-2}}$ in our experiment.

The total number of emitted photons from a MOT containing N atoms over time interval ΔT is approximately $NR\Delta T$. By measuring the fluorescence from the MOT we can estimate the number of atoms in the MOT. For MOTs such as ours which are optically thick, not all atoms are illuminated with the same intensity,

thus reducing the scattering rate for atoms deep inside the MOT. In addition, some scattered photons may be re-scattered by other atoms, thus NR is an overestimate of the total fluorescence.

This fluorescence is spread evenly over 4π sr. We image only a small fraction of this, captured by a lens of radius $r_{\rm l} = 25\,$mm, onto the CCD (charge coupled device) of our camera. This lens is located a distance $d = 150\,$mm from the atoms, and hence captures a small fraction

$$\kappa = \pi r_{\rm l}^2/(4\pi d^2) \tag{2.2}$$

of the light scattered by the MOT. Furthermore, each optic reduces the intensity of this captured light, and the camera's CCD detects this light with an efficiency of approximately 0.18 counts per photon [71]. Taking into account the vacuum chamber window, two lenses, and the mirror shown in fig.2.15a in the apparatus section below, our combined detection efficiency η is approximately 0.16. We take an image of the fluorescing cloud with an exposure time ΔT, typically 2 ms. We select a region around the cloud in this image, over which we sum the pixel counts. Outside this region there may be scattered light from other objects in the chamber such as the atom chip assembly or the MOT coils. The number of atoms in the MOT is estimated from the totalled pixel counts $n_{\rm pxl}$ as,

$$N = n_{\rm pxl}/\left(R\Delta T\eta\kappa\right). \tag{2.3}$$

For our setup this corresponds to approximately 0.12 atoms per pixel count.

Absorption Imaging

For other stages where there is no light, we image the cloud through a technique known as absorption imaging. The cloud of atoms is illuminated by a laser beam close to resonance with an optical transition - we use the cooling transition $5^2{\rm S}_{1/2} \longrightarrow 5^2{\rm P}_{3/2},\ {\rm F} = 2 \longrightarrow {\rm F}' = 3$. Atoms scatter some of the light from this beam, which for an intensity small compared to $I_{\rm sat}$ is distributed evenly over 4π sr. This casts a shadow of the atoms in the beam, which we image onto a camera. We measure

the column density of the atomic cloud by comparing this shadow image to an image taken shortly after, where no atoms are present. Unlike fluorescence imaging of atom in a MOT, this technique is destructive for magnetically trapped atoms, since scattering can leave atoms in un-trapped states, and the photon recoil heats leading to considerable trap loss.

Let $I_0(x, y)$ be the intensity of a beam propagating in a direction we label $\hat{\mathbf{z}}$. Then the intensity of this beam after passing through a cloud with density $n(\mathbf{r})$ is given by the Beer Lambert law,

$$I(x, y) = I_0(x, y) \exp\left(-\sigma n_c(x, y)\right). \tag{2.4}$$

where

$$n_c(x, y) = \int \mathrm{d}z\, n(\mathbf{r}) \tag{2.5}$$

is the column density of the cloud. The scattering cross section σ of atoms in the beam is

$$\sigma \approx \frac{hc}{\lambda}\frac{\Gamma}{2}\frac{1/I_{\mathrm{sat}}}{1 + 4\left(\Delta/\Gamma\right)^2}, \tag{2.6}$$

assuming that the atomic transition is far from being saturated, i.e. $I \ll I_{\mathrm{sat}}$. In our experiment we typically have a peak intensity of $0.2\,\mathrm{mW\,cm^{-2}}$ in our imaging beam. The frequency is tuned to resonance such where eq.(2.6) becomes $\sigma = 3\lambda^2/(2\pi)$, using $I_{\mathrm{sat}} = \hbar\omega^3\Gamma/(12\pi c^2)$ [46]. By measuring the attenuated intensity profile $I(x, y)$, and the initial intensity $I_0(x, y)$, we can invert eq.(2.4) to find the column density of the cloud,

$$n_c(x, y) = \frac{1}{\sigma}\log\left(I_0(x, y)/I(x, y)\right). \tag{2.7}$$

We measure $I(x, y)$ by imaging it onto the CCD of our camera. Each pixel on the CCD gives a number of counts $N_{\mathrm{pxl}}(x_i, y_j)$ which is proportional to the $A\Delta t I(x_i, y_j)$, where $A = 3.45 \times 3.45\,\mu\mathrm{m}^2$ is the pixel area and Δt is the exposure time, and (x_i, y_j) are the pixel coordinates. In addition to this shadow image we take a second image a few tens of ms later, but without any atoms present when the light intensity imaged onto the CCD is $I_0(x, y)$. Similarly, in this image, a pixel at (x_i, y_j) gives the number of counts $N_{\mathrm{pxl}_0}(x_i, y_j) \propto A\Delta t I_0(x_i, y_j)$. The ratios $N_{\mathrm{pxl}_0}(x_i, y_j)/N_{\mathrm{pxl}}(x_i, y_j)$ and $I_0(x_i, y_j)/I(x_i, y_j)$ are equal provided that the intensity varies approximately

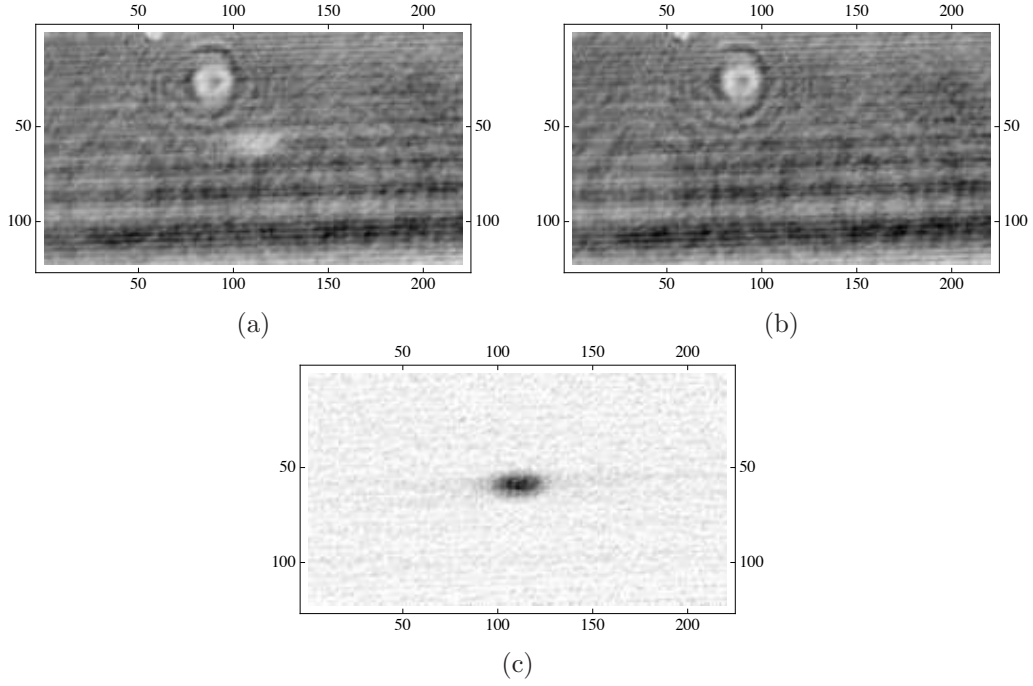

Figure 2.5: Absorption images of a Bose-condensed cloud of atoms. Figure 2.5a is the shadow image proportional to $I(x_i, y_j)$. The shading is negative, so darkest regions indicate higher intensity. Figure 2.5b is the background image, proportional to $I_0(x_i, y_j)$. Figure 2.5c is the processed image, proportional to $n_c(x_i, y_j)$, where the darker regions indicate higher density. The scale on all images are the pixel indices i and j, and each pixel is $3.45 \times 3.45\,\mu$m.

linearly over a pixel, as it is the case for the images discussed in this thesis.[3] Thus, the column density at (x_i, y_j) is,

$$n_c(x_i, y_j) = \frac{1}{\sigma} \log\left(\frac{N_{\mathrm{pxl}_0}(x_i, y_j)}{N_{\mathrm{pxl}}(x_i, y_j)}\right) \tag{2.8}$$

We can find the 1D density profile by summing $n_c(x_i, y_j)$ over the pixels in the vertical (j) or horizontal (i) directions and multiplying by the pixel width $\sqrt{A}$. The atom number is found by summing over both i and j, and multiplying by the pixel area A.

Figure 2.5 shows the absorption images before and after processing. The first image, fig.2.5a, is the shadow image. The second image, fig.2.5b, is the background image without any atoms. The shading in these images is negative in the sense that the darkest points correspond to brightest parts of the imaging beam intensity, where the pixel count is highest. In both these images there are many fringes visible from

[3]From a second order taylor expansion of these intensities with respect to x and y, it is straight forward to show that this condition is $A\nabla^2 I(x,y)|_{x_i,y_j} / (24 I(x_i, y_j)) \ll 1$.

optical aberration in our imaging system, but these disappear once the absorption image is processed. The only difference between the fig.2.5a and fig.2.5b is the light colour spot in the centre of fig.2.5a which is the shadow of a Bose condensed cloud of atoms. Figure 2.5c shows the the absorption image found by dividing the background image by the shadow image and taking the logarithm. The shading in this image is proportional to the column density of the cloud, with the darkest region representing the highest density.

2.2 Apparatus

This section describes the main components of the experiment and how they work together to form our BEC experiment. A flow diagram of the apparatus is shown in figure 2.6, with experimental components organised into blocks by their function.

The focus of the experiment, the atom chip, is housed within a ultra-high vacuum chamber. Here, ^{87}Rb is captured from the 'low velocity intense source' (LVIS) by a MOT, before it is magnetically trapped and evaporatively cooled to a BEC at the surface of the atom chip where experiments are then performed. The vacuum system described in section 2.2.1, includes a high vacuum chamber and an ultra-high vacuum chamber, vacuum pumps, the atom chip, and all the magnetic field generating coils that are mounted around and inside it.

The laser system has four sets of beams that feed into the vacuum chambers, each requiring the correct polarisation, intensity, precise timing, and frequency control. The lasers used for laser cooling and trapping of ^{87}Rb, optical pumping, and detection of the atoms are discussed in section 2.2.3.

The experimental sequence is computer controlled by two separate PCs. PC1 is programmed to give, with sub millisecond accuracy, a timed sequence of digital and analogue voltages to the experimental control hardware, and instructions to the USB and firewire devices. The hardware controls the light and magnetic fields for the experimental sequence. PC2 stabilises the magnetic field around the vacuum chamber at the request of PC1. Images of the BEC are then taken and sent back to PC1. Components of the experiment are described in detail in the following sections.

2.2.1 Vacuum Chamber and Coils

The vacuum system consists of the science chamber (fig.2.7) where we produce the BEC, and the LVIS chamber (fig.2.9), where we dispense, pre-cool and produce a cold collimated beam of ^{87}Rb vapour. They are connected through a 1 mm diameter

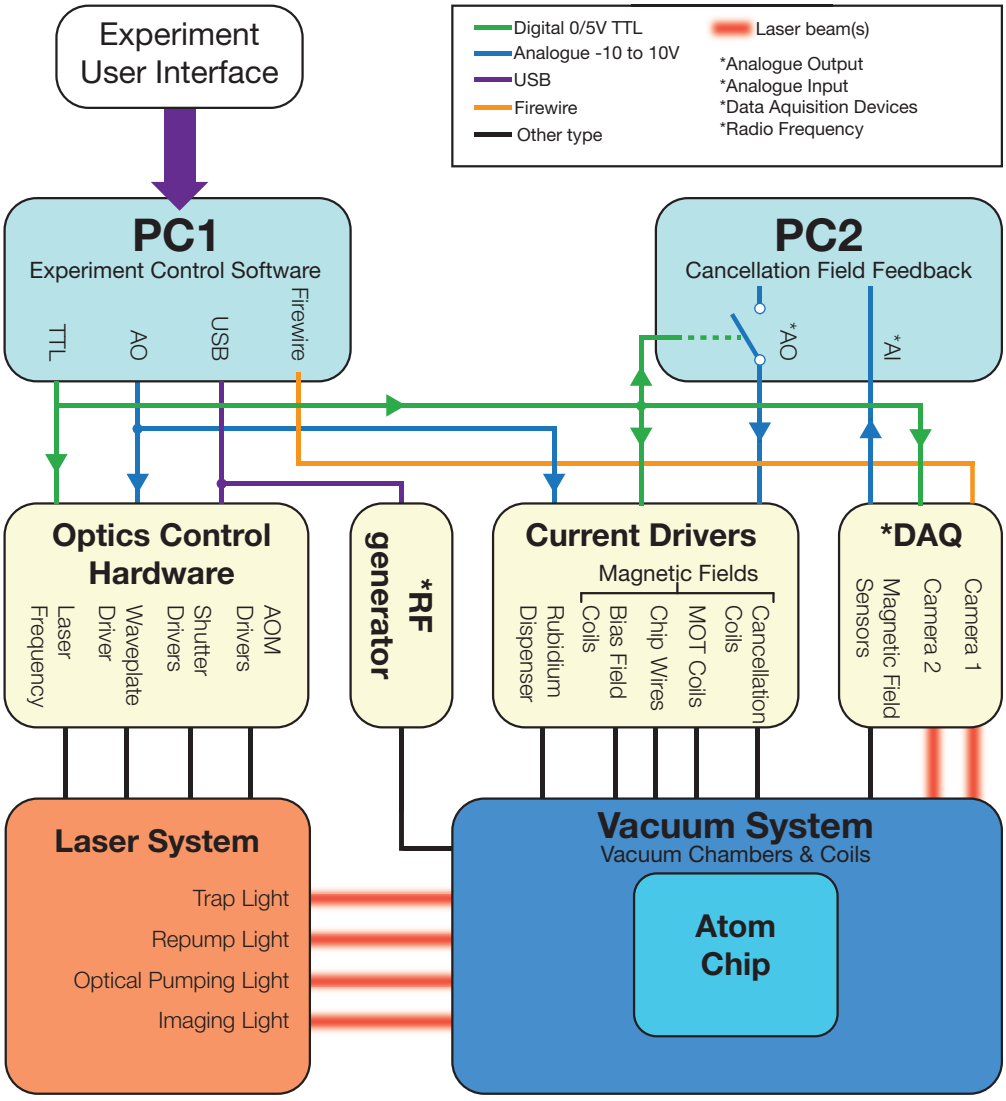

Figure 2.6: Apparatus flow diagram. Components are grouped into the following categories: User interface, computers, experimental control hardware, laser system, vacuum system & coils, and atom chip contained within. From top to bottom these categories are; the user interface, computers, experiment control hardware, the laser system (left), the vacuum system (right), and the atom chip contained inside it. The computers interface with the control hardware, which in turn control laser system and magnetic fields in the experiment. The type of interface used is indicated by the colour coded lines. Arrows show the direction of the interface. USB and firewire provide 2-way communication.

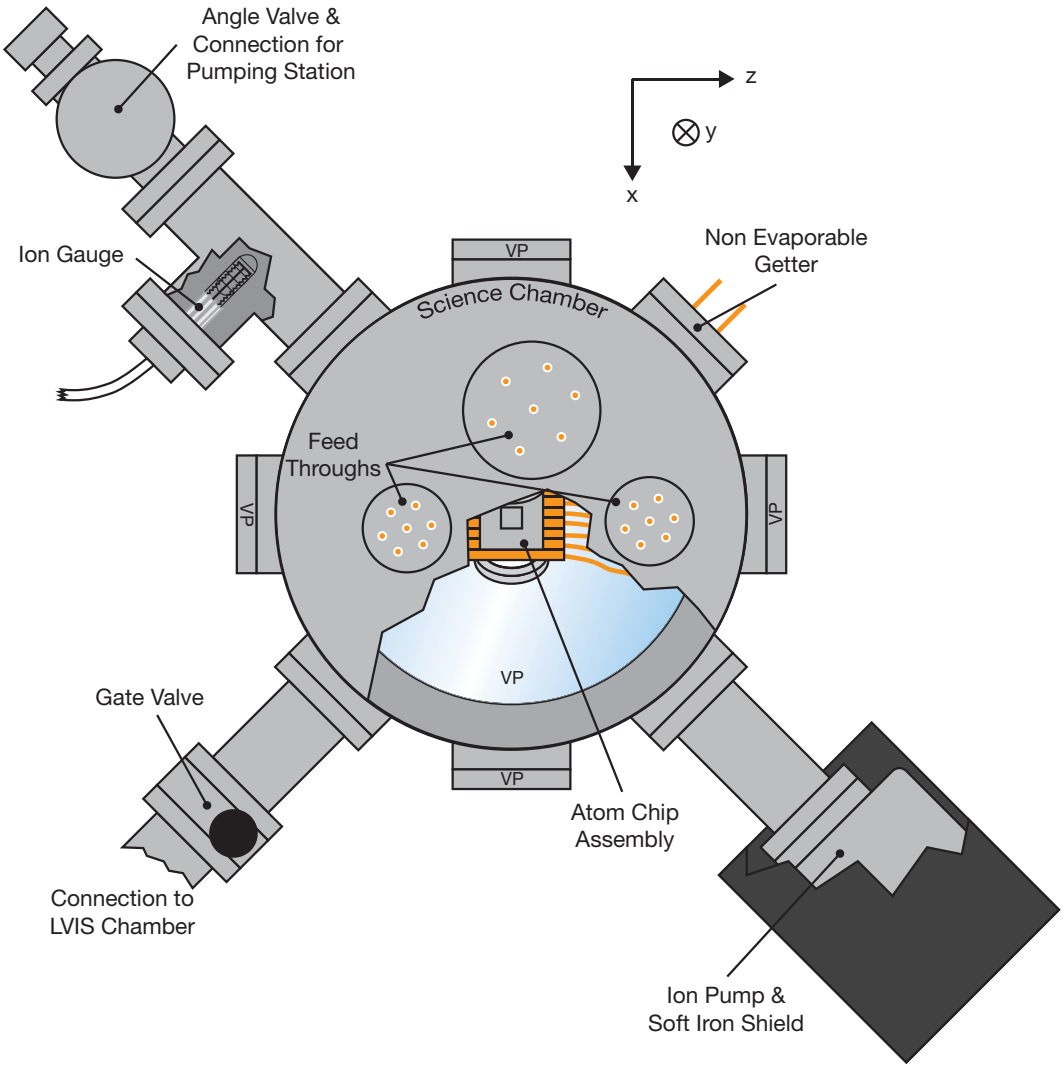

Figure 2.7: The science chamber. Parts labelled VP are view ports. The section labelled connection to LVIS chamber joins with the connection in the LVIS chamber diagram in figure 2.9.

hole in the 6 mm thick extraction mirror, through which the ^{87}Rb beam passes. The low conductance through this hole, and the continual pumping on science chamber supports a high pressure differential between the two chambers. In the science chamber we measure a pressure between 5×10^{-11} and 10^{-10} Torr on a Bayard-Alpert ionisation gauge, and in the LVIS chamber we measure a pressure between 10^{-8} and 10^{-7} Torr from the current reading on our ionisation-pump.

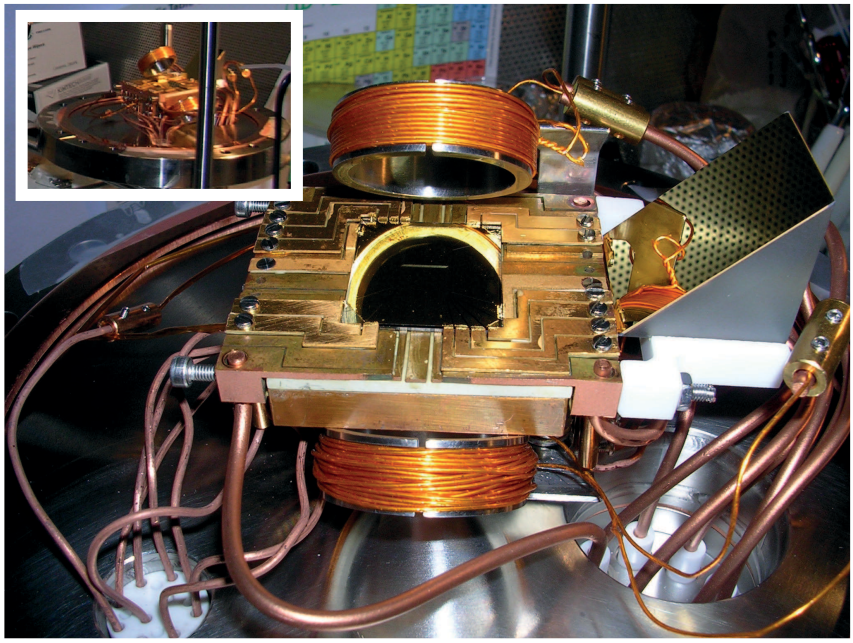

Figure 2.8: A photograph of the inside of the top flange before it was bolted to the top of the science chamber. The atom chip assembly is attached to this flange. Electrical connections to the atom chip are made through feed throughs in this flange. Note that the atom chip will be suspended upside down once the flange is attached. The inset shows more of the same flange. The vertical posts are a temporary support structure used during construction and are not part of the final flange assembly.

Science Chamber

As shown in fig.2.7, the science chamber is a 10 port spherical octagon vacuum chamber, made of 316 grade stainless steel by Kimball Physics inc, with 8″ DN160 CF conflat ports on the top and bottom, and eight $2\frac{3}{4}''$ DN40 CF conflat ports around the sides.

Figure 2.8 shows the top flange together with the atom chip assembly (see sec.2.2.2 below) which is mounted to it. The top flange is a customised 8″ DN160 CF flange onto which the atom chip assembly is attached (see 2.2.2). This flange contains 3 feed-through flanges, that provide electrical connection to the atom chip assembly, and the MOT coils.

The bottom flange is an 8″ DN160 CF view port with 8 mm thick glass, through which some of the MOT beams enter and leave the science chamber. The z-axis imaging, described in shown in sec.2.2.4, is also through this port. Four view ports are also mounted on the side ports along the x and z axes of the chamber. These

provide optical access for the remaining MOT beams, imaging beams, and optical pumping beams, and for viewing fluorescence (sec.2.1.8).

The four other side flanges connect to the LVIS chamber, a Varian VacIon Plus 20 ionisation pump, a UHV-24p Nude Bayard-Alpert ionisation gauge, and a non evaporable getter. The getter is mounted directly opposite the incoming beam of atoms from the LVIS chamber. The ion pump is connected by a $6''$ long tube, and is magnetically shielded by a 4 mm thick mild steel case to limit its influence on the magnetic trap. The ion gauge is mounted on a T-piece, the third arm of which is attached to an angle valve for pumping down and venting the science chamber. The connection to the LVIS chamber can be closed by a Lesker SS copper bonnet gate valve. This allows a pressure of 10^{-11} Torr to be maintained in the science chamber whilst venting the LVIS chamber to atmosphere when replacing the rubidium dispensers.

The magnetic field coils, described later in sec.2.2.1, are mounted around the science chamber and on the view ports. These coils produce the bias fields in the $\hat{\mathbf{x}}, \hat{\mathbf{y}}$, & $\hat{\mathbf{z}}$ directions, with high uniformity over the trapping region[4].

LVIS Chamber

Figure 2.9 shows the LVIS chamber which consists of two six-way crosses, with a number of adjoining sections. The parts are labeled ① to ⑦. ① The LVIS MOT sits in the centre of one of these, a modified $2\frac{3}{4}''$ conflat six-way cross. The four ports on the top, bottom and sides of the cross are fitted with $2\frac{3}{4}$" view ports, giving optical access for the LVIS MOT beams. Coils for the magnetic quadrupole, and two orthogonal bias fields are wound round the arms of these ports. A 45° view port enables fluorescence imaging of the LVIS MOT.

The extraction mirror ② is fitted into a CF DN40 flange connected to the arm of the six way cross leading to the science chamber. The extraction mirror is a 6 mm thick $\lambda/4$ waveplate with its back surface gold coated and a 1 mm diameter hole through its centre.

[4]The trapping region is defined as points within 10 mm from the centre of the chip. The MOT, UMOT, and magnetic trap fall within this region

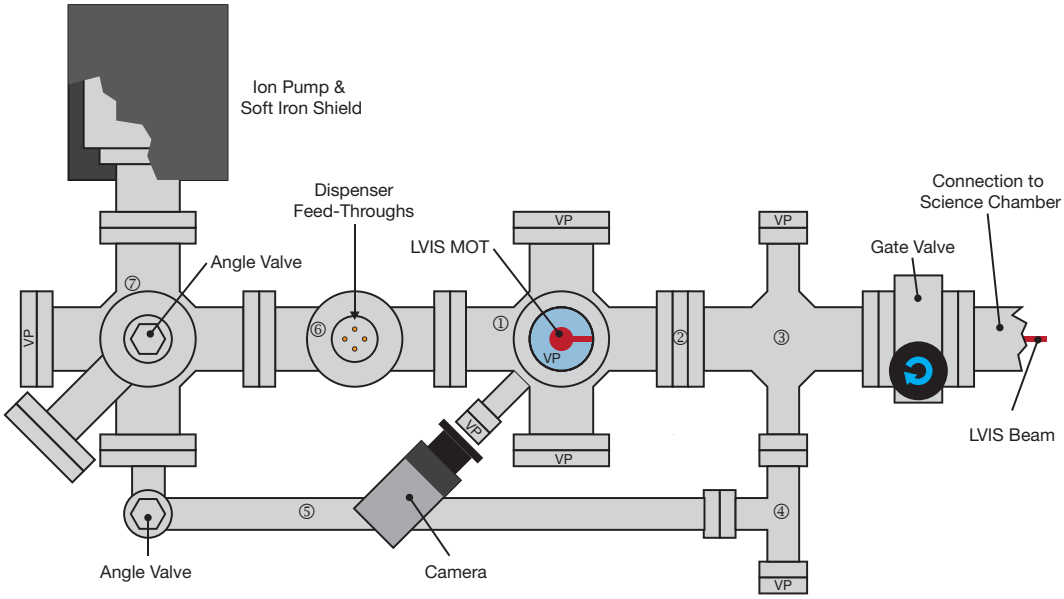

Figure 2.9: The LVIS vacuum chamber. The sections are numbered and listed following the sequence of the main text. ① LVIS MOT six-way cross. ② Extraction mirror flange. ③ Four-way cross (UHV). ④ By-pass T-piece (UHV). ⑤ By-pass tube (UHV) and angle valve. ⑥ Dispenser T-piece. ⑦ Six-way cross. Sections ③ to ⑤ are under UHV. Other sections are under HV ($10^{-8} - 10^{-7}$ Torr), maintained by a 25 l s-1 ion pump. Flanges labelled VP are view ports

A four way cross ③ is connected on the UHV side of the extraction mirror. This connects the LVIS chamber to the gate valve separating the LVIS and science chambers. On one side of the four-way cross is a $1\frac{1}{3}''$ view port, and the other the bybass T-piece ④, also fitted with a $1\frac{1}{3}''$ view port. These view ports give optical access for diagnostics on the LVIS beam. The by-pass T-piece connects the UHV side of the extraction mirror back to the HV side, through the by-pass tube ⑤ and angle valve. Under operating conditions the by-pass angle valve is closed. Since the extraction hole has low conductance, the by-pass is opened to increase the pumping speed on the UHV side of the extraction mirror when pumping out the LVIS chamber. When venting, it is used to equalise the pressure difference across the extraction mirror.

The dispenser T-piece ⑥ is attatched to the opposite side of the LVIS MOT six-way cross. The adjoining flange to the dispenser T-piece is a $2\frac{3}{4}''$ to $1\frac{1}{3}''$ adapter, fitted with a $1\frac{1}{3}''$ feed through flange. The four feed throughs provide electrical connection for three SAES Rb/NF/6.4/17/FT10+10 rubidium dispensers.

The dispenser T-piece connects to a second six-way cross ⑦ ($2\frac{3}{4}''$ conflat). The

top port of this six-way cross is fitted with an angle valve for pumping out the LVIS chamber. On one side of the six-way cross is another ionisation pump (same as science chamber). This ion pump is also magnetically shielded. The other side connects to the by-pass angle valve and tube ⑤. The end port has a $2\frac{3}{4}''$ view port, providing optical access for the LVIS MOT beam that is partially retro-reflected from the extraction mirror, known as the 'push beam'.

The LVIS collects atoms from the background vapour of Rubidium atoms in the LVIS chamber. A stream of atoms (with typical velocity between 10 and 30 $\mathrm{m\,s^{-1}}$ [54, 55, 72, 73, 74, 75]) is then pushed through to the science chamber, where they are captured by the mMOT, cooled, and passed into the magnetic trap.

Bias Field Coils

Five pairs of magnetic field generating coils are mounted around the science chamber, and produce the bias fields for the mMOT, UMOT and magnetic trap. Table A.1 of appendix A gives the specifications for each pair. The currents run through these coils are controlled by the current drivers shown in 2.2.6.

These coils produce uniform bias fields in the directions $\hat{\mathbf{x}}$, $\hat{\mathbf{y}}$ and $\hat{\mathbf{z}}$ as labelled in figures 2.3 and 2.7. They are used in conjunction with the chip wires to form and shift the position of UMOT field and magnetic trap, and shift the position of the mMOT field.

Cancellation Coils

As well as bias field coils, there are three orthogonal pairs of magnetic field cancellation coils. These use measurements from three orthogonal flux gate magnetometers (Stephan Mayer FLC100) mounted on top of the science chamber, 50 mm from the chip surface, to null the stray lab fields from sources far from the chip [5]. The coils are 25 strand ribbon cables mounted round the science chamber in the Helmholtz

[5] An excellent test is the cancellation of the stray field from a 3 T superconducting magnetic 2 floors above our lab! With the cancellation coils the magnetic field measured at the minimum of the magnetic trap remains stable as the stray field is ramped up and down over 20 min cycles.

configuration with diameter 300 mm and separation 150 mm. They produce fields up to 1 G.

A field dependent voltage from the flux gates is sent to PC2, where it is time averaged, scaled, and fed back into the cancellation coil current drivers. For the cancellation of stray background fields the cancellation coils should be highly uniform over the distance between the chip and the field probes. The diameter of these coils is therefore 300 mm, larger than the other coils. We calculate by integrating the Biot-Savart law that this will provide field uniformity of better than 2% over the area covered by our atom chip.

The magnetic field cancellation system is limited by the flux gates which can only measure fields up to 1 G. They therefore cannot operate when the experiment is running. We sample and cancel the stray field between cycles.

2.2.2 Atom Chip Assembly

The atom chip is a 20×20 mm square, cut from a p-type silicon wafer with micro-fabricated wires milled into a $3\,\mu$m thick reflective gold surface. The micro-wires carry high current densities - routinely 6700 $\mathrm{A\,mm^{-2}}$ during the magnetic trapping stage - and produce tight magnetic micro-potentials with ω_r up to $2\pi \times 3$ kHz close to the surface of the chip. The gold surface reflects the MOT beams for the mirror MOT.

The silicon wafer has a resistivity of $17 - 33\,\Omega\,\mathrm{cm}$ [56]. Electrical insulation between the gold wires is provided by a 100 nm insulating layer of $\mathrm{Si\,O_2}$ deposited on the surface by wet oxidation. Since gold has poor adhesion to the $\mathrm{Si\,O_2}$ surface, a 50 nm layer of chromium is evaporated onto the surface prior to the gold. Gold is then evaporated onto the surface in five 600 nm layers.

To make the wires, a photo-resist mask is spun onto the gold surface. Areas to be etched away are removed through photo-lithograpy. The gaps between the wires are then ion beam milled through the Au, Cr and SiO_2 layers and $\approx 1\,\mu$m into the Si layer beneath. Figure 2.10 shows the dimensions of the wires. Further description of the fabrication process can be found in [56, 76, 77].

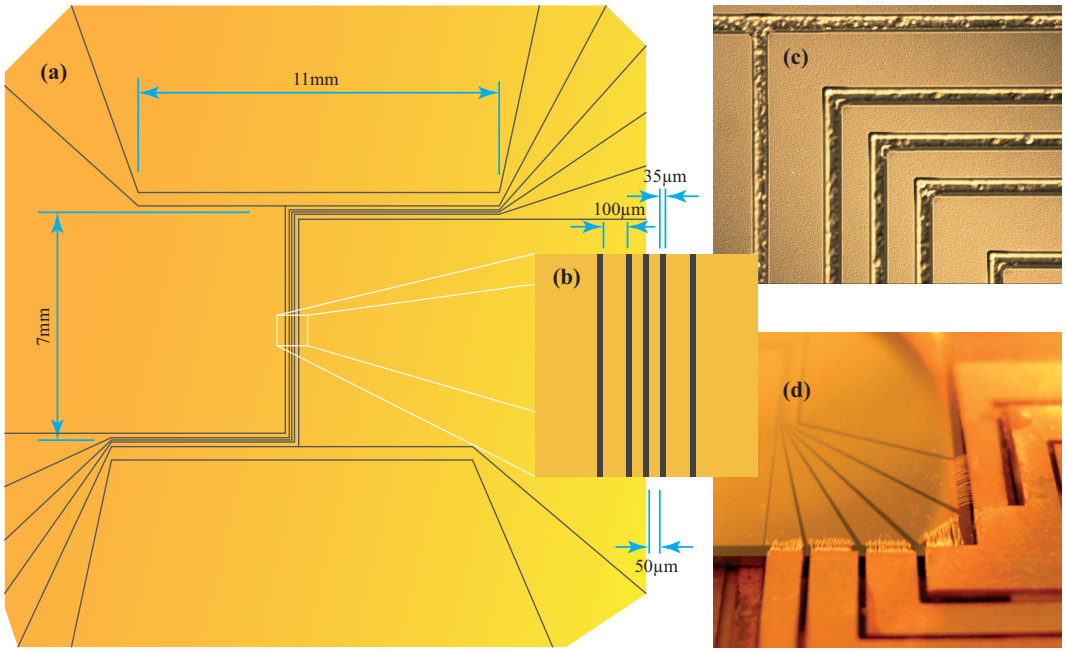

Figure 2.10: Figure (a) shows wire pattern milled into chip surface with relevant dimensions. Figure (b): Dimensions of Z wires. The inner pair (50 μm) we refer to as the small Z wires, and produce the (DC) magnetic trapping field. The outer pair (100 μm) we refer to as the large Z wires, and are used for RF manipulation of the atoms. Figure (c) is a light microscope image of a $650 \times 500\,\mu$m area at the top end of the Z wries. Figure (d) shows the wire bonds that form the electrical connection between the chip and the copper connections in the surrounding substructure.

Bulk defects, rough edges, and grain boundaries in the Au wires cause roughness in the magnetic potential when close to the chip [78, 77, 79]. They cause small transverse currents that produce fields with components in the $\hat{\mathbf{y}}$, and $\hat{\mathbf{z}}$ directions. The field fluctuations along $\hat{\mathbf{z}}$ alter the energy at the trap bottom, and are large enough to alter the distribution of atoms for clouds about μK or less, at 110 μm from the chip. This causes the cloud to split into fragments close to condensation.

The chip and substructure are designed to conduct heat rapidly away from the chip. To operate the magnetic trap, 1 A is run through each small Z wires for up to 10 s. Their resistance is measured to increase by 18% running 1 A for 10 s, corresponding to a temperature increase of 50° C. The $Si\,O_2$ (thermal conductivity $1.3\,W\,m^{-1}\,K^{-1}$) is kept thin to improve conduction [56]. This silicon chip sits directly on a 5 mm thick shapal-M base plate. This aluminium-oxide ceramic compound is electrically insulating, but has good thermal conductivity of $90\,W\,m^{-1}K^{-1}$. Recessed into this is a copper H, with 2×2 mm cross section. The central bar of the H is 2 mm long, and runs directly beneath the central part of the chip Z wires. It helps

dissipate the heat generated by the chip wires into the surrounding shapal. As well as dissipating heat, the copper H is use to generate the RF field for evaporative cooling. The shapal block is bolted into an aluminium support and suspended from the top flange.

The ends of the chip wires fan out, enlarging the area available for electrical contact. Their shape and direction also reduces the effect of the magnetic field they generate on the trap at the chip centre. The chip wires connect to an array of copper fingers mounted on top of the chip substructure. Figure 2.10 (d) shows these connections, made by batches of 50 μm thick gold wires, pressure bonded to the gold surface. Uncoated copper wires are screw clamped to the copper fingers, and connect them to the vacuum feed-throughs on the top flange.

The mirror MOT quadrupole coils are mounted to the chip sub-structure. The centre of the coil pair sits 1.8 mm below the chip surface, and their axis is at 45° to the surface in the x-y plane. Their centre-to-centre separation is 45 mm and they produce a quadrupole field with peak gradient 25 G cm^{-1} A^{-1}. They are wound with polyimide coated wire. Outgasing limits their maximum operation temperature and the maximum temperature for baking to 120° C. They run a 1.8 A continuous current for a maximum of 5 mins.

A gold coated prism is also mounted to the chip substructure, and redirects the z-axis imaging beam down through 8″ view port on the bottom of the science chamber. This helps maximise the numerical aperture.

2.2.3 Laser System

Our optical system uses three lasers: a Coherent® MBR110 titanium doped sapphire laser, and two home made diode lasers - the reference and repump lasers. Figure 2.11 shows the frequencies of these lasers and of the beams derived from them. Light from the MBR110 is used for two purposes: 'trap light' for laser cooling and trapping of ^{87}Rb in the various MOTs, and absorption imaging. The reference laser is locked to the ^{87}Rb F $= 2 \rightarrow$ F' $= 3$ transition in a vapour cell, and serves as a frequency reference for the MBR110 which is offset locked to it. The reference laser also provides light for optical pumping. The repump laser is locked to the

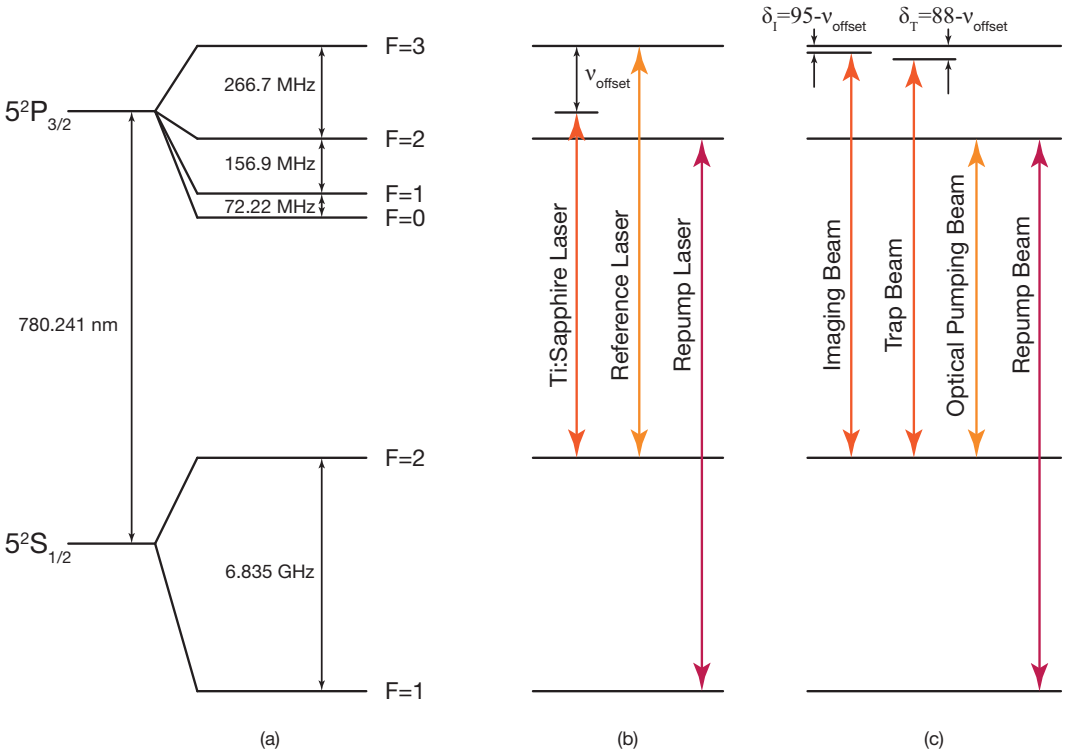

Figure 2.11: ^{87}Rb energy levels for the D_2 line, and laser frequencies. The first column shows the energy levels of the ^{8}7Rb D_2 line, for which the ground state configuration is $5^2S_{1/2}$, and the excited state configuration is $5^2P_{3/2}$. These are split into hyperfine levels with quantum number F with their detuning shown [46, 47, 48, 49]. The second column illustrates the laser frequencies relative to the D_2 line transition. The Ti:Sapphire laser is detuned from the reference laser by an frequency ν_{offset}. The third column illustrates the frequencies of the imaging, trap, optical pumping and repump beams which are derived from the lasers as indicated by their matching colour coding. The imaging beam is detuned by $\delta_{\text{I}} = 95 - \nu_{\text{offset}}$ MHz from resonance with the F $= 2 \rightarrow$ F' $= 3$ transition, and the trap beam by $\delta_{\text{I}} = 88 - \nu_{\text{offset}}$ MHz from the same transition. For imaging, we usually set $\nu_{\text{offset}} = 95$ MHz, and while loading the MOT, ν_{offset} is typically 100 MHz.

^{87}Rb F $= 1 \rightarrow$ F' $= 2$ 'repump' transition in another vapour cell. Light from the repump laser is overlapped with the trap light and optical pumping light. It pumps atoms that have decayed into the $|5^2S_{1/2}, F = 1\rangle$ state back into the $|5^2S_{1/2}, F = 2\rangle$ state, where they can be excited by trap or optical pumping light.

The trap light can be tuned between 10 and 76 MHz to the red of the trapping transition, $|5^2S_{1/2}, F = 2\rangle \rightarrow |5^2P_{3/2}, F = 3\rangle$. The maximum detuning is limited by the input voltage to the voltage controlled oscillator in fig.2.14. The detuning is typically 12 MHz while loading the MOT, which is then increased to 76 MHz for the optical molasses stage. The imaging light is tuned to be resonant with this transition. The optical pumping light is resonant with the $|5^2S_{1/2}, F = 2\rangle \rightarrow |5^2P_{3/2}, F = 2\rangle$ transition, and the repump light is resonant with the $|5^2S_{1/2}, F = 1\rangle \rightarrow |5^2P_{3/2}, F = 2\rangle$

transition.

Figure 2.12 is a schematic of the laser system and the different beams derived from it. It includes the three lasers, with accompanying spectroscopy and feedback units. Each beam has a shutter for exposure control. All but the repump light can also be switched with an acousto-optical modulator for sub 100 ns control. The beams shown in fig.2.12 derived from the reference, repump and MBR110 lasers are described in turn below.

Reference and Repump lasers

The reference and repump lasers follow the extended cavity diode laser design of [80]. We use a Sanyo DL7140-201 laser diode, with nominal wavelength 785 nm and a free-running linewidth $\sim$ 100MHz. An external cavity is formed by the back facet of the laser diode, and a diffraction grating mounted at the Littrow angle after the diode output. The first-order diffracted light fed back into the diode provides frequency selection. The diode lasers operate at 780 nm with an output power of 20 mW. Mode-hop free scans of 2.5 and 1 GHz are possible for the repump and reference lasers respectively. Both lasers are frequency stabilised by fast feedback to the diode current and slow feedback to the angle of the grating. The diode lasers are vibrationally damped, and temperature regulated for added frequency stability.

The reference and repump lasers are frequency locked to the $|5^2\mathrm{S}_{1/2}, F = 2\rangle \rightarrow |5^2\mathrm{P}_{3/2}, F = 2\rangle$ and $|5^2\mathrm{S}_{1/2}, F = 1\rangle \rightarrow |5^2\mathrm{P}_{3/2}, F = 2\rangle$ transitions respectively. Approximately 2% of the output beams from each of these lasers is picked off by the glass plates GP1 and GP4, and fed into the respective polarisation spectrometers (see [81, 82, 83], and for the setup in our experiment [84]). An error signal, approximately proportional to the deviation from the desired frequency, is generated by the polarisation spectrometer. The error signal is fed back to the piezoelectric stack and laser current via a proportional, integral and differential (PID) gain circuit.

A further 2% of the reference laser output is picked off by GP4, and used as a frequency reference for the MBR110 described further below.[6] The remaining

[6]The glass plates which are set a 45% to beams reflect approximately 2% of the light from their front face, and 2% from their back face, allowing 96% to pass straight through. Where only on reflected beam is shown in fig.2.12, e.g. at GP1, it is assumed that the other reflected beam is sent

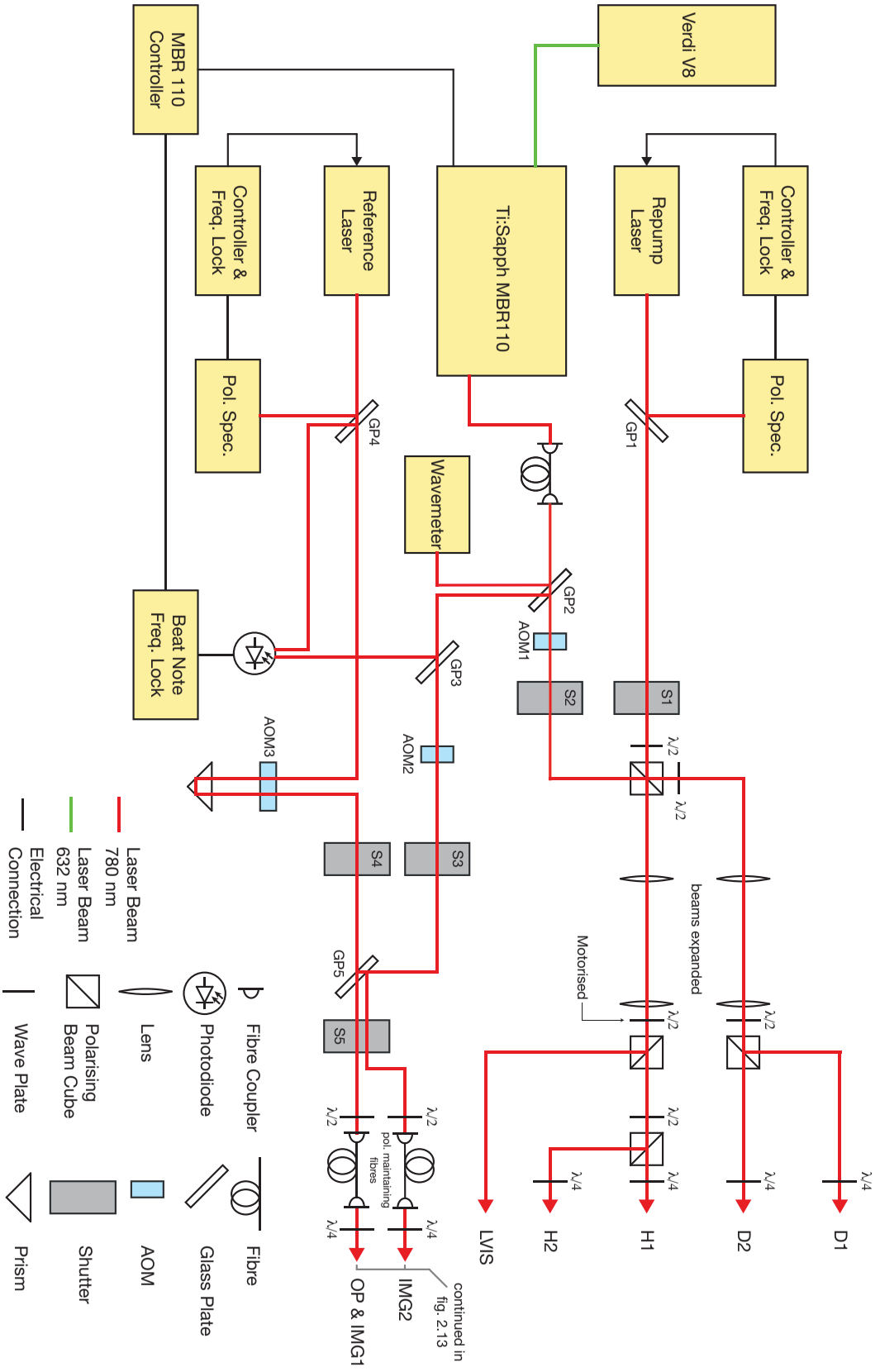

Figure 2.12: The laser system and beams derived from it.

to a beam dump and not used.

fraction is red detuned by 267 MHz using acousto-optical modulator AOM3 in the double pass configuration, shown in fig.2.12 and fig.2.13, where it is resonant with the optical pumping transition. The AOM is operated at 133.5 MHz with $\sim$ 60% of the light diffracted into the first-order red shifted mode. When the rf power to the AOM is turned off, 99.99% of the light passes through in the zeroth order mode, which is then blocked. This allows the optical pumping light to be switched off with an extinction ratio of $1 : 10^4$, in the time that the rf can be controlled, $\sim$ 50 ns. This provides the μs timing required of the optical pumping beam. A shutter (S4) excludes any remaining light 1.5 ms after the AOM is switched off. After passing through S4 the optical pumping beam is overlapped with one of the two imaging beams (IMG1) by the glass plate GP5. It then follows the same path as IMG1 through another shutter, S5, into a polarisation maintaining fibre, through a telescope which expands the beam, and into the vacuum chamber. The telescope and vacuum chamber are shown in fig.2.15a.

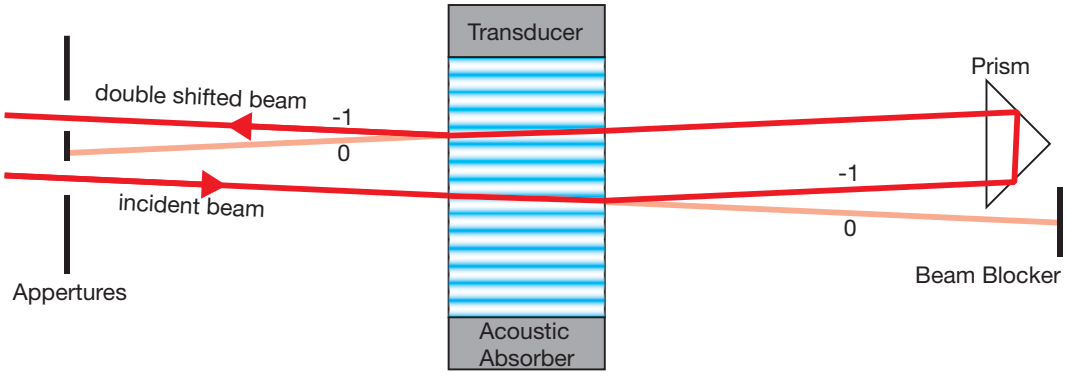

Figure 2.13: An a.o.m. in double pass configuration. With this layout, the AOM can be used to switch the output beam on or off at the 50ns operation time of the AOM. Variation of the operation frequency in the double pass configuration makes only a small lateral shift to the output beam, but does alter its direction.

The repump laser beam is passed through the mechanical shutter S1, then combined with the trap light with a polarising beam cube, PBS1. The shutter blocks the repump beam following the optical pumping stage. This shutter takes 1.5 ms to switch between being fully open and fully closed. This switching time, which is slow compared to the switching speed of an AOM, is sufficient for the repump light which is far off resonance with atoms in the $|5^2S_{1/2}, F = 2, m_F = 2\rangle$ state ready to be magnetically trapped.

The polarising beam cube PBS1 which combines the repump and trap light gives

two output beams. One of these is used for the two diagonal MOT beams D1 and D2, the other for the two horizontal MOT beam H1 and H2 together with the LVIS beam used in the formation of the LVIS MOT. Before the two outputs of PBS1 are separated, they are expanded to have a $1/e^2$ radius of approximately 20 mm.

MBR110

The MBR110 shown in fig.2.12 is a titanium:sapphire laser pumped by an 8 W 532 nm Verdi V8 Laser. The ti:sapph lasing crystal is mounted in a confocal bow-tie cavity. The laser frequency is tuneable by varying the cavity length (see [85] for further details). The laser is internally locked to a reference cavity (finesse $30 - 70$ and FSR 225 GHz). We externally lock the laser through feedback to the length of the reference cavity. The MBR110 has a linearly polarized output in the TEM_{00} mode with an output power between 700 and 850 mW. The MBR110 requires regular maintenance to operate consistently. The output beam is fibre coupled so that re-alignment of the MBR110 does not affect the alignment of the beam in the rest of the experiment.

Two low power beams ($\lesssim 10$ mW) are picked off after the fibre with the glass plate GP1. One of these goes to a wave-meter which is used for corse frequency alignment of the MBR110 to within a few GHz of the trapping transition. Corse adjustments in frequency are made using a birefringent filter inside the MBR110 laser cavity. A small fraction ($\sim 2\%$) of the second beam is picked off with GP3, and used for fine frequency alignment, locking the MBR110 output frequency to the frequency of the reference laser within a small offset. This beam is mixed with a beam from the reference laser on a diode. The beat note of frequency ν_b is used to offset lock the frequency of the MBR110 between 85 and 165 MHz below the trapping transition frequency. Figure 2.14 shows a schematic of the offset lock. The beat note at $\nu_{\rm b}$ is mixed with the output of a voltage controlled oscillator (VCO) operating between 210 and 290 MHz. The signal at the difference frequency $\nu_{\rm vco} - \nu_{\rm b}$ is attenuated again and fed into an error circuit [86]. This circuit produces a DC voltage linearly proportional to the difference between $\nu_{\rm vco} - \nu_{\rm b}$ and 125 MHz. The error signal is fed back to the MBR110 reference cavity via a PID gain circuit. The proportional, integral and differential gain are optimised to give the fastest response

with minimal ringing when detuning during the UMOT and optical molasses stages.

In this way, the MBR110 is locked to the red of the reference laser with a detuning of $\nu_{\mathrm{vco}} - 125\,\mathrm{MHz}$. The beam that continues on to form the trapping beams, is then blue shifted 88 MHz by a single pass through AOM1, whose operation frequency is held fixed. The result is a beam that can be varied from resonance with the trap transition to 70 MHz red detuned, by varying the voltage to the VCO.

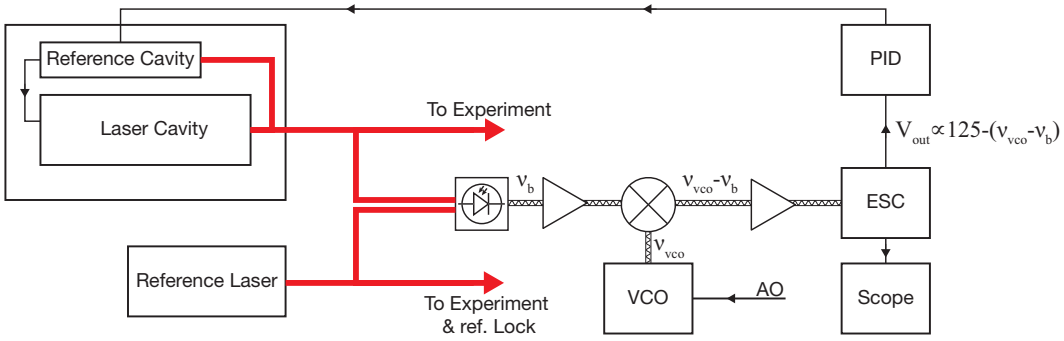

Figure 2.14: The offset lock. This provides a tuneable lock point for the MBR110 relative to the reference laser frequency

AOM1 is also responsible for fast extinction of the trap light. The shutter S2 provides full extinction up to 1.5 ms after the AOM is switched off. The coupling efficiency through this AOM better than 60%. Following AOM1 and S2, the beam is then combined with the repump beam, then expanded and split into components for the diagonal MOT beams D1 and D2, and the horizontal MOT beams H1 and H2 and LVIS beams.

The beam taken from the MBR110 output that is picked off by GP2 and passes through GP3 is used for the absorption imaging. This beam, initially at the output frequency of the MBR110, is blue shifted 100 MHz by AOM2. This means that when the trap beams are 12 MHz detuned, the imaging beam is on resonance with the cooling transition. AOM2 and shutter 3 provide exposure control. The imaging beam is split into two beams by GP5, IMG1 and IMG2 as shown in fig.2.12. Each beam contains approximately 200 μW of imaging light. Shutter 5 selects which beam is exposed. As described above, the optical pumping beam is overlapped with IMG1. The beams are spatially filtered by polarisation maintaining fibres, before being expanded and passed into the science chamber.

2.2.4 Imaging System

Figures 2.15a & 2.15b show the two imaging axis x & z. The x imaging axis can be used for absorption and fluorescence imaging (sec.2.1.8), without any adjustments being made. The z imaging axis is unsuitable for fluorescence imaging, since light from the horizontal imaging beams saturates the CCD.

Both axis are setup in an 4f configuration, using lenses with focal length f, and gives 1:1 magnification. This configuration allows the image to be transported while collimated. Limiting the transport length to 2f maintains the original beam intensity at the CCD for good optical contrast. For the x axis $f = 150\,\mathrm{mm}$, and $f = 120\,\mathrm{mm}$ for the z axis. It also has a only small magnification $\approx 2\%$ error when the lenses are misplaced by a few mm along the optical axis. All optical components are $D = 50\,\mathrm{mm}$ in diameter. The resolution is diffraction limited by the smallest numerical aperture in the system, which is approximately $2f/D$. From the Rayleigh criterion, the minimum distance between two equally bright point sources that can be resolved is $1.22f\lambda/D$ which is $2.9\,\mu\mathrm{m}$ for our setup. To measure the resolution in our imaging system, we setup a similar rig using the same apparatus, before installing it around the science chamber. We imaged a microscope graticule using this test rig, and found that we could resolve lines separated by $3\,\mu\mathrm{m}$ when illuminated with an incoherent light source, and $6\,\mu\mathrm{m}$ when illuminated by a coherent source which produced interference fringes in the image. The resolution of our imaging system is similar to the CCD pixel size which is $3.45 \times 3.45\,\mu\mathrm{m}$ on the x axis, and $7.4 \times 7.4\,\mu\mathrm{m}$ on the z axis. The z axis can be further fitted with a $\times 6$ microscope objective. The cameras are an AVT Pike F303B and F505B for the x and z axis respectively.

The imaging beam is spatially filtered by a polarisation maintaining optical fibre before being expanded to a $1/e^2$ radius of 7.5 mm by a Thorlabs F810FC-780 output collimator. On the x axis where the cloud is longer, the beam is expanded by a further factor of 3/2. The beam is circularly polarised to maximise the scattering rate with the $|F = 2, m_F = 2\rangle \rightarrow |F' = 3, m'_f = 3\rangle$ transition, for which $I_{\mathrm{sat}} = 1.67\,\mathrm{mW\,cm^{-2}}$ [46, 47, 48, 49]. Optical pumping light is also delivered along the x imaging axis.

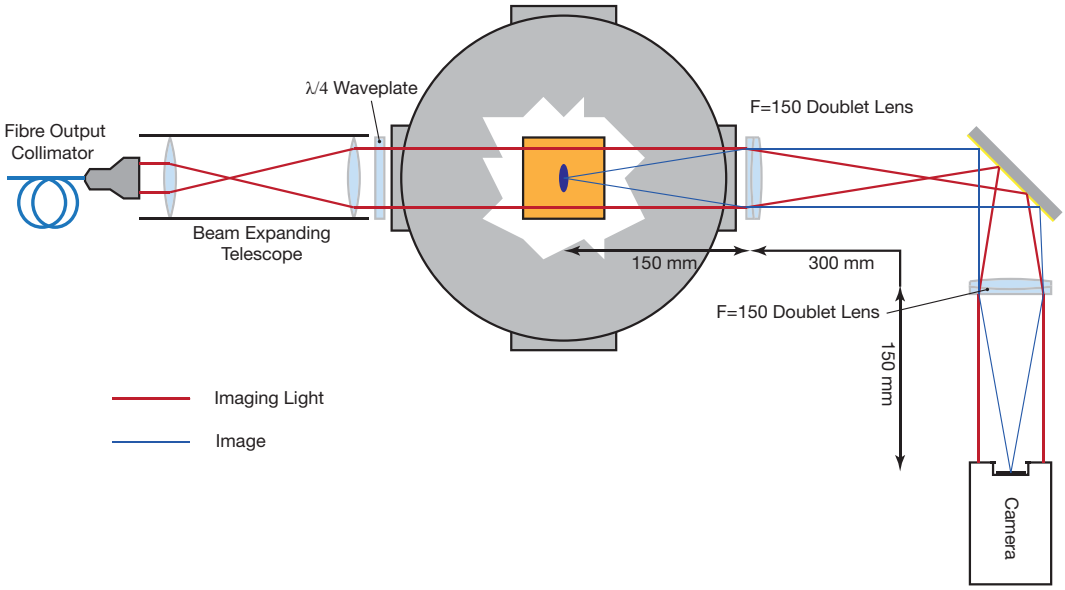

(a)

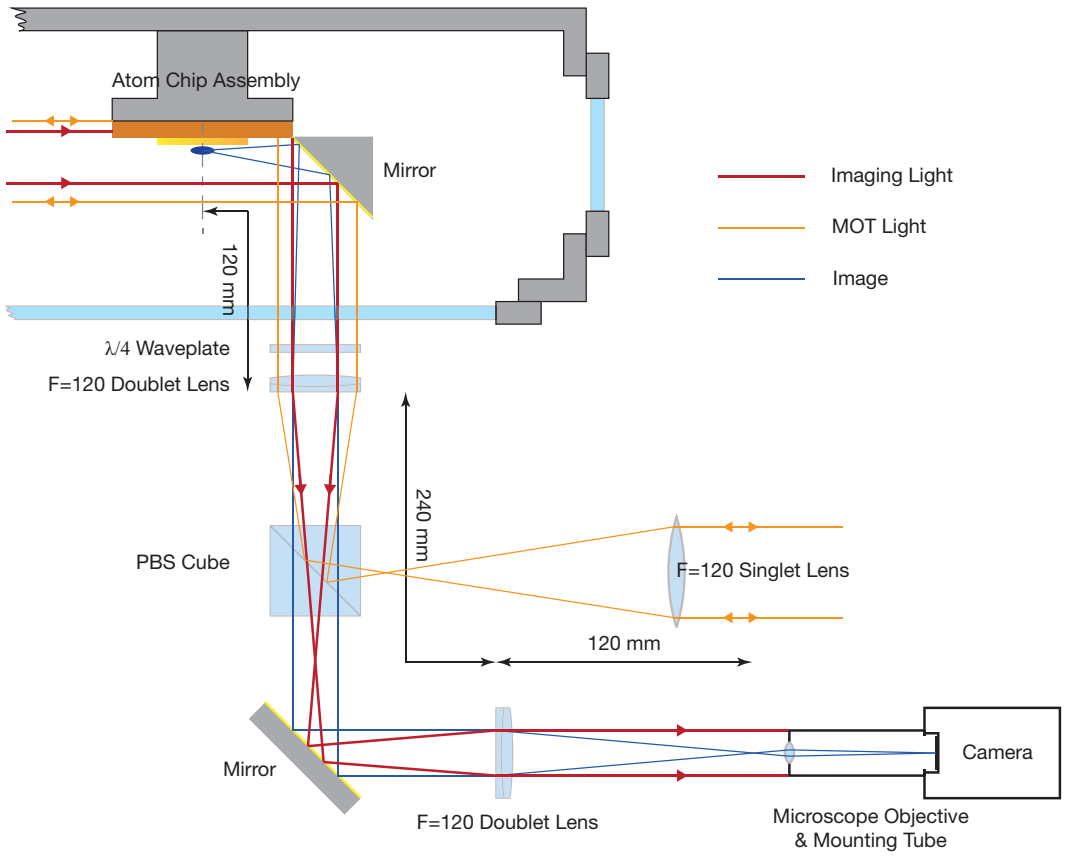

(b)

Figure 2.15: Imaging axes. Figure (a) shows the x image axis, and (b) shows the z imaging axis.

The z axis has the added complication of providing optical access for the horizontal MOT beams. The imaging beam is overlapped with the MOT beam path before entering the chamber using a polarising beam cube. It therefore has orthogonal polarisation to the MOT beam. The beams are then separated again by the 50 mm beam cube in the image transport section. A further enhancement was made on this axis to improve the NA by reflecting the imaging beam down through the bottom view port. Previously, the direct path through the side view port limited the NA and therefore the resolution.

In addition to these two axis, we have a camera with a diagonal view of the MOT through the bottom view port, and camera pointed at the LVIS MOT. These have real time feeds, and allow us to quickly diagnose problems with MOT loading stage.

2.2.5 Computer Control

The experiment is controlled through two computers, PC1 & PC2. PC1 has primary control, and the experimental sequence is programmed and executed on this machine. PC2 updates feedback to the magnetic field cancelation coils while the atoms are not being cooled or trapped. PC2 can also be used to measure long term drifts, e.g. of background magnetic fields, beam polarisation and directional drifts.

The experimental sequence is controlled through a bespoke programme called Tyche [87].[7] Tyche interfaces directly with two National Instruments data aquisition cards (NI-DAQ), a Labview camera control programme, and software for the versatile rf frequency generator (VFG). Tyche has a Python user interface, from which pre-defined sets of commands can be executed. Tyche makes the experimental sequence highly programmable, with relative ease.

The NI-DAQ 6713 card is set up for 8 analogue output channels with range ± 10 V. The NI-DAQ 6543 card has 32 digital 0 / 5 V (TTL) output channels. Values and triggers throughout the experimental sequence are set by these cards. The analogue outputs connect to current drivers for the coils and chip wires. The digital outputs control level setters and triggers for other pieces of experiment hardware. The

[7] Developed by R. Nyman and M. Succo

time resolution is approximately[8] 10 μs, and the analogue channels can be set to an accuracy of 4 mV. A user writes a script of commands in Tyche, which are broken down to a level of primitive commands. The primitive commands in Tyche instructs the DAQ card what channel to change and when. More complex commands can be easily built up from these primitive commands, for example a simple command for a ramp between two values with specified time steps is built from a loop over primitive commands.

Before the experimental sequence is run, the user written script for the experimental sequence is converted into a list of primitive commands by Tyche. This list is sent to the DAQ cards own internal buffer, ready for execution. [9] An on board 10 MHz clock controls the timing of execution. The clocks are synchronised between the two cards.

The Labview camera control programme configures the camera prior to imaging. It then reads and saves the images once the cameras have been triggered by a TTL line. It also processes both fluorescence and absorption images for on the fly observations. This program is activated through Tyche at the start of each experimental cycle.

As well as the Labview camera contoller, Tyche also interfaces with the software that controls the versatile frequency generate (VFG), used to generate the rf fields for evaporative cooling and dressing the trap potential. The VFG receives a list of commands stating at what frequency, phase and amplitude to operate and when. Like the DAQ cards, the VFG stores these in its own buffer, and executes them when triggered by a digital output line. This allows an arbitrary rf signal sequence to be programmed.

2.2.6 Experiment Control Hardware

The pieces of hardware directly controlled by the computer are detailed below. These control the light and magnetic fields used in the BEC sequence.

[8]The exact timing depends on how many channels are being executed. The cards operate at 1Msamples per s over all channels

[9]The length of list of commands is limited by the buffer size. For seamless execution of a long list of commands, the queue protocol must correctly set to update the buffer with the next batch of commands before the current batch runs out, otherwise the experimental sequence pauses mid run!

Current Drivers

A number of current drivers are used for the chip wires, bias field coils, and the ^{87}Rb dispenser. These are all powered by power op-amps which servo the current by comparing a reference voltage with the voltage drop over a sense resistor in series with the load.

The bias coils carry up to 10 A, and require a supply with potential difference of up to 25 V to quickly turn on the current through their self-inductance. The OPA 549 op-amp is used due to its high power output and heat dissipation. Some of the coils require more power than the maximum rating of a single OPA 549 op-amp, so their current driver circuits have an additional OPA 549 built into a follower stage. The op-amps are heat sunk and water cooled.

The chip wires are powered by similar circuits to the bias coils, that additionally have a tuneable stage of integral gain and a trimmer circuit that allows accurate setting of the current to zero when the input voltage is zero [56]. These circuits provide fast switching of the chip wires, from 0 to 1 A in 100 μs, and a current stability of order 1 part in 10^4. The chip wires require less power, so OPA 548 power op-amps are used instead of the OPA 549. These are also heat sunk but not water cooled.

Both software and wire fuses are used to prevent the wires being left on, or drawing more than their maximum tested current. The software fuse limits the maximum current a user command in Tyche can set. For the Z wires this limit is 1A, and for the end wires it is 3A. The wire fuses have a rated current of 0.5 A, and we find they blow after running 1 A for approximately 12 s. These fuses values where chosen following tests on the chip wires. The small wires have been tested to 0.8 A for 60 mins, 1 A for 10 s repeated every minute (similar to normal operation of experiment), and 1.6 A for 100 ms. The much larger end wires have been tested at 2.4 A for 60 mins.

AOMs, Shutters and drivers

The trap, repump, optical pumping, and imaging beams are each independently controlled by the mechanical shutters S1 to S4. These take 2 ms to open or close fully and have a maximum reliable switching frequency of 20 Hz. They are actuated by a pulsed solenoid and have a latch to hold the state. They require a ± 15 V pulse to drive them, triggered by a TTL line. There is also the selection shutter S5, that alternately blocks the x or z axis imaging beam. This can operate at up to 50 Hz. This shutter is also actuated by a solenoid, and is spring loaded with a magnetic latch when the spring is compressed.

Precise shutter timing is important during the transfer from the UMOT to the magnetic trap. The entire process takes less than 5 ms, with some elements highly sensitive to stray light. There is approximately a 5 ms lag between the TTL control pulse and full extinction of the beam. Each shutter is carefully calibrated for the exact opening and closing time delays, and these delays are accounted for when Tyche determines the control sequence.

For the trap, imaging and optical pumping beams AOM1-3 are used in addition to the shutters to give sub μs timing. These extinguish the light to 1 part in 10^4. The residual light is enough to effect the magnetic trap - see section 4.2.3, so shutter operation must follow swiftly. The AOMs are driven by an rf voltage source, whose output is switched on or off using a TTL controlled attenuator.

USB Contolled Devices

A motorised waveplate and two VFG 150 are each controlled through a USB connection in addition to a TTL trigger. The motorised waveplate is used in conjunction with a linear polariser to reduce the intensity of the horizontal MOT beams prior to transferring atoms to the UMOT.[10]

The VFG produces rf signals used for evaporative cooling and rf dressing of the trap potential. The output of the VFG has a frequency range of 100 kHz to 150 MHz,

[10]The additional light is diverted into the LVIS beams. However, the LVIS quadrupole field is turned off once the MOT is loaded, and the LVIS is no longer in use during this stage.

and a tuneable output power from −69 to 0 dBm. The VFG output is amplified by a mini-circuits ZHL-32A +25 dB rf amplifier before being coupled into the copper H for evaporative cooling, or large z wires for rf dressing. The VFG output has extinction below −80 dBm over its entire output spectrum. Therefore, no additional rf switches are required when just a single stage of amplification is used.

Chapter 3

Trapping ^{87}Rb Atoms with Our Atom Chip

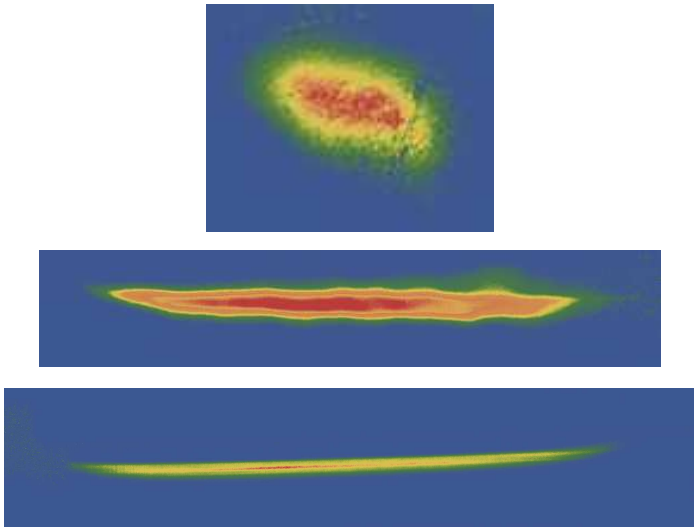

Figure 3.1: Images of mMOT, UMOT and magnetic trap. The latter two are 'chip traps', close to the surface of our atom chip. Their shape is defined by the magnetic fields from the current-carrying chip wires.

In this chapter the techniques we use to trap and manipulate ^{87}Rb atoms close to the surface of our atom chip are discussed in detail. In section 3.1 a new technique for efficiently transferring atoms from the mirror MOT into the UMOT is presented. Section 3.2 explains how the cloud is then prepared for magnetic trapping. The magnetic trap is described in section 3.3, where we introduce different approximations to the trap potential, used to give new insight elsewhere in this thesis. Then in section 3.4 we develop the theory of loading chip-wire magnetic traps such as ours, and use it to explain our experimental observations.

3.1 Transferring Atoms into the UMOT

The mirror MOT (mMOT), with its large capture volume is well suited for rapid capture of atoms from the LVIS. However, it is not good for transferring atoms to the magnetic trap. The MOT cloud is an oblate spheroid, very different from the elongated cigar shaped magnetic trap, and too large to be brought close to the chip. Therefore, magneto-optically trapped atoms are first transferred from the MOT into the UMOT, which is much closer in shape to the magnetic trap and can be brought to within 500 μm of the chip.

The same light beams are used for both mMOT and UMOT; only the quadrupole fields are different. We devise a simple strategy to deform these quadrupole fields smoothly in order to transfer the atoms from the MOT to UMOT. In section 3.1.1 & 3.1.2 formulae that describe the mMOT and UMOT quadrupoles are given. Section 3.1.3 uses these to develop a suitable ramp from one quadrupole to another. Section 3.1.4 describes the implementation of the transfer ramp, and presents measurements of the path the magneto-optically trapped cloud takes.

3.1.1 MOT Quadrupole Field

The MOT quadrupole field is generated by a pair of parallel coils as shown in fig.3.2. The coils have a centre-to-centre separation $2a$ of 45 mm, and a radius R of 14 mm. The centre point between the two coils is located $\Delta_y = 1.8$ mm beneath the upper surface of the atom chip as shown in fig.3.2. The central point on the upper surface of the atom chip is indicated by the red cross, and in the plane of the chip surface is taken to be half way along the central section of the Z wires. Atoms are trapped above the upper surface as depicted here. In fig.3.2 we also define the coordinate vectors $\mathbf{x}$, $\mathbf{y}$, $\mathbf{z}$ and the cartesian coordinate origin at the centre point on the upper surface of the chip. These cartesian coordinates are used throughout this thesis. In addition to these cartesian coordinates, we define the cylindrical coordinates $\tilde{\mathbf{r}}$, $\tilde{\mathbf{z}}$ which are orientated along the axis of the coils and are used in the description of the quadrupole field in this section.

In reality, the apparatus shown in fig.3.2 are suspended upside down inside the

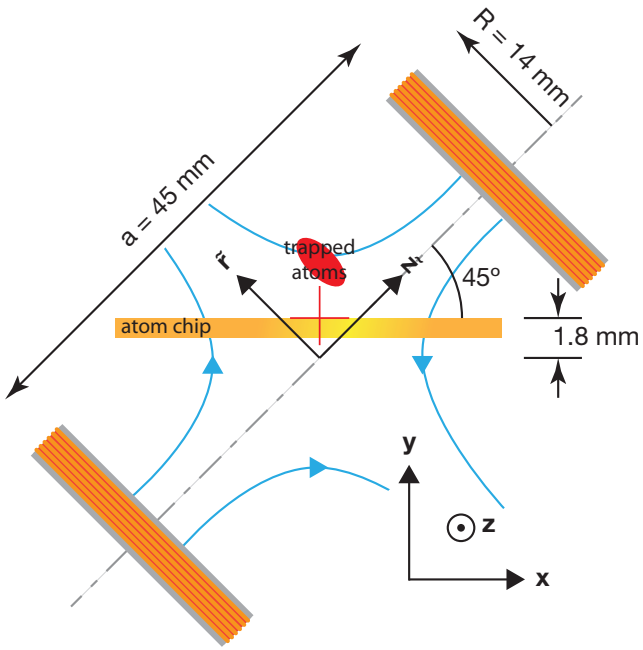

Figure 3.2: Schematic of MOT coils. The unprimed coordinates are those used throughout this thesis, with origin at the red cross. Primed coordinates are used when discussing the mMOT quadrupole in relation to these coils. Without any bias fields, the minimum of this field sits 1.8 mm beneath the chip surface.

vacuum chamber, as one would observe standing in the laboratory. This means that Earth's gravity pulls atoms in the $+\mathbf{y}$ direction. However, our convention throughout this thesis (and in the previous paragraph) is to refer to the (top) surface of the chip as being on the side of the chip where we trap atoms. We therefore also speak of trapping atoms 'above' the surface of the chip throughout, and refer to the $+\mathbf{y}$ direction as upwards.

Current is run in opposite directions through these two coils to create a quadrupole field. The quadrupole field generated by these coils is zero at the centre point, $\tilde{z} = \tilde{r} = 0$. Each coil has $N = 100$ turns of wire carrying current I set to 1.8 A for loading of the MOT, and stepped up to 2 A at the beginning of the transfer ramp. To first order, the magnitude of the field increases linearly with distance from the field zero at the centre point. An analytic calculation of the field from the coils shows that higher order terms contribute only 1.8% of the total field at a distance of 8 mm above the centre point (6.2 mm above chip surface).

This quadrupole field defines an oblate spheroid or 'pancake' shaped MOT, since the field gradient along the coil axis ($\tilde{\mathbf{z}}$) is twice the radial ($\tilde{\mathbf{r}}$) field gradient at

the centre point between the coils. This follows from the cylindrical symmetry, together with $\nabla \cdot \mathbf{B} = 0$. The z-field at distance z on the axis of a single coil is $\frac{1}{2}\mu_0 NIR^2/(z^2 + R^2)^{3/2}$. For two coils, centred at $z = a$ and $z = -a$ and carrying opposite currents, the z-field is 0 at $z = 0$ and the axial field gradient $\partial B_z/\partial z = 3\mu_0 NIR^2 a \left(R^2 + a^2\right)^{-5/2}$. For our coils whose dimensions are given in fig.3.2, $|\partial_{\tilde{z}}\mathbf{B}| = 25.4\,\mathrm{G\,cm^{-1}}$, and $|\partial_{\tilde{r}}\mathbf{B}| = 12.7\,\mathrm{G\,cm^{-1}}$, where the directions $\tilde{\mathbf{r}}$ & $\tilde{\mathbf{z}}$ are illustrated in figure 3.2.

Bias fields in the $\mathbf{x}$, $\mathbf{y}$ and $\mathbf{z}$ directions, B_x, B_y and B_z, shift the quadrupole centre predominantly in the $\mathbf{y}$, $\mathbf{x}$, and $-\mathbf{z}$ directions respectively. In the absence of any bias field, the quadrupole centre sits beneath the chip surface. A uniform bias field with value $-\mathbf{B}_{\mathrm{mot}}(\mathbf{r})$, shifts the quadrupole centre to $\mathbf{r}$. The size of the MOT is small and the shift in its position is modest compared to the dimensions a and R. Therefore, the overall shape and field gradient of the shifted quadrupole field varies only slightly. We define the parameter β as the shift in mMOT height per Gauss of the applied bias field B_x, per Ampere through the mMOT coils. Applying the bias field B_x, shifts the quadrupole centre to height y_{mot} above the chip surface as given by

$$y_{\mathrm{mot}} = \frac{B_x}{\beta I_{\mathrm{mot}}} - \Delta_y. \tag{3.1}$$

Since the mMOT height is small, $y_{\mathrm{mot}} \ll a, R$, the parameter β is approximately the field gradient of the quadrupole field along the $+\mathbf{y}$ direction from the quadrupole centre,

$$B'_{\mathrm{mot}} = \beta I_{\mathrm{mot}}. \tag{3.2}$$

To position the mMOT 4.5 mm above the chip centre whilst the mMOT loads, we use a bias field of $B_x = -11\,\mathrm{G}$. We also apply a y-bias field of $B_y = 2\,\mathrm{G}$ to align the mMOT over the centre of the chip in the $\mathbf{x}$ direction. During the transfer ramp, we smoothly lower the mMOT quadrupole centre towards the chip, simultaneously reducing I_{mot} to lower the mMOT quadrupole field to zero. We use eq.(3.1) to calculate how we need to vary B_x to achieve this.

As the mMOT is lowered, a small lateral shift is also expected. Figure 3.3a shows the mMOT quadrupole field in the $z = 0$ plane, calculated through integration of the Biot Savart law for the coils. Since $|\partial_{\tilde{z}}\mathbf{B}| = 2|\partial_{\tilde{r}}\mathbf{B}|$ at the coil centre, the

mMOT takes the slightly curved path shown in red, rather than directly along the y axis. The sideways shift of the mMOT can be corrected with small adjustments to B_y where required. The small effect this has on our transfer ramp is discussed in section 3.1.4. With this consideration, the field gradient β is specifically the gradient $\partial_y \mathbf{B}_{\mathrm{mot}}(\gamma(y))$, where $\gamma(y)$ specifies this path parameterised by y.

Figure 3.3b shows the result of experimental calibration of β. To make this calibration the mMOT was loaded form the LVIS for longer than 12 s until it ceased to increase in size as observed from its fluorescence, indicating saturation of the atom number in the mMOT. The height of the mMOT was then varied by changing the value of B_x to one of six different values between 5 and 12 G. The current in the mMOT coils was kept constant at 2 A throughout. At each value a fluorescence image was taken of the MOT from the side, from which the height was measured. A typical image of the mMOT is shown in the top image of fig.3.1. The value of B_x was switched suddenly without observing from the fluorescence any loss in atom number due to the rapid movement of the quadrupole field. However, for positions closer to the chip, the mMOT was observed to decay over a few seconds to a smaller size since the trap volume is reduced by its proximity to the chip surface. The fluorescence and therefore size of the mMOT was left to reach a steady state after B_x was changed, prior to taking the fluorescence image from which the height was measured.

To measure the height, the mMOT centre of mass was found by summing the product of (normalised) pixel counts and pixel y coordinate in an image. The heights measured in this way are plotted against the value of the bias field B_x in fig.3.3b. The data points follow a straight line, with gradient equal to β. The line fitted in fig.3.3b gives its value, $\beta = 8.25\,\mathrm{G\,cm^{-1}\,A^{-1}}$. It is noted that the shape of the mMOT varies depending on its position due to the inhomogeneous nature of the trapping beam profiles. This leads to small differences in the measure height than from the straight line prescribed by eq.(3.1).

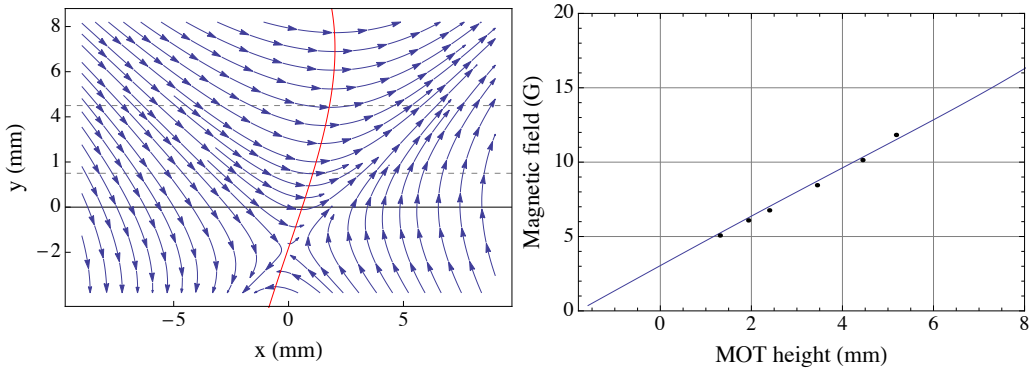

(a) (b)

Figure 3.3: (**a**) MOT quadrupole magnetic field. The red line is the path that the quadrupole minimum takes when shifted by the x bias field. The path forms where the quadrupole field points in the $\pm\hat{\mathbf{x}}$ direction. The solid line at $y = 0$ is at the chip surface. The region between the dashed lines indicates the typical range the mMOT height takes during the transfer ramp into the UMOT. (**b**) Magnetic field strength along the red path in (a) as a function of height y. The field is highly linear ($< 1.8\%$ deviation) with height, with a gradient of $16.5\,\mathrm{G\,cm^{-1}}$ with the MOT coils running 2A. The data points are the measured height of the MOT centre when the given magnetic field is applied. Each data point is the height measured from a single fluorescence image of the MOT.

3.1.2 UMOT Quadrupole Field

We next introduce the UMOT quadrupole field in the absence of the mMOT field, before discussing how we deform one field into the other in the next section, sec.3.1.3. The UMOT quadrupole field is generated by a U-shaped current distribution (figure 2.3 in section 2.1.2) on the atom chip surface, together with a uniform x bias field. The central section of the U is formed by the 7 mm central sections of the two small Z wires, each carrying current $I_{\mathrm{umot}}/2 = 2\,\mathrm{A}$. One end of the Z forms one end of the U. At the other end, the Z current is cancelled by the end wire carrying 2 A in the opposite direction, which provides the other end of the U. By applying a bias field B_x, a 2D quadrupole field forms a distance y_{umot} above the central section of the U. Figure 3.4a shows the UMOT quadrupole field in the $z = 0$ plane, calculated by integrating the Biot-Savart law for the U-shaped current distribution on our chip. This 2D quadrupole, together with the MOT beams, gives rise to the transverse confinement of the UMOT. The ends of the U support the axial confinement.

Since y_{umot} is small compared to the length of the central section of the U, we can approximate the transverse (x, y) field as that from a long thin wire carrying current I_{umot} along the z axis. In this approximation the x bias field cancels this at

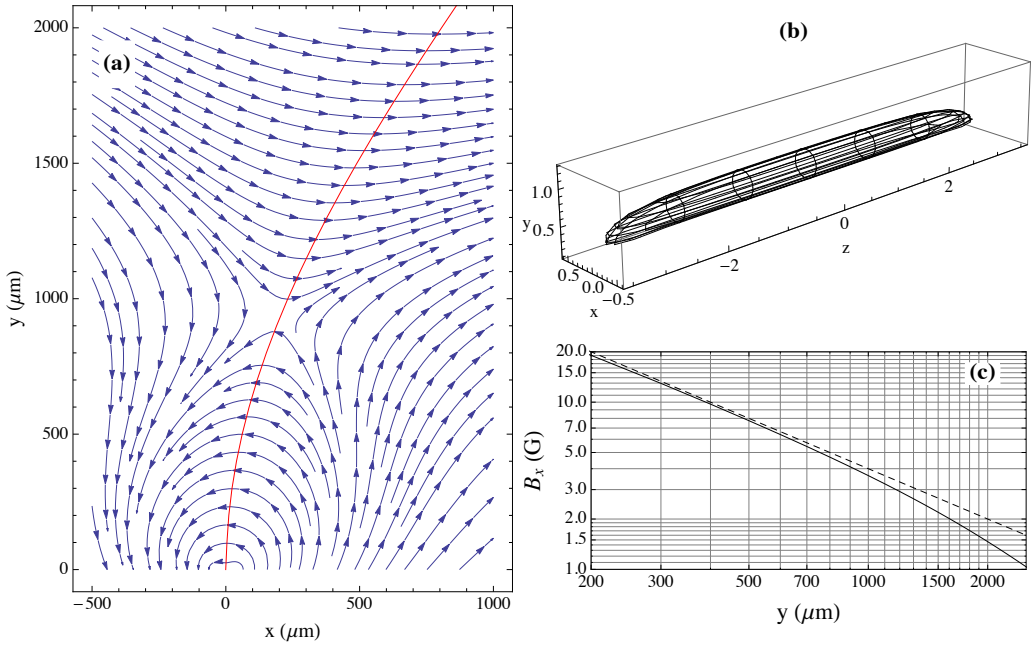

Figure 3.4: (**a**) Shows the UMOT quadrupole field centred 1 mm above the chip. The red line shows the path the field minimum takes as the x bias field is varied. (**b**) Demonstrates elongated shaped trap that the UMOT field produces. The mesh surface is where the field corresponds to a $\Gamma/2$ detuning compared to the centre of the UMOT. (**c**) Gives the required x bias field to centre the UMOT at a given height. Far from the chip this deviates from the dotted line predicted by equation 3.3 as the field from the end sections of the U becomes significant.

height

$$y_{\mathrm{umot}} = \frac{\mu_0 I_{\mathrm{umot}}}{2\pi B_x} \tag{3.3}$$

forming a 2D quadrupole field centred here. The transverse field gradient of the UMOT at its centre is

$$B'_{\perp} = \frac{\mu_0 I_{\mathrm{umot}}}{2\pi y_0^2}. \tag{3.4}$$

At the end of the transfer ramp, $y_{\mathrm{umot}} = 500\,\mu$m, and the UMOT has a transverse field gradient of $160\,\mathrm{G\,cm^{-1}}$. The axial field is much weaker over much of its length, and has a field gradient of $3\,\mathrm{G\,cm^{-1}}$ at the centre. Figure 3.4b shows the surface where $|\mathbf{B}| = 3\,\mathrm{G}$. This gives an indication of its elongated shape, which provides good overlap with the magnetic trap.

At larger distances from the chip the end and central sections of the U give comparable contributions to the magnetic field. The net field from the end sections shifts the quadrupole minimum away from x=0, to where $\hat{\mathbf{y}} \cdot \mathbf{B}_{\mathrm{umot}} = 0$. The

calculated field in the z=0 plane shown in 3.4a exhibits this shift. The red path in 3.4a is that taken by the quadrupole centre as B_x is varied. Moving up this path, $\hat{\mathbf{x}} \cdot \mathbf{B}_{\text{umot}}$ becomes increasingly weaker than that predicted by 3.3. Figure 3.4c shows the UMOT height, y_0 calculated from the full U model, as well as from the single wire model which gives an underestimate of the y_0.

As with the mMOT, the x-shift of the UMOT is corrected in our experiment with a small y bias field. The implications of the shift for the transfer from mMOT to UMOT are discussed in section 3.1.3.

3.1.3 Transferring Atoms from the MOT to the UMOT

A transfer ramp is designed to overlap the UMOT quadrupole with the mMOT quadrupole such that their minima are located at the same position, then to move them towards the chip surface, gradually reducing the mMOT field. For optimal transfer we suggest the trajectory of the quadrupole centre $y(t)$ should be continuous, and the field gradient of the combined field should be maintained or increased throughout the ramp. We use equations 3.1, 3.2, 3.3, & 3.4 for the mMOT and UMOT height and field gradient to formulate this ramp, which is controlled by variation of the U and MOT coil currents, I_{mot} & I_{umot}, and the x bias field B_x.

The two fields have similar orientation, so we assume the field gradient of the combined field B', is the sum of the two. Our requirements of the field gradient are thus

$$\begin{aligned} \frac{\mathrm{d}}{\mathrm{d}t} B'(t) \geq 0, \qquad & t > t_0 \\ \text{where } B'(t_0) = B'_{\text{mot}}(t_0) + B'_{\text{umot}}(t_0). & \end{aligned} \tag{3.5}$$

Since we want B'_{umot} to be as large as possible, we choose to set $I_{\text{umot}} = 2\,\text{A}$ throughout the transfer ramp.

The ramp is broken into two stages. Over the first stage we keep $B'(t)$ constant at its initial value $B'(t_0)$. As B_x is increased, $y(t)$ descends towards the chip and

eq.(3.2), eq.(3.4) and eq.(3.5) define how $I_{\rm mot}(t)$ must be decreased:

$$I_{\rm mot}(t) = I_{\rm mot}(t_0) + \frac{\mu_0 I_{\rm umot}}{2\pi\beta}\left(\frac{1}{y^2(t_0)} - \frac{1}{y^2(t)}\right). \tag{3.6}$$

At time t_1, the MOT coil current $I_{\rm mot}$ reaches zero, and the height must be $y(t) = y_1$ for the field gradient to be provided by UMOT quadrupole alone:

$$y_1 = \left(\frac{2\pi\beta I_{\rm mot}(t_0)}{\mu_0 I_{\rm umot}} + \frac{1}{y^2(t_0)}\right)^{-1/2} \tag{3.7}$$

Once we decide on the desired $y(t)$, this determines the required bias field $B_x(t)$ through eq.(3.1) and eq.(3.3), and the required mMOT coil current $I_{\rm mot}(t)$ through eq.(3.6). Over the second stage, with $I_{\rm mot} = 0$, we ramp up $B'_{\rm umot}$ by further increasing B_x. This also moves the UMOT further towards the chip to position y_2, defined as the final height of the UMOT at the end of the ramp. This also defines the time t_2, at which $y(t) = y_2$.

3.1.4 Implementing the Transfer Ramp

The equations eq.(3.1), eq.(3.3), eq.(3.6) and eq.(3.7), together with a function $y(t)$, specify how B_x and $I_{\rm mot}$ must be varied to transform the initial combined quadrupole field at height $y(t_0) = y_0$ into the tight UMOT field at position $y_(t_2) = y_2$. Three forms for $y(t)$ were tested experimentally: $y = y_0/(1+vt)$, $y = y_0 - vt$, & $y = y_0 - vt^2$, where t_0 is set to 0. The first suits the scenario where the UMOT should be brought to rest slowly at y_2. The second maintains equally rapid motion over each stage. The third accelerates, reducing time spent close to the chip, where atom number decays faster.

These three ramps were each tested with initial height $y_0 = 4\,\text{mm}$, final height $y_2 = 0.5\,\text{mm}$, and duration $t_2 = 50\,\text{ms}$. For $y = y_0 - vt^2$, the shape of the cloud in the UMOT at the end of the ramp was observed to be much shorter and wider than for the other two functions. This shape is poor for loading atoms into the magnetic trap so this function was rejected. To compare the ramps with $y = y_0/(1 + vt)$ and $y = y_0 - vt$ we looked at the atom number before and after the transfer. However, the final shape of the UMOT at y_2 was different for the two ramps, making a comparison

in atom number from the fluorescence difficult for these clouds which were optically thick.[1] Leaving the atoms to redistribute for a second or so in the final UMOT was not a good option for their comparison since the atom number in the UMOT decays significantly over this time scale. We therefore implemented them to complete the transfer to the UMOT at y_2, then reverse it back out to y_0. This allowed us to compare (in real time) the fluorescence before and after the out-and-back ramp in the initial MOT, where they could be left for a second or so to redistribute. Thus the fluorescence after each ramp could be compared in the same MOT as it was initially held, after giving the cloud sufficient time to redistribute. This allowed for a more reliable comparison of the transfer efficiency of the two ramps.

Using this method, for both functions we observed approximately 50% of the initial number of atoms were in the MOT after the out-and-back ramp. The linear ramp,

$$y(t) = y_0 - vt \qquad 0 < t < t_2, \tag{3.8}$$

was subsequently chosen due to its greater simplicity. We then optimised the duration of the two separate stages of the ramp, stage1 where $0 < t < t1$ and stage two where $t_1 < t < t_2$. The optimal durations are those found to maximise the atom number that is loaded into the magnetic trap. The details of each of the two stages of this ramp are given next.

The first stage of the transfer takes the cloud from $y_0 = 4\,\mathrm{mm}$ to $y_1 = 1.4\,\mathrm{mm}$. The optimal stage duration, given by t_1, was found to be 80 ms, and ramp rate therefore $32.5\,\mathrm{mm\,s^{-1}}$. The MOT coil current and x bias field vary during the first stage as

$$I_{\mathrm{mot}}(t) = I_{\mathrm{mot}}(0) + \frac{\mu_0 I_{\mathrm{umot}}}{2\pi\beta}\left(\frac{1}{y_0^2} - \frac{1}{(y_0 - vt)^2}\right) \qquad 0 < t \leq t_1 \tag{3.9}$$

$$B_x(t) = -\beta I_{\mathrm{mot}}(t)\,(y_0 - vt + \Delta_y) + \frac{\mu_0 I_{\mathrm{umot}}}{2\pi(y_0 - vt)} \qquad 0 < t \leq t_1. \tag{3.10}$$

[1] For low density clouds almost all scattered light escapes the cloud without being re-scattered by another atom, the the fluorescence is a good measure of the atom number. For an optically thick clouds, some of the light is re-scattered by other atoms before leaving the cloud. Without already knowing the density and shape of the cloud it is difficult to know how much light is re-scattered, and therefore how many atoms there are.

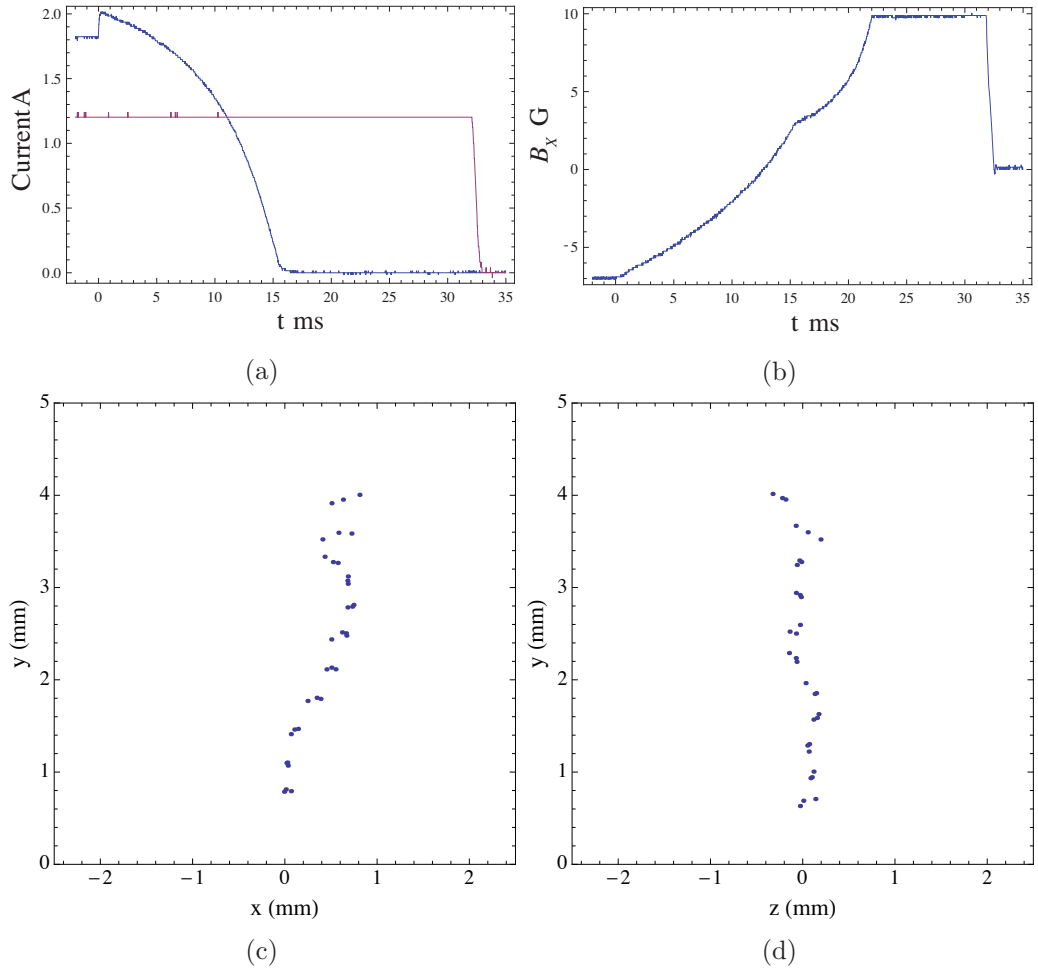

Figure 3.5: (**a**) MOT coil current during transfer ramp from MOT to UMOT. (**b**) B_x during transfer ramp, measured from current through the x bias coils. The coil and wire currents were measured on some of our initial tests of this transfer process with $v_1 = 170\,\mathrm{mm\,s^{-1}}$ and $v_2 = 130\,\mathrm{mm\,s^{-1}}$. Velocities were later optimised, but the form of the ramps remains identical. (**c**) & (**d**) Shows the path taken by the magneto-optically trapped cloud's centre of mass in the $x-y$ and $z-y$ planes. The horizontal x-shift with height of the quadrupole minimum is seen in the path in the $x-y$ plane. The wiggles in the $z-y$ are due spatial variation of the MOT beam intensities.

The second stage takes the cloud from y_1 to $y_2 = 0.5\,\mathrm{mm}$ over the duration $t_2 - t_1 = 20\,\mathrm{ms}$. The ramp rate was therefore $52\,\mathrm{mm\,s^{-1}}$. Over the second stage, $I_{\mathrm{mot}} = 0$, and

$$B_x(t) = \frac{\mu_0 I_{\mathrm{umot}}}{2\pi y(t)} \qquad t_1 < t \leq t_2 \tag{3.11}$$

Figures 3.5a & 3.5b show the MOT coil and the current in the x bias coils measured in our experiment during the transfer ramp. For the best transfer, a small amount of experimental adjustment is required, correcting for the shift of

the quadrupole centres in the y direction, as well as imbalances between the MOT beams. Our method is to position the MOT over the chip centre, then pulse on I_{u} for 1 s, reducing B_x to the value required by eq.(3.10) at t=0. Small adjustments are made to the y bias field B_y, and the initial MOT height until the UMOT 'pulse' gives minimal shift in the position of the trapped cloud. Once transferred to the UMOT the compensation from B_y is no longer required. It is therefore reduced over the course of the transfer ramp.

Figures 3.5c & 3.5d show data from an experiment where the centre of mass of the trapped cloud was measured as it is lowered during the transfer ramp. In the experiment, the MOT was initially loaded for 12 s, 4 mm above the chip, with $I_{\mathrm{mot}} = 1.8$ A. Then, I_{mot} was stepped up to 2A, the U-current switched on, and the x-bias set to $B_x(0)$ given by eq.(3.10). The cloud was then transferred into the UMOT following the linear transfer ramp discussed above. At various times between 0 and t_2, a fluorescence image of the cloud was taken from the side, from which the centre of mass of the cloud was measured. To measure the centre of mass in the y-z plane, the image was taken along the **x** direction (imaging axis 1). To measure the centre of mass in the x-y plane, the cloud cannot be imaged directly along the **z** direction since the horizontal MOT beams saturate the camera CCD. Instead a camera was (temporarily) aimed into the chamber at approximately 15° below the **z** direction, therefore avoiding the MOT beam. The x coordinate of the cloud centre of mass was taken from these positions. The y coordinate was taken from images in the $y - z$ plane.

Figures 3.5c shows the measured position x and y coordinates of the cloud during the transfer ramp. The data points therefore sketch out the trajectory of the cloud in the x-y plane. Slight variation in the y position with height is observed, and due to the lateral shifts in the MOT and UMOT discussed in the previous sections. In order to make sure we understand the observed trajectory, we calculated the minimum of the combined quadrupole from accurate models of the wires and coils, with the same values of $B_x(t)$, $B_y(t)$, & $I_{\mathrm{m}}(t)$ used in the experiment. The calculated trajectory in the $x - y$ plane is similar to that in figure 3.5c, with the same characteristic kink at $y = 1.4$ mm, where the mMOT field goes to zero.

The trajectory in the y-z plane does not suffer from such lateral shifts in the

quadrupole fields, and the path is predicted to be a straight vertical line. The small wiggles in measured path in the $y-z$ plane, clearly seen in fig.3.5d, are instead due to imbalances between the MOT beams. Such wiggles also occur in the trajectory in the $x-y$ plane, but these are overshadowed by the larger lateral variations discussed above.

The same field calculations described above to study the clouds trajectory were also used to investigate how the field and field gradient evolve during the transfer ramp, taking into account the lateral (x) shifts in the quadrupole minimum as its height changes. These shifts, neglected in the design of the transfer ramp, reduce the overall field gradient. Figure 3.6 shows the field and field gradient calculated along the two axes (eigenvectors) of the quadrupole in the x-y plane, which are orientated along the directions $\hat{\mathbf{e}}_\mathbf{1}$ & $\hat{\mathbf{e}}_\mathbf{2}$ and have coordinates λ_1 and λ_2. These axes are defined such that to first order expansion in λ_1 and λ_2, the direction of the field along either axis is parallel to that axis.[2]

Figures 3.6a & 3.6c show the amplitude of the field along $\hat{\mathbf{e}}_\mathbf{1}$ & $\hat{\mathbf{e}}_\mathbf{2}$ at 8 times during the transfer. Initially (red lines) they are linear, when dominated by the mMOT quadrupole field. Towards the end (blue lines), they follow the UMOT field. In fig.3.6a the field gradient, indicated by the slope of these lines, stays constant or increases for successive times. For later times a turning point also appears in the region $\lambda_1 < 0$, and leads to a reduction in the width of the trap in the latter part of the transfer when the quadrupole field is provided by the U-current alone. However, the field gradient has increased significantly the end of the transfer ramp, leading to tighter confinement within this reduced width. Similar behaviour is seen for the field along $\hat{\mathbf{e}}_\mathbf{2}$ in fig.3.6c. The trap width along this direction is also reduced by the turning point, this time in the region $\lambda_2 > 0$, towards the end of the transfer. Along this axis however, the field gradient, which starts higher than the initial value along $\hat{\mathbf{e}}_\mathbf{1}$, at first reduces before increasing again towards the end of the transfer ramp.

Figures 3.6b and 3.6d show explicitly the time dependence of the field gradients

[2]For the mMOT quadrupole in the absence of the U current as shown in fig.3.3a, $\hat{\mathbf{e}}_\mathbf{1}$ & $\hat{\mathbf{e}}_\mathbf{2}$ would therefore be the diagonals of $\tilde{\mathbf{r}}$ and $\tilde{\mathbf{z}}$ used in sec.3.1.1. For the UMOT quadrupole without the MOT as shown in fig.3.4a, one notices that these are only approximately these diagonals, since the UMOT quadrupole is rotated slightly and skewed. For the quadrupole during the transfer ramp, $\hat{\mathbf{e}}_\mathbf{1}$ & $\hat{\mathbf{e}}_\mathbf{2}$ are likewise only approximately the diagonals of the x-y plane due to the rotation and skew from the U-current.

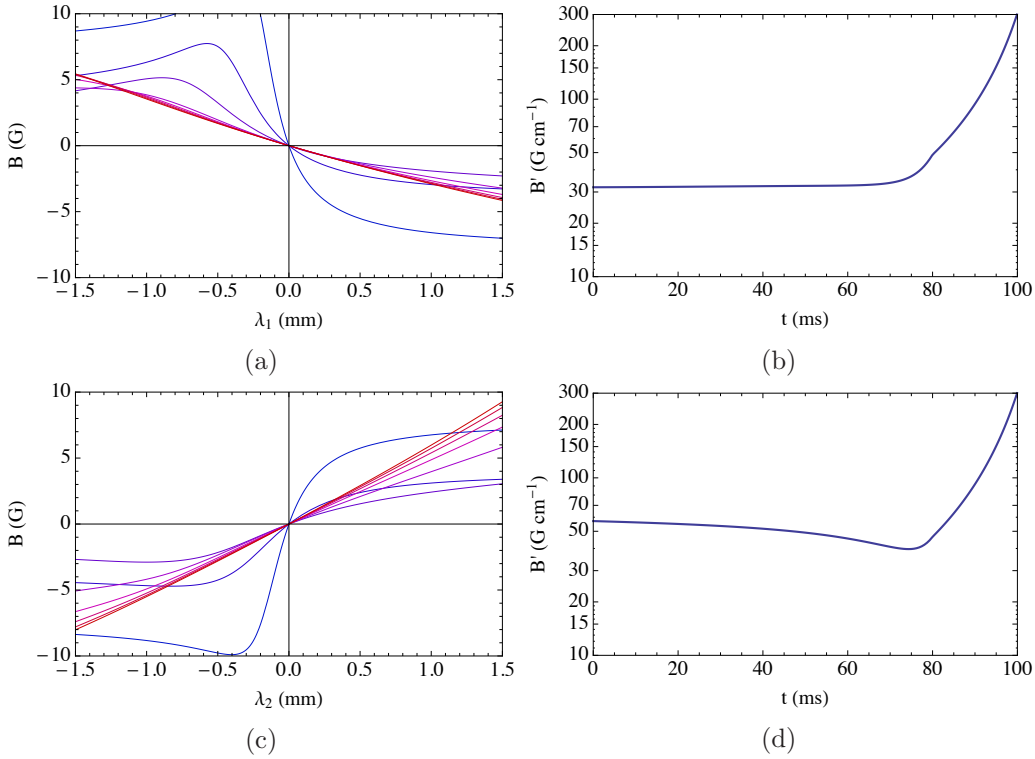

Figure 3.6: (**a**) & (**c**) Show the value of the magnetic quadrupole field along the directions $\hat{\mathbf{e}}_1$ and $\hat{\mathbf{e}}_1$ (as defined in the text) respectively at 8 evenly spaced times over the duration of the transfer ramp. (**b**) & (**d**) Show the field gradient at the the quadrupole minimum along $\hat{\mathbf{e}}_1$ & $\hat{\mathbf{e}}_2$ respectively.

$\partial\mathbf{B}/\partial\lambda_1$ and $\partial\mathbf{B}/\partial\lambda_2$ during the transfer ramp, evaluated at $\lambda_1 = \lambda_2 = 0$. In fig.3.6b it is clear that the field gradient remains constant until $6/10^{\text{th}}$ of the way through the ramp, after which it increases. In fig.3.6d the field gradient $\partial\mathbf{B}/\partial\lambda_2$ starts almost twice than that along λ_1, but reduces to a minimum $7/10^{\text{th}}$ of the way through the ramp, before starting to increase. Although the field gradient dips below its original value along this axis, it still remains higher than the field gradient along λ_1. These detailed simulations do not show any points during the transfer ramp where significant atom loss may occur due to deformations of the quadrupole field, despite the lack of consideration of the lateral shift and field asymmetries in the design of the transfer ramp in sec.3.1.3. Neither do we observe any points of significant atom loss from the same images taken during the transfer as used to study the cloud position in fig.3.5d.

Once the MOT has been loaded, the intensity of the horizontal MOT beams (along $\mathbf{z}$) is reduced. This results in a more elongated UMOT at the end of the transfer, which provides a better shape to load into the magnetic trap. During

the second stage of the transfer ramp, the MOT beams are red detuned by a further 60 MHz, reducing the scattering rate in the UMOT. This reduces the outward radiation pressure [53, 88], increasing the density, and lowering the temperature.

The number of atoms in the initial mMOT is not easy to measure with our setup due to partial obstruction of line of sight by our MOT coils. It is also hard to determine the number of atoms in the UMOT from fluorescence images because of the high optical density. Instead, the efficiency of the ramp is tested by executing the ramp, then reversing it to bring the atoms back into the original MOT, as described by the out-and-back sequence at the beginning of this section. We compare the shape of the MOT before and after the double ramp. Starting from a MOT under normal operating conditions, we estimate that we transfer 2/3 of the original atoms to the UMOT. For the largest initial MOTs we can produce, the efficiency is lower, as the initial MOT volume is much larger than the later stages of the combined MOT and UMOT. After release from the UMOT, we measure up to 6×10^7 atoms with absorption imaging.

3.2 Preparation for Magnetic Trapping

Once transferred to the UMOT, the cloud is held for 2 ms before the quadrupole is switched off for an optical molasses stage. The control signals to the bias field current drivers are switched sharply to zero at this time. The bias fields fall to zero over 0.5 ms, due to the inductance of the coils. The chip wires which have a much lower inductance respond rapidly. Starting to switch the Z wires and x-bias off at the same time would therefore result in the field minimum moving rapidly towards the chip surface, giving the cloud a sharp kick towards the chip surface. Instead Z wires are turned off with a small delay Δt to reduce or even reverse the direction of this kick. We use the offset Δt to fine tune the kick the cloud gets on release from the trap. This is used to tune the position of the cloud for optimal loading of the magnetic trap.

Once released, the cloud is cooled in an optical molasses for 3 ms. Here, there is efficient polarisation gradient cooling over the entire cloud, which reduces the temperature well below the doppler limit. Although the friction is high, the cloud still

expands and the position drifts during the molasses stage. For optimal loading into the magnetic trap, there is a balance to be struck between temperature reduction, and expansion of the cloud. The 3 ms molasses duration is the experimentally determined optimum. At the end of the molasses, the trap light is switched off, but the repump light is kept on. The measured temperature of the cloud after this molasses stage is typically found to be between 40 and 80 μK (see sec.3.2.2 below).

3.2.1 Optical Pumping

Next, the atoms are optically pumped into the F = 2, $m_F = 2$ low field seeking ground state for magnetic trapping. They are pumped with a 500 μs to 800 μs pulse of optical pumping light, σ_+ polarised relative to a 3 G x bias field and tuned to the $F = 2 \rightarrow F' = 2$ D2 line. The state $F = 2, m_F = 2$ is dark to this light. The optical pumping beam has a peak intensity of 1.7 mWcm^{-2}.

Correct polarisation is essential for a high population transfer into the magnetic trap. The optical pumping beam is circularly polarised with a $\lambda/4$ waveplate (as shown in fig.2.15a of sec.2.2.4) with orientation measured to be correct within 2°, and a manufacturer quoted (Thorlabs WPQ10M-780) retardation error of $\lambda/200$. We then align the bias field to the direction of the optical pumping beam. We do this by measuring the linear momentum transferred to the atoms after a 1 ms pulse. When correctly aligned, all atoms are rapidly pumped into the dark state where they no longer gain momentum from the light. For imperfect alignment there is a non-zero steady state population of other states, and the cloud gains momentum at a rate $N \sum_i \hbar \mathbf{k} \Gamma \rho_{ii}$, where i is summed over the excited state populations $N\rho_{ii}$.

The movement Δx of the cloud along the direction of the optical pumping beam is measured. The y & z bias fields are scanned, and the values for which Δx is minimised is found. Figure 3.7 shows the optimisation of the z bias field in this way. The sensitivity of this method can be increased by increasing the duration of the optical pumping pulse, and by decreasing the amplitude of the x bias field.

For correctly aligned optical polarisation and magnetic field, giving negligible π or σ_- components, almost all atoms are expected to be transferred to the dark state within approximately 5 scattering events. This approximate result can be seen by

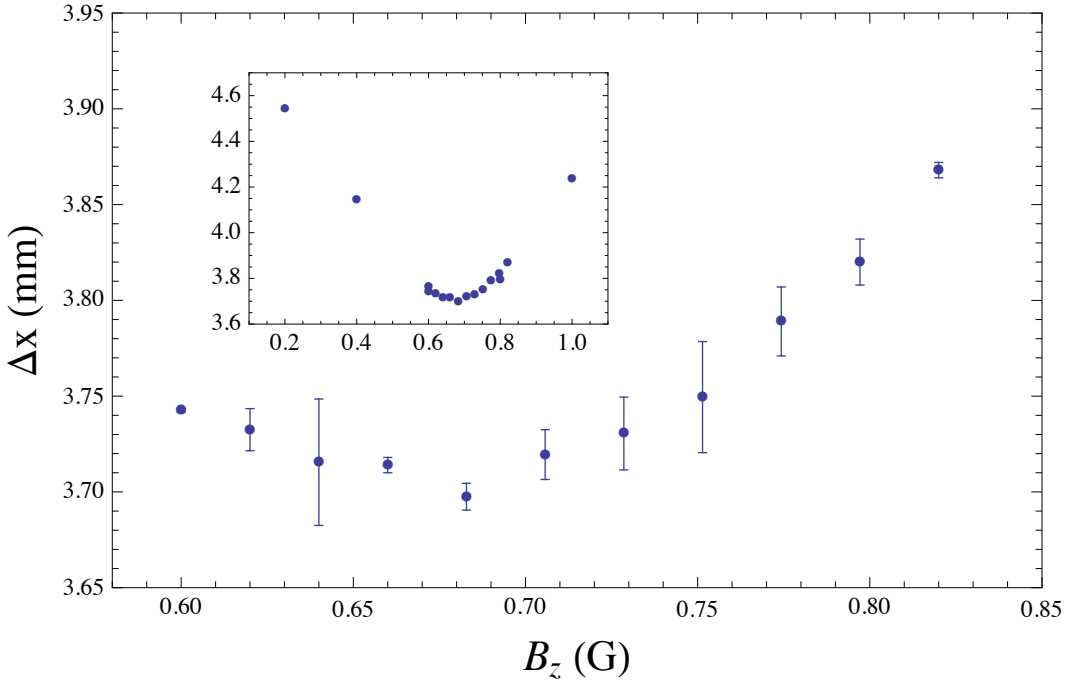

Figure 3.7: Optimisation of alignment of quantisation field to the optical pumping beam by measuring the momentum transfer. In this case B_z is optimised. For the minimum Δx, the component of the quantisation field in the x-z plane is aligned with the optical pumping beam. The inset shows a broader scan over B_z.

inspection of the branching ratios for the decay of atoms from the $5^2P_{3/2}$ F' = 2 excited state to the F = 2 ground state, assuming negligible decay to the F = 1 ground state.[3] In practice, some atoms will decay to the F = 1 ground state, and for this reason the repump light stays on during the optical pumping stage.

For this small number of scattering events, the momentum transfer should give a velocity increase of less than $3\,\mathrm{cms}^{-1}$ (one-photon recoil velocity $\hbar k/m \approx 6\,\mathrm{mm\,s}^{-1}$). For our pulse the additional momentum transferred through 267 MHz off resonant $\mathrm{F} = 2 \rightarrow \mathrm{F}' = 3$ scattering is between 1/6 and 1/3 of this. The cloud net velocity is measured to be $3.7\,\mathrm{cm\,s}^{-1}$ after a 0.5 ms pulse. Once captured in the magnetic trap this energy is shared between 6 degrees of freedom, and the corresponding increase in temperature is $mv^2/6k_B$, is $2\,\mu$K. This is small compared with the temperature of the cloud which is typically between 40 to $80\,\mu$K at this point.

To check the populations of the $\mathrm{m_F} = 0, 1, 2$ states after optical pumping in a thermal cloud we apply a field gradient by pulsing on the two small Z wires for 2 ms

[3]The exact evolution of state populations can be found from numerical solutions to the optical Bloch equations, as for example is done in [82].

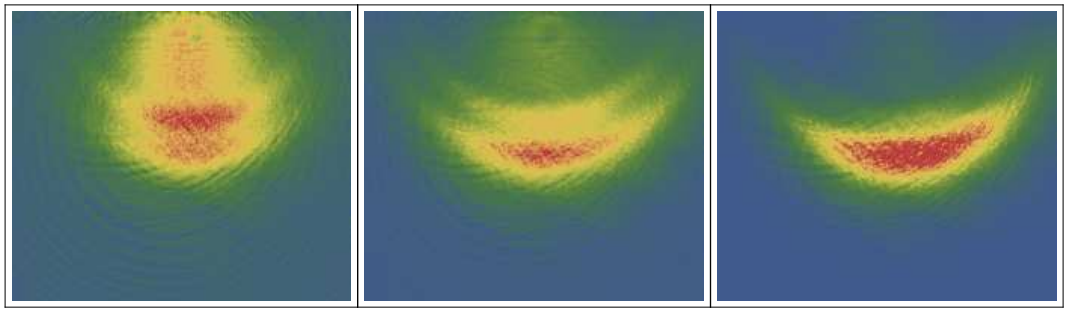

Figure 3.8: Stern-Gerlach experiment after optical pumping. These are absorption images taken after optical pumping, followed by a 2 ms pulse of the chip wires and further expansion. The $m_F = 0$ cloud remains circular as its dipole moment is zero. The $m_F = 2$ cloud is pushed furthest away from the wires. The left hand image has poor alignment, while the right hand is near optimal. The images are approximately 4.1 mm tall and 4.8 mm wide.

at 1 A each. This gives a Stern-Gerlach force $\mathrm{m_F} g_F \mu_B \nabla |\mathbf{B}|$ that spatially splits the cloud. Figure 3.8 shows three absorption images of split clouds taken looking along the z-axis. In the first the optical pumping light was blocked. The second was taken before we performed the alignment of the magnetic fields described above, and third after this alignment was completed.

In the first image of fig.3.8, there is a round cloud of atoms in the $\mathrm{m_F} = 0$ state, and two crescent shaped clouds, of which the top one is the $\mathrm{m_F} = 1$ cloud and other is the $\mathrm{m_F} = 2$ cloud below it. The crescent shape arises because of the shape of the magnetic field which decays like $1/r$ with distance r from the Z wires, together with the initial phase space distribution of the cloud. The $\mathrm{m_F} = -2$ and -1 states are not visible since they are rapidly accelerated into the surface of the chip wires when they are pulsed on. In the second image (with optical pumping but before careful alignment), there is only a small population in the $\mathrm{m_F} = 0$ cloud, with the most atoms found in the $\mathrm{m_F} = 2$ cloud. The third image, for which the magnetic field for the optical pumping was carefully aligned, shows almost all atoms are in the $\mathrm{m_F} = 2$ cloud. We sum the pixel counts of the absorption images over the regions of these clouds to estimate the relative populations of these three $\mathrm{m_F}$ states. How the clouds can be resolved from one another is limited by the field gradient, cloud temperature and time of flight. From the third image in fig.3.8, we estimate more than 9/10 of atoms are in the $\mathrm{m_F} = 2$ state after the careful aligned optical pumping stage.

3.2.2 Thermal Expansion

After release from optical molasses, the cloud expands ballistically. We measure a gaussian radial distribution with squared width $\sigma_r(t)^2$, which expands linearly with t^2. This is consistent with free thermal expansion of a cloud after release from a harmonic potential. However, the phase space distribution in a MOT or optical molasses cannot be derived through Boltzmann statistics. A brief description of why this distribution can be assumed is given below, following the arguments of [43].

In an optical molasses the force experienced by an atom can be broken into two parts, a continuous force $F_c(\mathbf{p}, t)$, and a stochastic force $F_s(\mathbf{p}, t)$. In the doppler theory of laser cooling, the continuos force is the net force on the atom from each of the n beams $F_{c_i} = R_{\mathrm{sc}_i}\hbar k_i$.[4] The net force has linear velocity dependence $F_c(\mathbf{p}, t) = -\beta v$ for $v \lesssim \Gamma/k$. The stochastic force comes from the emission of scattered photons, which are distributed evenly over 4π sr. Its mean value is therefore zero, but mean squared value $R_{\mathrm{sc}}^2\hbar^2k^2/\pi$ (in three dimensions).

In the limit where the correlation time of the stochastic force tends to zero, the velocity of an atom undergoes a random walk, with each step depending only on the current momentum, and not previous values. In this case the evolution of the momentum distribution $f(p, t)$ can be described by a Fokker-Planck equation [43]

$$\frac{\partial f(p,t)}{\partial t} = -\frac{\partial}{\partial p}\left(F_c(p)f(p,t)\right) + \frac{\partial^2}{\partial p^2}\left(Df(p,t)\right). \tag{3.12}$$

In the steady state $\partial f/\partial t = 0$, integrating the r.h.s. gives the solution

$$f(\mathbf{p}) \propto \exp -\frac{\beta p^2}{2mD}. \tag{3.13}$$

This has the same form as the Maxwell Boltzmann momentum distribution for a gas with equilibrium temperature $T = D/(k_{\mathrm{B}}\beta)$. Polarisation gradient cooling reduces the temperature below doppler theory limit. However, at low velocities the first order expansion of the continuous force is still proportional to v, and the stochastic force quantised in steps of $2\hbar k_i$, so the form of 3.13 is still valid.

Within the low velocity limit, but at high optical densities this theory breaks

[4] The scattering rate is must be modified to account for the presence of the other beams.

down. Re-scattered photons give an additional force, and the high optical density means that the intensity from each beam depends on where the atom is. At the end of the UMOT stage and during the optical molasses, the trap light detuning is increase to 72 MHz, significantly reducing the optical density and these effects.

The spatial distribution of the expanding cloud in the optical molasses originates from the shape of the UMOT trapping potential. From the Doppler limited theory, the spatially dependent part of the continuous force in the UMOT is proportional to the distance from the centre of the MOT r when the magnetic field is linear. This gives rise to a harmonic potential. Since there is strong coupling between motion in the **x**, **y** and **z** directions, and random distribution of the phase of motion, the gaussian momentum distribution leads to a gaussian spatial distribution. The phase space distribution in the optical molasses is therefore gaussian, which also what we observe experimentally. In three dimensions, with harmonic confinement from the UMOT in each direction, this is

$$f_0(\mathbf{r},\mathbf{p}) = \frac{N}{(2\pi)^{3/2}\sigma_p^3}\exp\left(-\frac{\mathbf{p}^2}{2\sigma_p^2}\right)\prod_{i=1}^{3}\frac{1}{\sqrt{2\pi}\sigma_i}\exp\left(-\frac{r_i^2}{2\sigma_i^2}\right). \tag{3.14}$$

Normalising $f_0(\mathbf{r},\mathbf{p})$ to 1 and calling the result $\tilde{f}_0(\mathbf{r},\mathbf{p})$, $\tilde{f}_0(\mathbf{r},\mathbf{p})\,\mathrm{d}\mathbf{r}\,\mathrm{d}\mathbf{p}$ gives the probability of finding an atom with $\mathbf{r}$ & $\mathbf{p}$ between $\mathbf{r}$ & $\mathbf{r}+\mathrm{d}\mathbf{r}$, $\mathbf{p}$ & $\mathbf{p}+\mathrm{d}\mathbf{p}$. Once all light and fields are turned off, there are no forces acting on the cloud, and it expands ballistically from its initial distribution at $t_0 = 0$. At a later time $t > 0$, the probability of finding an atom at position $\mathbf{r}$ is given by the probability of it initially sitting at $\mathbf{r}_0$ with momentum $\mathbf{p} = m(\mathbf{r}-\mathbf{r}_0)/t$. Substituting this in for $\mathbf{p}$ in $\tilde{f}_0(\mathbf{r}_0,\mathbf{p})$, then integrating over all initial positions $\mathbf{r}_0$ gives

$$f(\mathbf{r},\mathbf{p},t) = N\prod_{i=1}^{3}\frac{1}{\sqrt{2\pi}\sigma_i(t)}\exp\left(-\frac{r_i^2}{2\sigma_i(t)^2}\right), \tag{3.15}$$

after performing the gaussian integrals that arise. In eq.(3.15) we have dropped the subscript 0 from the distribution f, and included t in its argument to indicate that this is the distribution of the cloud after it has expanded for some time t, starting

from $f_0(\mathbf{r}, \mathbf{p})$. The time dependence of the spatial widths σ_i of $f(\mathbf{r}, \mathbf{p}, t)$ is given by

$$\sigma_i(t)^2 = \sigma_i^2 + \frac{k_\mathrm{B}T}{m}t^2, \tag{3.16}$$

where the σ_i on the r.h.s. are the initial spatial widths in 3.14.

In more a more general shaped trap potential $U(\mathbf{r})$, a cloud in thermal equilibrium and well described by Maxwell-Boltzmann statistics has spatial distribution $\exp\left(-U(\mathbf{r})/k_\mathrm{B}T\right)$. The integral over $\tilde{f}(\mathbf{r}, \mathbf{p})$, with $\mathbf{p} = m(\mathbf{r} - \mathbf{r}_0)/\Delta t$ can instead be evaluated in k-space using the convolution theorem.

In preparation for what follows we also describe the phase space distribution of the cloud in the magnetic trap potential $U(\mathbf{r})$. The phase space distribution here also is given by a Maxwell-Boltzmann distribution;

$$f(\mathbf{r}, \mathbf{p}) = \frac{N}{Z}\exp\left(-\frac{\epsilon(\mathbf{p}, \mathbf{r})}{k_\mathrm{B}T}\right), \tag{3.17}$$

with partition function given by $Z = \int \exp(-\epsilon(\mathbf{p}, \mathbf{r})/k_\mathrm{B}T)dV$ integrated over all phase space, and $\epsilon(\mathbf{p}, \mathbf{r}) = \mathbf{p}^2/(2m) + U(\mathbf{r})$. The atomic ensemble cannot be thought as being in equilibrium with an external heat bath as is usually the case in the application of these statistics. Instead, an equilibrium momentum distribution is reached through elastic collisions between atoms that redistribute the momentum. If the atoms are free to explore all regions of the trap in timescale τ, then an equilibrium spatial distribution is also reached after times larger than this. If the magnetic trap potential is conservative and the collisions are elastic the total energy E in the trap is conserved. The equilibrium temperature can be found from the mean particle energy E/N and the density of states $\rho(\epsilon)$.

3.3 Magnetic Trap

In this section we briefly introduce the concept of magnetic trapping of neutral atoms in static fields [58, 40], before exploring the trap potential generated by our atom chip. Three approximate models for the radial potential of our trap are introduced. These give descriptions valid up to three different energy scales. These models are used in sections 3.4 & 4.1 to study loading of the magnetic trap and evaporative cooling. We look at what assumptions can reasonably be made about the axial trap potential above a few μK (below which fragmentation occurs, section 4.3). Finally, predictions from trap models are compared to experimental measurements on the trap, and shown to be in excellent agreement.

3.3.1 Magnetic Trapping

The energy of atoms in a magnetic field can be described by the Hamiltonian

$$\mathbf{H} = \frac{\mathbf{p}^2}{2m} + g_F \mu_B \mathbf{F} \cdot \mathbf{B}(\mathbf{r}), \tag{3.18}$$

with atomic spin operator $\mathbf{F} = \mathbf{S} + \mathbf{J} + \mathbf{I}$, momentum operator $\mathbf{p}$, and magnetic field $\mathbf{B}$, which is treated classically for the static trap of this section. The first term is the kinetic term, and the second, the magnetic dipole interaction. The constants g_F, μ_B, & m are the Landé g-factor, Bohr magneton, and atomic mass. When the atomic spin follows the direction of the local magnetic field adiabatically i.e. without changing spin state, the interaction term leads to the potential,

$$U(\mathbf{r}) = g_F \mu_B m_F |\mathbf{B}(\mathbf{r})|, \tag{3.19}$$

where m_F is the spin projection of $\mathbf{F}$ along the local field direction, and labels the Zeeman sub-level of the atom. Atoms can be stably trapped in a minimum of the field magnitude $B = |\mathbf{B}(\mathbf{r})|$, in a state where $g_F m_F > 0$. For the ^{87}Rb $F = 2$ ground state, $g_F = 1/2$. States $m_F = 1, 2$ are trapped in the local field minimum, and $m_F = -1, -2$ repelled away from it.

The condition for spin adiabaticity can be understood from the semi-classical

picture[5], where the atom precesses about the direction of the local field at the Larmor frequency $\omega_l = m_F g_F \mu_B B/\hbar$. For example, let θ be the angle of the magnetic field at the atoms location $\mathbf{r}(t)$, relative to the field orientation at the position of the atom a small time δt previously, $\mathbf{r}(t-\delta t)$. Then, provided that the rotation frequency ω_B of the field orientation is slow compared to ω_l,

$$\omega_{\mathrm{B}} = 2\pi \frac{\mathrm{d}}{\mathrm{d}t}\theta \ll \omega_l, \tag{3.20}$$

the axis of the precessing spin follows the field adiabatically, and $\mathrm{F_z}$ is an adiabatic invariant. In this case the probability of spin flips is negligible [57, 89].

Where the magnetic trapping field is low, ω_l is small, and ω_{B} in eq.(3.20) can exceed ω_l where the field orientation changes rapidly, causing trap loss through spin flips. This makes trapping in a 3D quadrupole unstable at ultra low temperatures, where atoms pass close to the zero field minimum [91]. An Ioffe-Pritchard (IP) trap avoids this problem, as it is formed by a 2D quadrupole with perpendicular 'offset' field that raises the field minimum above zero. The offset field $B_0\hat{\mathbf{z}}$ smooths the variation of the field direction, and raises ω_l sufficiently high compared with any oscillating stray fields, preventing spin flip loss. This IP potential is given by

$$U(\mathbf{r}) = \mu |\, B'_\perp(x\hat{\mathbf{i}} - y\hat{\mathbf{j}}) + \mathbf{B}_0(z,r)| \tag{3.21}$$

$$\approx \mu \sqrt{B'^2_\perp r^2 + B_0(z)^2}, \tag{3.22}$$

where $\mu = m_F g_F \mu_B$. The offset field $\mathbf{B}_0(z,r)$ also has a minimum along $\mathbf{z}$ that provides axial confinement. The transverse components of $\mathbf{B}_0(z,r)$ shift the position of the trap minimum in the transverse directions, and the transverse gradient, curvature, and higher order derivatives will distort the shape of the 2D quadrupole described by $B'_\perp(x\hat{\mathbf{i}} - y\hat{\mathbf{j}})$. However, for typical IP traps $\mathbf{B}_0(z,r)$ varies much more gradually than the 2D quadrupole such that the distortion to its shape is negligible, and its small magnitude (typically $|\mathbf{B}_0(z,r)| \sim 1\,\mathrm{G}$) means that transverse shifts in the field minimum are negligible also. In this case the transverse components of

[5]Quantum mechanically a position dependent rotation is performed with the unitary operator $\mathbf{U}_{\mathrm{rot}}(\mathbf{r})$, so $\mathbf{B}$ points along the local $\hat{\mathbf{z}}'$ at $\mathbf{r}$. Then the interaction term in 3.18 gives the magnetic potential energy $U(\mathbf{r}) = g_F \mu_B F_z |\mathbf{B}(\mathbf{r})|$, but the rotated kinetic term $\mathbf{U}^\dagger \mathrm{p}^2/(2m)\mathbf{U} = \mathrm{p}^2/(2m) + \mathbf{\Delta T}$ where $\mathbf{\Delta T}$ couples the spin states [89, 90]. If the adiabatic condition 3.20 holds, $\mathbf{\Delta T}$ is negligible and atoms follow the field without flipping spin.

$\mathbf{B}_0(z,r)$ can be ignored, and $U(\mathbf{r})$ is given by eq.(3.22). In the second line, eq.(3.22), the transverse components of $\mathbf{B}_0(z,r)$ have been neglected. Under such conditions, IP traps also have an elongated cylindrical shape.

For chip traps such as ours, oscillating stray fields primarily arise from thermally induced current fluctuations in the gold layer [92, 93, 94].[6] At $100\mu m$ from the surface, the thermally induced spin flip rate is negligible for modest offset fields of $B_0(0) \sim \frac{1}{2}\,\mathrm{G}$ or greater.

3.3.2 Z Wire Trap

An accurate model of the trap potential can be made by integrating the Biot-Savart law over the current distribution of our chip wires. However, such a model is not always convenient for calculations such as those in sections 3.4 & 4.1. For this reason three simplified models are described that cover the potential up to three energy scales $\sim 10\,\mu\mathrm{K},\ 100\,\mu\mathrm{K}$ and $1\,\mathrm{mK}$.

Simple Z model and Finite Wire Models

A simple Z wire model consists of an infinitely long thin wire carrying current I along $\hat{\mathbf{z}}$ for the central part of the z, and two semi-infinite thin wires at $\pm a = \pm 3.5\,\mathrm{mm}$ for the ends. Since the atoms are trapped near the centre of the central wire[7], the semi infinite wires at each end can be replaced by infinite wires carrying current $I/2$.

The centre wire together with B_x describe the 2-d quadrupole, similar to that of the UMOT. The transverse field at position (x,y,z) is

$$B_\perp = \frac{\mu_0 I}{2\pi r}\left(\frac{y}{r}\hat{\mathbf{x}} - \frac{x}{r}\hat{\mathbf{y}}\right) - B_x\hat{\mathbf{x}}. \tag{3.23}$$

The axial offset field $B_0\hat{\mathbf{z}}$ is the sum of the bias field B_z and the $\hat{\mathbf{z}}$ component of the

[6] They also arise from the motion of the atom through the trapping field. However, in our trap this motion is in the range of a few Hz to a few kHz, which is much less ω_l which is typically $\sim$ MHz.

[7] More specifically the x-coordinates of trapped atoms satisfy $x \ll \sqrt{y^2 + (z \pm a)^2}$.

field originating from the wires at each end.

$$B_0 = \frac{\mu_0 I}{4\pi}\left(\frac{y}{y^2+(z+a)^2}+\frac{y}{y^2+(z-a)^2}\right)\hat{\mathbf{z}} + B_z\hat{\mathbf{z}}. \tag{3.24}$$

This provides axial confinement. The end sections of wire also have $\hat{\mathbf{y}}$ component which we call $B_{\circlearrowleft}$.

$$B_{\circlearrowleft} = \frac{\mu_0 I}{4\pi}\left(\frac{z+a}{y^2+(z+a)^2}+\frac{z+a}{y^2+(z+a)^2}\right)\hat{\mathbf{y}} \tag{3.25}$$

A field with direction $+\hat{\mathbf{y}}$ shifts the centre of the quadrupole in the $+\hat{\mathbf{x}}$ direction, and a field in $-\hat{\mathbf{y}}$ in the $-\hat{\mathbf{x}}$ direction. Since the field $B_{\circlearrowleft}$ changes sign for $z \gtrless 0$, it twists the trap in the $x-z$ plane, as shown in figure 3.10e. The axis of the trap is rotated by about 2 mrad at the centre of the trap. This small rotation is important to consider when calculating the trap frequencies and the axial potential from the finite wire model. Experimentally, it also couples the motion of atoms in the $\hat{\mathbf{x}}$ & $\hat{\mathbf{y}}$ directions. However, for this model it is ignored.

This model offers an accurate description of the radial profile right up to the trap depth when gravity is also included (the effect of gravity is discussed in detail along with the trap depth in sec.3.3.5). The tightness of radial confinement is overestimated close to the chip $\lesssim 100\,\mu$m since the actual current distribution is $85\,\mu$m wide. It also overlooks the second minimum that arises from having two Z wires.

A more accurate description of the trap field is given by integrating the Biot-Savart law for the current distribution $\mathbf{J}(x,z)$ on the surface of the chip. The geometrical shape of $\mathbf{J}(x,y)$ can be broken down into many straight segments of wire as illustrated in fig.3.9. The central parts of the each Z wire is represented by 10 strands of this wire carrying $1/10^{\text{th}}$ of the current[8]. With this consideration the trap forms a few microns closer to the chip and has slightly weaker radial confinement.

The $35\,\mu$m gap between the central wires means a second minimum is formed close to the chip, where the field from the two wires cancel each other. The barrier between this minimum and the main trap minimum is typically larger than 1 mK,

[8]The field can be solved for a finite length wire of finite width, but we find such a solution slow to compute in subsequent calculations based on the trapping field. The 10 strand wire gives negligible difference at the distances from the chip we are concerned with.

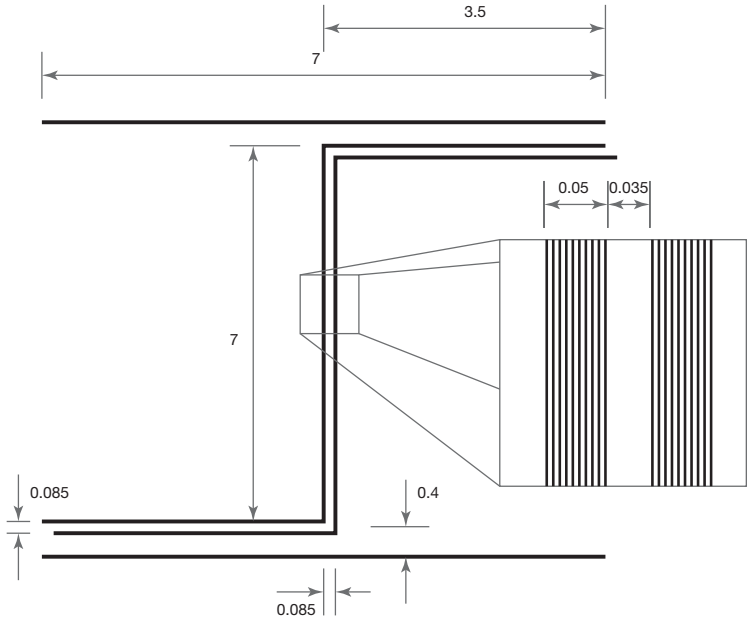

Figure 3.9: Layout of wires for the finite length wire model. All lengths are specified in millimetres.

but can be lower for traps closer than $100\,\mu$K from the chip, and can effect the trap depth. The two minima are found to coalesce $35\,\mu$m from the chip when $B_x = 50\,$G, when the width of the wires is taken into account.

This model provides an accurate description of the axial potential. The radial trap eigen-frequencies can be found from it by diagonalising the Hessian matrix for the potential. The axial profile and radial eigen-frequency are shown to be in excellent agreement with experimental values in section 3.3.4.

IP and harmonic models

A slightly simpler model than the Z wire model is one we shall refer to as the IP model. This consists of a 2D quadrupole in the $x-y$ plane, together with the axial offset field $B_0\hat{\mathbf{z}}$. The centre of the quadrupole is at $(0, y_0)$, where y_0 is its distance from the chip surface set by the value of B_x and the total current I through the two Z wires,

$$y_0 = \frac{\mu_0 I}{2\pi B_x}. \tag{3.26}$$

The radial coordinate $\rho^2 = x^2 + (y - y_0)^2$ is introduced as the distance from the quadrupole centre. For $\rho \ll y_0$, the magnitude of the quadrupole field is given to

first order in ρ by

$$|B_\perp| = B'_\perp \rho, \qquad \text{where } B'_\perp = \frac{\mu_0 I}{2\pi y_0^2}. \tag{3.27}$$

The axial offset field $B_0\hat{\mathbf{z}}$ has minimal variation over the central 5 mm of the trap. Shortly beyond this, it rises sharply. A harmonic approximation is often used to describe this, but our finite wire model shows this to be quite a poor approximation above just a few μK. A more complicated function could be used, but a square well approximation is quite adequate for our work on loading the trap and evaporative cooling.[9]

In a power law potential, $U \propto c_x x^{p_x} + c_y y^{p_y} + c_z z^{p_z}$, the trap volume, number density, and energy density of states depend on the reciprocal of the scaling indices p_i. The theory of trap loading and evaporative cooling presented in sections 3.4 & 4.1, depends on integrals over the density and energy distributions. So for traps where $1/p_z \ll 1/p_x + 1/p_y$, the dependence of the density and energy integrals on p_z is negligible. The IP model has $p_r = p_x = p_y$ with value between 1 & 2, and for $T > 10\mu K$ the axial potential scales with $p_z \gtrsim 10$. Hence, we ignore the axial dependence, making the approximation $1/p_z \approx 0$. Equivalently, when $p_z \to \infty$, the axial potential becomes perfectly square.

The IP model is

$$U(\rho, z) = \begin{cases} \sqrt{\mu^2 {B'_\perp}^2 \rho^2 + U_0^2} - U_0, & |z| < a \\ \infty, & |z| > a \end{cases} \tag{3.28}$$

where $U_0 = \mu B_0$.

This describes the trap potential as the standard Ioffe-Pritchard trap radially, and a square well axially. In this model the energy is shifted such that the potential $U(\rho, z)$ is zero at the centre of the trap, $\rho = z = 0$. At energies large compared to U_0, the radial potential scales linearly with r. For energies less than U_0, the radial

[9] Further considerations are made in section 4.1 for evaporative cooling below 10 μK where the length of the trap shortens rapidly with temperature.

potential becomes harmonic, with angular frequency

$$\omega_\rho^2 = \frac{\mu {B'_\perp}^2}{mB_0} = \frac{\mu}{m}\left(\frac{2\pi}{\mu_0 I}\right)^2 \frac{B_x^4}{B_0}, \tag{3.29}$$

where eq.(3.26) and eq.(3.27) were used in the second equality. The harmonic approximation allows us to express the trap as a simple power law potential $U(r) = \frac{1}{2}m\omega_\rho^2\rho^2$, for temperatures $k_\mathrm{B}T \ll U_0$.

3.3.3 Comparison of Trap Models

The finite-wire model is the most realistic and provides a benchmark for examining the other approximations. Figures 3.10a, 3.10b & 3.10c show potential energies along the x, y & z directions through the centre of the trap, with energy in units of μK. The current in each Z-wires is $I = 2\,\mathrm{A}$, the x-bias is $B_x = 31.5\,\mathrm{G}$, and the externally applied z-bias is $B_z = 1\,\mathrm{G}$. The ends of the Z-wires only contribute a further 10 mG to the z component of the field at the trap minimum, such that $B_0 = 1.01\,\mathrm{G}$. For points of reference: The temperature of cloud is between 100 & 200 μK when we begin forced evaporative cooling; the cloud that we load has a width on the 100 μm scale, and thermalises with temperatures in the range of 100 to 500 μK; and at the low energy end, at about 1 μK, roughness in the axial potential becomes an important consideration, and leads to fragmentation of the cloud.

Figures 3.10a & 3.10b show that the harmonic model fits the shape of the radial potential only up to about $50\mu K$. The IP model provides good agreement beyond $500\mu K$ in the x direction, and is correct within 20% up to 500 μK in the y direction. The inset in fig.3.10b shows that beyond this, the simple z model is required to take into account the $1/r$ decay of the trapping field.

Figure 3.10c shows the axial potential, which is highly elongated, and rises sharply within 1/2 mm from the ends of the z wire. The z wire model is in good agreement over the central 6 mm, but the harmonic approximation is quite poor. The potential is plotted with a logarithmic energy scale in figure 3.10d, together with power law potentials to demonstrate the scaling index. The shape of the ends of the trap scales approximately with power 2 up to 1 μK, power 6 from about 10 to 20 μK, power 10 at about 30 μK. Above 100 μK with power greater than 20. This supports our

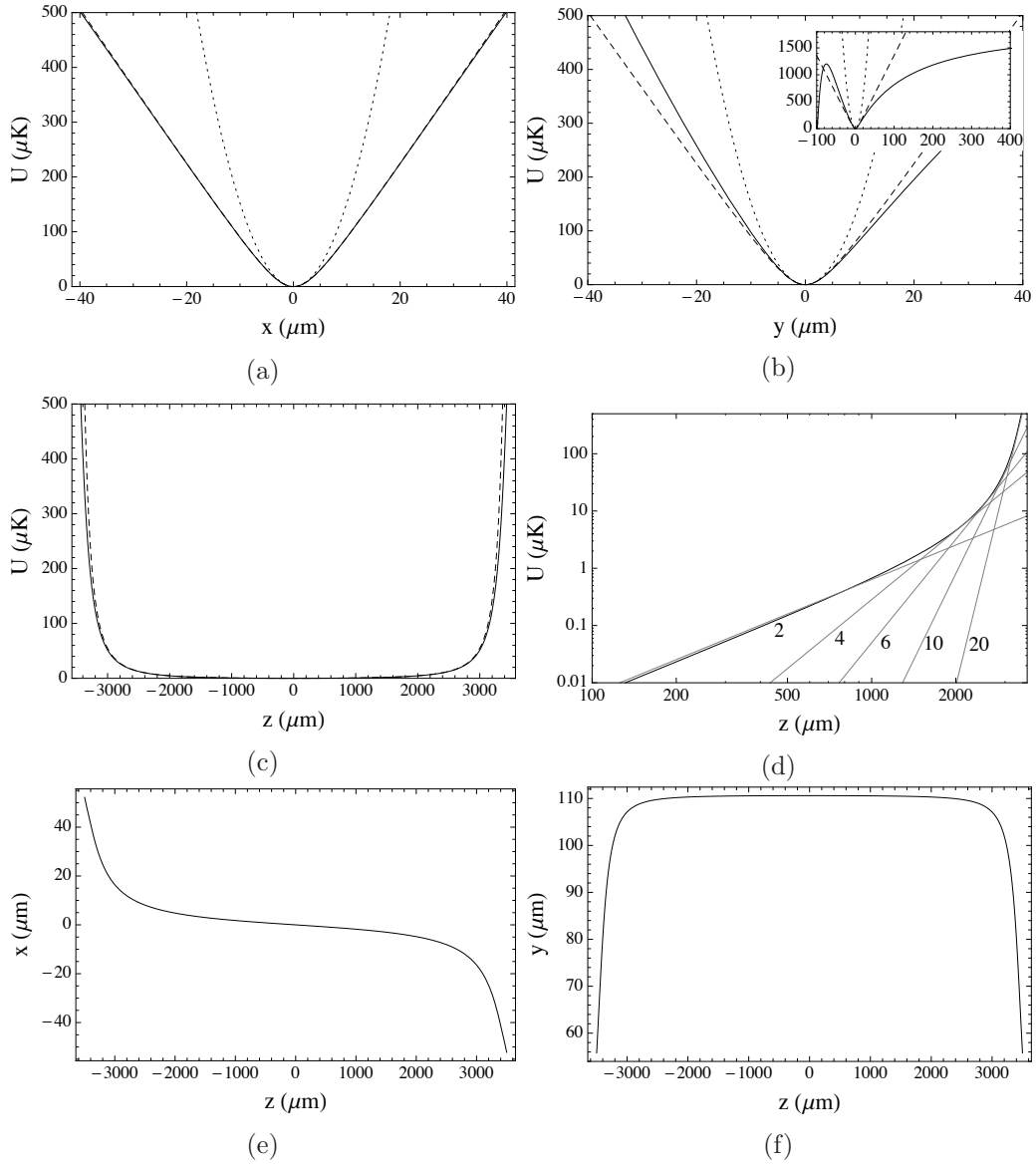

Figure 3.10: All solid lines are results from the finite-wire model. In (**a**), (**b**) and (**c**) the dashed line is the IP approximation of our trap given by equation 3.28, and the dotted line the harmonic approximation. (**a**) The transverse potential in the $\hat{\mathbf{x}}$ direction. The dashed line is the IP approximation of our trap given by equation 3.28, and the dotted line the harmonic approximation. (**b**) As previous, but in the $\hat{\mathbf{y}}$ direction. The inset shows the same functions over a wider range of y and U. (**c**) Axial potential taken as the minimum trap energy at a given z. The dashed line is the potential given by the infinite wire model of equation 3.24. (**d**) Part of the same axial potential. The grey lines, tangential to the trap potential are for potentials $\propto z^{p_z}$, with index shown. (**e**) & (**f**) are the position of the trap minimum in the x-z and y-z planes, calculated from the finite wire model. The chip surface is at $y = -110\,\mu$m. The trap potential is rotated in the x-z plane by the $\hat{\mathbf{y}}$ components of the magnetic fields from the end sections of wire.

square approximation in section 3.3.2.

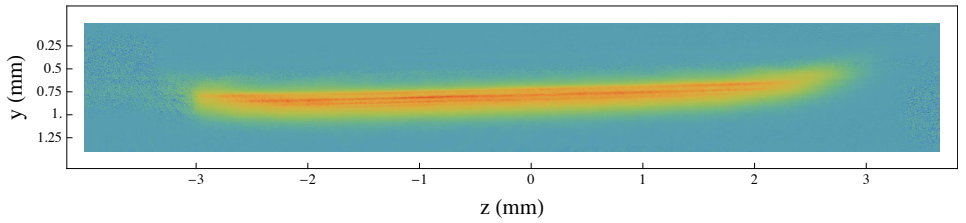

(a)

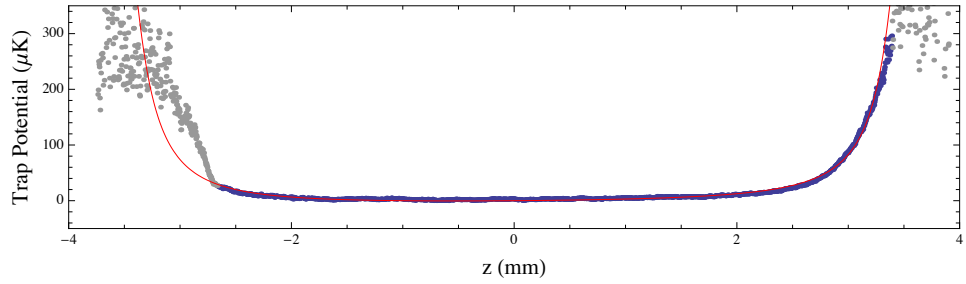

(b)

Figure 3.11: (**a**) Absorption image of a 80 μK cloud released from the magnetic trap after 2 ms. During this time, the cloud expands radially to 35 times its original width, while axial expansion is only a few percent, which shows the highly elongated nature of our trap. (**b**) Trap potential reconstructed from the cloud density profile, shown by the blue data points. The red line is the predicted profile from the finite-wire model, and shows excellent agreement to the experimentally measured profile. The grey data points to the left are excluded, where the chip substructure obstructs the image, giving a false sharp rise in the potential. The grey data points to the right are excluded where the cloud density signal to noise ratio is poor.

3.3.4 Measurements on the Trap Potential

Predictions of the trap frequency and axial potential made by the finite-wire model are compared to experimental measurements, and shown to be in excellent agreement. The axial trap potential is reconstructed from the axial density profile of the cloud taken from absorption images. The radial frequency is measured by transverse shaking of the trap and finding the resonance.

The equilibrium density distribution of the trapped cloud is given in equation 3.17 of section 3.2.2, assuming Maxwell Boltzman statistics. A trapped thermal cloud has this distribution provided its temperature is several times lower than the trap depth so it is in a quasi-thermal-equilibrium state with negligible evaporation. We measure the density distribution of an 80 μK cloud for a trap with a depth of $> 1500\,\mu$K. Given the axial density profile and temperature of the cloud, equation 3.17 can be inverted to recover the axial potential.

The density profile of the cloud is hard to measure while the atoms are trapped because the optical density is high and the width is small ($\approx 10\,\mu$m). We therefore image the cloud a few ms after release from the magnetic trap. Figure 3.11a shows an absorption image of an $80\mu K$ cloud 2 ms after it was released from the trap. In this time we estimate its transverse Gaussian width to have expanded by a factor of roughly 35. The expansion in the axial direction is only a few percent of its original length.

The axial density distribution $n(z, t = 2)$ is found by summing over columns of pixels in this image. The momentum distribution of the cloud is Gaussian, and equal at all points. The brief period of thermal expansion blurs the resolution by root mean squared distance $\sigma = \sqrt{k_{\rm B}T/m}\,t$, to give density distribution

$$n(z,t) = \int_{-\infty}^{\infty} n(z',0)\frac{1}{\sqrt{2\pi}\sigma(t)}\exp\left(-\frac{(z-z')^2}{2\sigma(t)^2}\right)\mathrm{d}z' \tag{3.30}$$

This limits the resolution to about $200\,\mu$m for $T = 80\,\mu$K, and slightly broadens the ends of the cloud[10].

Figure 3.11b shows the experimental trap potential reconstructed from the cloud density 3.11a averaged over 5 absorption images. The grey data points are excluded where features on the chip substructure obscure the image, leading to inaccurate measurements. The blue data points are in excellent agreement with potential predicted by the finite wire model, shown by the red line, which has been rescaled by 1.5 %, consistent with the magnification error in our imaging system. The predicted and measured potentials are both with external bias fields $B_x = 31.5\,$G & $B_z = 0.9\,$G, and have 1 A running through each z wire.

The resolution with this method is too low to be used for measuring the tight radial potential. However, the radial potential is characterised by angular frequency ω_r, and is highly harmonic at low temperatures. We excite transverse oscillations in a $\sim 10\,\mu$K trapped cloud by shaking it with amplitude $X_0 \approx 1\,\mu$m in the $\hat{\mathbf{x}}$ direction. Elastic collisions damp the transverse oscillations, heating the cloud. We measure the axial rms width of the cloud which grows with the increase in temperature. We plot this width versus the drive frequency in fig.3.12a, and identify the resonant

[10]Deconvolution to recover $n(z,0)$ is very difficult, as a tiny amount of high frequency noise in the Fourier transform $\hat{n}(k,t)$ will dominate the signal on division by the Gaussian $\hat{g(k)}$.

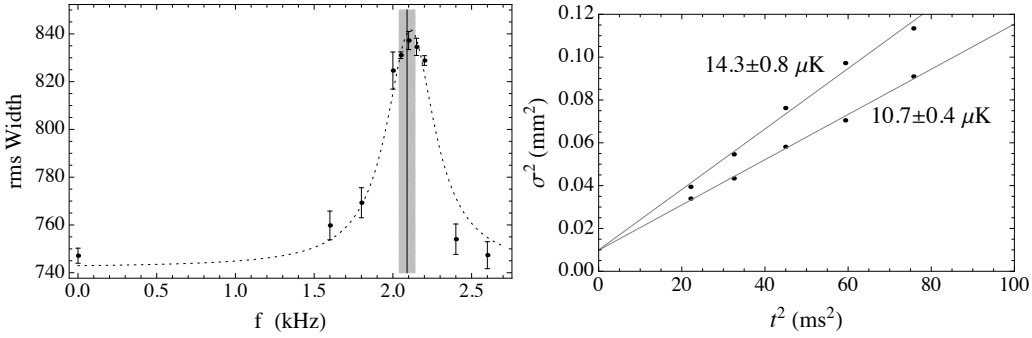

(a) (b)

Figure 3.12: (**a**) Shows the radial trap resonance, when the trap centre of mass is shaken sinusoidally $x_{\rm com} = B\sin(2\pi ft)$, with an amplitude of $B \approx 1\,\mu$m. The axial rms width of the trapped cloud is plotted against the driving frequency. Each data point is the mean value of between 3 and 5 measurements, and the error bars indicate the maximum deviation of these measurements from the mean value. The dotted line is a Lorentzian function, fitted to the points shown as an approximate response function. The solid vertical line is the radial trap frequency predicted by the finite wire model. The shaded region illustrates the uncertainty in this predicted value, due to uncertainty in the exact value of the x-bias field applied in the experiment. The oscillations are damped by elastic collisions, leading to an increased temperature of the cloud. (**b**) Shows the temperature increase, estimated from the widths of the cloud as it expands (data points), which is released from trap 50 ms after we stop driving oscillations. The temperature is taken from the gradient $k_{\rm B}T/m$ of the fitted straight lines. The errors in the temperatures are given by the standard error in the gradient of the fitted lines, and assumes equal weighting of the data points.

frequency of the trap where the rms width is largest.

To oscillate the trap, we run an AC current through the large Z wires, with a π phase lag between them. This creates a field $B\sin(\omega t)\hat{\mathbf{y}}$, which shakes the trap in the $\hat{\mathbf{x}}$ direction. After $\Delta t = 100\,$ms we stop oscillating the trap and wait 50 ms for the cloud to thermalise (the elastic collision rate is $\sim 100\,\mathrm{s}^{-1}$), before releasing it from the trap and measuring the cloud's length. Figure 3.12a shows the axial rms width of the cloud, measured as a function of frequency. Each data point is the mean value of between 3 and 5 separate measurements. The error bars show the maximum deviation in the individual measurements from this mean. The points show a distinct resonance close to 2.1 kHz. We have fitted a Lorentzian function, $b + a/(\gamma + (f - f_0)^2)$, to these data points, as a rough approximation of the frequency response of the axial width of the cloud to transverse oscillations. This is fitted fitted with weight factors proportional to the inverse of the error bars.[11] The peak of the fitted Lorentzian is at $2.11 \pm 0.01\,$kHz. The error is determined from the standard error in the fit parameter f_0, however, this does not include the

[11] We fit this function using the function "NonlinearModelFit" in Mathematica.

systematic error due to the assumption that the frequency response of the axial width is Lorentzian. From the theoretical finite wire model, we calculate that the trap frequency is $2.09 \pm 0.05\,\mathrm{kHz}$. The uncertainty in this predicted value is limited by accuracy with which we determine the x-bias field used for the magnetic trap potential. The experimental measurement of the radial trap frequency is in excellent agreement with this calculated value.

Figure 3.12b shows the temperature increase from $10.7 \pm 0.4\,\mu\mathrm{K}$ without shaking, to $14.3 \pm 0.8\,\mu\mathrm{K}$ after shaking the cloud at resonance for 100 ms. These temperatures were measured from the rate at which the cloud expands in the transverse direction after it was released from the trap. The errors quoted are from the gradient in the fitted line (which is equal to $k_\mathrm{B}T/m$), and assume equal weighting of all data points. The small temperature increase of approximately $4\,\mu\mathrm{K}$ highlights the need to perform this resonance experiment at a sufficiently low temperature to obtain a good signal to noise ratio in the increase in the axial width of the cloud.

3.3.5 Trap Depth

We now discuss the depth trap, which is an important consideration for the loading of the magnetic trap, described in the next section. Figure 3.13a shows the trap potential along the y axis, with two saddle points at y_2 & y_3 (discussed below), over which atoms can be lost.

Neglecting gravity, the trap depth is given by the magnetic field at infinity $\sqrt{B_x^2 + B_z^2}$, minus the field at the trap bottom B_0. Since the B_x is inversely proportional to distance of the trap from the chip, $B_x = \mu_0 I/(2\pi y_0)$, traps closer to the chip with maximum current in the Z wires are deepest.

The trap depth is lowered when gravity is included, which creates a saddle point at y_2 along the y-axis where the field magnitude has gradient $\partial_y|\mathbf{B}| = mg/\mu_\mathrm{B} = 15\,\mathrm{G\,cm^{-1}}$. Gravity also shifts the trap minimum at y_1 further from the chip than y_0. This shift is small for our trap when $y_0 \lesssim 200\,\mu\mathrm{m}$. Since the location of these gravitational turning points (at y_1 and y_2) are dependent only on the transverse potential at $z = 0$, the simple Z model with gravity included is sufficient. The two

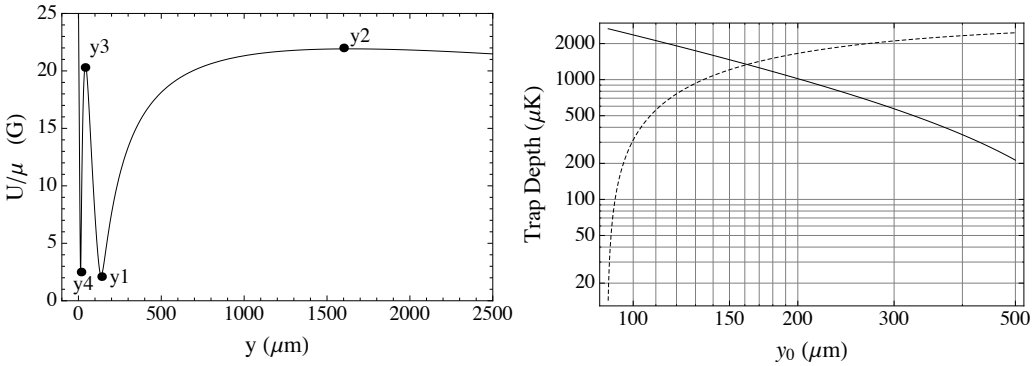

(a) (b)

Figure 3.13: Figure (**a**) shows the two saddle points in the trap potential in the region $y > 0$. This limit the trap depth. The first is due to the field from one Z wire cancelling the field from the other. The second, farther from the chip, is the turning point due to gravity. Figure (**b**) shows the depth of the trap limited by the turning points at y_2 and y_3, as a function of y_0, the height of the trap minimum above the chip. The solid line is the energy difference between the trap bottom and the saddle at y_2. The dashed line is the energy difference between the trap bottom y_1 and the saddle at y_3. For $y_0 < 160\,\mu$m, the trap depth is limited by the saddle at y_3 (dashed line), and for $y_0 > 160\,\mu$m it is limited by the saddle at y_2.

turning points y_1 and y_2 are given by the solutions of

$$\partial_y \sqrt{\left(\frac{\mu_0 I}{2\pi}\right)^2 \left(\frac{1}{y} - \frac{1}{y_0}\right)^2 + B_0^2} = \frac{mg}{\mu_B}, \tag{3.31}$$

and the trap depth E_t is

$$E_t = U(0, y_2, 0) - U(0, y_1, 0). \tag{3.32}$$

Figure 3.13b shows the trap depth E_t plotted against the distance y_1 of the trap minimum from the chip.

The gravitational saddle at y_2 is an effective loss channel for atoms with energy $\epsilon > E_t$, which leave the trap when they pass through this region. The hole this forms widens rapidly along y and z with increasing energy. The loss of atoms through this hole shortly after the magnetic trap is loaded is discussed in the next section.

Let us turn now to the saddle at y_3 between the main trap minimum and the second minimum close the the chip. A finite width wire model is required to determine this with accuracy, as the distances involved are comparable to the width

of the current distribution.[12] The dashed line of figure 3.13b shows the trap depth limited by this barrier.

This saddle only becomes lower than $U(y_2)$ when the trap is formed closer than $140\,\mu$m from the chip. Atoms can be lost through spin flips if they escape the barrier, and pass close to the second minimum at y_4 with sufficient velocity. We typically load a trap that is greater than $150\,\mu$m from the chip, so this loss channel is ignored.

The second minimum at y_4 is also of potential interest to us. By trapping atoms in this minimum, we could bring the atoms much closer to the surface of the chip. Here we could investigate various atom-surface interactions such as spin flips induced by eddy-currents in the gold surface [92, **?**], and the Casimir-Polder interaction between the atoms and the surface itself [95, 96]. We have not yet attempted to load atoms into this minimum, but this could be an objective of future work.

[12] The barrier is higher and closer to the chip than predicted by a double infinite wire model.

3.4 Loading the Magnetic Trap

Section 3.4.1 introduces a simple method for calculating the temperature rise when atoms are loaded from the molasses into a (infinitely) deep magnetic trap. In sec.3.4.2 we then develop a loading model that takes into account the finite depth and more complicated shape of our magnetic trap. In section 3.4.3 we describe our experimental loading procedure and compare results to this theoretical model. In section 3.4.4 we use the theory to comment on the possible sensitivity of number and temperature in the magnetic trap to fluctuations in the pre-trapped cloud.

Loading the cold atomic cloud from the optical molasses into the magnetic trap with sufficiently high number and density is crucial in the production of a BEC through evaporative cooling. The number of atoms captured, and the temperature of the loaded cloud depend on the shape, depth and position of the trap potential. We can interdependently vary the trap radius, position and depth, and the position of the molasses cloud for the best possible loading conditions. After much optimisation, we capture more than half the thermal cloud which at the end of the molasses stage contains approximately 6×10^7 atoms at $80\,\mu$K. After 600 ms, 25×10^6 atoms remain at a temperature of $120\,\mu$K, once the hottest atoms have escaped.

Optimal loading occurs when phase space density of the trapped cloud is maximised. This is most readily achieved when the shape of the cloud is similar in both UMOT and magnetic trap. The UMOT provides us with a cloud of similar length to our magnetic trap. However, the radial size of the UMOT corresponds to a radial trap frequency of only about 100 Hz. Such a weak trap produced by our chip would only be $40\,\mu$K deep - about half the temperature of the pre-trapped cloud. Because of atoms loss, we (and others [84]) find that a deeper, and therefore tighter magnetic trap loads with a higher phase space density.

3.4.1 Loading into an Infinitely Deep Trap

It is useful first to consider loading infinitely deep traps of general shape. In this case, all the atoms are captured, so we need only define how the trap energy E is altered by the trap potential, and not the number of atoms N.

Consider a 3D molasses cloud in free expansion with initial phase space distribution $f(\mathbf{r}, \mathbf{p}, t_0)$, normalised to N. The momentum distribution, assumed to be Gaussian, is characterised by temperature T_0, and remains constant during expansion. The internal energy of this cloud is

$$E_0 = \frac{3}{2} N k_B T_0 = \int \mathrm{d}^3 p \, \mathrm{d}^3 x \frac{p^2}{2m} f(\mathbf{r}, \mathbf{p}, t). \tag{3.33}$$

After the trap potential $U(\mathbf{r})$ is rapidly switched on at time t_0, the internal energy E is raised to

$$E_1 = \int \mathrm{d}^3 p \, \mathrm{d}^3 x \left(\frac{p^2}{2m} + U(\mathbf{r}) \right) f(\mathbf{r}, \mathbf{p}, t_0). \tag{3.34}$$

Provided all regions of the trapping potential are well connected (by particle trajectories) over an experimental timescale, the trapped cloud reaches thermal equilibrium at T_1 through interatomic elastic collisions. The trapped equilibrium temperature is related to the internal energy through the Maxwell Boltzmann distribution, with energy density of states $\rho(\epsilon)$

$$E_1 = \int_0^\infty \epsilon \rho(\epsilon) \exp^{-\epsilon / k_B T_1} \, \mathrm{d}\epsilon. \tag{3.35}$$

The new equilibrium temperature T_1 can be found after equating results of the two integrals 3.34 & 3.35 for trap potential $U(\mathbf{r})$. Other thermodynamic quantities such as density and phase space density can subsequently be found from N and T_1.

For our experiment, we assume both the initial cloud and the trapped cloud to be highly elongated and uniform over almost their entire length L. We will take the initial phase space distribution to be thermal, Gaussian across the cloud, and uniform along its length:

$$f(\mathbf{r}, \mathbf{p}, t_0) = \begin{cases} \frac{N \beta^{3/2}}{(2\pi m)^{3/2} 2\pi L \sigma_\rho^2} e^{-\rho^2 / 2\sigma_\rho^2} e^{-\beta p^2 / 2m} & \text{if } |z| \leq L/2, \\ 0 & \text{if } |z| > L/2, \end{cases} \tag{3.36}$$

where ρ is the radius in cylindrical coordinates, $\beta = 1/(k_\mathrm{B} T)$, and σ_ρ is the radial width of the density distribution. The distribution eq.(3.36) describes our molasses cloud.

For the magnetic trap to match this distribution, it must be axially square with

length L, and radially harmonic with frequency ω_ρ (c.f. our harmonic model of sec.3.3.2 which has this shape). For this trap the energy density of states is $\rho(\epsilon) \propto \epsilon^{3/2}$ (see section 4.1.2). Using the distribution eq.(3.36) in eq.(3.34), and equating to eq.(3.35) gives the temperature relation

$$\frac{5}{2}T_1 = \frac{3}{2}T_0 + \frac{\omega_\rho^2}{\omega_0^2}T_0, \tag{3.37}$$

where $\omega_0 = \sqrt{k_B T/m\sigma_\rho}$.

When $\omega_\rho = \omega_0$, then $T_1 = T_0$, and the phase space distribution of the trapped cloud is identical to its pre-trapped distribution, hence phase space density is preserved. However, for our molasses cloud ω_0 is approximately $2\pi \times 100\,\mathrm{Hz}$, and for our trap ω_ρ is (initially) $2\pi \times 1.5\,\mathrm{kHz}$. This simple model suggests we would find an temperature rise by a factor of approximately 90. This is not what we observe in our experiment, where the temperature is only a few times higher than in the molasses, and not all of the atoms are captured. To understand this, we build on this theory to produce a more sophisticated model that takes into account the finite depth and the actual shape of our trap.

3.4.2 Loading into Realistic Potentials of Finite Depth

In this section we extend the theory of the previous section to consider traps of finite depth, then present theoretical results for realistic Z wire model of our transverse trap potential $U(x, y)$.

For traps of finite depth ϵ_t, the phase space distribution of the cloud is truncated, as the hottest atoms escape. For our initially trapped clouds, the radial oscillation period ($< 10\,\mathrm{ms}$) is much shorter than the average time between elastic collisions ($\sim 100\,\mathrm{ms}$). Therefore, almost all atoms with $\epsilon = p^2/2m + U(\mathbf{r}) > \epsilon_t$ escape, before distributing their energy through elastic collisions. The number N_1 of atoms that remain is estimated by integrating $f(\mathbf{r}, \mathbf{p})$ over the phase space region defined by $\epsilon < \epsilon_t$. Likewise, the internal energy E_1 of the trapped gas is found by integrating

$\epsilon f(\mathbf{r},\mathbf{p})$ over the same region:

$$N_1 = \int_{\epsilon<\epsilon_t} \mathrm{d}^3p\,\mathrm{d}^3r f_0\, e^{-\frac{r^2}{2\sigma_r^2}} e^{-\frac{p^2}{2mk_\mathrm{B}T_0}} \tag{3.38}$$

$$E_1 = \int_{\epsilon<\epsilon_t} \mathrm{d}^3p\,\mathrm{d}^3r f_0 \left(U(x,y)+\frac{p^2}{2m}\right) e^{-\frac{r^2}{2\sigma_r^2}} e^{-\frac{p^2}{2mk_\mathrm{B}T_0}} \tag{3.39}$$

$$\text{with} \quad f_0 = \frac{N_0}{2\pi\sigma_r^2 L(2\pi m k_\mathrm{B}T_0)^{3/2}},$$

where $r^2 = x^2+y^2$ and σ_r is the pre-trapped cloud width. Equations 3.38 & 3.39 are written in a suitable form for numerical integration over x & y, by integrating first over momentum space up to $p^2/2m = \epsilon_t - U(x,y)$, and z over the length of the trap, L.

$$N_1 = \frac{N_0}{\sqrt{\pi}\sigma_r^2}\int \mathrm{d}x\mathrm{d}y\,\Theta\left(U(x,y),\epsilon_t\right) e^{-\frac{r^2}{2\sigma_r^2}}\,\Gamma_c\left(\tfrac{3}{2},\left(\epsilon_t - U(x,y)\right)/k_\mathrm{B}T_0\right) \tag{3.40}$$

$$E_1 = \frac{N_0}{\sqrt{\pi}\sigma_r^2}\int \mathrm{d}x\mathrm{d}y\,\Theta\left(U(x,y),\epsilon_t\right) e^{-\frac{r^2}{2\sigma_r^2}}\times \tag{3.41}$$
$$\left[U(x,y)\,\Gamma_c\left(\tfrac{3}{2},(\epsilon_t - U(x,y)/k_\mathrm{B}T_0)\right) + k_B T_0 \Gamma_c\left(\tfrac{5}{2},\left(\epsilon_t - U(x,y)\right)/k_\mathrm{B}T_0\right)\right]$$

In eq.(3.41), the first term in the square brackets accounts for the contribution from the potential energy, and the second term from the kinetic energy. The Θ function enforces the correct integration limit,

$$\Theta(x,y) = \begin{cases} 1 & \text{for } x,\ y \text{ such that } U(x,y) < \epsilon_t \\ 0 & \text{otherwise,} \end{cases} \tag{3.42}$$

and $\Gamma_c(z,\eta)$ is the complimentary gamma function $\Gamma(z) - \Gamma(z,\eta)$. The integrals are performed numerically, over a rectangular region in space with dimensions of the maximum trap widths in the x and y directions.

For the integrals 3.40 & 3.41 and the definition 3.42, we must use the more accurate Z wire model (including gravity) for the transverse potential U(x,y), since the pre-trapped clouds extends over a large region of the trap, not accurately covered by the IP model. However, the internal energies predicted for clouds relevant to our experiment are found to be equivalent to temperatures under $400\,\mu$K. Hence, the IP model can be used to derive the density of states (as given in table 4.1 of sec.4.1.6),

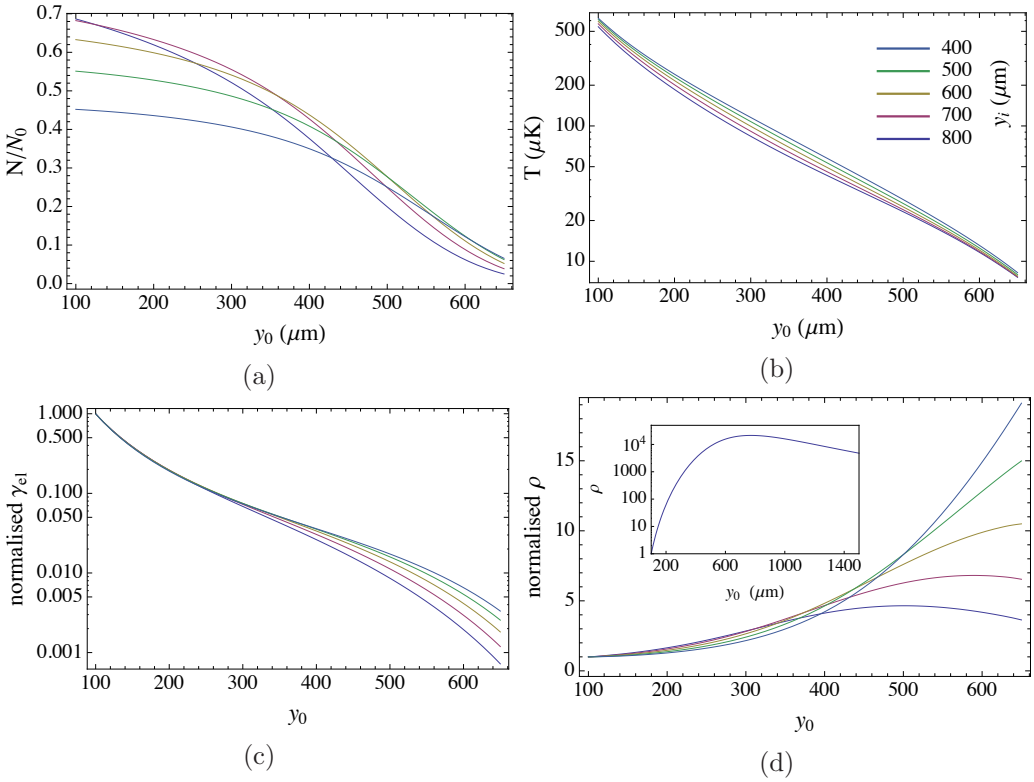

Figure 3.14: The simulations of trapped cloud properties performed for a pre-trapped cloud with temperature $T = 80\,\mu$K and radial width $\sigma_r = 250\,\mu$m. (**a**) shows how fraction of atoms captured varies with the position of the magnetic trap minimum y_0. This is calculated from results of section 3.4.2. Several different positions of the pre trapped cloud are shown, varying between 400 and 800 μm from the chip. (**b**), (**c**) & (**d**) show the variation of temperature, elastic collision rate and phase space density with y_0 respectively. The elastic collision rate and phase space density are normalised to their values in the pre-trapped cloud. The inset in (**d**) shows the variation in normalised phase space density predicted by the infinitely deep harmonic trap model for comparison. In this case y_i is set to the same position as y_0 where it is known to be best.

from which the energy-temperature relation can be found by integrating 3.35.[13] For the IP model,

$$E_1 = \frac{7}{2}\frac{\frac{5}{7} + \frac{k_B T_1}{U_0}}{1 + \frac{k_B T_1}{U_0}} N_1 k_B T_1. \tag{3.43}$$

The temperature T_1 is found by equating this to the result E_1 of 3.41, and substituting in the result for N_1. The results eq.(3.40), eq.(3.41) and eq.(3.43) described here we do not find elsewhere in the literature.

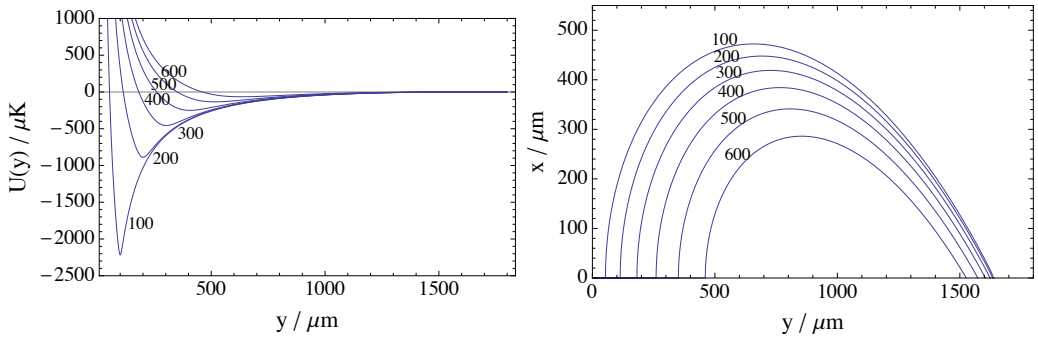

Figure 3.15: These plots aspects of the capture volume of the magnetic trap. Figure (**a**) shows the trap potential U(x=0,y) from the Z wire model. As the trap is moved closer to the chip, the trap becomes deeper with steeper sides. Figure (**b**) shows the maximum capture radius in the x-y plane for different y_0. Outside the capture radius the potential energy is greater than that at the gravitational saddle point.

Results of Loading Model

We calculate N_1 & T_1 as a function of y_0, the distance of the magnetic field minimum from the chip. From N_1 & T_1, we also calculate the phase space density ρ_{psd} and elastic collision rate γ_{el}. These are plotted in figure 3.14 for five different molasses cloud positions y_i. The molasses cloud width is $250\,\mu$m, consistent with our experiment.

The results show that the tightest traps capture the most atoms for a given y_i, but also have the highest temperatures. The plots of the trap potential 3.15 demonstrate two reasons for this. Firstly, for y_0 closer to the chip, the trapping region is larger in all directions, increasing the capture volume. Secondly, the trap bottom is deeper, and the potential steeper. An atom at position $\mathbf{r}$, when the trap is turned on, requires a higher initial kinetic energy $p^2/2m$ to escape the trap, when y_0 is smaller. Hence, an atom at the same position has higher probability of being captured for smaller y_0. The corollary of this is that more higher energy atoms are captured for smaller y_0, leading to a higher internal energy and subsequently a greater temperature. Figure 3.17b shows this effect.

However, the trap temperature doesn't rise as rapidly with decreasing y_0 as it does for the infinitely deep mode matched case. Subsequently the change in ρ_{psd},

[13] Another version of 3.35 can account for finite depth [97], but leads to only a small correction, and is not considered here.

shown in figure 3.14d, isn't nearly as great. Plots fig.3.14c & fig.3.14d show the variation of $\gamma_{\rm el}$ and $\rho_{\rm psd}$ with y_0. Figure 3.14c shows that the tighter traps which are close to the chip have a higher elastic collision rate. The difference in $\gamma_{\rm el}$ over the range $100 < y_0 < 600\,\mu$m is quite substantial, falling about three orders of magnitude. As will be discussed in Ch.4, the higher the elastic collision rate the better for evaporative cooling.

On the other hand, fig.3.14d shows that the highest phase space densities are achieved for y_0 further from the chip. In fact, the optimal y_0 for the phase space density is found at a similar distance predicted by the deep harmonic trap model of sec.3.4.1, which is shown in the inset in fig.3.14d. However, for the finite depth IP trap model the range of variation of $\rho_{\rm psd}$ is much smaller - when the molasses is $800\,\mu$m (bottom blue line) from the chip the range of variation is only about a factor of 4.

For effective evaporative cooling, a balance must be struck between high elastic collision rate and high phase space density: if the elastic collision rate is too low, the evaporative cooling is not sustainable, and we run out of atoms before reaching BEC. The lower the phase space density, the further the cloud must be cooled. The results of our simulation show the gain in $\gamma_{\rm el}$ is large and the loss in $\rho_{\rm psd}$ small by forming the trap with y_0 closer to the chip. Thus, these results show loading into a tighter, deeper trap, can be favourable. Both the finite depth and the trap shape are responsible for this. Firstly, the finite depth of the trap allows the highest energy atoms to escape, reducing the overall temperature. Secondly the potential doesn't rise as sharply as predicted by the harmonic model, or even the IP model (particularly for $y > y_0$). Atoms far from the trap centre do not get as big an energy increase due to the $1/r$ roll-off of the trap potential.

3.4.3 Experimental Loading Procedure

The position of the molasses cloud in the $\hat{\mathbf{x}}$ & $\hat{\mathbf{z}}$ directions is aligned to the magnetic trap by comparing absorption images taken before and after the trap is turned on. We then perform scans over y_0, y_i, and the detuning of the trap light at the end of the UMOT to find their optimal values from measurements of the number and

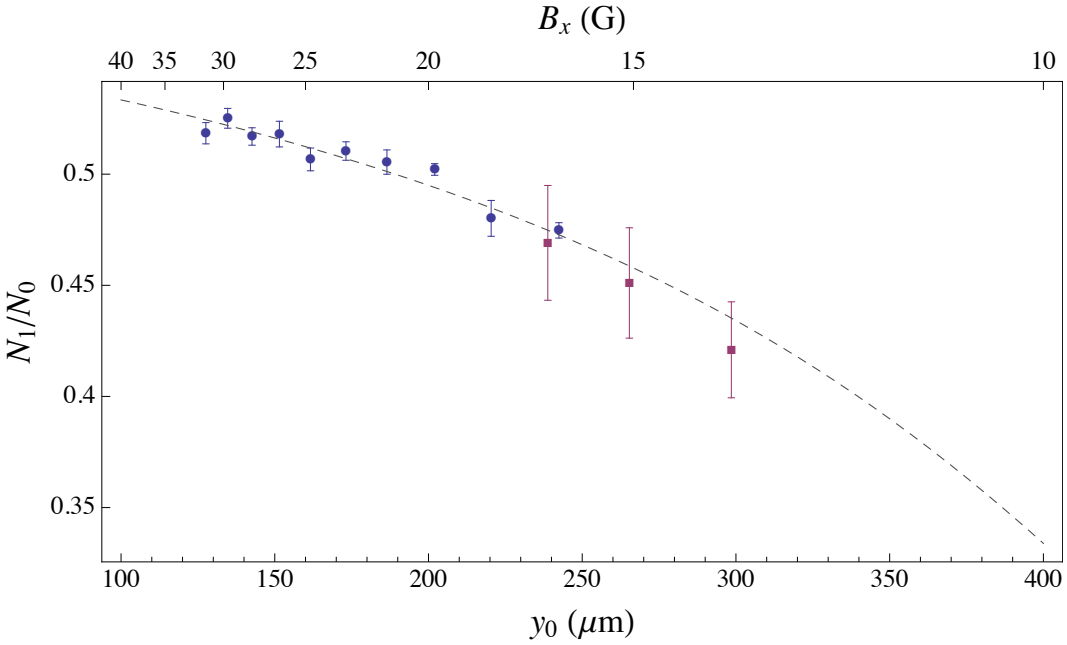

Figure 3.16: Fraction of atoms N_1/N_0 in the magnetic trap 50 ms after it is switched on, for various trap heights. Two datasets were taken on two different days: the round data points are one data set for which $N_0 = 5.5 \times 10^7$ atoms, and the square data points are another data set, for which $N_0 = 2.5 \times 10^7$ atoms. The dashed line shows N_1/N_0 from the theory eq.(3.40) for typical experimental parameters, $\sigma_0 = 250\,\mu$m, $T_0 = 80\,\mu$K and $y_i = 500\,\mu$m.

temperature of the cloud after it has been held for 600 ms in the trap. During this time atoms with energy $\epsilon > \epsilon_t$ escape, at first due to their initial momentum and position in the trap potential when it is turned on, and later due to evaporation from the trap as the cloud thermalises. By this time, evaporative loss from the finite depth trap typically reduces the cloud to a similar temperature of about 120 μK for a wide range of the parameters y_0, y_i and the trap light detuning. For the maximum elastic collision rate, we therefore need only find the parameters that maximise the atom number.

We find more atoms are captured for the largest detuning we can make in the optical molasses, since this gives gives the molasses the lowest temperature. We vary y_i by changing the time offset δt (sec.3.2) between the Z wires and x-bias being switched off. We only observe a small variation in N over the several hundred μm range we can vary y_i.

The largest and most controllable variation in the atom number is with y_0. Figure 3.16 shows the captured fraction of atoms N_1/N_0 50 ms after the trap is switched on

with a range of different values of y_0. The captured fraction increases over this range as y_0 approaches the chip, as expected by our theoretical model plotted in fig.3.17a. The data points are from two different data sets, and have different N_0. For the round data points N_0 was approximately 5.5×10^7, and for the square data points N_0 was approximately 2.5×10^7 atoms. The data shows the shape of N_1/N_0 with y_0 is similar to that expected from the model. The predicted dashed line shows the curve expected for typical experimental values ($y_i = 500\,\mu$m, $\sigma_r = 250\,\mu$m, $T_0 = 8\,\mu$K).

Based on these results we chose the height $y_0 = 170\,\mu$m to load the magnetic trap, where the captured fraction is close to the highest we measure. We expect that the marginal gain in atom number for smaller y_0 than this is offset by the reduction in phase space density. Once the trap is loaded, we ramp y_0 down to $110\,\mu$m, over 50 ms. This increases the characteristic frequency ω_r to 2.1 kHz, adiabatically compresses the cloud, and increases the elastic collision rate to a few hundred per second.

We wait 600 ms for the cloud to reach its quasi-equilibrium state over the entire trap. Any net axial velocity of the pre-trapped cloud manifests itself as slow anharmonic axial oscillation [45, 98]. The period depends on the velocity and we have observed periods in the range of 5 Hz to 8 Hz. Careful axial alignment of the UMOT to the magnetic trap all but removes these. However, there are several lumps in the UMOT/molasses shape due to inhomogeneities in the MOT beams. These smooth out over the first 600 ms.

3.4.4 Sensitivity to Variations in Molasses Cloud

During daily operation of our experiment, we observe fluctuations and drifts in the number of magnetically trapped atoms, and subsequently in our condensate. For evaporation to reach BEC, we find there is a threshold in the initial number at about 2.2×10^7 atoms. This number produces a small condensate of just $5-10\times10^3$ atoms. For an increase in N_1 by 15% the number of condensed atoms more than doubles, and for $N_1 > 2.7 \times 10^7$ the condensate has over 4×10^4 atoms. Our loading model is useful for understanding the sensitivity of the initial trap number to variations in the molasses cloud.

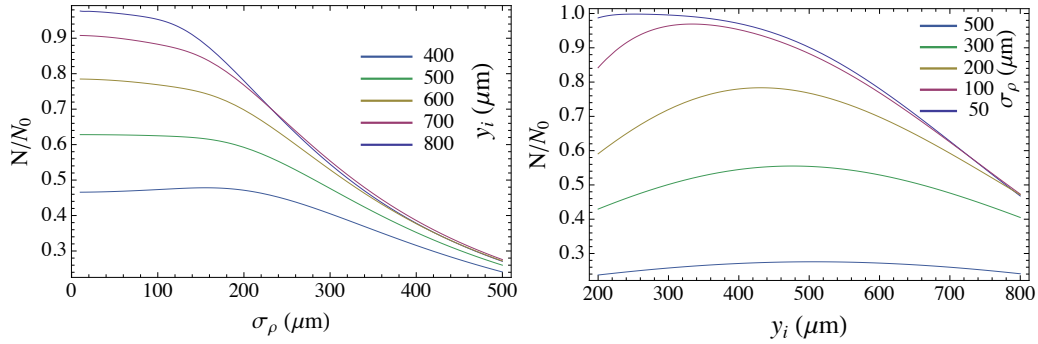

(a) (b)

Figure 3.17: This figure shows the sensitivity of captured fraction to variations in (**a**) the molasses cloud width σ_r, and (**b**) the molasses cloud height y_i above the chip. These results are calculated using the model described in section 3.4.2, with $y_0 = 150\,\mu$m as it is in our experiment.

Figure 3.17a shows the calculated variation of the captured fraction with the molasses cloud width σ_ρ. This plot suggests that for σ_ρ below $100 - 150\,\mu$m, the captured fraction is relatively insensitive to width variations, while in the range $200 - 400\,\mu$m, it is most sensitive. We load in this sensitive region with $\sigma_\rho \approx 250\,\mu$m. The cloud width depends on the molasses temperature, and the confinement and atom number in the UMOT, which in turn depend largely on the alignment, polarisation and detuning of the trapping beams.

Figure 3.17b shows the predicted variation of the captured fraction with position y_i of the pre-trapped cloud. The sensitivity $\frac{\Delta N/N}{\Delta y_i/y_i}$ to y_i in our typical range is 2 or 3 times lower than for σ_r. This is a consequence of the decreasing gradient of the $1/r$ shaped potential at distances $y > y_1$, as can be seen in fig.3.15a, where y_1 is the location of the trap minimum as defined in sec.3.3.5. As y_i approaches (and becomes less than) y_1, the sensitivity increases, as does the potential gradient. For smaller widths σ_ρ, the optimal y_i is closer to the trap minimum y_1.

Chapter 4

Evaporative Cooling to BEC

4.1 Evaporative Cooling in Elongated Potentials

In this section we develop further the theory of evaporative cooling. In sec.4.1.1, we start by introducing two differential equations for the rate of change of number and temperature which can be found in the present literature (e.g. [99] and references therein). Elements of thermodynamics in power law traps relevant to following sections are then introduced in section 4.1.2. In sections 4.1.3 & 4.1.4 we derive the critical condition for runaway evaporation, and find the evaporation trajectory that maximises the elastic collision rate. Section 4.1.5 gives the general solution to the evaporation rate equations for any power law trap. These are then used to study the effect of the trap geometry on evaporative cooling. They provide the limiting cases for the numerical solutions given in section 4.1.6 for number and temperature evolution in our IP trap. Section 4.2.2 compares solutions for our trap against results from our experiment.

4.1.1 Evaporation rate equations

For a classical gas at thermodynamic equilibrium at temperature T, the fraction of atoms with energy greater than $\eta k_{\mathrm{B}} T$ is is found from the Maxwell Boltzmann distribution,

$$\frac{\Delta N}{N} = \int_{\eta k_{\mathrm{B}} T}^{\infty} \rho(\epsilon) e^{-\epsilon/k_{\mathrm{B}} T} \mathrm{d}\epsilon. \tag{4.1}$$

The fraction of total internal energy contained in this high energy tail is

$$\frac{\Delta E}{E} = \frac{\int_{\eta k_{\rm B}T}^{\infty} \epsilon\rho(\epsilon)e^{-\epsilon/k_{\rm B}T}{\rm d}\epsilon}{\int_{0}^{\infty} \epsilon\rho(\epsilon)e^{-\epsilon/k_{\rm B}T}{\rm d}\epsilon}. \tag{4.2}$$

The mean energy per atom in the high energy tail, $\Delta E/\Delta N$ is greater than mean energy per atom E/N over the whole cloud. Removing these atoms results in a reduction of E/N for the remaining atoms, which leads to cooling.

These atoms can be removed by reducing the trap depth to $\eta k_{\rm B}T$. In our case, this is achieved with an rf field, resonant with the magnetic field at this energy $\mu|\mathbf{B}(\mathbf{r})| = \eta k_{\rm B}T$. This forms a resonant shell around the trap. Atoms with energy $\eta k_{\rm B}T$ or greater are driven into an un-trapped state and ejected from the trap when they pass through this shell. These atoms are removed from the trap on a time scale of half the period of their oscillation in the trap, π/ω_ρ.

If an atom with $\epsilon_1 > \eta k_{\rm B}T$ collides elastically with another atom then both could recoil with energy lower than $\eta k_{\rm B}T$ and neither would be removed. The removal is thus most efficient when ω_r is fast compared to the elastic collision rate $\gamma_{\rm el}$, so the probability of a collision before removal is small. We assume this is the case in what follows, unless otherwise stated.

Once the high energy tail of the distribution has been rapidly removed, further atoms are slowly removed as they repopulate this tail through elastic collisions at rate $\gamma_{\rm el}$. This repopulation rate is typically smaller than $\gamma_{\rm el}$ by a factor q =4-6 according to numerical simulations [100, 59], and an argument of thermodynamic balance [59].

As in [101] we treat evaporation as a quasi-equilibrium process, assigning a temperature T to the cloud and describing it by the Maxwell Boltzmann energy and phase space distributions $f(\mathbf{r}, \mathbf{p})$. Simulations based on numerical solution to the Boltzmann equation support this approximation [97]. When this is the case, the fractional rate of change of number and energy are just γ_{el}/q times eq.(4.1) & eq.(4.2).

The peak elastic collision rate itself evolves with N and T, and is given by

$$\gamma_{\rm el}(t) = n_0 v_{\rm rel}\sigma_s \tag{4.3}$$

where σ_s is the s-wave scattering cross section, $v_{\rm rel}$ the root mean squared relative velocity, and n_0 the peak density. The root mean squared relative velocity and the peak density are found from the momentum and position parts of the quasi-equilibrium phase space distribution,

$$v_{\rm rel} = \sqrt{6k_{\rm B}T/m} \tag{4.4}$$

$$n_0 = N \Big/ \int_0^\infty {\rm d}^3 r e^{-U(\mathbf{r})/(k_{\rm B}T)}. \tag{4.5}$$

The peak density depends on the shape of the potential $U(\mathbf{r})$. The scattering cross-section σ_s is given by,

$$\sigma_s = \frac{8\pi a^2}{1 + \left(\frac{2\pi a}{\lambda_{dB}}\right)^2}, \tag{4.6}$$

where $a = 5.4\,{\rm nm}$ is the s-wave scattering length [102], and $\lambda_{\rm dB} = h/(2\pi m k_{\rm B}T)^{1/2}$ is the thermal deBroglie wavelength. In the limit that $k_{\rm B}T \ll \hbar^2/(2\pi a^2 m)$ ($t \ll 30\,\mu{\rm K}$), the denominator in σ_s is approximately 1, and $\sigma_s \approx 8\pi a^2$. For the elastic collision rate (eq.(4.3)), we will ignore the temperature dependence due the denominator in eq.(4.6) which defines σ_s, since this dependence is much weaker than that through n_0 and $v_{\rm rel}$, and tends towards a constant value at low temperatures. Instead, we will take the value $\sigma_s(T = T_0)$, where T_0 is the initial temperature of the cloud, which will give a slightly conservative estimate for $\gamma_{\rm el}$ in our models.

In addition to forced evaporative loss, atoms are also lost through other unwanted mechanisms. In our experiment, the dominant loss process is from collisions with background gas particles. This loss is indiscriminate of energy, and the fractional loss rates for number and energy are both $-\gamma_{\rm bkg}$.

To summarise,

$$\frac{1}{N}\frac{{\rm d}N}{{\rm d}t} = -\frac{\gamma_{\rm el}}{q}\int_{\eta k_{\rm B}T}^\infty \rho(\epsilon) e^{-\epsilon/k_{\rm B}T}{\rm d}\epsilon - \gamma_{\rm bkg} \tag{4.7}$$

$$\frac{1}{E}\frac{{\rm d}E}{{\rm d}t} = -\frac{\gamma_{\rm el}}{q}\frac{\int_{\eta k_{\rm B}T}^\infty \epsilon\rho(\epsilon) e^{-\epsilon/k_{\rm B}T}{\rm d}\epsilon}{\int_0^\infty \epsilon\rho(\epsilon) e^{-\epsilon/k_{\rm B}T}{\rm d}\epsilon} - \gamma_{\rm bkg} \tag{4.8}$$

Since $\gamma_{\rm el}$ explicitly depends on N & T, it is easier to solve rate equations for N & T rather than E. The explicit dependence of $E(N,T)$ is then found from integrating

$N\epsilon\rho(\epsilon)e^{-\epsilon/k_{\rm B}T}\mathrm{d}\epsilon$. Differentiating this with the chain rule gives

$$\frac{\mathrm{d}E(N,T)}{\mathrm{d}t} = \frac{\partial E}{\partial N}\frac{\mathrm{d}N}{\mathrm{d}t} + \frac{\partial E}{\partial T}\frac{\mathrm{d}T}{\mathrm{d}t}. \tag{4.9}$$

The evaporation rate equations that will be studied over the following sections are thus,

$$\frac{1}{N}\frac{\mathrm{d}N}{\mathrm{d}t} = -\frac{\gamma_{\rm el}}{q}\int_{\eta k_{\rm B}T}^{\infty}\rho(\epsilon)e^{-\epsilon/k_{\rm B}T}\mathrm{d}\epsilon - \gamma_{\rm bkg} \tag{4.10}$$

$$\frac{1}{E}\frac{\partial E}{\partial T}\frac{\mathrm{d}T}{\mathrm{d}t} = -\frac{\gamma_{\rm el}}{q}\left(\int_{\eta k_{\rm B}T}^{\infty}\rho(\epsilon)e^{-\epsilon/k_{\rm B}T}\mathrm{d}\epsilon - \frac{N}{E}\frac{\partial E}{\partial N}\frac{\int_{\eta k_{\rm B}T}^{\infty}\epsilon\rho(\epsilon)e^{-\epsilon/k_{\rm B}T}\mathrm{d}\epsilon}{\int_0^{\infty}\epsilon\rho(\epsilon)e^{-\epsilon/k_{\rm B}T}\mathrm{d}\epsilon}\right) \tag{4.11}$$

We will show below that in many cases, the energy takes on the simple form $E \propto Nk_{\rm B}T$, and the terms $\frac{1}{E}\frac{\partial E}{\partial T}$ and $\frac{1}{E}\frac{\partial E}{\partial N}$ simplify greatly to $1/T$ and $1/N$.

4.1.2 Thermodynamics of Power Law Traps

It is useful to study the behaviour of evaporation in power law traps, as they give the limiting behaviour of a wide range of other traps. Our IP model is harmonic for $k_{\rm B}T \ll \mu B_0$ and linear in the opposite regime. Also often considered are the 3D harmonic and linear cases. Importantly, analytic solutions (section 4.1.5) to the rate equations 4.10 & 4.11 as well as other useful conditions (sections 4.1.3 & 4.1.4) can be found for these simple traps.

In the general potential $U(\mathbf{r})$, the energy distribution for a trapped cloud in equilibrium at temperature T is given by

$$P(\epsilon)\mathrm{d}\epsilon = \frac{1}{Z_\epsilon}\rho(\epsilon)e^{-\epsilon/(k_{\rm B}T)}\mathrm{d}\epsilon, \tag{4.12}$$

where $\rho(\epsilon)$ is the density of states for the trap, and $Z_\epsilon = \int_0^{\infty}\rho(\epsilon)\exp -\epsilon/(k_{\rm B}T)\mathrm{d}\epsilon$ is the partition function. The density of states depends on $U(\mathbf{r})$ and is found from [97]

$$\rho(\epsilon) = (2\pi\hbar)^{-3}\int \mathrm{d}^3r\mathrm{d}^3p\delta\left(\epsilon - U(\mathbf{r}) - p^2/2m\right). \tag{4.13}$$

After integrating over all momentum space,

$$\rho(\epsilon) = \frac{2\pi(2m)^{3/2}}{(2\pi\hbar)^3} \int_0^{U(\mathrm{r})=\epsilon} \mathrm{d}^3 r \sqrt{\epsilon - U(\mathbf{r})}. \tag{4.14}$$

We now consider 3D power law potentials, defined by

$$U(\mathbf{r}) = a_1 x_1^{p_1} + a_2 x_2^{p_2} + a_3 x_3^{p_3}, \tag{4.15}$$

for positive integers p_i. x_1, x_2 and x_3 are the three cartesian coordinates with origin at the minimum of the potential. For these potentials, the integral in eq.(4.14) gives $\rho \propto \epsilon^n$ where

$$n = \frac{1}{p_1} + \frac{1}{p_2} + \frac{1}{p_3} + \frac{1}{2}, \tag{4.16}$$

We note that eq.(4.15) and eq.(4.16) can also describe 2D power law traps by setting $p_3 \to \infty$, and 1D trap setting $p_2,\ p_3 \to \infty$. Given the dependence on ϵ the quantity $\rho(\epsilon)/Z_\epsilon$ can be easily found without first solving eq.(4.14) by ensuring $\int_0^\infty P(\epsilon)\mathrm{d}\epsilon = 1$.

When ρ has this simple ϵ^n dependence, the internal energy is

$$E = \frac{\Gamma(n+2)}{\Gamma(n+1)} N k_\mathrm{B} T \tag{4.17}$$

and the relation eq.(**??**) connecting rates of change of E, N, & T becomes simply

$$\frac{1}{E}\frac{\mathrm{d}E}{\mathrm{d}t} = \frac{1}{N}\frac{\mathrm{d}N}{\mathrm{d}t} + \frac{1}{T}\frac{\mathrm{d}T}{\mathrm{d}t}. \tag{4.18}$$

The temperature dependence of γ_{el} is found from 4.3, 4.4 & 4.5. Making the substitution $u_i = (a_i/k_\mathrm{B}T)^{1/p_i}\, x_i$ in the integral 4.5 gives

$$\frac{N}{n_0} = 8 \left(\prod_i \left(\frac{k_\mathrm{B}T}{a_i} \right)^{1/p_i} \right) \prod_i \int_0^\infty \mathrm{d}u_i e^{-u_i^{p_i}}. \tag{4.19}$$

where the definite integrals are independent of any parameter and contribute only an overall factor. Hence the density scales as

$$n_0 \propto \frac{N}{T^{n-\frac{1}{2}}} \tag{4.20}$$

The mean relative velocity contributes a factor of $\sqrt{T}$ to γ_{el}, so the elastic collision rate scales as

$$\gamma_{el}(N,T) = C\,\frac{N}{T^{n-1}} \tag{4.21}$$

where C is a constant.

On collecting together these results for power law traps, the rate equations for E, N & T become

$$\frac{1}{E}\frac{\mathrm{d}E}{\mathrm{d}t} = -\frac{\gamma_{\mathrm{el}}}{q}\frac{\Gamma(n+2,\eta)}{\Gamma(n+2)} - \gamma_{\mathrm{bkg}}, \tag{4.22}$$

$$\frac{1}{N}\frac{\mathrm{d}N}{\mathrm{d}t} = -\frac{\gamma_{\mathrm{el}}}{q}\frac{\Gamma(n+1,\eta)}{\Gamma(n+1)} - \gamma_{\mathrm{bkg}}, \tag{4.23}$$

$$\frac{1}{T}\frac{\mathrm{d}T}{\mathrm{d}t} = -\frac{\gamma_{\mathrm{el}}}{q}\left(\frac{\Gamma(n+2,\eta)}{\Gamma(n+2)} - \frac{\Gamma(n+1,\eta)}{\Gamma(n+1)}\right), \tag{4.24}$$

where $\Gamma(z)$ and $\Gamma(z,\eta)$ are the complete and incomplete gamma functions.

We briefly consider the validity of the axial square well approximation made in our magnetic trap models of section 3.3.2 in light of these relations. The power dependence of the potential enters the rate equations through n in the Γ functions. The Taylor expansion of $\Gamma(z+\varepsilon,\eta)$ is

$$\begin{aligned}\Gamma(n+\varepsilon,\eta) &= \Gamma(n,\eta) + \varepsilon(n-1)\Gamma(n,\eta) + \mathcal{O}\varepsilon^2 \\ &\approx \left(1 + \frac{(n-1)\Gamma(n-1,\eta)}{\Gamma(n)}\,\varepsilon\right)\Gamma(n,\eta).\end{aligned} \tag{4.25}$$

The coefficient of ε is 1 for $\eta = 0$, and approximately $1/4$ for typical values of $n,\ \eta$ in our experiment. The correction to terms $\Gamma(z,\eta)/\Gamma(z,\eta)$ is of order $1 - \frac{3}{4}\varepsilon$, where $\varepsilon = 1/p_z$.

We also see in section 4.2.2 below, that the correction to the scaling of γ_{el} through n_0 is counteracted by the slow thermalisation along the length. This is because the criterion for efficient removal $T_{\mathrm{osc}} \ll 1/\gamma_{\mathrm{el}}$ breaks down along the length of the trap. This is irrelevant for a perfectly square axially potential where the evaporation is

two-dimensional, and the axial distribution remains uniform over the length of the trap. But for weak axial variation for $|z| < L/2$, this results in length reduction when $k_{\rm B}T < U(z/2 - \delta) - U_0$, as the cloud thermalises to lower temperatures. However, the RF knife also shortens the trap as it approaches the trap bottom. If it does so faster than they thermalise, the length is reduced without density increase from axial redistribution.

4.1.3 Runaway Evaporation

When evaporation causes the elastic collision rate to increase, the cooling rate accelerates. In turn the elastic collision rate increases faster, and the evaporation is a 'runaway' process. Conversely, if $\gamma_{\rm el}$ decreases, evaporation slows, and more atoms are wasted through background loss, leading to further decrease in $\gamma_{\rm el}$. Eventually the phase space density will cease to increase, making condensation unachievable. Whether or not evaporation is in the runaway regime depends on the elastic collision rate, trap geometry, and background loss rate. Next, we derive a general condition for runaway evaporation that embodies these three elements for all power law traps.

The requirement for runaway evaporation is that γ_{el} increases with time, $\mathrm{d}\gamma_{el}/\mathrm{d}t > 0$. Differentiating eq.(4.21), and dividing by CN/T^{n-1}, this condition leads to the inequality

$$\frac{1}{N}\frac{\mathrm{d}N}{\mathrm{d}t} - (n-1)\frac{1}{T}\frac{\mathrm{d}T}{\mathrm{d}t} > 0. \tag{4.26}$$

Substituting in 4.23 and 4.24, then rearranging gives the critical condition for runaway evaporation in terms of the ratio of 'good to bad' collisions $\kappa = \gamma_{el}/\gamma_{bkg}$:

$$\kappa \geq \kappa_c = \frac{q}{(n-1)\ \Gamma(n+2,\eta)/\Gamma(n+2) - n\ \Gamma(n+1,\eta)/\Gamma(n+1)}, \tag{4.27}$$

where κ_c is the ratio $\gamma_{\rm el}/\gamma_{\rm bkg}$ when $\mathrm{d}\gamma_{\rm el}/\mathrm{d}t = 0$.

Figure 4.1a shows κ_c for three different trap geometries: (i) linear radially and axially square for which $n = 5/2$, (ii) harmonic, $n = 2$, and (iii) axially square and radially harmonic, $n = 3/2$. The evaporation is a runaway process within the shaded regions. With all three curves, there is a minimum value for the truncation parameter η_{min} where κ_c becomes infinitely large. Below this, runaway evaporation

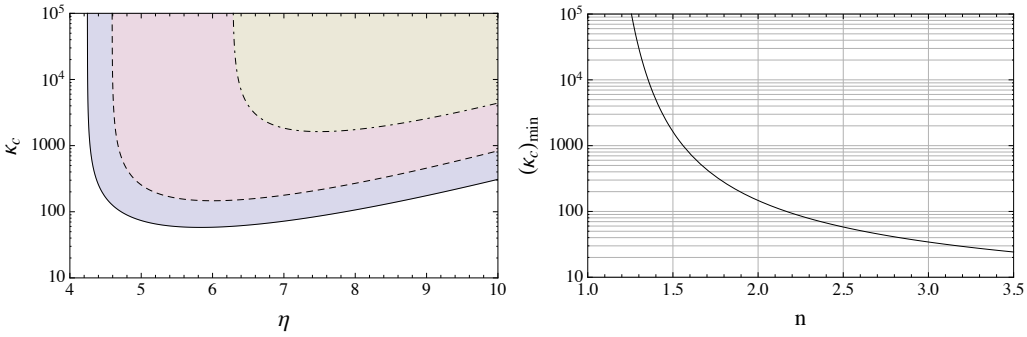

(a) (b)

Figure 4.1: The critical condition for runaway evaporation in terms of the ratio $\kappa_c = \gamma_{\rm el}/\gamma_{\rm loss}$ - the ratio of 'good to bad' collisions. Figure (**a**) shows κ_c versus the truncation parameter η for three different values of n, $\frac{5}{2}$ (solid line), 2 (dashed line), and $\frac{3}{2}$ (dot-dashed line). Figure (**b**) shows the minimum value $(\kappa_c)_{\rm min}$ as a function of n. From this plot is it seen that runaway evaporation cannot be achieved below $n = 1$.

is impossible no matter how high γ_{el} is.

The critical curve κ_c, for a given trap geometry, has a minimum at

$$\eta_0 = \frac{n}{n-1}\frac{\Gamma(n+2)}{\Gamma(n+1)} \tag{4.28}$$

found by differentiating 4.27. Figure 4.1b shows the corresponding value, $(\kappa_c)_{\rm min}$, plotted as a function of n. Runaway evaporation becomes impossible for traps with $n = 1$.[1] In this case, $(\kappa_c)_{\rm min}$ occurs only for $\eta_0 \to \infty$ as can be seen from the factor $n-1$ on the denominator of eq.(4.28). Conversely, for a finite truncation parameter k_c becomes singular, so an infinite elastic collision rate is required. In reality, where one has a discrete statistical distribution of a finite number of particles, this requires all the energy of the gas to be carried away by one particle. To reach such an extreme micro-state of the system in finite time essentially requires an infinitely high elastic collision rate.

4.1.4 Optimal Truncation Parameter

We now prove that $\partial\gamma_{el}/\partial t$ is maximised (in a power law trap) when $\eta = \eta_0$. This result (which to our knowledge is not found elsewhere in the literature) answers the much asked question in the laboratory; what truncation parameter is best?

[1] Equation 4.16 shows that this singularity occurs in a spherically symmetric trap that scales as r^6, or for a trap that is linear in one dimension and square in the other two, amongst many other examples.

We first prove the statement that, given any initial values $N(t) = N_0$, $T(t) = T_0$ at time $t = t_0$,

$$\dot{\gamma}_{\mathrm{el}}(t)\Big|_{t_0} \text{ is maximal for } \eta = \eta_0. \tag{4.29}$$

Proof. Differentiating γ_{el} in equation 4.21 gives[2]

$$\frac{\partial \gamma_{el}}{\partial t} = \gamma_{el}\left(\frac{1}{N}\frac{\mathrm{d}N}{\mathrm{d}t} - (n-1)\frac{1}{T}\frac{\mathrm{d}T}{\mathrm{d}t}\right). \tag{4.30}$$

The rate equations 4.23 & 4.24 are used to write $\partial\gamma_{el}/\partial t$ as a function of η, then differentiated once and twice w.r.t. η using the using the Leibniz integral rule:

$$\frac{\partial \gamma_{el}}{\partial t} = \gamma_{el}\left(\left((n-1)\frac{\gamma_{el}}{q}\frac{\Gamma(n+2,\eta)}{\Gamma(n+2)} + \gamma_{bkg}\right) - n\left(\frac{\gamma_{el}}{q}\frac{\Gamma(n+1,\eta)}{\Gamma(n+1)} + \gamma_{bkg}\right)\right) \tag{4.31}$$

$$\frac{\partial}{\partial \eta}\frac{\partial \gamma_{el}}{\partial t} = -\frac{\gamma_{el}^2}{q}\left(\frac{n-1}{\Gamma(n+2)}\eta^{n+1} - \frac{n}{\Gamma(n+1)}\eta^n\right)e^{-\eta} \tag{4.32}$$

$$\frac{\partial^2}{\partial \eta^2}\frac{\partial \gamma_{el}}{\partial t} = \frac{\gamma_{el}^2}{q}\left(\frac{n-1}{\Gamma(n+2)}\left(\eta_0^{n+1} - (n+1)\eta_0^n\right) + \frac{n}{\Gamma(n+1)}\left(n\eta_0^{n-1} - \eta_0^n\right)\right)e^{-\eta} \tag{4.33}$$

Setting equation 4.32 to zero, and solving for η gives

$$\eta_0 = \frac{n}{n-1}\frac{\Gamma(n+2)}{\Gamma(n+1)} \tag{4.34}$$

which is the same as expression 4.28. Evaluating the second differential at $\eta = \eta_0$ gives

$$\frac{\partial^2}{\partial \eta^2}\frac{\partial \gamma_{el}}{\partial t}\Big|_{\eta=\eta_0} = -\frac{\gamma}{q}\frac{n-1}{\Gamma(n+2)} < 0 \qquad \text{for} \quad n > 1 \tag{4.35}$$

□

Since the statement 4.29 depends on t_0 only through $N(t_0)$ & $T(t_0)$, and is true for any N_0 & T_0, it is equivalent to the statement:

$$\text{Given any } N_0,\ T_0, \quad \frac{\partial \gamma_{el}}{\partial t}\Big|_{N_0,T_0} \text{ is maximal for } \eta = \eta_0. \tag{4.36}$$

[2]Note that this makes no assumption that η is constant in time

Now suppose the number and temperature evolve along the trajectories $N(t)$ & $T(t)$ to new values N_1& T_1 at an arbitrary time later, t_1. Since 4.36 is true given any N_0 & T_0, we can relabel $N_1 \rightarrow N_0$ and $T_1 \rightarrow T_0$. Hence $\partial\gamma_{el}/\partial t$ is maximised throughout the evaporation ramp by keeping $\eta = \eta_0$.

4.1.5 General Solution to Evaporative Cooling Rate Equations in Power Law Traps

Let us make the substitution $u = (N/N_0)(T/T_0)^{1-n}$, such that the ellastic collision rate can be written as $\gamma_{\rm el} = \gamma_{\rm el_0} u$ (c.f. eq.(4.21)), where $\gamma_{\rm el_0}$ is its initial value. Taking the time derivative of u gives its rate equation,

$$\frac{1}{u}\frac{\mathrm{d}u}{\mathrm{d}t} = \frac{1}{N}\frac{\mathrm{d}N}{\mathrm{d}t} - (n-1)\frac{1}{T}\frac{\mathrm{d}T}{\mathrm{d}t}. \tag{4.37}$$

Substituting in the rate eq.(4.23) and eq.(4.24) for E & N, and working in the dimensionless time coordinate $\tau = \gamma_{\rm bkg} t$ normalised to the trap lifetime $\gamma_{\rm bkg}$, this equation becomes

$$\frac{\mathrm{d}u(\tau)}{\mathrm{d}\tau} = Au^2 - u \qquad \text{where} \quad A = \frac{\kappa_0}{q}\left((n-1)\frac{\Gamma(n+2,\eta)}{\Gamma(n+2)} - n\frac{\Gamma(n+1,\eta)}{\Gamma(n+1)}\right), \tag{4.38}$$

where $\kappa_0 = \gamma_{\rm el_0}/\gamma_{\rm bkg}$ This is solved by direct integration, then substituted into the temperature rate equation to give

$$\frac{\mathrm{d}}{\mathrm{d}\tau}\frac{T}{T_0} = -Bu \qquad \text{where} \quad B = \frac{\kappa_0}{q}\left(\frac{\Gamma(n+2,\eta)}{\Gamma(n+2)} - \frac{\Gamma(n+1,\eta)}{\Gamma(n+1)}\right), \tag{4.39}$$

This also is solved by direct integration. The solutions to 4.38 & 4.39, which give the time evolution of the normalised collision rate and temperature respectively, are

$$u(\tau) = \frac{1}{(1-A)e^{\tau} + A} \qquad \text{for} \quad A \leq 1 \tag{4.40}$$

$$\frac{T}{T_0} = \left(1 - A\left(1 - e^{\tau}\right)\right)^{B/A}, \tag{4.41}$$

and the time evolution of atom number is,

$$\frac{N}{N_0} = u(\tau)\left(\frac{T}{T_0}\right)^{n-1}. \tag{4.42}$$

From these, the density and phase space density are easily calculated. These solutions provide simple analytic equations for evaporative cooling in power law traps. As such they give the limiting behaviour of other traps. They are compared with theoretical evaporation in a model IP trap in the next section.

4.1.6 Evaporative Cooling in our Ioffe Pritchard Trap

We now consider evaporative cooling in the IP potential introduced in sec.3.3.2,

$$U(r,z) = \sqrt{\mu^2 {B'_\perp}^2 r^2 + U_0^2} - U_0, \quad |z| < L/2 \tag{4.43}$$

which approximates our trap up to $500\,\mu$K. Here, $U_0 = \mu B_0$, which is the magnetic potential of an atom at the trap bottom and is constant during evaporation. Since we talk about energies relative to this point during evaporation, the potential in eq.(4.43) has been shifted by U_0 so that its minimum is at zero.

This IP potential is not a power law potential, but is approximated by power law traps in two temperature regimes for which U_0 is the threshold. At low temperatures, $k_{\rm B}T/U_0 \ll 1$, the radial potential is harmonic. At high temperatures, $k_{\rm B}T \gg U_0$, the potential becomes linear. The axial potential remains square for all temperatures. Evaporation in these two limiting cases of the IP potential are hence the power law solutions for $n = 3/2$ (harmonic), and $n = 5/2$ (linear). These two power law solutions will be compared to the solutions for evaporative cooling which we derive below for the IP potential eq.(4.43).[3]

The relevant quantities for the rate equations 4.10 & 4.11, applied to the IP trap eq.(4.43), are given in table 4.1. Using these, the rate equations are for the

[3] Previous models to describe evaporation in traps like ours have assumed a 3-d harmonic potential, $n = 2$. These predicted faster and more efficient cooling than we find experimentally.

normalised parameters $v(\tau) = N(\tau)/N_0$ and $s(\tau) = kT/U_0$ are

$$\frac{1}{v}\frac{\mathrm{d}v}{\mathrm{d}\tau} = -\frac{\gamma_{el_0}}{q\gamma_{loss}}\ \frac{1+s_0}{1+s}\ \frac{v}{\sqrt{s/s_0}}\ \frac{\frac{5}{2}\Gamma(5/2,\eta)+s\Gamma(7/2,\eta)}{\frac{5}{2}\Gamma(5/2)+s\Gamma(7/2)} - 1, \tag{4.44}$$

$$\frac{7s^2+14s+5}{7s^2+12s+5}\ \frac{\mathrm{d}s}{\mathrm{d}\tau} = -\frac{\gamma_{el_0}}{q\gamma_{loss}}\ \frac{1+s_0}{1+s}\ \frac{v}{\sqrt{s/s_0}}\times \tag{4.45}$$
$$\left(\frac{\frac{5}{2}\Gamma(7/2,\eta)+s\Gamma(9/2,\eta)}{\frac{5}{2}\Gamma(7/2)+s\Gamma(9/2)}\ -\ \frac{\frac{5}{2}\Gamma(5/2,\eta)+s\Gamma(7/2,\eta)}{\frac{5}{2}\Gamma(5/2)+s\Gamma(7/2)}\right),$$

where $\tau = \gamma_{\mathrm{bkg}}t$ as before.

These coupled differential equations are solved numerically with the initial conditions $v(0) = 1,\ s(0) = kT_0/U_0$. The truncation parameter η can either be kept constant, or defined by the frequency $f_{rf}(\tau)$ of the rf field and temperature $T = s(\tau)U_0/k_{\mathrm{B}}$,

$$\eta(\tau)\, k_{\mathrm{B}}T = hm_F\left(f_{\mathrm{rf}}(\tau) - f_0\right), \tag{4.46}$$

and solved simultaneously with 4.44 & 4.45. In eq.(4.46), $f_0 = U_0/(2h)$ is the frequency of the rf field when resonant with the magnetic energy at the trap bottom. The power law trap rate equations, eq.(4.23) & eq.(4.24), can also be solved (numerically) with the variable truncation parameter defined by eq.(4.46).

However, in this section we investigate the isolated effect of the trap geometry by solving for constant η and comparing the IP numerical solutions for N and T to the power law (analytical) solutions eq.(4.41) and eq.(4.42).[4] Figures 4.2a & 4.2b show the numerical solutions for s and N/N_0 in the IP trap, with initial values $s = 10,\ v = 1,\ \kappa = 500$, and $\eta = 8$. The analytical power law trap solutions, $n = 3/2$ the dashed line, and $n = 5/2$ the dot-dashed line, are also plotted for comparison, starting at $s = 10,\ 1,\ 0.1$ & 0.01.

For $s \gg 1$, the number and temperature in the IP model follow the $n = 5/2$ power law trap case, as seen for $\tau \lesssim 0.1$ in fig.4.2a and fig.4.2b. For the $n = 5/2$ power law trap, the lowest permitted κ for runaway evaporation is $(\kappa_c)_{\min} > 28$, so evaporation is well within the runaway regime with the initial value $\kappa = 500$. However, for $n = 3/2$, $(\kappa_c)_{\min} = 1630$, and this power law solution doesn't runaway

[4] Variable $\eta(\tau)$ solutions are given in the sec.4.2.2, where we compare them to measurements from our experiment.

Density of States	$\rho(\epsilon)/Z_\epsilon = \dfrac{\frac{5}{2}\epsilon^{3/2} + \frac{1}{U_0}\epsilon^{5/2}}{(k_\mathrm{B}T)^{5/2}\left(1+\frac{k_\mathrm{B}T}{U_0}\right)\Gamma(7/2)}$
Total Energy	$E = \dfrac{7}{2}\,\dfrac{\frac{5}{7}+\frac{k_\mathrm{B}T}{U_0}}{1+\frac{k_\mathrm{B}T}{U_0}}\,Nk_\mathrm{B}T$
Peak Number Density	$n_0 = \dfrac{\mu_B^2 {B'_\perp}^2}{k_\mathrm{B}T}\dfrac{N}{2\pi L U_0}\dfrac{1}{1+\frac{k_\mathrm{B}T}{U_0}}$
Elastic Collision Rate	$\gamma_{el} = n_0\sqrt{\dfrac{6k_\mathrm{B}T}{m}}\sigma_s$
$\frac{1}{E}\frac{\partial E}{\partial T}$	$\dfrac{k_\mathrm{B}}{U_0 s}\dfrac{7s^2+14s+5}{7s^2+12s+5}, \quad s = \dfrac{k_\mathrm{B}T}{U_0}$

Table 4.1: Thermodynamic properties for the IP model potential 3.28.

for $\kappa = 500$. In the IP trap evaporation is boosted for large s since it is highly linear at such temperatures, thus behaving like the $n = 5/2$ power law trap.[5]

At low temperatures where $s \ll 1$, evaporation in the IP trap follows the $n = 3/2$ solution. This can be seen for $\tau \gtrsim 0.4$ in in fig.4.2a and fig.4.2b. By this point, evaporation is also runaway for $n = 3/2$. For $s \sim 1$, the behaviour smoothly varies between the two cases, as can be seen for the intermediate times $0.1 < \tau < 0.4$.

In our experiment, we start with s between 2 & 3. We have found that our evaporation is only sustainable to BEC for κ much greater than the often quoted value of 150 [55, 84, 99], which is for the $n = 2$ case. The more generalised theory presented here demonstrates we need $\kappa > \kappa_c(3/2) = 1630$ by the time we reach the harmonic regime of our trap, if evaporation is to run away. Our theory also suggests that a lower value of $U_0 = \mu B$ increases the efficiency of evaporative cooling, by keeping the linear shape of the trap to lower temperatures.

[5]The 1/r of the Z wire model at even higher temperatures may even boost it further. The critical value κ_c decreases for larger n. For $n > 3.5$, the power scaling of the trap must be fractional in at least one dimension. Such traps have a negative curvature, as does $1/r$.

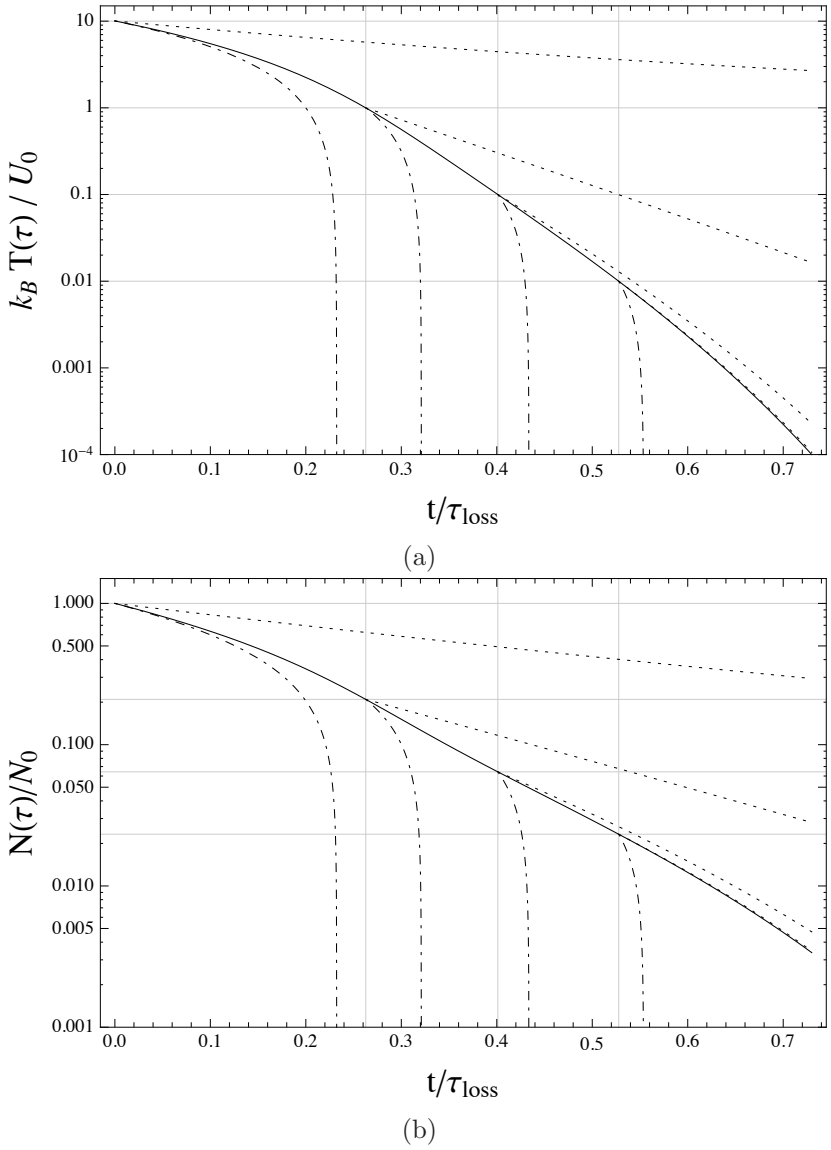

Figure 4.2: Comparison of solutions to the evaporative cooling rate equations for the normalised temperature $s(\tau) = k_{\rm B}T/U_0$ and normalised number N/N_0 for the IP potential and two power law traps, $n = 3/2$ and $n = 5/2$. The solutions are shown as a function of the dimensionless time $\tau = \gamma_{bkg}t$. The initial collision ratio at $\tau = 0$ is $\kappa = 500$. The truncation parameter is constant throughout at $\eta = 8$. (**a**) Solutions for $s(\tau)$, with initial value 10, show how the (normalised) temperature evolves during evaporative cooling. The solid line shows the numerical solution to the rate equation eq.(4.45) for the IP trap for with $U_0/k_B = 160\,\mu$K. The dotted lines show the analytic power law solutions from eq.(4.41) with $n = 3/2$, and radial trap frequency $\omega_\rho = 2\pi \times 2\,$kHz as found in the low temperature approximation for the IP potential. The dot-dashed line shows the analytic power solution for the linear case ($n = 5/2$) which approximates the IP potential in the high temperature limit. These analytic solutions are shown with different initial values $s = 10,\ 1,\ 0.1$ and 0.01. The value for κ for each starting point is that of the IP solution at that point. Thus the trajectory of the IP solution for $s(\tau)$ can be compared to the power law cases $n = 3/2$ and $n = 5/2$ at similar collision ratio κ. (**b**) Solutions for evolution of N/N_0. Similarly, the solid line is the IP solution, the dotted line the analytic power law solution with $n = 3/2$, and the dot-dashed line the analytic power solution with $n = 5/2$. The analytic solutions are shown for the same four initial conditions as in (**a**). Comparisons of the different solutions are discussed in main text.

We compare our theory for evaporation to experimental data in sec.4.2.2. Before doing this, we give a description of how we experimentally optimise the evaporation ramp in the next section.

4.2 Experimental Optimisation

4.2.1 Constructing the Best rf Sweep

We estimate how we should ramp down the frequency f_{rf} of the rf field, and use this as the starting point for how we ramp it down in our experiment. We use the evaporation theory of the previous section to calculate how the temperature should evolve for a constant truncation parameter $\eta \approx 8$ in our trap based on the initial atom number $N_0 \approx 2 \times 10^7$, temperature $T_0 \approx 150\,\mu$K measured from our experiment. We initially estimate the trap bottom $U_0/h \approx 1\,$MHz, based on the applied bias field $B_z \approx 1\,$G. We use the analytic power law models (which are both insightful and quick to execute) with the appropriate value $n = 3/2$ or $n = 5/2$ based on $k_{\mathrm{B}}T/U_0$ to calculate T(t), with γ_{bkg} also measured in our experiment (as will be explained in sec.4.2.3). Then, inverting eq.(4.46) with constant truncation parameter and our estimate of $T(t)$, we predict how we should ramp down f_{rf} for runaway evaporation. We typically use a constant truncation parameter η between 8 and 12, as it is important that it is larger than the minimum value η for which runaway evaporation can occur - $(\eta)_{\mathrm{min}} = 4.2$ when $n = 5/2$, and $(\eta)_{\mathrm{min}} = 6.3$ when $n = 3/2$.

Such predictions typically suggest that f_{rf} should be ramped down at first like an exponentially decaying function, with time constant on the order of one second. Towards the end of the ramp, when the runaway evaporation accelerates, f_{rf} should be ramped down faster than exponentially. To implement this in the laboratory, we break the frequency ramp down into 5 segments. For the first two segments, we follow an exponential decaying function. These take the cloud temperature from $150\,\mu$K down to just a few μK. The remaining segments we ramp f_{rf} down linearly towards the frequency at trap bottom $f_0 = U_0/h$, with each segment taking around 1 s. We optimise the decay rate or duration of each segment in turn. For the first

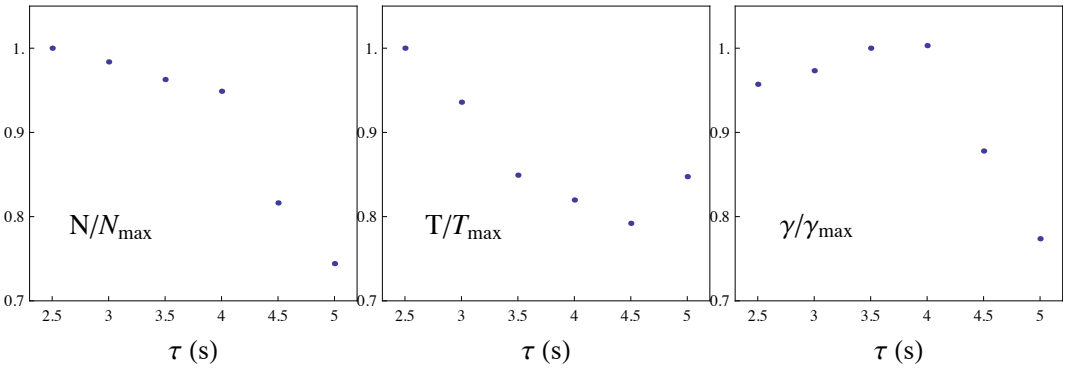

Figure 4.3: Optimisation of evaporation ramp rate. This example is for the first stage, sweeping exponetialy $f(t) = f_1 e^{-t/\tau_{\rm ramp}}$ from $f_1 = 18\,\mathrm{MHz}$ to $f_2 = 8\,\mathrm{MHz}$ above the trap bottom ($\approx 1\,\mathrm{MHz}$), for different exponential decay times $\tau_{\rm ramp}$.

few segments we optimise for the maximum elastic collision rate γ_{el}, which takes us deeper into the runaway regime. For the final segments we optimise for the phase space density ρ_{psd}, which we ultimately must raise above 1 to form a Bose-Einstein condensate.

Based on the initial temperature T_0 and a truncation parameter of $\eta = 10$, we start our evaporation ramp 17 MHz above the trap bottom f_0. For the first segment we ramp down f_{rf} exponentially to 7 MHz above f_0. Figure 4.3 shows the normalised values of N, T and γ_{el} for different exponential decay times $\tau_{\rm ramp}$. We obtained these values from absorption images of the cloud taken at the end of the the ramp segment, after releasing the cloud from the trap. To measure the relative atom number we sum the pixel counts in the images. To measure the temperature, we drop the cloud and measure its thermal expansion to find T as described in sec.3.2.2. For this first ramp segment we optimise $\tau_{\rm ramp}$ for the maximum γ_{el} which we calculate from N and T. From fig.4.3 we find that $\tau_{\rm ramp}$ is best between 3.5 and 4 s. This process was repeated for each consecutive ramp segment, but for the last 3 (linear) segments we optimise the segment duration for the maximum phase space density which we also estimate from measurements of N and T.

Near the end of the rf sweep, it is essential to know what rf frequency f_0 ejects atoms from the very centre of the trap where hf_0 is the energy at the trap bottom, $\mu_{\rm B} B_0$. We measure f_0 accurately using RF spectroscopy [103, 104]. Following evaporation, we pulse the rf on at frequency $f_{\rm spec}$ for 50 ms, slightly above f_0. This removes a fraction of the cloud. We repeat this for different values of $f_{\rm spec}$, measuring

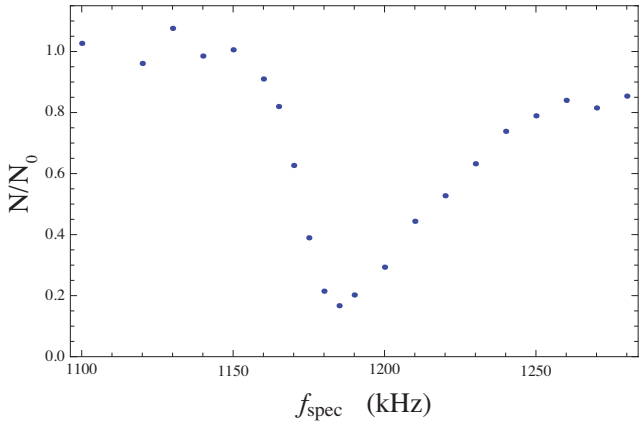

Figure 4.4: Loss spectrum for a 50 ms RF pulse close to the trap bottom. From this the trap bottom is located at 1160 ± 10 kHz. This value is determined by the frequency at which the the fraction of atoms in the spectrum starts to drop below 1. There is an experimental uncertainty at with which this point can be identified in the spectrum above where single measurements were made at each frequency. We estimate that this point can be determined to within 10 kHz. The thermal cloud used for this measurement was between 600 & 1000 nK. For a condensate which sits lies within approximately 2 kHz of the trap bottom, f_0 can be determined even more accurately.

the number of atoms remaining each time from absorption images. These images are taken at the end of the pulse, 2 ms after the cloud has been released from the trap. The highest loss is when $h(f_{\rm spec} - f_0)$ corresponds to about $4k_{\rm B}T$, and for $f_{\rm spec} < f_0$ there is no loss. Figure 4.4 shows a typical loss spectrum for a cloud at $1\mu K$. The frequency f_0 can be determined here with uncertainty of 10 kHz, which is about $k_{\rm B}T/(2h)$ for this 1 μK cloud. This accuracy is sufficient for optimising the final stages of the evaporation ramp. For the final segement of the evaporation ramp, varying the final rf frequency for a segment of fixed duration was found to be better than varying the ramp time. The optimisation of $f_{\rm rf}$ was otherwise carried out much the same way.

This optimisation process is time consuming. A reliable measurement of absolute temperature takes 4 to 5 experimental cycles (more at temperatures lower than 1 μK), imaging the cloud after release from trap along the z axis. Atom number is more accurately measured using the imaging axis along x instead, where the optical density is lower, and our signal to noise ratio is better. Number measurements are averaged over several runs also. This means optimisation of a frequency ramp segment can easily take an hour. Over this time we often found that drifts in the experiment, for example in initial atom number, caused problems. It was often difficult to know how such drifts would affect the quality of the ramp. In addition

we encountered several technical defects that give rise to heating or loss in the trap. These are discussed in more detail in sec.4.2.3.

Subsequently, working swiftly on the optimisation of the evaporation ramp was key, so that drifts would not be important over the timescale of the measurements. A number of shorthand ways of making relative measurements of temperature and density were invaluable in overcoming this. For example, measuring the curvature of the axial potential allowed us to gauge the temperature from the length of the cloud when at low temperatures, provided sufficient time ($\sim 10^2$ ms) was given for it to thermalise. Peak optical density of the cloud as measured by absorption images, $\Omega = \sigma \max \int \mathrm{d}x n(x, y, z)$, can be used together with number to estimate γ_{el} in a single absorption image (along x). $n(x, y, z)$ is the number density, and σ the scattering cross section for the imaging optical transition. For a radially harmonic, axially square potential $\gamma_{\mathrm{el}} \propto \sqrt{N\Omega}$. For a 3-d harmonic potential as may occur at low temperature, especially in the presence of fragments, $\gamma_{\mathrm{el}} \propto N^{1/3}\Omega^{2/3}$.

A prime example of the need for slick operation of the experiment was experienced on the day after we first achieved BEC. The evaporation was made up of five ramps segments. We took 3 to 5 number and cloud width measurements at the end of each stage for future reference, and carried out a small amount of optimisation on the end frequency of the final ramp. This process was started at 12:13, a BEC emerged at 13:40, and the condensate fraction was in decline by 14:00.

Of course, not everything could or should be approached with such haste. Once reliable measurements are taken to locate the source of a problem, more time could be taken to fix it. We have since fixed several technical issues with current drivers and lasers, optimised the evaporation to give the most robust route to BEC, and now understand more of the early signs of problems. For example, we used to required more than 1.8×10^7 atoms to work on the evaporation ramp to BEC. We now know we need a minimum of about 2.2×10^7 atoms[6] for the evaporation ramp to yield a small condensate of 10^4 atoms. We have since made adjustments to the LVIS, UMOT and loading of the magnetic trap so we routinely have between 2.2 & 2.7 $\times 10^7$ atoms at the start of the evaporation ramp.

[6]This is by no means a universal condition! It depends on many things such as temperature, lifetime, trap parameters and geometry etc, but is a useful gauge in our experiment.

4.2.2 Comparison of Evaporation Models to our Experiment

We evaluate the IP evaporation rate equations eq.(4.44) & eq.(4.45) for variable truncation parameter 4.46 based on the same RF frequency ramp used in our experiment. Figure 4.5 shows plots of the atom number, cloud temperature, peak density and phase space density alongside values measured from our experiment. For comparison, we also plot the numerical solutions to the power law trap rate equations 4.23 & 4.24 with variable $\eta(\tau)$ given by 4.46, for the square harmonic $n = \frac{3}{2}$, square linear $n = \frac{5}{2}$, and 3D harmonic $n = 2$ cases. The initial values of $N_0 = 10^7$ and $T_0 = 77\,\mu$K are taken from the experiment.[7] The trap lifetime is $1/\gamma_{\rm bkg} = 12\,$s.

All experimental measurements are made from absorption images taken after release from the trap. The temperature is measured from time of flight expansion in the transverse directions. The number is the average from five absorption images in the y-z plane, where the optical density is lower. The density is calculated from the peak axial density averaged over five images, together with measurements of temperature and radial trap frequency for the radial density distribution. This makes the density measurements independent of pre-conceptions about the axial distribution and length. The radial distribution is well understood. The peak phase space density $\rho_{\rm psd} = n_0\lambda_{\rm dB}^3$ is calculated from the density and temperature measurements. The trajectory of the RF frequency relative to the trap bottom is shown in 4.5a normalised to 1. The initial frequency is 9 MHz.

Figure 4.5a shows the measured temperature closely follows the predicted trajectory from the IP model. The square linear and 3-d harmonic models for which evaporation is more efficient, predict lower temperatures. While the evaporation remains runaway as it is here, the trajectory of $T(\tau)$ follows $f_{\rm rf}(\tau)$. The final two data points, where $T < 2\,\mu$K, show a slightly increased cooling rate. At these energies the roughness in the axial potential modifies the axial confinement over distances $\lesssim 10^{-2}\,\mu$m (see section 4.3 for roughness in the potential). For this data the evaporation ramp shown in 4.5a has been well optimised at these temperatures for BEC production. At the end of the ramp the roughness was used to boost the axial

[7] This is 1.7 s after the start of the 8 s evaporation ramp. Earlier images of hotter clouds expand more rapidly, and are partially obstructed by sub-chip features. Number measurements from these are unreliable.

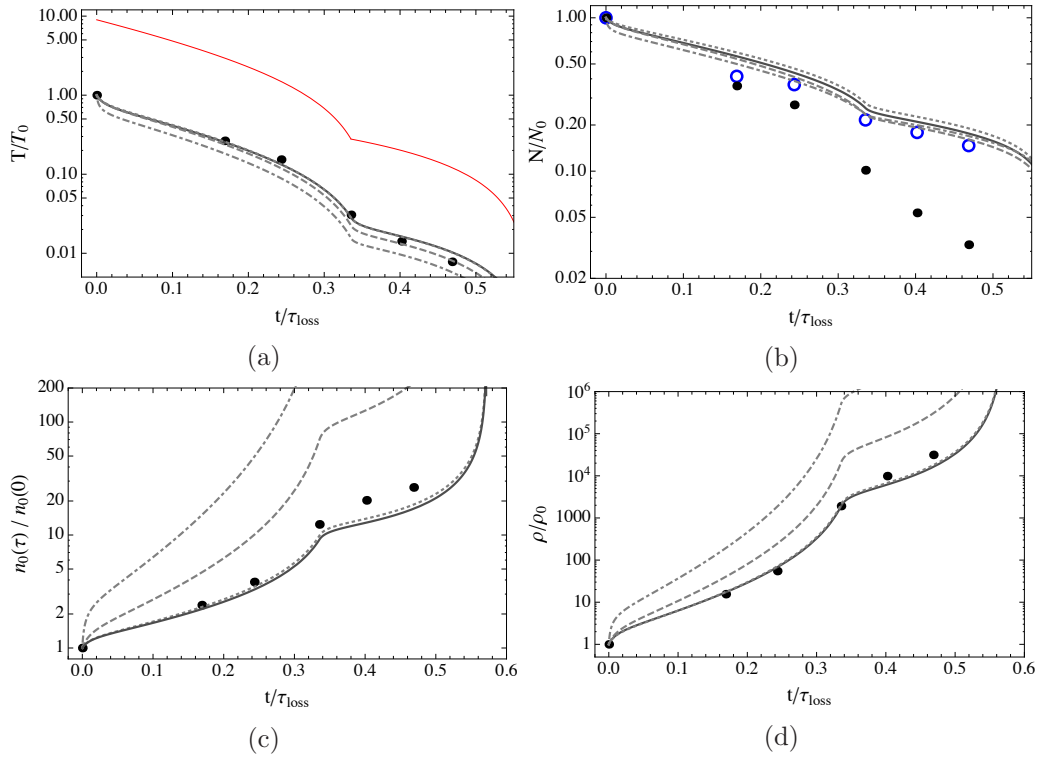

Figure 4.5: Evaporation trajectories for (**a**) temperature, (**b**) atom number, (**c**) peak number density, and (**d**) peak phase space density. Predictions from the evaporation models in the IP potential (solid lines), radially harmonic (dotted lines), radially linear (dot dashed lines), and 3-d harmonic potentials (dashed lines) are shown against experimental data points. The red line in (**a**) shows the value of the RF knife relative to the initial cloud temperature $T_0 = 77\mu K$. At $t = 0$ there are 10^7 atoms. In figure (**b**), the measured atom number is shown by the black data points. The blue circles show the atom number rescaled by factor $\Delta L/L$ to take into account the length reduction in the trap, as explained in the text.

confinement at the cloud centre, increasing the evaporation efficiency.

Figure 4.5b shows the evolution of atom number. The measured number reduces faster than than the IP trajectory predicts, even more so at lower temperatures. An explanation can be made for this effect based on the shallow gradient at the bottom of the axial potential in our experiment, which is not considered in the square axial IP model. This shallow gradient means that the length of trap will be rapidly reduced at low temperatures as the depth of the trap is reduced by the RF knife (for the square axial model, atoms can explore the entire length of the trap until the RF knife reaches the bottom of the trap). If the length reduction is slow compared to the axial oscillation period, then atoms are redistributed along the length of the trap as the temperature reduces. The subsequent reduction in number is small, as only the high energy tail is removed. However, in our trap

the rate of change of trap length can be faster than the mean atomic velocity v_z, particularly at low temperatures $T \lesssim 10\,\mu$K. The axial distribution is initially highly uniform over the length of the cloud, so rapid reduction in the length of the trap by a factor $\Delta L/L$ will results in number reduction by approximately $N\Delta L/L$. To support this argument, the circular data points show the measured number rescaled by factor $L/\Delta L$. The length L is taken as the FWHM length of the cloud for the first datapoint in fig.4.5b. The change in length ΔL is taken as the difference in the FWHM length of the cloud for the subsequent data points. The rescaled data points are in much closer agreement to the IP predictions.

Figure 4.5c shows the evolution of the peak density. The measured values are close in value to IP model. For the case of fast length reduction compared to the axial redistribution of atoms in the cloud, one would expect the density to evolve as given by the square axial IP model. This further supports the explanation given above for the faster than expected decay in atom number.

In figure 4.5d, the evolution of peak phase space density is shown. Measurements are exclusively dependent on n_0 and T, so also match the IP model very well. Nonetheless, the absolute values of ρ_{psd} provide further confidence in our evaporation model in the square IP potential. The initial peak phase space density is 10^5.[8] The IP model predicts an increase by 10^5 after $\tau = 0.53$, while the square linear and 3-d harmonic models predict this increase at $\tau = 0.32$ & 0.42 respectively. Experimentally, we have an appreciable condensate fraction at $\tau = 0.55$.

4.2.3 Heating & Loss

Provided the initial magnetic trap has favourable number, collision rate, and phase space density, almost all obstacles for evaporative cooling fall into one of two categories; heating of the trap, or loss of atoms from it. In diagnosing problems with the evaporative cooling, the first step is to measure which of these it is.

[8] We specify the phase space density as the dimensionless quantity of the number of atoms in a box of dimensions λ_{dB}^3, as used in [52] for example.

Heating

Heating slows evaporation, making it less efficient. Close to condensation when the cooling rate can be as low as a few hundred $\mathrm{nK\,s^{-1}}$ a comparable heating rate will prevent further cooling altogether. Once condensed, heating reduces the number of condensed atoms, limiting its lifetime. Main sources of heating in the magnetic trap are vibrations - parametric or centre of mass - and light close to an optical resonance.

Resonant scattering from a unidirectional beam gives average increase in energy of $\hbar^2k^2/(2m)$ per scattered photon per atom, with photon wave vector $k = 2\pi/\lambda$. This leads to a heating rate of $\mathrm{d}T/\mathrm{d}t = R(\hbar k)^2/(3k_\mathrm{B}2m)$, where R is the scattering rate. The factor of 3 in the denominator corresponds to a harmonically trapped cloud, where this energy is shared between six degrees of freedom (three potential and three kinetic). This heating rate is largest for resonant light on the $|F = 2, m_F = 2\rangle \longrightarrow |F' = 3, m'_F = 3\rangle$ cycling transition. Scattering of π or σ_- polarised light additionally gives trap loss, and is mentioned below.

Vibrational heating can be mechanical, or from a magnetic field. Energy is transferred to the atoms when this is resonant with a radial trap frequency ω_r or a harmonic of it. This type of heating is therefore sensitive to noise on the order of a few kHz. Since the 8 mm thick walls of the vacuum chamber have a skin depth of 1 mm at 1 kHz, magnetic noise is likely to come from inside the chamber. Noise on the chip Z wire current I_z is the most likely source. A frequency component at $2f_r$ gives rise to parametric heating through modulation of the trap frequency $f_r \propto 1/\sqrt{I}$. There is a much smaller sensitivity on the end wire currents through modulation of offset field B_0. Parametric heating transfers more energy than centre of mass motion since it also increases the mean relative velocity between trapped atoms. We aim for a current stability of 1 part in 10^4 to prevent significant heating from current fluctuations in our chip wires. We measure a heating rate from the temperature increase in a cold thermal cloud of less than $300\,\mathrm{nK\,s^{-1}}$.

Trap Loss

The dominant trap loss mechanism is from collisions with the background gas. The loss rate is $-\gamma_{\rm bkg}N$, giving exponential decay. We measure a $1/e$ lifetime of $1/\gamma_{\rm bkg} = 12\,{\rm s}$. The chamber pressure is limited by outgassing from surfaces on its interior. Stray light close to an optical [9] resonance can also give a reduction in lifetime if it drives atoms into un-trapped states. We increased our trap lifetime by almost a factor of 2, by isolating much of the optics from the science chamber. Both of these loss mechanisms give an overall reduction of the trap lifetime, independent of temperature.

Another loss channel is through stray RF, which drives spin flips $m_F \rightarrow \pm m'_F$. This is energy selective, exactly as the RF knife is. It is usually a sharp spike or series of spikes in the spectrum with much lower background noise level, originating from electrical equipment close or connected to our chamber. If the noise is a few MHz above the trap bottom f_0, then the cloud is quite rapidly evaporated to a temperature greater than η below it, where it no longer causes a problem. RF noise resonance below $k_{\rm B}T$ for colder clouds is more of a problem, as more atoms spend more time in the resonant region of the field. The characteristic sign of such RF noise is an increased loss rate around a particular temperature.

Another loss mechanism often considered is 3-body recombination loss. In 3-body collisions, two atoms can form a bound state, while the third carries away the remaining energy. All 3 atoms are usually lost. The bound atoms are no longer trapped, and the free atom gains enough energy to escape from the trap. The loss rate is proportional to n_0^2, and for ^{87}Rb becomes significant for densities above $10^{14}\,{\rm cm}^{-3}$ [105]. We only approach this density around the point where condensation occurs. Three-body loss can be included in evaporative cooling models [106], and decelerates the cooling rate. Including a 3-body loss term in our numerical evaporation model for our ramp shows little difference in the evolution of N & T. Furthermore, we performed ramps where the radial trap frequencies were reduced in the later stages, but gave no boost to the atom number.

[9] Microwave transitions to un-trapped states would give trap loss, but as we do not operate anything in this frequency range it is not considered.

4.3 Fragmentation

Fluctuations $\delta B_z(z)$ of the axial field give rise to roughness in the axial potential $U(z) = U_0(z) + \delta U(z)$. These cause significant axial density fluctuations in the trapped gas when $k_\mathrm{B}T \lessapprox \Delta U(z)$.

At a distance of 110 μm, our atoms experience such field fluctuations on the order of a few mG or less due to inhomogeneity of the current density in the Z wires. Transverse field fluctuations cause a transverse position shift in the trap minimum. We estimate that these shifts are less than a few 100 nm and can be ignored.

Figure 4.6a shows the average of five repeated absorption images of a thermal cloud at 1 μK, and demonstrates the strong density fluctuations along z. As the temperature is reduced further, the cloud separates completely into several clouds. Condensates can form in these fragments. The axial density of a cloud in thermodynamic equilibrium can be inverted to reveal the fluctuating potential $\delta U(z)$ which fragments the cloud:

$$\delta U(z) = -k_\mathrm{B}T \log(n_1(z)) - U(z), \tag{4.47}$$

where $n_1(z)$ is axial density rescaled to have peak value 1, and $U(z)$ is the axial potential expected from the Z wires trap without the inhomogeneities in the current density.

Figure 4.6b shows the field fluctuations $\delta B_z(z) = \delta U(z)/\mu$ found from the cloud in figure 4.6a. The blue line is a filtered version of the grey data points to remove the effect of higher frequency interference fringes in the absorption images. The spatial resolution of $\delta U(z)$ is limited to 40 μm by the 2 ms expansion period before imaging, after the trap is turned off. A more accurate determination of the depth and shape of the individual fragments would require either images in the trap or measurements using a condensate [79].

The density profile of another thermal cloud, 800 μm further to the left of the cloud in fig.4.6a, was also inverted. The field fluctuations $\delta B_z(z)$ found from density profile of this cloud are shown by the blue line (on the left hand side) in fig.4.6c.

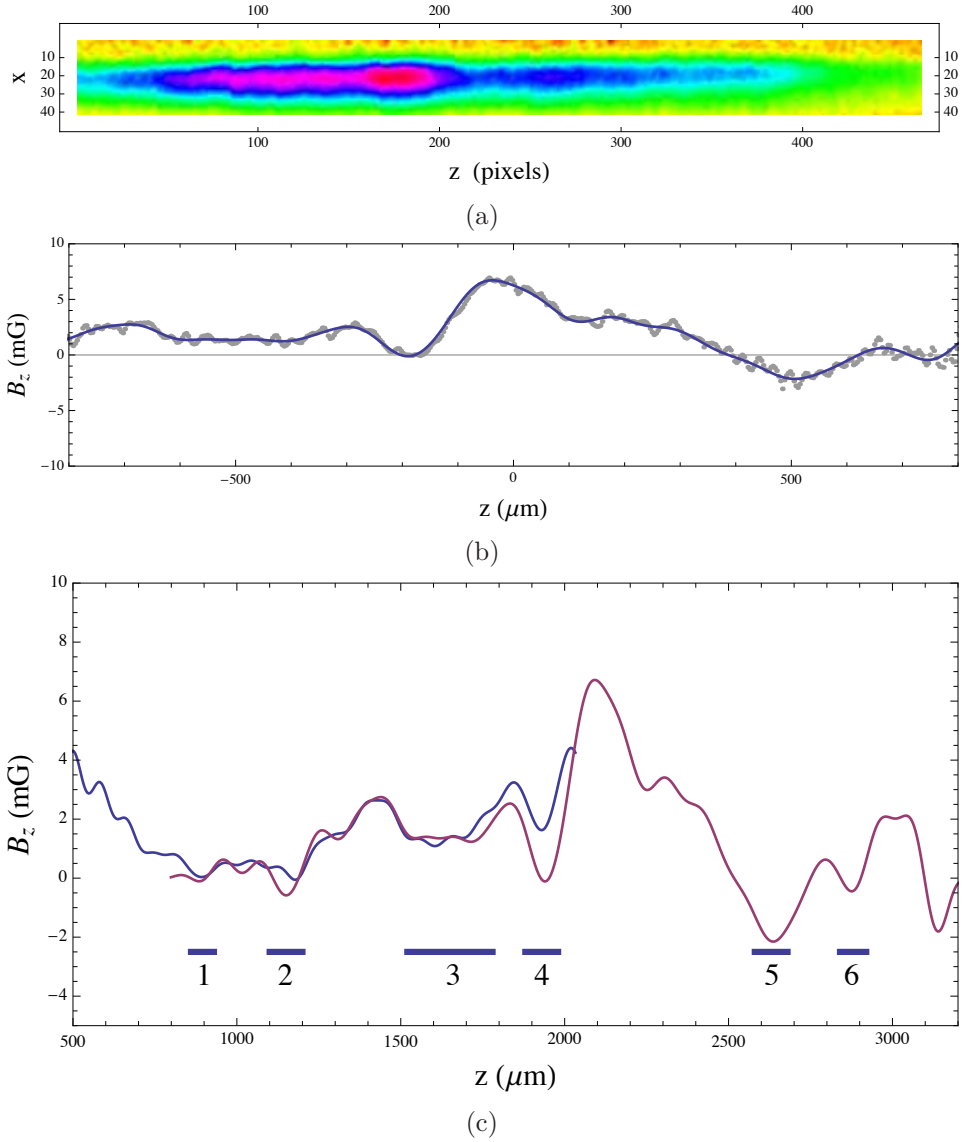

Figure 4.6: (**a**) Absorption image of a cold thermal cloud in rough potential. (**b**) Anomalous B_z component of the magenetic trapping field that produces roughness in the potential. (**c**) Anomalous B_z field over a larger spatial region, measured from clouds at two different axial positions. The numbered blue bars label the dimples that we are able to condense into.

The value of $\delta B_z(z)$ found from the cloud in fig.4.6a are shown by the purple line in fig.4.6c. Where the two measurements of $\delta B_z(z)$ overlap (between $z = 1\,\text{mm}$ and $2\,\text{mm}$), they agree within the limit of the spatial resolution of this method. Figure 4.6c is a useful map of the fragments that we have condensed into, numbered 1 to 6. These fragments shall be referred to by these numbers hereon.

The magnetic field variations $\delta B_z(z)$ arise from transverse current components in the central leg of the z wires, due to three main defects: (1) Grain boundaries in the gold wires: The grain size is $< 100\,\text{nm}$ [56] for our chip, similar to that

in [107, 79]. (2) Bulk defects in the gold layer. The chip shown in [56] was produced in the same batch as our current chip. Their scanning electron microscope images show structures as large as several hundred nm. Surface defects are also visible on the wires of [56], with size up to $\sim 1\,\mu$m. (3) Roughness in the edges of the wires [108, 78]. Fluctuations in the x-position of the wire edge can span a wide range in length scales along z. The smallest is defined by the grain boundaries. The largest arises from instabilities during the fabrication process, that give small x-deviations $\sim 10 - 100\,$nm over large distances along the wire $\sim 10 - 100\,\mu$m. Most probably it is the large scale-length fluctuations of (3) that cause the field fluctuations shown in figure 4.6c. These fluctuation of the potential play a useful role, by providing dimples in which the Bose-Einstein condensate forms more readily than it would in a smooth potential [109].

4.4 Emergence of a Bose Einstein Condensate

The critical temperature in our experiment usually lies between 300 and 600 nK depending on the atom number. The rf frequency at which this occurs depends on the truncation parameter η, but it is typically 30 to 60 kHz above the trap bottom.

Figure fig.4.7a shows the emergence of a condensed fraction in the axial density profile of a thermal cloud as the rf frequency is lowered towards the trap bottom at 1.48 MHz. At $f_{\rm rf} = 1.51\,$MHz, the sharp peak shows the first signs of a BEC emerging. However, tight fragments in the potential can also create sharp features. As the rf frequency is reduced further, we look for the characteristic bimodal distribution: a narrow condensate with Thomas Fermi density profile at the centre of a wider Gaussian thermal distribution. We also measure the temperature and phase space density close to condensation to confirm they are close to the critical values. As we reduce the rf frequency further, the fraction of condensed atoms in the central peak increases. For the final image in 4.7a, the rf frequency was held at its final value for 100 ms, and we estimate that the condensed fraction of atoms is $\frac{8}{10}$. This fraction was estimated by fitting a simple bimodal distribution to the cloud given by eq.(7.20) in sec.7.2.1, following a method similar to [110].

Figure 4.7b shows our first ever observation of a Bose-Einstein condensate (on

this atom chip). At this point we had not optimised the final stage of the evaporation ramp to produce the high condensed fraction as in fig.4.7a. At 1.42 MHz a sharp spike appears on the left hand side of the cloud. This series of images demonstrates that the early signs of a BEC are not always as dramatic as the images popularly presented! To increase the condensed fraction we shifted the centre of the thermal cloud to sit over the fragment where the condensate forms (fragment 1 in fig.4.6c). For the original evaporation ramp we also relaxed the radial trap frequencies by decreasing B_x in case three body loss was limiting progress. Consequently the trap was further from the chip and the fragment potential weaker. We found this not to be necessary, and maintaining the axial confinement resulted in a higher condensed fraction.

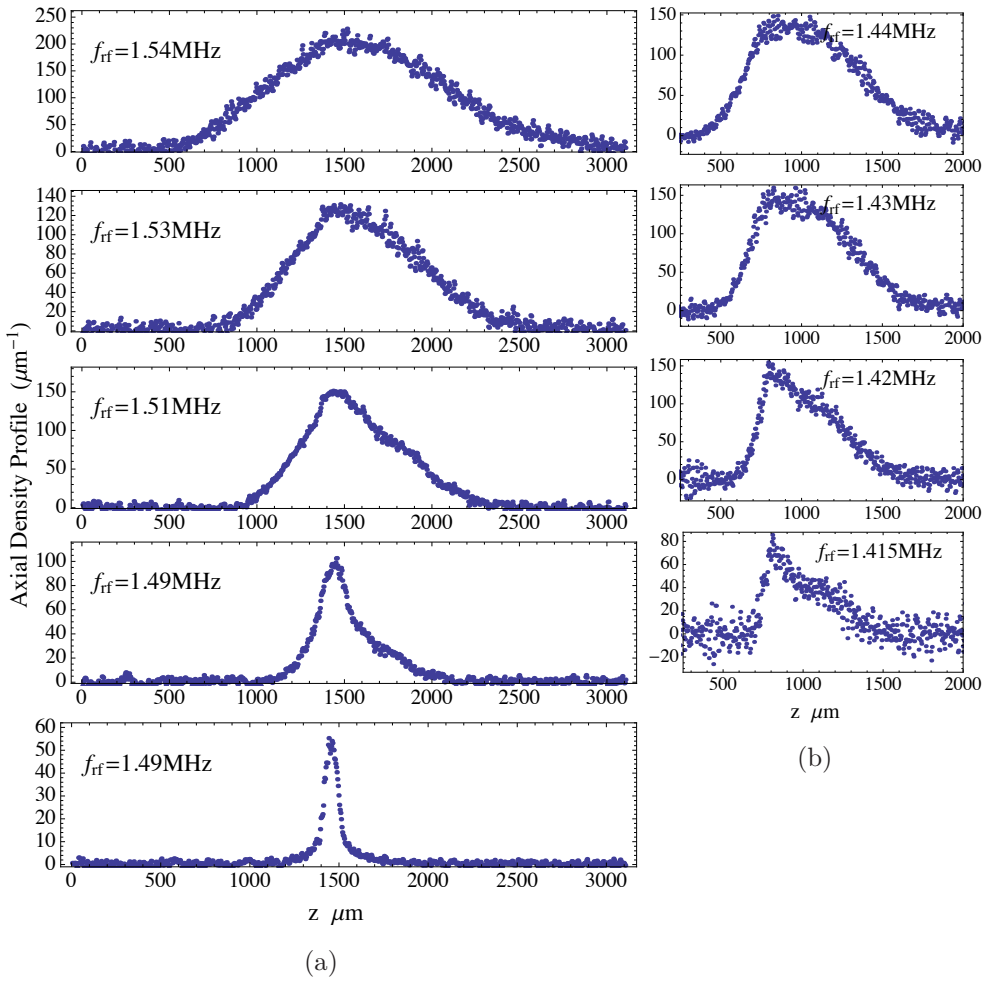

Figure 4.7: Axial density profile of trapped gas as the rf frequency is scanned through the BEC transition. Figure (**a**) shows the emergence of the BEC after the final stage of the evaporation ramp was optimised. The value of the rf frequency fro the bottom two plots are the same, but the rf knife was held on for a further 100 ms at the end of the ramp to increase the condensed fraction in the final image. Figure (**b**) shows our first observations of BEC on this chip prior to optimisation. The vertical scale in each image is the number of counts per column of pixels found from the absorption images.

Chapter 5

Characteristics and Manipulation of the BEC

This chapter describes aspects of a trapped Bose Einstein condensate and its dynamics. We begin with a description of a static condensate as the ground state of a system of N interacting trapped bosons. We discuss the analytic approximations of the ground state density distribution, and show numerical solutions of the density distribution evaluated with the parameters of our condensate. Section 5.2 then introduces the time dependent theory, and some dynamics that arise from it. Oscillations of the condensate's centre of mass and length are described, along with measurements of these modes in our experiment. Finally, a description of the expansion of the condensate once the trap potential is turned off is given in sec.5.3.

5.1 Form of the Ground State

In this section the concept of the order parameter $\psi(\mathbf{r})$ is introduced for the condensate, together with the Gross Pitaevskii equation for which it is the solution [111, 112, 113]. In doing so a flavour for the complexity of the many-body problem is given, together with the simplifications that are needed to describe the condensate in terms of this single function of a single coordinate vector. A more detailed derivation can be found in appendix B.

The multi-particle state of N bosons can be written as the sum of product states of the N single particle states $|\psi_i\rangle$, symmetric under the interchange of particles. In the position representation, the wave function for this state consists of products of the N single particle functions, each parameterised by its own coordinate vector $\mathbf{r}_i$, and summed over distinct particle orderings. For a BEC this state can be simplified by making the Hartree approximation in which all particles are considered to be in the same single particle state, $|\psi\rangle$. The wave function of this state is now the single product of N identical functions, each parameterised by one of the N position vectors $\{\mathbf{r}_i\}$.

The exact form of the condensed state depends on the trap potential $V(\mathbf{r})$ and the interaction between particles. For ultra-cold Rubidium atoms in the $F = 2$ internal ground state, the inter-particle interactions are almost exclusively due to s-wave scattering between pairs of particles. For low densities - as found in experiments with magnetically trapped ^{87}Rb atomic vapour - the scattering potential can be approximated with an effective 'contact' potential $g\delta(\mathbf{r}_i - \mathbf{r}_j)$, where $g = 4\pi\hbar^2 a/m$ and a is the s-wave scattering length [11]. The condensate forms in the ground state of the many body Hamiltonian

$$H = \sum_i \frac{\mathbf{p}_i^2}{2m} + V(\mathbf{r}_i) + \sum_{i<j} g\delta(\mathbf{r}_i - \mathbf{r}_j). \tag{5.1}$$

The ground state is that which minimises the expectation value of the energy $E[\psi(\{\mathbf{r}_i\})] = \langle\psi(\{\mathbf{r}_i\})|\, H\, |\psi(\{\mathbf{r}_i\})\rangle$. In calculating $E[\psi(\{\mathbf{r}_i\})]$, the respective sums in the Hamiltonian can be replaced by the factors N and $N(N-1)/2 \approx N^2/2$ for $N \gg 1$, and the subscripts of $\mathbf{r}$ dropped. Subsequently, the expectation value depends on a function of a single coordinate vector, $\psi_0(\mathbf{r}) = \sqrt{N}\psi(\mathbf{r})$, where ψ is the single particle mean-field wavefunction. This is often referred to as the 'wave function' or order parameter of the condensate. It has normalisation N, and the mean condensate density can be conveniently expressed as $n(\mathbf{r}) = |\psi_0(\mathbf{r})|^2$.

For the multi-particle ground state $|\psi(\{\mathbf{r}_i\})\rangle$ to minimise the energy $E[\psi(\{\mathbf{r}_i\})]$, the order parameter $\psi_0(\mathbf{r})$ must equivalently obey the time-independent Gross Pitaevskii equation

$$\left(-\frac{\hbar^2}{2m}\nabla^2 + V(\mathbf{r}) + g|\psi_0(\mathbf{r})|^2\right)\psi_0(\mathbf{r}) = \mu\psi_0(\mathbf{r}). \tag{5.2}$$

This equation takes the form of a non-linear Shrödinger equation for the order parameter $\psi_0(\mathbf{r})$ in external potential $V(\mathbf{r})$, and mean field potential $g|\psi_0(\mathbf{r})|^2$ due to the interaction between atoms. The ground state energy is the chemical potential μ of the condensate.

5.1.1 Approximate Solutions of the Gross Pitaevskii Equation

We now look at two approximations for the Gross Pitaevskii ground state solution $\psi_0(\mathbf{r})$. The three terms on the left hand side of eq.(5.2) can be identified with the kinetic, potential and interaction energy of the condensate. The external potential term provides confinement of the condensate. The kinetic term and the interaction term (for $a > 0$) both oppose the compression by the external trapping potential. The two approximations to be discussed are the regimes where the kinetic energy dominates over the interaction energy, and where the interaction energy dominates over the kinetic energy.

We first look at the magnitude of the three different energies to understand when the various contributions can be ignored. The individual contributions of kinetic, potential and interaction energy to the chemical potential are found by taking the inner product of the Gross Pitaevskii equation 5.2. Following the discussion in [11, 114], these energies are estimated for a condensate in an isotropic harmonic potential. Taking the condensate radius where its density goes to zero to be on the order of R_0, then it has kinetic energy per particle $\sim \hbar^2/(2mR_0^2)$, potential energy per particle $\sim m\omega^2 R_0^2/2$ and interaction energy per particle $\sim gN/R_0^3$. In the ground state, the sum of these terms must be minimised with respect to R_0:

$$\frac{\partial}{\partial \tilde{R}_0}\left(\frac{8\pi N a}{a_{\rm ho}}\frac{1}{\tilde{R}_0^3}+\frac{1}{\tilde{R}_0^2}+\tilde{R}_0^2\right)=0. \tag{5.3}$$

The radius $\tilde{R}_0$ has been written in units of the harmonic oscillator length $a_{\rm ho} = \sqrt{\hbar/(m\omega)}$. As asserted above, the potential energy favours a small radius, while the kinetic and interaction energies favour larger R_0. Two regimes for the approximate solutions can be identified by $8\pi Na/a_{\rm ho} \ll 1$ where the interaction term can be neglected and $8\pi Na/a_{\rm ho} \gg 1$ where the kinetic term is neglected. For a given trap potential and scattering length, these regimes are synonymous with small and large

atom number N respectively. For small N, eq.(5.3) estimates the condensate radius $R_0 \sim a_{\rm ho}$. For large N, the condensate radius is $R_0 \sim a_{\rm ho}\,(Na/a_{\rm ho})^{1/5}$.

A more detailed calculation is made in [11] for radially symmetric anisotropic traps characterised by their radial frequency $\omega_\perp$ and axial frequency ω_z. The aspect ratio of the trap is given as $\lambda = \omega_z/\omega_\perp$. From their result the two regimes are instead given by $Na/a_\perp \ll \sqrt{\lambda}$ and $Na/a_\perp > \sqrt{\lambda}$, where $a_\perp = \sqrt{\hbar/(m\omega_\perp)}$.

In the regime of weak interaction energy the Gross Pitaevskii equation is well approximated by the usual Shrödinger equation of a particle in potential $V(\mathbf{r})$. For a harmonic potential the ground state wave function has the familiar form,

$$\psi(r) = \frac{\sqrt{N}}{\left(\pi a_{\rm ho}^2\right)^{3/4}} \exp\left(-\frac{r^2}{2a_{\rm ho}^2}\right). \tag{5.4}$$

This becomes the exact solution for the case of a non-interacting BEC.

The opposite regime, refered to as the Thomas Fermi limit, is much more common in most realisations of a BEC in an atomic vapour. In the Thomas Fermi limit, the kinetic term is dropped from the Gross Pitaevskii equation, which becomes

$$\left(V(\mathbf{r}) + g|\psi(\mathbf{r})|^2\right)\psi(\mathbf{r}) = \mu\psi(\mathbf{r}) \tag{5.5}$$

Since the condensate density is by definition

$$n(\mathbf{r}) = |\psi(\mathbf{r})|^2, \tag{5.6}$$

the density profile in the Thomas-Fermi limit is

$$n(\mathbf{r}) = \begin{cases} (\mu - V(\mathbf{r}))/g & \text{for } n > 0 \\ 0 & \text{otherwise.} \end{cases} \tag{5.7}$$

The axial density profile to which we commonly fit our experimental data is found by integrating over the radial dimensions. Integrating over x and y in an axially

symmetric harmonic trap gives the axial density profile

$$n(z) = \begin{cases} \frac{\pi}{m\omega_r^2 g}\left(\mu - \frac{1}{2}m\omega_z^2 z^2\right)^2 & \text{for } |z| < \sqrt{\frac{2\mu}{m\omega_z^2}} \\ 0 & \text{otherwise.} \end{cases} \tag{5.8}$$

The 1d density profiles in the x and y directions are obtained similarly, interchanging x or y for z in eq.(5.8).

Figure 5.1 shows the mean of four absorption images of condensates, together with the 1D profiles $n(y)$ and $n(z)$. To produce these almost pure condensate shown here, we evaporate down to approximately 10 kHz above the trap bottom, where we hold the rf knife for a further 100 ms. Images were taken after the condensate has been released from the trap and allowed to expand for 2 ms. This process was repeated 10 times, to produce 10 different images. Due to fluctuations in our evaporation efficiency, the atom number in the condensate varies from shot to shot. We then selected the four images that had an atom number in the range $2.40 \pm 0.05 \times 10^4$. The mean of these four images in shown in fig.5.1a.

From these four images, we also find the mean 1D density profiles, by summing over the pixels in the vertical or horizontal directions. For a condensate well described in the Thomas Fermi limit, and with $\omega_z \ll \omega_x,\ \omega_y$, the axial density $n_z(z)$ changes by a negligible amount over the 2 ms that the cloud is allowed to expand for. In the transverse direction the expansion is significant. However, this expansion only scales the transverse profile $n(y)$, with its functional form remaining the same. This is discussed in sec.5.3, after we introduce the dynamics of the condensate. Therefore, if the condensate is well described by a Thomas Fermi density distribution in the trap, it will also be well described by a Thomas Fermi after it has been released, differing only by a scale factor in the transverse directions.

The data points in fig.5.1b and fig.5.1c show the mean density profiles found from these four images. The error bars show the standard error in the mean density from these images. The red lines show the Thomas Fermi approximation $n(y)$ and $n(z)$ fitted to the mean profiles. We generally find that the Thomas Fermi profile in the axial direction, $n(z)$, provide a good fit the data, passing within the 1σ standard error of most of the data points. Only in the tails do we see much deviation from

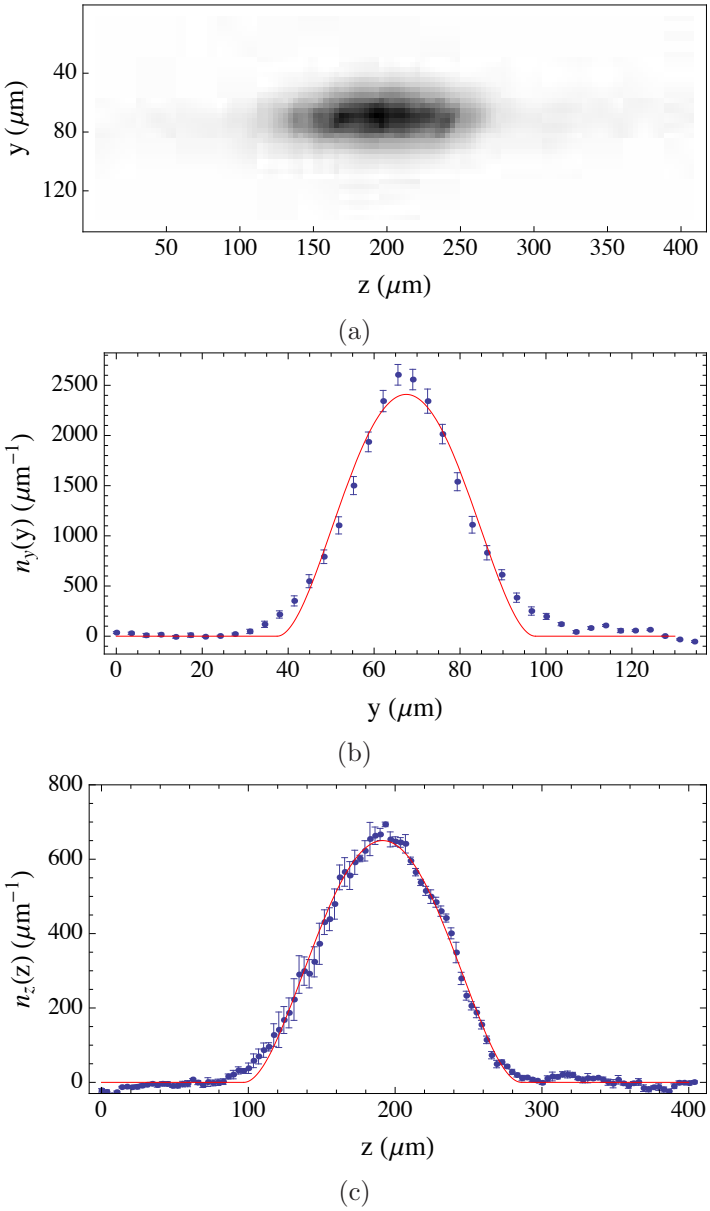

Figure 5.1: Images and 1D density profiles of an almost pure condensate. Figure 5.1a shows the mean of four absorption images of condensates 2 ms after it has been released from the magnetic trap. These four clouds images were selected from a larger set of 10 images, for the close agreement in atom number. The atom number in each image, found by summing over the pixel counts, was $2.40 \pm 0.05 \times 10^4$. Figure 5.1b and fig.5.1c show the 1D density profiles measured by summing over either rows or columns of pixels in the mean image in fig.5.1a. The error bars show the standard error in the 1D density. The density profile eq.(5.8), given by the Thomas Fermi approximation of the Gross Pitaevskii equation, is fitted to the measured profiles (red lines).

this. In the y direction, the features of the measured profile in our absorption images are diffraction limited to a resolution of approximately $6\,\mu$m. The density of the condensate in the y direction varies significantly over a lengths scale on this order, and the measured image is a blurred version of the actual condensate density in the y-

direction. Subsequently, from fig.5.1b one cannot judge how well the Thomas-Fermi profile approximates the actual condensate density $n(y)$, due to this systematic error. We therefore discuss the accuracy of the Thomas Fermi approximations further in the next section, by comparing it to exact numerical solutions to the Gross Pitaevskii equation with parameters similar to those in our experiment.

We next find an expression for the chemical potential μ of the condensate. Integrating the condensate density eq.(5.7) over all three directions and setting the result to the total atom number N, the chemical potential in the TF approximation is given by

$$\mu = \frac{\hbar\omega_{\rm ho}}{2}\left(\frac{15Na}{a_{\rm ho}}\right)^{2/5}, \tag{5.9}$$

for geometric mean frequency $\omega_{\rm ho} = (\omega_x\omega_y\omega_z)^{1/3}$, and the corresponding geometric mean harmonic oscillator length $a_{\rm h0}$. This result is equally valid for symmetric and asymmetric traps. For our atom number $N \sim 10^4$ and frequency $\omega_{\rm ho} \approx 2\pi \times 300\,{\rm Hz}$, the chemical potential is of the order $\mu \sim 2\,{\rm kHz}$.

The Thomas Fermi approximation is often used in BEC experiments as it offers an analytic model which is accurate over the bulk of the condensate for a sufficiently large value of $Na/(a_\perp\sqrt{\lambda})$. In our experiment $Na/(a_\perp\sqrt{\lambda})$ is of order 10. However, for highly elongated condensates such as ours, the kinetic energy $\frac{\hbar^2}{2m}\partial^2\psi/\partial r^2$ is not necessarily negligible compared to the interaction energy due to the tight radial confinement of the trap. The Thomas Fermi limit breaks down near the surface of the condensate where the density becomes small and the gradient of ψ is larger. For highly elongated condensates, this surface region can be much larger than for a condensate in a nearly isotropic potential. In particular this is likely to effect the density distribution in the transverse directions such as $n(y)$ in fig.5.1b. As explained above, the resolution limits how accurately we can determine $n(y)$ from our absorption images. To check the accuracy of the Thomas Fermi approximation the solution 5.7, we compare it to the exact solution of the full GPE obtained numerically in the next section [115, 116, 117].

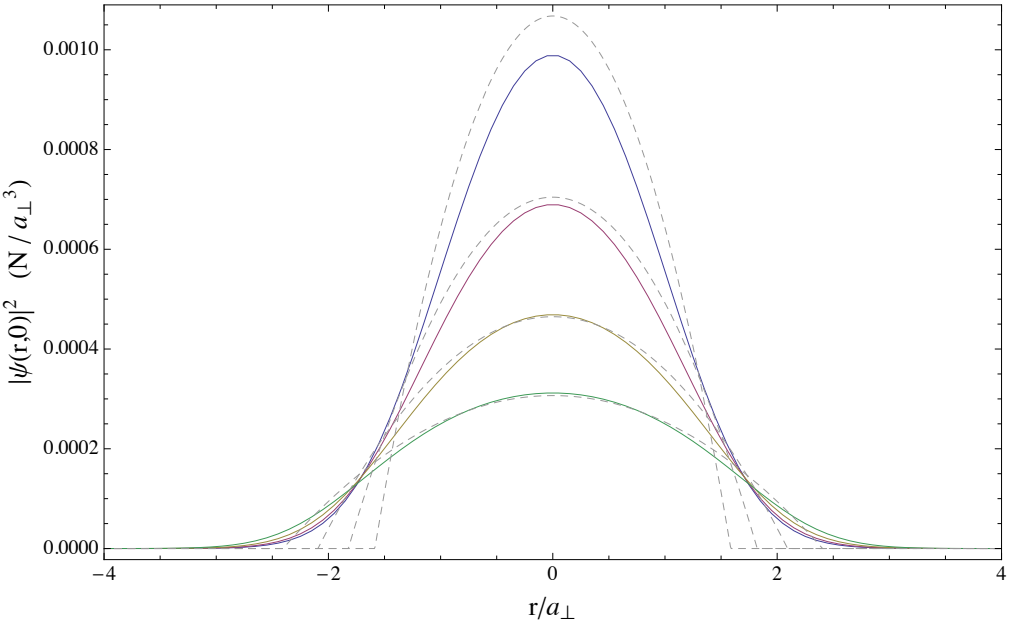

(a)

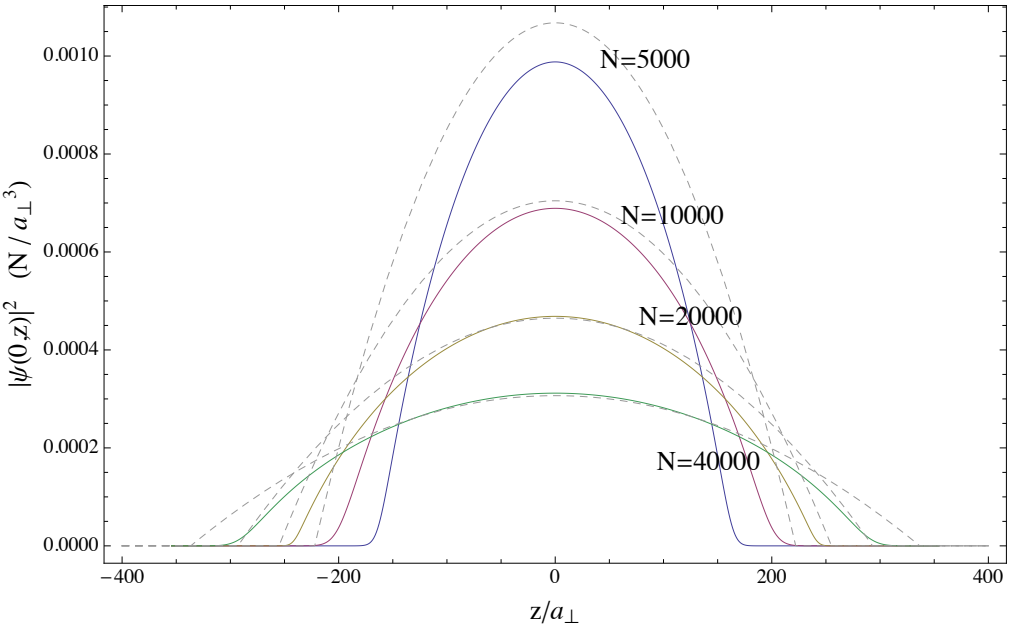

(b)

Figure 5.2: Condensate line density profiles along the lines $z = 0$ and $r = 0$, as found from numerical solutions of the GPE and from the Thomas-Fermi approximation. Figure 5.2a shows the normalised line density $|\psi(r, 0)|^2/N$ in the radial direction in units of the radial harmonic oscillator length $a_\perp = 2.88 \times 10^{-7}$ m. The solid lines show the numerical solutions for $N = 5 \times 10^3,\ 10^4,\ 2 \times 10^4$ and 4×10^4 atoms, with the colours as labelled in fig.5.2b. The dashed lines show the Thomas-Fermi profiles for the same atom numbers. Figure 5.2b shows axial line density $|\psi(0, z)|^2/N$, for the indicated atom numbers. Solid lines show the numerical solution and dashed line the Thomas-Fermi profiles.

5.1.2 Numerical Solutions of the GPE

To find a numerical solution of the GPE, we follow the approach of [117]. In this method, the energy functional $E[\psi]$ is minimised by making gradual variations to

an initial test function ψ_0. This is chosen to be either the Thomas Fermi solution eq.(5.7) or the non-interacting solution eq.(5.4). The value of the wave function is then varied at a point $\mathbf{r}$ by an amount proportional to the functional derivative

$$\frac{\delta E[\psi(\mathbf{r})]}{\delta\psi(\mathbf{r})} = H\psi(\mathbf{r}), \tag{5.10}$$

where the Hamiltonian H is that in the Gross Pitaevskii equation eq.(5.2). This ensures variation by an amount proportional to the slope $E[\psi]$ at $\mathbf{r}$ with which $E[\psi]$ approaches its minimum. Thus, as $E[\psi]$ approaches a minimum, it is varied by an amount proportional to the gradient $\delta E[\psi(\mathbf{r})]/\delta\psi(\mathbf{r})$ with which it approaches this minimum. The variation of ψ must be constrained to ensure the correct normalisation $\int \mathrm{d}^3r|\psi|^2 = N$.

To do this numerical minimisation we start with a test function $\psi_0(r,z)$, which is either taken as the Thomas-Fermi wave function or a Gaussian wave function. Values of $\psi_0(r,z)$ are first calculated over a 2D grid r_i and z_j. At each point (i,j) of the grid, $H\psi_0(r_i,z_j)$ is then calculated and used to generate a new solution

$$\psi_{k+1}(r_i,z_j) = \psi_k(r_i,z_j) + \Delta t\, H\psi_k(r_i,z_j) \qquad \text{where } 0 \le k < M. \tag{5.11}$$

This equation is in fact a finite difference version of a time-dependant non-linear schrödinger equation, but with imaginary rather than real time. This imaginary time propagation means that the excited states decay (rather than oscillate) at a rate proportional to their energy, leaving only the ground state after it has been iterated for a sufficiently long time.

The numerical derivatives of $H\psi$ in eq.(5.11) are performed using finite difference formulae. Once $\psi_{k+1}(r_i,z_j)$ has been generated over the whole grid, $|\psi_{k+1}|^2$ is re-normalised to N. This process is iterated. Provided the energy functional $E[\psi]$ varies smoothly, and Δt is sufficiently small, the sequence $\{\psi_k\}$ converges to value that minimises the energy $E[\psi]$ and therefore to the solution of the Gross Pitaevskii equation, 5.2.

For our highly elongated trap we use a 400×100 grid for the radial and axial coordinates r and z. The grid spacings are $\Delta r = a_\perp/5$, and $\Delta z = a_\perp/(5\sqrt{\lambda})$ where $a_\perp = \sqrt{\hbar/(m\omega_r)}$ is the harmonic oscillator length of the radial ground state, and

$\lambda = \omega_z/\omega_r$. The two step procedure of variation followed by normalisation is iterated between 1000 and 5000 times.

We have found that our numerical solutions for ψ agree with the TF approximation for large N, and with the non-interacting Gaussian ground state for small N, which help verify that our numerical solutions are correct. In the intermediate range as well as for highly anisotropic traps such as ours, results can be validated using the virial theorem. For a harmonic trap this gives the relation

$$2E_{\mathrm{k}} = 2E_{\mathrm{pot}} - 3E_{\mathrm{int}} \tag{5.12}$$

between the kinetic energy E_{k}, potential energy E_{pot}, and interaction energy E_{int} [117, 118]. For our numerical results the values of 5.12 agree to within 0.1% for between 1000 and 5000 iterations.

Numerical results are shown in fig.5.2 for a range of atom numbers, with trap parameters close to those found in our experiment. The radial trap frequency used was $\omega_r = 2\pi \times 1.4\,\mathrm{kHz}$, and $\lambda = 1/140$. The radial harmonic oscillator length was $a_\perp = 0.3\,\mu\mathrm{m}$. The results are shown against the TF solutions 5.7. Figure 5.2a shows the normalised line density $|\psi(r,0)|^2/N$ in the radial direction in units of the radial harmonic oscillator length $a_\perp = 2.88 \times 10^{-7}\,\mathrm{m}$. The solid lines are the numerical solutions, and the dashed lines are found from the Thomas-Fermi approximation. Figure 5.2b shows the line density in the axial direction, $|\psi(0,z)|^2/N$, and fig.5.2a shows the line density in the transverse direction.

For an isotropic trap, or one with modest $\lambda \sim 1/10$, the TF approximation provides reliable estimates for both μ and the density distribution. For elongated condensates such as ours, the density distribution in the axial direction is expected to have a similar overall shape to that given in the Thomas Fermi approximation, but the exact value of the chemical potential is modified. In the transverse direction, where the kinetic energy contribution is largest, the overall shape of the density profile is expected to differ from that expected in the Thomas Fermi limit. The plots in fig.5.2a show that the actual wave function has tails in the radial direction which extend appreciably beyond the Thomas-Fermi radius. This is due to the kinetic energy in the surface region of the condensate being relatively high compared to the

interaction energy, due to the tightness of the trap. Subsequently, the peak density is slightly lower and the chemical potential lowered. In the axial direction, fig.5.2b shows that the density profile takes a similar functional form of $n(z)$ given in the Thomas Fermi limit, but with a slightly lower axial width than predicted in this limit.

It is possible that the tails visible in the measured density profile $n(y)$ in fig.5.1b are due to this effect. However, the edges of the condensate are blurred in a Gaussian fashion due to the limited resolution of our absorption images. So even though our numerical solutions show such tails are expected for our condensate, the tails we see in fig.5.1b could equally be an artefact of the absorption images.

5.2 Dynamics of the Condensate

A time-dependent Gross Pitaevskii equation [111, 112, 113], can be derived by minimising the action (see [11] for example),

$$S = \int_{t_0}^{t} \mathrm{d}t' L(\psi(t), \dot{\psi}(t), t). \tag{5.13}$$

By noticing that a condensate wave function within the Hartree approximation must evolve unitarily with $U(t) = \exp\left(-i\frac{\mu}{\hbar}t\right)$, one can derive the Lagrangian

$$L = \int \mathrm{d}\mathbf{r} \left[\frac{i\hbar}{2}\left(\psi^*(\mathbf{r},t)\frac{\partial\psi(\mathbf{r},t)}{\partial t} - \psi(\mathbf{r},t)\frac{\partial\psi^*(\mathbf{r},t)}{\partial t}\right)\right] - E[\psi(\mathbf{r},t)]. \tag{5.14}$$

The time-dependent version of eq.(5.2) is thus

$$i\hbar\frac{\partial\psi(\mathbf{r},t)}{\partial t} = \left(-\frac{\hbar^2}{2m}\nabla^2 + V(\mathbf{r}) + g|\psi(\mathbf{r})|^2\right)\psi(\mathbf{r}). \tag{5.15}$$

This equation describes the dynamical evolution of the condensate at zero temperature.

There are two approaches used to study the dynamics of ψ as given by the time dependent Gross Pitaevskii equations 5.15 in the linearised limit. In this limit, one expands either the wave function or the density in terms of its ground state form plus a small perturbation. On substituting this expansion into the equation of motion,

which for ψ is eq.(5.15), and $n(\mathbf{r})$ are a set of hydrodynamic equations, one only retains the terms up to first order in the small perturbation. The difficulty in solving 5.15 comes from the non-linear term. In the linearised limit one generally considers fluctuations $\delta\psi$ about the stationary ground state, how these are effected by the ground state Hartree mean field $g|\psi|^2$, but not how they effect themselves i.e. terms like $|\delta\psi|^2$.

5.2.1 Small Amplitude Excitations

In the first approach, due to Bogoliubov [119], the wavefunction of the gas is expanded perturbatively,

$$\psi(\mathbf{r},t) = \psi_0(\mathbf{r},t) + \delta\psi(\mathbf{r},t), \tag{5.16}$$

where $\psi_0(\mathbf{r},t)$ is the ground state solution from the time-independent Gross Pitaevskii equation, with a time dependent overall phase, $\delta\psi(\mathbf{r},t)$ is a small fluctuation about this. The ground state evolves unitarily with the chemical potential, and the fluctuating term is written in terms of the Bogoliubov modes $u_j(\mathbf{r})$ and $v_j(\mathbf{r})$ of energy $\hbar\omega_j$;

$$\delta\psi(\mathbf{r},t) = \left(u(\mathbf{r})e^{-i\omega t} + v^*(\mathbf{r})e^{i\omega t}\right) e^{-i\mu t/\hbar} \tag{5.17}$$

Substituting this into the time dependent Gross Pitaevskii equation and retaining only terms linear in the small amplitudes u_j and v_j gives the set of coupled equations

$$\hbar\omega_j u_j(\mathbf{r}) = \left(-\frac{\hbar^2}{2m}\nabla^2 + V(\mathbf{r}) - \mu + 2gn(\mathbf{r})\right) u_j(\mathbf{r}) + gn(\mathbf{r})u_j(\mathbf{r}) \tag{5.18}$$

$$-\hbar\omega v_j(\mathbf{r}) = \left(-\frac{\hbar^2}{2m}\nabla^2 + V(\mathbf{r}) - \mu + 2gn(\mathbf{r})\right) v_j(\mathbf{r}) + gn(\mathbf{r})u_j(\mathbf{r}) \tag{5.19}$$

Solutions of these coupled equations give a spectrum of elementary excitations of the condensate as a set of eigenvalues and eigenmodes. The Bogoliubov approximation gives a valuable way to picture the excitations of the condensate, which we return to in the finite temperature description of a bose gas in the second quantised limit in Ch.7. However, for low energy excitations of a condensate at zero temperature, it is perhaps easier to work with the condensate density $n_0(\mathbf{r},t)$ and small density fluctuations about it $\delta n(\mathbf{r},t)$, rather than with $\psi(\mathbf{r},t)$ directly. This approach is given by the hydrodynamic theory of the condensate which we describe next.

5.2.2 Hydrodynamic Equations

In the Hartree approximation the condensate is treated as a classical mean-field ψ, ignoring quantum fluctuations which are typically small and short range (see, for example [11]). An intuitive picture of the dynamics arises by considering the density and velocity fields of the condensate, much like for a classical fluid. This approach leads to a pair of coupled hydrodynamic equations, which can be simplified first by taking them in the Thomas Fermi limit, and further still by looking for linearised solutions. These equations can be solved analytically in particular cases. Here we highlight solutions that describe length and centre of mass oscillations of the condensate in a harmonic potential, as well as how the condensate expands after it is released from the trap. As point for comparison it is noted that the linearised hydrodynamic and Bogoliubov approaches are exactly equivalent in the case of a uniform bose gas, and yield the same energy spectrum of excited modes.

To derive the hydrodynamic equations the condensate wave function is first written with explicit dependence on the mean density $n(\mathbf{r},t)$,

$$\psi(\mathbf{r},t) = \sqrt{n(\mathbf{r},t)}e^{i\phi(\mathbf{r},t)}. \tag{5.20}$$

Using this the time derivative of the density can be written in terms of $\psi(\mathbf{r},t)$ as $\frac{\partial n(\mathbf{r},t)}{\partial t} = \psi^*\frac{\partial \psi}{\partial t} + \psi\frac{\partial \psi^*}{\partial t}$. The time derivatives can be expanded by substitution of the time dependent Gross Pitaevskii equation, whereby all but the terms containing the operator ∇^2 cancel. Thus

$$\begin{aligned}\frac{\partial n(\mathbf{r},t)}{\partial t} &= i\frac{\hbar}{2m}\left(\psi^*\nabla^2\psi - \psi\nabla^2\psi^*\right)\\ &= -\frac{\hbar}{m}\,n(\mathbf{r},t)\nabla\phi(\mathbf{r},t).\end{aligned} \tag{5.21}$$

where the explicit from of $\psi(\mathbf{r},t) = \sqrt{n(\mathbf{r},t)}e^{i\phi(\mathbf{r},t)}$ is used in the second line. Since the particle number is conserved, the term on the right hand side must be the divergence of the current density $\nabla\cdot\mathbf{J}(\mathbf{r},t)$.[1] This gives the first of the two hydrodynamic

[1] Conservation of N is explicit in the Hartree approximation. The Hartree Fock approximation must instead be used when the condensate fraction is not conserved. For example where there is exchange or loss of condensed atoms through interactions with the thermal cloud. In this case the hydrodynamic equations do not hold, and the Bologluibov approach should be used instead

equations, the continuity equation

$$\frac{\partial n(\mathbf{r},t)}{\partial t} + \nabla \cdot \mathbf{J}(\mathbf{r},t) = 0 \tag{5.22}$$

The current density can be written in terms of the velocity field $\mathbf{v}(\mathbf{r},t)$, as $J(\mathbf{r},t) = n(\mathbf{r},t)\mathbf{v}(\mathbf{r},t)$. Comparison of the continuity equation with its explicit form eq.(5.21) shows that the velocity field is proportional to the gradient of the phase

$$\mathbf{v}(\mathbf{r},t) = \frac{\hbar}{m}\nabla\phi(\mathbf{r},t). \tag{5.23}$$

An equation for $\phi(\mathbf{r},t)$ is found by direct substitution of eq.(5.20) into the time dependent Gross Pitaevskii equation eq.(5.15). Using the continuity equation to eliminate terms and factorizing out ψ, the equation of motion for $\phi(\mathbf{r},t)$ is

$$-\hbar\frac{\partial\phi(\mathbf{r},t)}{\partial t} = \frac{1}{2}m\mathbf{v}^2(\mathbf{r},t) + V((\mathbf{r},t)) + gn(\mathbf{r},t) - \frac{\hbar^2}{2m\sqrt{n(\mathbf{r},t)}}\nabla^2 n(\mathbf{r},t) \tag{5.24}$$

The left hand side is clearly the local energy of the condensate in the vicinity of $\mathbf{r}$ since ψ evolves unitarily as $\exp\left(-i\frac{H}{\hbar}t\right)$. The energy terms on the right hand side can be identified in order as the kinetic energy associated with the local motion of the condensate, the external potential energy, the mean field interaction energy, and the so called 'quantum pressure' term which is the dynamical equivalent to the zero point kinetic energy term in the time independent Gross Pitaevski equation 5.2.

As with the time independent theory, the Thomas Fermi limit can be taken, neglecting the final term in eq.(5.24). Since the velocity field is proportional to the gradient of the phase, taking the gradient of eq.(5.24) gives an equation for the evolution of $\mathbf{v}(\mathbf{r},t)$. The two coupled hydrodynamic equations are

$$m\frac{\partial\mathbf{v}}{\partial t} + \nabla\left(\frac{1}{2}m\mathbf{v}^2 + V + gn\right) = 0 \tag{5.25}$$

$$\frac{\partial n}{\partial t} + \nabla \cdot \mathbf{J} = 0 \tag{5.26}$$

Together these equations describe the dynamics of the condensate in the Thomas Fermi limit. For $\mathbf{v} = 0$, eq.(5.25) reduces to the stationary density profile in this limit given by eq.(5.7).

Apart from the trivial $\mathbf{v} = 0$ case, these non-linear coupled equations are difficult to solve numerically. For small variations they can be solved in the linearised limit, where the density is taken as $n(\mathbf{r}, t) = n_0(\mathbf{r}) + \delta n(\mathbf{r}, t)$, and $n_0(\mathbf{r})$ is the stationary ground state density in the Thomas Fermi limit eq.(5.7). Substituting into the hydrodynamic equations and keeping terms at most linear in $\delta n(\mathbf{r}, t)$ leads to the equation

$$\frac{\partial^2}{\partial t^2}\delta n(\mathbf{r}, t) = \nabla \cdot c(\mathbf{r})^2 \nabla \delta n(\mathbf{r}, t) \qquad \text{where } c(\mathbf{r})^2 = g n_0(\mathbf{r})/m. \tag{5.27}$$

This equation is separable in time and space, and since it is second order in the time derivative gives solutions oscillating in time. For a condensate of uniform density, $c(\mathbf{r})$ is constant, and eq.(5.27) describes density waves, or phonons that propagate with phase velocity (sound velocity) c. For non-uniform density, the sound velocity varies across the condensate. The eigenvalues of the spatial equation define the spectrum of the oscillator frequencies.

5.2.3 Axial Monopole and Dipole Modes

The spatial solutions of eq.(5.27) can be separated into a radial part expressed by polynomial $P^n(r)$, and an angular part expanded in spherical harmonics $Y_l^m(\theta, \phi)$. In our experiment we are able to excite the $l = 2$, $m = 0$ 'breathing' mode through modulation of the axial trap frequency ω_z. The eigenfrequency ω_b of the breathing mode can be found from the linearised equation, eq.(5.27). In the limit $\omega_z \ll \omega_r$, which is amply satisfied for our trap, it is given by

$$\omega_b^2 = \frac{5}{2}\omega_z^2 \tag{5.28}$$

The dipole modes which correspond to centre of mass oscillations can also be found from eq.(5.27) or alternatively by Kohn's theorem in harmonic traps. These have oscillation frequency ω_i in the i^{th} direction. This can be easily understood from the fact that in a harmonic trap the gradient of the restoring force is the spring constant of the trap $m\omega_i^2$. Therefore the forces on the condensate in its centre of mass frame are the same as those when it is at rest. Subsequently the

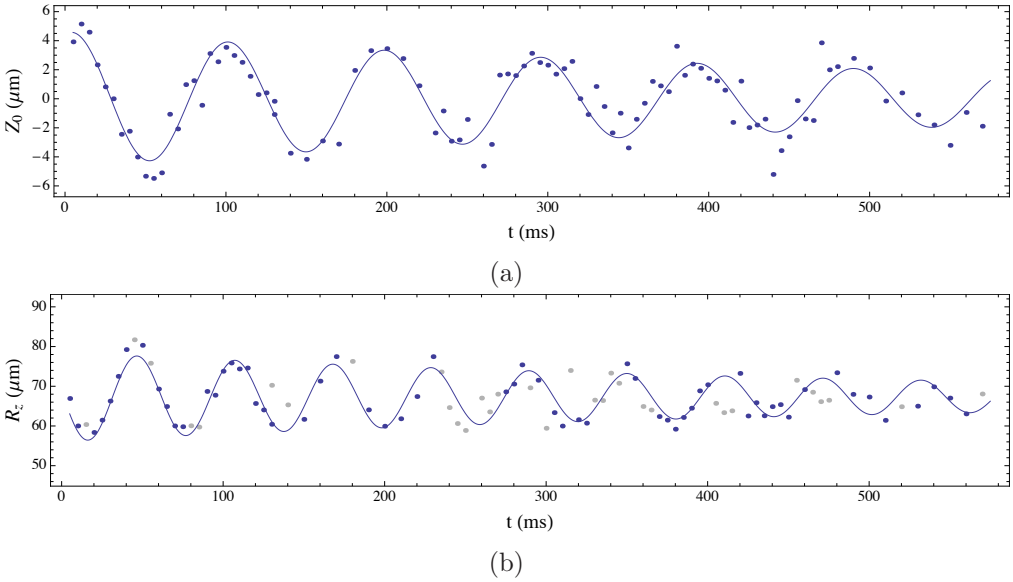

Figure 5.3: Collective oscillations of our condensate in the axial direction. Figure 5.3a shows measurements the condensate centre of mass (data points) as a function of time after centre of mass oscillations were excited. To these we fit an exponentially damped sinusoidal function. The frequency of this fitted function gives us an oscillation frequency of $\omega_z = 2\pi(10.3 \pm 0.1)$ Hz Figure 5.3b shows measurements of the breathing mode oscillations (datapoints). As for the centre of mass oscillations, we fit a damped sinusoid to the data and found a frequency of $\omega_b = 2\pi(16.5 \pm 0.1)$ Hz. Since the frequency of the breathing mode is effected by the atom number, we post selected data points that we fit the sinusoid to based on the measured atom number. We only included data points in the fit for which the atom number is between 8.2×10^3 and 1.18×10^4, which corresponds to a range of standard deviation from the mean value of 10^4 atoms. These data points are shown in blue in fig.5.3b, while the data points where the atom number lies outside this range are shown in grey.

shape of the condensate is not distorted in any way as its centre of mass oscillates. Conversely the forces from the mean field and quantum pressure at position $\mathbf{r}'$ in the centre of mass frame are constant. Condensed atoms experience no variation in force other than that of the external potential as they oscillate. They therefore oscillate at the frequencies of the trap.

Figure 5.3 shows experimental measurements of these two axial modes for our condensates. The axial dipole oscillations are excited by sinusoidal variation of the trap centre in the axial direction close to the axial frequency. The axial breathing mode is excited by sinusoidal compression of the axial potential with frequency close to its resonance $\sqrt{5/2}\omega_z$. In both cases we drive the oscillations for two periods, returning to their initial unperturbed value where they remain thereafter. The centre of mass or length are measured at later time t. This is repeated to build up a set of data in which we observe these oscillations. From these we measure

the frequencies of these centre of mass and breathing modes to be $10.3 \pm 0.1\,\mathrm{Hz}$ and $16.7 \pm 0.1\,\mathrm{Hz}$ respectively. These errors are based on the standard error in the frequency in the model $Ae^{-\gamma t}\sin(2\pi f t + \phi) + B$, which was fitted to the data.[2] The ratio $\omega_b/\omega_z = 1.6 \pm 2$, which is in close agreement to the prediction of 1.58 from eq.(5.28) for these modes in the 3D Thomas Fermi regime.

As the trap potential is further elongated, the Thomas Fermi approximation becomes poor, and the linearised hydrodynamic equation eq.(5.27) is no longer valid. By contrast, the full hydrodynamic equations do not neglect the kinetic terms of the Gross Pitaevskii equation, so these are able to predict the behaviour of the ratio ω_b/ω_z in this regime in [120]. They predict that $\omega_b/\omega_z \to 2$ in the long thin limit. Measurements have been made through the crossover regime in [35, 36] and show good agreement with the theoretical predictions. Our result shows that our condensate is close to that predicted in the 3-D Thomas Fermi limit as far as the oscillation frequencies are concerned.

5.3 Expansion of the Condensate after Release from Trap

To understand the expansion of the condensate when it is released from the trap, we consider solutions of the hydrodynamic equations when the trap potential is scaled in time by the three trap frequencies $\omega_x(t)$, $\omega_y(t)$ and $\omega_z(t)$,

$$U(\mathbf{r}, t) = \frac{1}{2}\sum_{i=1}^{3}\omega_i^2(t)x_i^2. \tag{5.29}$$

It is shown by [121] that for time dependent potentials of this form a general solution for the Thomas Fermi density $n(\mathbf{r}, t)$ exists that is also scaled in time. This scaled solution is characterised by the scaled condensate radii, $R_i(t) = a_i(t)R_i(t_0)$, where

[2] To fit this, we used the 'NonlinearModelFit' function in Mathematica, and assumed that all data points in the oscillation datasets had equal weights.

$R_i(t_0) = \sqrt{2\mu/m\omega_i(t_0)^2}$. These solutions have the form

$$n(\mathbf{r},t) = n_0(t)\left(1 - \sum_{i=1}^{3} \frac{x_i^2}{R_i^2 a_i(t)^2}\right) \tag{5.30}$$

$$v(\mathbf{r},t) = \sum_{i=1}^{3} \gamma_i(t) x_i \tag{5.31}$$

where γ_i are a set of three scale factors for the cartesian coordinates that are related to the a_i in a way that is to be established. A system of coupled differential equations for the scaling parameters $a_i(t)$ and $\gamma_i(t)$ are found by substituting eq.(5.30) and eq.(5.31) into the hydrodynamic equations, eq.(5.25) and eq.(5.26).

First, the normalisation of $n(\mathbf{r},t)$ to N gives the relation for $n_0(t)$

$$n_0(t) = \frac{n_0(t_0)}{a_x(t)a_y(t)a_z(t)} \qquad \text{with } n_0(t_0) = \frac{8\pi N}{15 R_x R_y R_z}. \tag{5.32}$$

Next substituting 5.30 and 5.31 into the continuity equation 5.26, dividing by n_0 and setting the $x_i = 0$ gives the relationships

$$\gamma_i = \frac{\dot{a_i}}{a_i}. \tag{5.33}$$

The scaling solutions are now in terms of the single set of parameters $\{a_i\}$. Substituting this pair into 5.25 gives the coupled differential equations

$$\ddot{a_i} + \omega_i^2(t) a_i - \frac{\omega_i^2(t_0)}{a_i a_x a_y a_z} = 0 \tag{5.34}$$

These equations relate the components of the force on a volume element from which the $\ddot{a}$ term arises, to the trap potential and density gradient from which the second and third terms arise.

In the sub-section below measure the the expansion of a condensate after it released from our trap. We use the scaling solutions given here to describe the evolution of the condensate density as it expands.

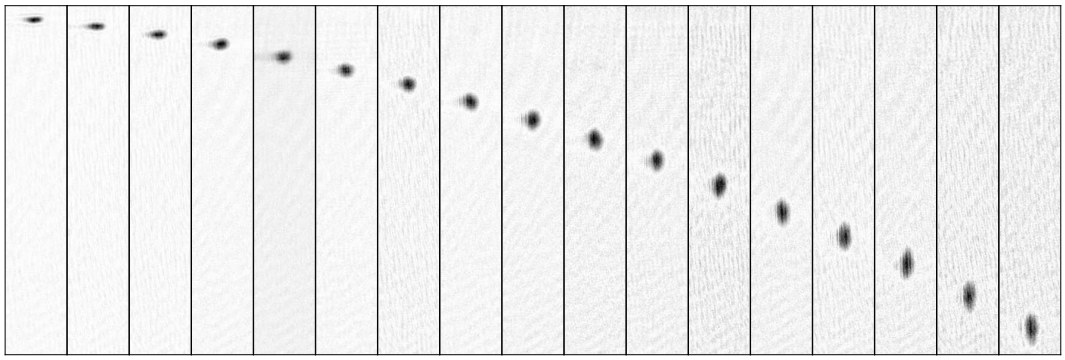

Figure 5.4: Absorption images of the condensate from 1 ms to 17 ms time of flight after release from the magnetic trap. This shows the distinct characteristic of a BEC, where the initial aspect ratio is inverted as the condensate expands. The height of each panel is 2 mm.

5.3.1 Expansion of our condensate

After a condensate is released from an anisotropic trap, the scaling theory can be used to show that the initial aspect ratio $\lambda = R_i/R_j$ of the trapped condensate (radii R_i) is inverted as it expands. This is in stark contrast to the ballistic expansion of a thermal cloud. A thermal cloud in equilibrium has the asymptotic behaviour $\lim_{t\to\infty} \lambda \to 1$ since the momentum distribution is isotropic. A change in aspect ratio is therefore a key signature of a BEC. In fig.5.4 which we discuss below, we show the change in aspect ratio observed in our experiment after the condensate is released from the trap.

For low atom number, the ground state energy is primarily the potential energy and the kinetic energy $\langle p_i^2\rangle/2m$, where $\langle p_i^2\rangle$ is the expectation value of momentum in the direction x_i. Once the trap is turned off, the potential energy is zero and the cloud expands. In an anisotropic trap the values $\sqrt{\langle p_i^2\rangle}$ in each direction are inversely proportional to the cloud widths as a direct consequence of Heisenberg's uncertainty principle $\sqrt{\langle p_i^2\rangle} \sim \hbar/\langle x_i\rangle$. Once released the cloud expands faster in the direction where the initial width is narrowest, hence inverts the aspect ratio. For large atom number, the aspect ratio is also reversed. For a short time after release the density is still high and the interaction energy is important. The gradient in the condensate density produces a gradient in the interaction energy, resulting in a force that accelerates the expansion of the cloud. In an anisotropic trap, the acceleration is greatest in the direction with the tightest initial confinement, and

therefore highest density gradient.

In the TF limit the expansion of the condensate after the trap is turned off is described by the scaling solutions 5.34 to the hydrodynamic equation. Prior to releasing the condensate, $t < t_0$, the trap frequencies are constant, and set to the values found in our experiment, $\omega_3 = \omega_z$ and $\omega_1 = \omega_2 = \omega_r$. We also assume that the condensate is stationary before release, such that $a_i(t < t_0) = 1$. At the time of release t_0, ω_i are suddenly set to zero (we set $t_0 = 0$ without loss of generality). Written in terms of $\tau = \omega_r t$ and $\lambda = \omega_z/\omega_r$, the equations eq.(5.34) for $a_z(\tau)$ and $a_r(\tau)$ become,

$$\frac{\mathrm{d}^2}{\mathrm{d}\tau^2} a_z(\tau) = \frac{\lambda^2}{a_z(\tau)^2 a_r(\tau)^2}, \tag{5.35}$$

$$\frac{\mathrm{d}^2}{\mathrm{d}\tau^2} a_r(\tau) = \frac{1}{a_z(\tau) a_r(\tau)^3}, \tag{5.36}$$

for $\tau > 0$. These have been solved analytically when $\lambda \ll 1$ in [121]. In this case, one first takes $a_z(\tau)$ to zeroth order in λ in 5.36 where $a_z(\tau) = 1$. Equation 5.36 is then decoupled and simplified, and has solution

$$a_r(\tau) = \sqrt{1 + \tau^2}. \tag{5.37}$$

After release, the condensate aspect ratio is given by the scaled Thomas Fermi radii,

$$\lambda(\tau) = R_z(\tau)/R_r(\tau) \tag{5.38}$$

$$= \frac{\lambda(0)}{\sqrt{1 + \tau^2}}, \tag{5.39}$$

where in the second line, eq.(5.37) has been used. For initial values $\lambda \ll 1$ as found in our trap, expanding eq.(5.39) with respect to $1/\tau$ shows that the condensate aspect ratio reaches 1 at time $t = 1/\omega_z$ after release from trap.

The solution eq.(5.37) for $a_r(\tau)$ can also be used to find a more accurate solution to 5.35,

$$a_z(\tau) = 1 + \lambda^2 \left(\tau \arctan \tau - \ln \sqrt{1 + \tau^2} \right). \tag{5.40}$$

For our trap parameters, this solution shows that the expansion of our condensates in the axial direction is negligible over the times scale $\tau \lesssim 1$ for which we observe

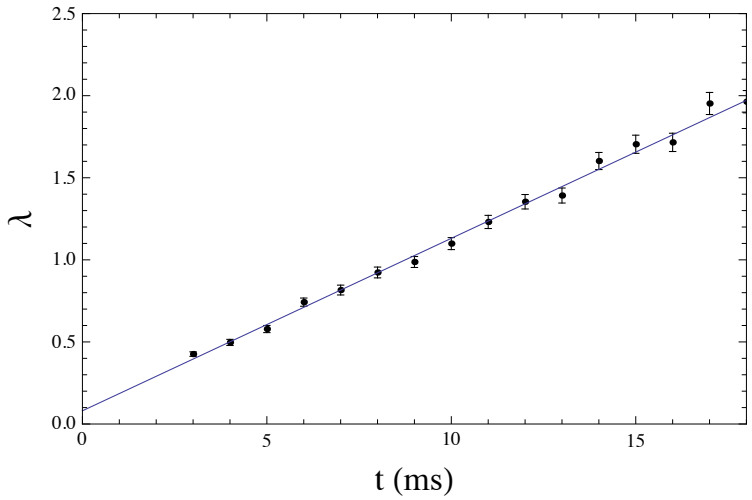

Figure 5.5: Aspect ratio of BEC radii $\lambda = R_r/R_z$, after release from trap, for the same data shown in figure 5.4. The data points show the aspect ratio of the condensate measured from the absorption images. The radii were measured by fitting a Thomas Fermi density profile 5.7 to the cloud. The errors are dominated by the shot to shot variations in the cloud widths due to atom number fluctuations, and noise in the measured density profiles that affect the accuracy of the TF fits. The blue line is a straight line fitted to these data points.

the condensate expanding.

The scaling solutions eq.(5.37) and eq.(5.35) assume that the condensate is well described in the Thomas Fermi limit. Our condensates are highly elongated and this is not strictly true. However, even though the radial wave function of a highly elongated condensate has a significant tail (up to surface depth δ) not described in this limit, the bulk of the condensate has a density distribution still well approximated in the Thomas Fermi limit. The hydrodynamic theory therefore still describes this part of the condensate well.

Figure 5.4 shows absorption images of condensates after they have been released from the trap and allowed to expand for a time between 2 and 18 ms. In the first image on the left, the condensate is narrow in the vertical direction and long in the horizontal direction due to the elongated shape of our trap potential. In the final image on the right of fig.5.4, the aspect ratio of the condensate has reversed, with its width in the vertical direction greater than its horizontal length.

We are also able to measure this expansion quantitatively by measuring the Thomas-Fermi radii $R_r(t)$ and $R_z(t)$ from theses images. First we extracted the

density profiles $n(y) = \int \mathrm{d}x\mathrm{d}z\ n(\mathbf{r})$ and $n(z) = \int \mathrm{d}y\mathrm{d}z\ n(\mathbf{r})$ by summing over the pixels in the horizontal and vertical directions respectively. We then fit the Thomas-Fermi profile eq.(5.8) to the profiles we measure, using the Thomas-Fermi radii $R_r(t)$ and $R_z(t)$ as fit parameters. Figure 5.5 shows the measured values of $\lambda = R_r(t)/R_z(t)$, which are in good agreement with the theoretical predictions. For the typical axial trap frequencies of our traps which range from 8 to 18 Hz, axial density of the condensate has expands by approximately 1% after 33.5 ms down to 6.8 ms respectively. Thus for our traps the axial expansion can be ignored. After the first ms, it is also predicted that the transverse expansion of the condensate density is highly linear. Thus the aspect ratio of the condensate in our experiment is expected to increase linearly for $t \gtrsim$ 1ms, just as we find in fig.5.5. In this figure we have therefore fit a straight line through the data points. This gradient of the line suggests that the axial frequency of our trap is close to 18.9 ± 0.5 Hz. In this fragment we measured an axial centre of mass oscillation frequency of 17 ± 0.1 Hz. This disagreement between these results is likely to be due to the anharmonicity in this fragment.

Chapter 6

Trapped Atoms in RF Fields

In addition to the static magnetic potential, we use rf fields to manipulate atoms whilst in the magnetic trap. The rf field interacts magnetically with the atoms, coupling the Zeeman sub levels $|m_{\rm F}\rangle$ of the ($^5{\rm S}_{1/2}$, $F = 2$) ground state. As with the static field, this interaction is well described in the dipole approximation $V = g_{\rm f}\mu_{\rm B}\mathbf{F}\cdot\mathbf{B}_{\rm rf}(\mathbf{r},t)$. For rf fields however, it is useful to consider the state of the atom and field together,

$$|n, m_{\rm F}\rangle = |n\rangle \otimes |m_{\rm f}\rangle \tag{6.1}$$

where $|n\rangle$ are rf photon Fock states, and $\otimes$ designates the tensor product. The Hamiltonian must therefore include the energy contributions from both the atom and field, and the coupling between them. The eigenstates of this Hamiltonian are referred to as the states of the atom dressed by the field, or 'dressed states'.

In the absence of an interaction, the Hamiltonian is just the field energy and the atom's energy:

$$H_0 = \hbar\omega(\mathbf{a}^\dagger\mathbf{a} + \frac{1}{2}) + \hbar\omega_0 F_z, \tag{6.2}$$

where ω is the frequency of the rf field, and $\hbar\omega_0 = g_{\rm F}\mu_B B_0(\mathbf{r})$ the Zeeman splitting due to the static magnetic field with $B_0(\mathbf{r}) = |\mathbf{B}_0(\mathbf{r})|$. The operators $\mathbf{a}_k$ and $\mathbf{a}_k^\dagger$ annihilate and create photons in mode k respectively. The rf field is assumed to be single mode here, so the subscript k is dropped. The eigenstates of H_0 are just the $|n, m_{\rm f}\rangle$ of eq.(6.1). Figure 6.1 depicts the infinite ladder of states these form. It is composed of manifolds $\mathscr{E}(N)$, each containing the five states for which $m_{\rm F} + n = N$.

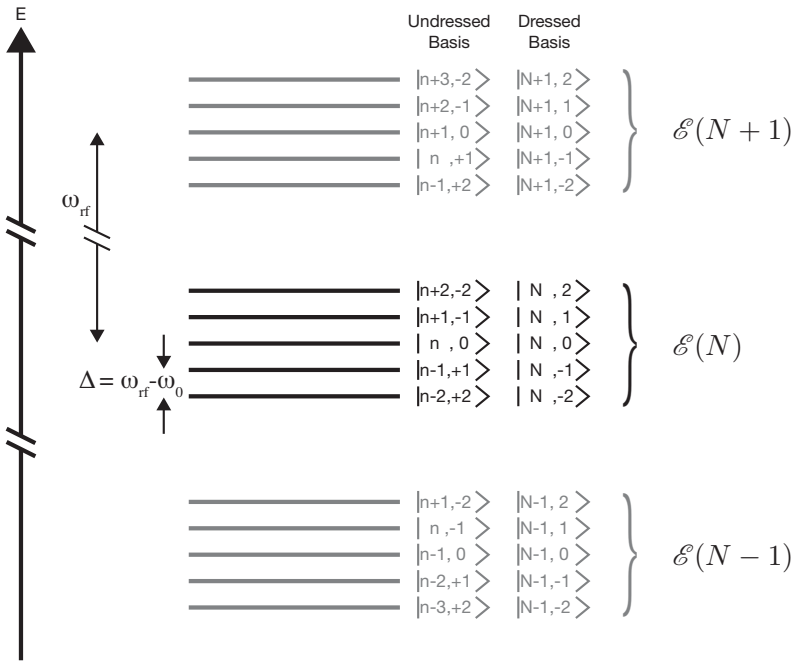

Figure 6.1: Dressed states of the atom and rf field in the absence of any interaction.

In the dressed basis these states are labelled $|N, \tilde{m}_{\rm F}\rangle$. Without coupling, the levels within each manifold are separated by energy differences of $\Delta E = \hbar\Delta$, where

$$\Delta = \omega - \omega_0, \tag{6.3}$$

is the detuning of the rf frequency from the bare resonance frequency. The effect of the coupling V is to increase the splitting ΔE.

By introducing an interaction which couples the dressed states $|N\tilde{m}_{\rm F}\rangle$, their energy can be shifted. For atoms in an rf field, the interaction is the dipole interaction

$$V = \mathbf{g}_F \mu_B \mathbf{F} \cdot \mathbf{B}_{\rm rf}, \tag{6.4}$$

where $\mathbf{F}$ is the vector operator of atoms angular momentum, and $\mathbf{B}_{\rm rf}$ the vector of the magnetic component of the rf field. The energy shift of the dressed states is a function of the detuning Δ, and magnitude of the rf field. In our experiment, both Δ and the rf field strength can be setup to vary spatially in the region where the atoms sit, thus altering the shape of the potential in which they are trapped.

To calculate the interaction eq.(6.4), we first write the rf field $\mathbf{B}_{\rm rf}$ in terms of its component $\mathbf{B}_z$ along the direction $\hat{\mathbf{z}}$, and its components in the $x-y$ plane in

terms of an anti-clockwise rotating part $\mathbf{B}_a$, and a clockwise rotating part $\mathbf{B}_c$. In the cartesian basis $(\hat{\mathbf{x}}, \hat{\mathbf{y}}, \hat{\mathbf{z}})$ these components are

$$\begin{aligned}
\mathbf{B_z} &= |\beta_z| \cos(\omega t + \phi_z)\hat{\mathbf{z}} \\
\mathbf{B_a} &= |\beta_a| \left[\cos(\omega t - \phi_a)\hat{\mathbf{x}} - \sin(\omega t - \phi_a)\hat{\mathbf{y}}\right] \\
\mathbf{B_c} &= |\beta_c| \left[\cos(\omega t + \phi_c)\hat{\mathbf{x}} + \sin(\omega t + \phi_c)\hat{\mathbf{y}}\right], \qquad (6.5)
\end{aligned}$$

where β_z, β_a and β_c are the amplitudes of these components, $\phi_z = \mathrm{Im}(\beta_z), \phi_a = \mathrm{Im}(\beta_a)$ and $\phi_c = \mathrm{Im}(\beta_c)$ their phase, and ω the rf frequency. We also write the angular momentum operator $\mathbf{F} = F_x\hat{\mathbf{x}} + F_y\hat{\mathbf{y}} + F_z\hat{\mathbf{z}}$, in terms of the three components

$$F_\pm = F_x \pm iF_y, \qquad \text{and } F_z. \qquad (6.6)$$

At this point it makes sense to choose the unit vector $\mathbf{z}$ in eq.(6.5) and eq.(6.6) such that it points along the same direction as the local static magnetic field $\hat{\mathbf{z}} = \mathbf{B}_0(\mathbf{r})/|\mathbf{B}_0(\mathbf{r})|$ at $\mathbf{r}$. This ensures the operator F_z measures the same projection of the angular momentum used in the uncoupled basis eq.(6.1).[1] Next, the interaction (eq.(6.10)) is expanded by decomposing the $\mathbf{F}$ and $\mathbf{B}_{\mathrm{rf}}$ in the spherical basis $\{\hat{e}_{+1}, \hat{e}_{-1}, \hat{e}_0\}$ (see, for example [122]),

$$\hat{e}_{\pm 1} = \frac{\mp 1}{\sqrt{2}}\left(\hat{\mathbf{x}} \pm i\hat{\mathbf{y}}\right), \qquad \hat{e}_0 = \hat{\mathbf{z}}. \qquad (6.7)$$

The scalar product of two vectors in this basis is $\mathbf{A} \cdot \mathbf{B} = -a_{+1}b_{-1} - a_{-1}b_{+1} + a_0 b_0$. In the spherical basis,

$$\mathbf{F} = \left\{\frac{-1}{\sqrt{2}}F_+,\ \frac{1}{\sqrt{2}}F_-,\ F_z\right\} \qquad (6.8)$$

and the rf field in second quantised form is

$$\mathbf{B}_{\mathrm{rf}} = \left\{\frac{-1}{\sqrt{2n}}\left(\beta_a\mathbf{a}^\dagger + \beta_c\mathbf{a}\right),\ \frac{1}{\sqrt{2n}}\left(\beta_a^*\mathbf{a} + \beta_c^*\mathbf{a}^\dagger\right),\ \frac{1}{2n}\left(\beta_z\mathbf{a}^\dagger + \beta_z^*\mathbf{a}\right)\right\} \qquad (6.9)$$

where n is the number in the rf field. Finally, the interaction can be rewritten in a

[1] A consequence of this choice for $\hat{\mathbf{z}}$ means that for a uniform rf field in the lab frame will have spatially dependent components in this local basis. This effect is exploited to change the shape of the rf dressed trap potential the atom experiences, as discussed in sec.6.1 below.

relatively simple expanded form,

$$V = \frac{g_{\rm F}\mu_{\rm B}}{2\sqrt{n}}\left[\beta_a^* F_+\mathbf{a} + \beta_c^* F_-\mathbf{a} + \beta_z^* F_z\mathbf{a} + \beta_a F_-\mathbf{a}^\dagger + \beta_c F_+\mathbf{a}^\dagger + \beta_z F_z\mathbf{a}^\dagger\right] \qquad (6.10)$$

The first and fourth terms are the near resonant coupling terms. They contain the operator products $\mathbf{aF}_+$ and $\mathbf{a}^\dagger\mathbf{F}_-$ which couple states only within each manifold $\mathscr{E}(N)$. Terms containing $\mathbf{aF}_z$ and $\mathbf{a}^\dagger\mathbf{F}_z$ couple manifolds with $\Delta N = \pm 1$, while those containing $\mathbf{aF}_-$ and $\mathbf{a}^\dagger\mathbf{F}_+$ couple manifolds with $\Delta N = \pm 2$.

The Hamiltonian $H = H_0 + V$ as defined by eq.(6.1) and eq.(6.10), can be simplified further by making the rotating wave approximation (RWA), where we keep only the near resonant terms and work with the Hamiltonian

$$H_{\rm rwa} = g_{\rm F}\mu_{\rm B}\left[B_0 F_z + \frac{1}{2\sqrt{n}}\left(\beta_a^* F_+\mathbf{a} + \beta_a F_-\mathbf{a}^\dagger\right)\right], \qquad (6.11)$$

where B_0 is the magnitude of the static magnetic field. We have also ignored the rf field energy $(\mathbf{a}^\dagger\mathbf{a} + \frac{1}{2})\hbar\omega$, which is essentially the same for all dressed atoms since the photon number fluctuations are small $\sqrt{\langle n^2\rangle} \ll \langle n\rangle$.

By making the rotating wave approximation, the system of many manifolds $\mathscr{E}(N)$ in fig.6.1 has been simplified to a single sub-system of just $2F+1$ states. The Hamiltonian eq.(6.11) can be written in terms of a small number of matrix elements. In the eigenbasis of H_0, the diagonal matrix elements of $H_{\rm rwa}$ are $m_{\rm F}\hbar\Delta$ (eq.(6.3)), and the off-diagonal terms due to the interaction are

$$\langle n-1, m_{\rm F}+1|\, H_{\rm rwa}\,|n, m_{\rm F}\rangle = \frac{g_{\rm F}\mu_{\rm B}}{2\sqrt{n}}\beta_a^*\sqrt{n}\sqrt{(F-m_F)(F+m_F+1)},$$
$$\langle n+1, m_{\rm F}-1|\, H_{\rm rwa}\,|n, m_{\rm F}\rangle = \frac{g_{\rm F}\mu_{\rm B}}{2\sqrt{n}}\beta_a\sqrt{n+1}\sqrt{(F+m_F)(F-m_F+1)},$$

where the factors $\sqrt{(n \pm m_F)/n}$ have been set to 1 since $n \gg F$. Defining the Rabi frequency as

$$\Omega = \frac{g_{\rm F}\mu_{\rm B}}{\hbar}\beta_a \qquad (6.12)$$

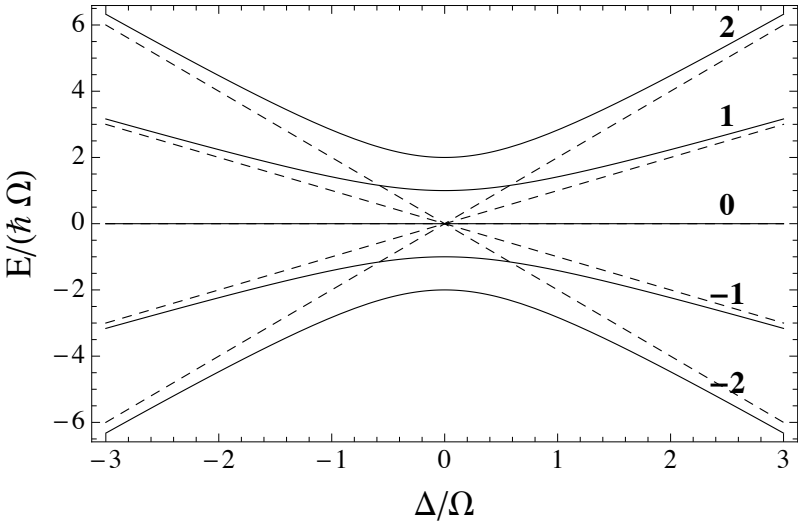

Figure 6.2: Effect of detuning $\Delta = \omega - \omega_0$ on the energy of rf dressed atoms. The solid line shows the energy of the dressed states with $\tilde{m}_{\rm F}$ as numbered. The dashed line shows the energy of the bare atomic states with $m_{\rm F}$ also as numbered on the right. The rf frequency is constant, but ω_0 is scanned over the range $\omega \pm 3\Omega$. The detuning Δ, and energy E, are shown in dimensionless units of Δ/Ω and $E/\hbar\Omega$ respectively. At $\Delta = 0$, where the bare states cross, the dressed states are separated by energy $\hbar\Omega$.

the matrix for $H_{\rm rwa}$ can be written in this basis as

$$H_{\rm rwa} = \hbar \begin{pmatrix} 2\Delta & \Omega & 0 & 0 & 0 \\ \Omega^* & \Delta & \sqrt{\frac{3}{2}}\Omega & 0 & 0 \\ 0 & \sqrt{\frac{3}{2}}\Omega^* & 0 & \sqrt{\frac{3}{2}}\Omega & 0 \\ 0 & 0 & \sqrt{\frac{3}{2}}\Omega^* & -\Delta & \Omega \\ 0 & 0 & 0 & \Omega^* & -2\Delta \end{pmatrix} \tag{6.13}$$

The matrix is straightforward to diagonalise to find the eigenstates and energies of $H_{\rm rwa}$. The new eigenstates $\{|\tilde{m}_{\rm F}\rangle$ are labelled by quantum number $\tilde{m}_{\rm F}$, and have energies,

$$E_{\tilde{m}_{\rm F}} = \tilde{m}_{\rm F}\hbar\sqrt{\Delta^2 + \Omega^2}. \tag{6.14}$$

In our experiment, where the rf frequency ω is constant but $\omega_0 = g_{\rm F}\mu_{\rm B}B_0(\mathbf{r})$ varies with $\mathbf{r}$, the detuning Δ also varies. Figure 6.2 shows the energy of the bare states $|m_{\rm F}\rangle$, and the energy of the dressed states $|\tilde{m}_{\rm F}\rangle$ as a function of Δ as ω_0 is varied between $\omega - 3\Omega$ and $\omega + 3\Omega$. The bare state energies (dashed lines) cross where $\Delta = 0$, but the energy of the dressed states (solid lines) are forced apart by the coupling, separated from each other by energy $\hbar\Omega$. In the limit where $|\Delta|$ is large

compared to Ω, the energies of the dressed states approach those of the undressed states. Since the bare states cross at $\Delta = 0$ but the dressed states do not, for $\Delta < 0$, the state $|\tilde{m}_{\rm F}\rangle$ approaches the state $|-m_{\rm F}\rangle$, and for $\Delta < 0$, $|\tilde{m}_{\rm F}\rangle$ approaches $|m_{\rm F}\rangle$.

In addition to the detuning varying in our trap, the Rabi frequency Ω also varies even though the rf field we apply is constant in magnitude and polarisation over the region where the atoms are trapped. The magnitude of the Rabi frequency depends on the magnitude β_a, which was defined in eq.(6.5) as the anticlockwise component of the rf field in the $x-y$ plane. However the $x-y$ plane is defined such that $\hat{\mathbf{x}} \times \hat{\mathbf{y}} = \mathbf{B}_0(\mathbf{r})/B_0(r)$, so it rotates along with the direction of the local static field. This causes a variation in β_a. In our trap, β_a and therefore Ω tend to be largest in the centre of the trap where $\mathbf{B}_{rf}$ oscillates in the $x-y$ plane, and weaker further out where there is a large projection of $\hat{\mathbf{z}} \cdot \mathbf{B}_{rf}$. This effect is described detail in the next section, in which we discuss how the rf field effects the shape of our trap potential.

6.1 RF Dressed Trap Potential

Atoms dressed by the rf field sit in the potential

$$U(\mathbf{r}) = \tilde{m}_F \hbar \sqrt{\Delta(\mathbf{r})^2 + |\Omega(\mathbf{r})|^2}. \tag{6.15}$$

Control of Δ and Ω allow us to manipulate the shape of the trap: We can control the ratio of the transverse trap frequencies ω_x/ω_y; smooth out the axial potential by reducing its dependence on the variation of the axial static field; and split the condensate into two parts.

In our experiment we trap atoms in this way using the static fields described in sec.3.3, and an rf field that is uniform in the laboratory reference frame:

$$\mathbf{B}_{\rm rf}(\mathbf{r}, t) = B_{\rm rf} \cos(\omega_{\rm rf} t + \phi_0)\hat{\mathbf{y}}. \tag{6.16}$$

To calculate the dressed potential (eq.(6.15)) we must find how Δ and Ω vary with $\mathbf{r}$. We begin by considering $\Delta(\mathbf{r})$. Since the rf frequency is constant, the spatial

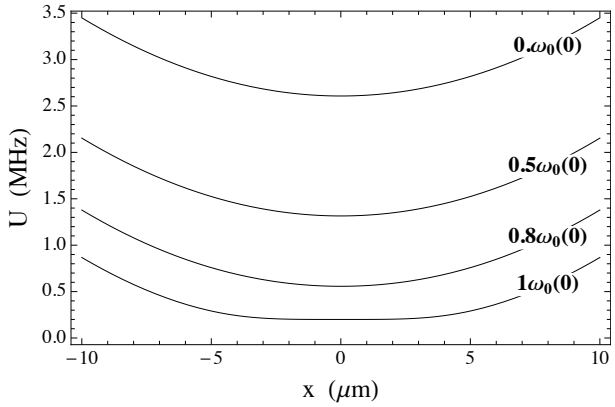

(a)

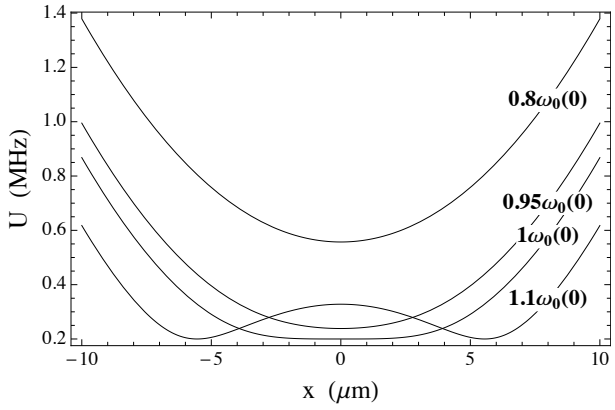

(b)

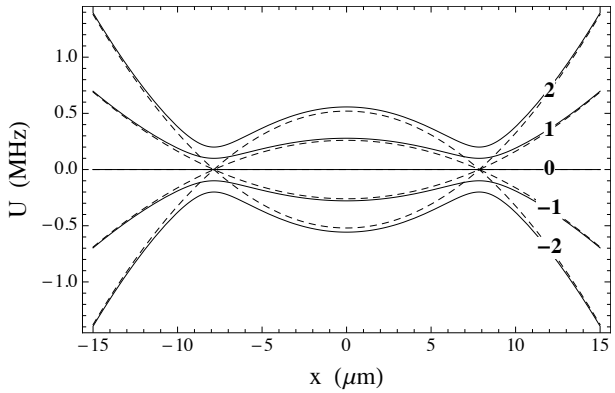

(c)

Figure 6.3: Change in the shape of the potential at various different rf frequencies close to $\omega_0(0)$, which is the minimum Zeeman splitting between the bare atomic states. Figure 6.3a shows the dressed potential over a wide range of $\omega_{rf} \leq \omega_0(0)$, illustrating minimal shape distortion to $U_s(x)$ when ω_{rf} is small. Figure 6.3b shows the dressed potential when ω_{rf} is close to $\omega_0(0)$, where its shape is significantly altered. These potentials were calculated from eq.(6.15) and eq.(6.17), with a constant Rabi frequency $\Omega/2\pi = 100\,\text{kHz}$, and a radial trap frequency of 1.4 kHz. Figure 6.3c shows the dressed states of H_{RWA} (solid lines) and the bare states of H_0 (dashed lines) for $\omega_{\text{rf}} = 1.2\omega_0(0)$, where the dressed potential ($U(x)$) is a double well. Number on the right indicate $\tilde{m}_{\text{F}}$ for the dressed states and m_{F} for the bare states.

dependence of Δ comes from ω_0. For our static field harmonic trap potential $U_s(\mathbf{r}) = \frac{1}{2}m(\omega_r^2(x^2+y^2)+\omega_z^2 z^2)+U_0$, which we have characterised for atoms trapped in the state $m_\mathrm{F}=2$, we find that $2\hbar\omega_0(\mathbf{r}) = U_s(\mathbf{r})$. Thus

$$\omega_0(\mathbf{r}) = \frac{m}{4\hbar}(\omega_r^2(x^2+y^2)+\omega_z^2 z^2)+\frac{U_0}{2\hbar} \tag{6.17}$$

where $U_0/2 = g_\mathrm{F}\mu_\mathrm{B}B_0 = \hbar\omega_0(0)$ is the (Zeeman) energy splitting between the m_F states at the trap bottom.

It is insightful to look first at the shape of the rf dressed potential caused by this spatial dependence of $\Delta(\mathbf{r}) = \omega_{rf}-\omega_0$, before going on to look at the $\Omega(\mathbf{r})$. Figure 6.3 shows the rf dressed potentials given by this spatial dependence of $\Delta(x)$, while the Rabi frequency is kept constant across the trap at $\Omega/2\pi = 100\,\mathrm{kHz}$. Figure 6.3a shows the dressed potential with $\omega_{rf} = \omega_0(0),\ 0.8\omega_0(0),\ 0.5\omega_0(0)$, as well as $\omega_{rf} = 0\omega_0(0)$ in which case the potential is just the static trap potential. From these, it is clear that when ω_{rf} is much less than $\omega_0(0)$ (e.g. $0.5\omega_0(0)$), the shape of the dressed potential is almost the same as the static potential, and the rf just lowers the energy of the trap minimum. When ω_{rf} is close to $\omega_0(0)$, the shape of the dressed potential changes significantly. Figure 6.3b shows the potential for several values of ω_{rf}, close to $\omega_0(0)$. As ω_{rf} approaches $\omega_0(0)$ from below, it widens the bottom of the potential. For $\omega_{rf} = \omega_0(0)$ the bottom of the potential is almost completely flat over several μm. For $\omega_{rf} > \omega_0(0)$, the potential is split into a double well. Figure 6.3c shows that the reason this double well occurs is because the crossings of the uncoupled states of H_0 (eq.(6.2)), located either side of $x=0$, are turned into anti-crossings by the interaction V. In the central region, the highest energy dressed state, $\tilde{m}_\mathrm{F}=2$ is similar to the uncoupled state $m_F=-2$, with which its overlap is large. In the outer region, $|\tilde{m}_\mathrm{F}=2\rangle$ is similar to $|m_\mathrm{F}=2\rangle$ instead.

We now consider the effect of the spatial variation of $\Omega(\mathbf{r})$ as well as $\Delta(\mathbf{r})$ on our trap potential. Equation 6.12 shows that Ω is proportional to the anticlockwise component of the rf field in the plane normal to $\hat{\mathbf{z}} = \mathbf{B}_0(\mathbf{r})/B_0(\mathbf{r})$:

$$\beta_a = \frac{i}{\sqrt{2}}\frac{|B_\mathrm{rf}\times\mathbf{B}_0(\mathbf{r})|}{|\mathbf{B}_0(\mathbf{r})|}. \tag{6.18}$$

Our static magnetic trap can be well approximated by a 2d quadrupole field in

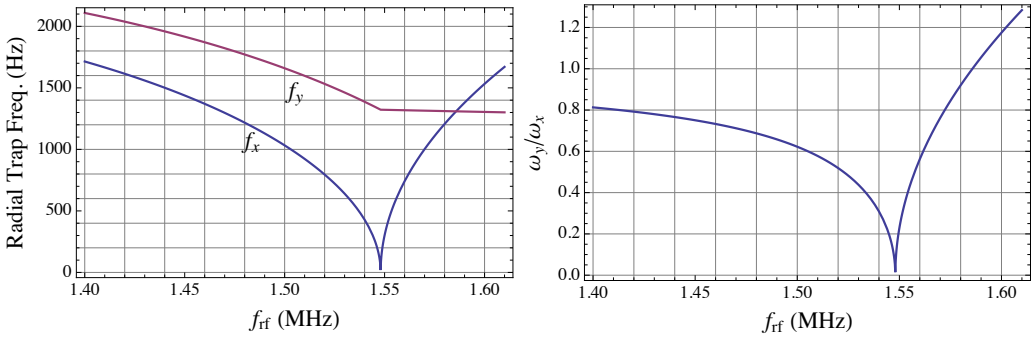

(a) (b)

Figure 6.4: Transverse trap frequencies calculated for our rf dressed trap. Figure 6.4a shows the trap frequencies f_x and f_y in the rf dressed trap, as a function of the frequency of the rf field. The Rabi frequency at $x = y = 0$ was 105 kHz, and $\omega_0/2\pi = 1.6$ MHz at the same point. The trap frequencies of the static magnetic trap were $f_x = f_y = 2.9$ kHz. Figure 6.4b shows the ratio of these two frequencies in the rf dressed trap.

the x-y plane in the laboratory frame, together with a field along $\hat{\mathbf{z}}$ (see sec.3.3.2). Moving away from the static field minimum in the $\pm\hat{\mathbf{y}}$ or $\pm\hat{\mathbf{z}}$ directions, the static field just rotates in the $x - z$ plane in the laboratory frame. Thus, the rf field in eq.(6.16) remains at a right angle to $\mathbf{B}_0(0, y, z)$ in the $x = 0$ plane. In this plane, the Rabi frequency Ω therefore remains constant, with $\beta_a = B_{\rm rf}/2$, and the dressed potential $U(0, y, z)$ has the constant Ω characteristic shown in fig.6.3.

In the $y = 0$ plane, the static field has a component in the direction $\hat{\mathbf{y}}$. This component varies linearly with y, and is zero at $y = 0$. Thus, the projection of $\mathbf{B}_{rf}$ into the plane with normal $\mathbf{B}_0(\mathbf{r})/B_0(\mathbf{r})$, decreases as one moves away from $y = 0$. Thus the anticlockwise component of the rf field β_a, and the Rabi frequency $\Omega(x, z, 0)$ decrease as one moves away from $y = 0$. This means the energy shift of the dressed states due to Ω, $\Delta E = \hbar\sqrt{\Delta^2 + \Omega^2}$, is largest at $y = 0$. As ω_{rf} approaches $\omega_0(0)$ from below, this boost to Ω close to $y = 0$ flattens out the bottom of the potential further still compared to the potentials in fig.6.3. It also causes the potential to form a double well before reaching the frequency resonance, $\omega_{\rm rf} = \omega_0(0)$.

The rf field allows us to smoothly change the shape of the trap potential by varying its magnitude $B_{\rm rf}$, and frequency $\omega_{\rm rf}$. One use of this to coherently split a trapped condensate in two, by smoothly deforming a single well into a double well. Split in this way, condensates have been used for interferometry in our experiment [76, 69] and by others [123]. Another use of these dressed potentials is to vary the confinement of the trap [68]. Since the value of $\Omega(x, y, z)$ behaves differently

in the $x = 0$ and $y = 0$ planes, the trap frequencies f_x and f_y can be made quite different to one another. This asymmetry is not possible in our static trap due to the restrictions of Maxwell's equations.

Figure 6.4a shows the transverse trap frequencies calculated for our dressed trap potential as a function of $\omega_{\rm rf}$. We calculate the rf potential given by eq.(6.15), static field given by the IP model of sec.3.3, the rf field eq.(6.16) which is what we apply in the laboratory, its detuning from eq.(6.17) and its anticlockwise component eq.(6.18). We then find the minimum of this potential, which is where our cold atoms or condensates sit, and expand the potential as a power series of x and y about this point. We find the trap frequencies from the coefficients of the quadratic terms of x and y. These frequencies characterise the trap potential over the small region of a few μm that the cold atoms explore, with the exception of when $\omega_{\rm rf}$ is within a few kHz from splitting point; here $f_x \to 0$ and higher order terms in this series become important. The study of this narrow anharmonic region is not our focus here, but is important in the study of how the condensate can be split into two parts for matter-wave interferometry experiments. In fig.6.4a, the splitting point is shown by the sharp change in behaviour of f_x and f_y. For rf frequencies up to the splitting frequency (1.547 MHz here), both frequencies decrease as the bottom of the single well potential is flattened out by the rf field. Above the splitting point, the two trap minima about which f_x and f_y are measured, move apart in the $\pm\hat{\mathbf{x}}$ direction. This increases the curvature in the $\hat{\mathbf{x}}$ direction at the trap minimum, as one can envisage fig.6.3c if $\omega_{\rm rf}$ is increased. The curvature in the $\hat{\mathbf{y}}$ direction stays roughly constant. Figure 6.4b shows how the rf frequency effects the ratio f_x/f_y. Since we can vary f_x and f_y together by changing the axial field of the static trap, and we can vary the ratio f_x/f_y with the rf field, we have independent control over the values of f_x and f_y in our trap.

We next discuss how the rf field effects the trap potential in the axial direction. Figure 6.5 shows ω_z versus $\omega_{\rm rf}$. Just as for the radial potential, two regimes of this plot can be identified: (i) for $\omega_{{\rm r}f}$ up to the frequency at which the potential is split in two, and (ii) where it becomes a double well, and the location of the trap minima move outward in the $\pm\hat{\mathbf{x}}$ directions. We have performed centre of mass oscillation experiments on condensates in rf dressed potentials in the regime (i), from which we

can determine the axial trap frequency.

In this regime, the trap minimum remains in the same position in the $x-y$ plane at $x = y = 0$ for all values of z that the atoms explore. Here the static field is orientated along the $\hat{\mathbf{z}}$ direction of the laboratory frame, and $\beta_a = B_{rf}/2$ and the Rabi frequency is constant $\Omega(0,0,z) = \Omega_0$ for all z. The shape of the dressed potential eq.(6.15) is therefore determined by the value of the static field through $\hbar\omega_0(0,0,z) = g_{\rm F}\mu_{\rm B}B_0(0,0,z)$. We decompose the static field along the axis of the trap into two parts, a constant part $B_z = B_0(\mathbf{0})$, which we define as the value of $B_0(\mathbf{r})$ at the trap minimum $\mathbf{r} = 0$, and z dependent part we call $\delta B_z(z)$.[2] Over the region where the condensate is trapped in our experiment, $\delta B_z(z)$ varies by up to 10 mG, corresponding to an energy up to 20 kHz, which is five times smaller than the our typical $\Omega_0 \approx 100$ kHz. We expand the dressed potential to first order in the small field $\delta B_z(z)$ about B_z,

$$\delta U(z) = \tilde{m}_F g_F \mu_B \frac{|\Delta_0|}{\sqrt{\Delta_0^2 + \Omega_0^2}} \delta B_z(z) \qquad \text{where } \Delta_0 = \omega_{\rm rf} - g_{\rm F}\mu_{\rm B}B_z/\hbar. \tag{6.19}$$

In the absence of an rf field we have $\delta U(z) = \tilde{m}_F g_F \mu_B \delta B_z(z)$. Equation 6.19 shows that the influence of $\delta B_z(z)$ on the trap potential is reduced by a factor $\Delta_0/\sqrt{\Delta_0^2 + \Omega_0^2}$ for the dressed potential.

The 'roughness' of the axial trap potential (see sec.4.3) due to transverse currents in the chip wires is included in $\delta B_z(z)$, and is therefore suppressed in the rf potential. This smoothing out of the axial potential has bee investigated in [68], and is a useful technique in atom chip experiments such as ours where such roughness is an inherent feature of the chip wire trap. In our experiment, we do not want to completely suppress the effect of $\delta B_z(z)$ since the slowly varying part (over a few hundred μm) of $\delta B_z(z)$ provides the axial confinement of our condensate. We typically trap our condensate in axial dimples of our trap with a potential that is approximately harmonic, characterised by a trap frequency ω_z. Making the substi-

[2] This differs slightly from our treatment in sec.4.3 where we defined $\delta B_z(z)$ as the contribution to this axial magnetic field from the transverse current fluctuations in the central leg of the chip wires.

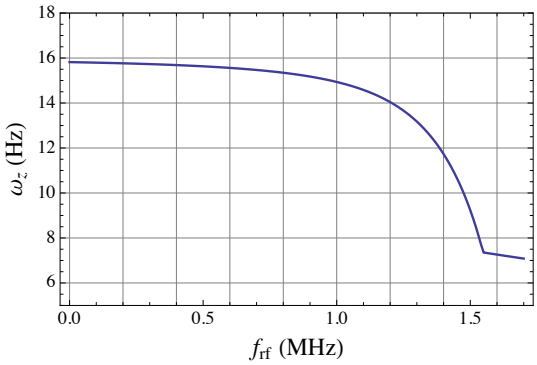

Figure 6.5: Axial trap frequencie of the rf dressed trap. The parameters for this trap are the same as for fig.6.4.

tution $2g_{\rm F}\mu_{\rm B}\delta B_z(z) = \frac{1}{2}m\omega_z^2 z^2$ in eq.(6.19), we find that in the rf potential

$$\omega_z^2 \to \omega_z'^2 = \frac{|\Delta_0|}{\sqrt{\Delta_0^2 + \Omega_0^2}}\,\omega_z. \tag{6.20}$$

Figure 6.5 shows the axial frequency of the rf dressed trap as a function of the rf frequency with $\Omega_0 = 105\,\text{kHz}$. As in fig.6.4, the frequency at which the potential becomes a double well is 1.547 MHz. Below this point the axial trap frequency is given by eq.(6.20), and above this point it was calculated from a second order expansion of the axial potential about one of the shifted trap minima of the double well.

In [68], they measure the variation of ω_z in the rf dressed trap by measuring the frequency of axial centre of mass oscillations of a condensate. We have made a similar measurement of ω_{rf} from axial centre of mass oscillations in our trap. Figure 6.6a shows the axial oscillations of our condensate when there is no rf field. These oscillations are found to have a frequency of 16 Hz, with the condensate trapped in the tightly confined local minimum labelled by 4 in fig.4.6c of sec.4.3. Oscillations were driven in the condensate using the same method as in sec.5.2.3. We then repeat the experiments, but after the atoms are dressed by an rf field of 1 G at a frequency of 1.53 MHz, which is just below the splitting point. This field is produced by running an rf current through the two large Z-wires (see sec.2.2.2), which are located either side of the small Z-wires, and are approximately 180 μm away from the atoms. This rf field is turned on by slowly increasing the rf frequency from 0, thus adiabatically transferring atoms from the $m_F = 2$ state to the $\tilde{m}_F = 2$

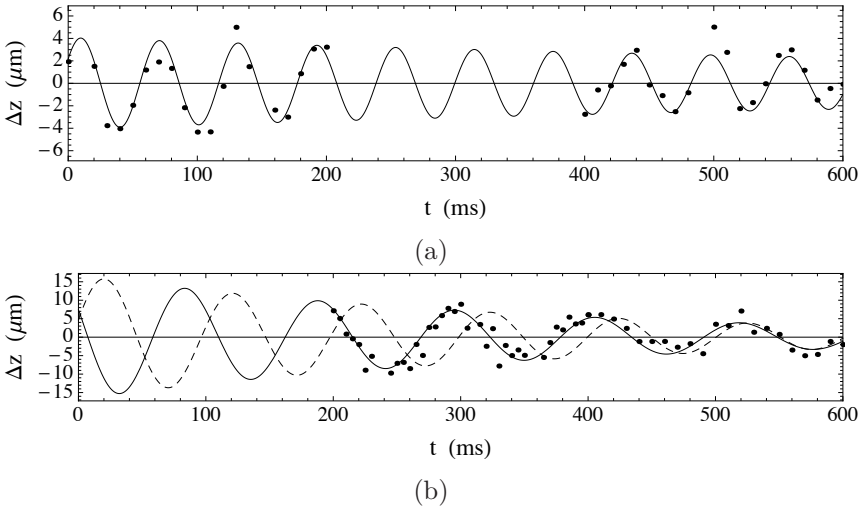

Figure 6.6: Axial centre of mass oscillations of a trapped condensate. Figure 6.6a shows the oscillations in the static magnetic trap. Data points show the condensate centre of mass, measured from absorption images. The line is a damped sinusoidal function, from which we extract the oscillation frequency 16.4 ± 0.7 Hz, where the error is given by the standard error in the frequency in the fitted model. Figure 6.6a shows the oscillations in the same trap but with an rf field applied at $\omega_{\rm rf}/2\pi = 1.53$ MHz and $\Omega_0 = 105$ kHz. The data points show the centre of mass measurements. The solid line is a damped sinusoid, but with a frequency that varied linearly with time. The dashed line is a damped sinusoid the same amplitude and damping rate of the solid line, but with a constant frequency of matching the data at the end of the oscillations shown.

dressed state. The oscillations in the rf dressed trap are shown in fig.6.6b, and have a frequency of approximately 9 Hz. This reduction in frequency is similar to that estimated theoretically and plotted in fig.6.5.

In the experiment described in [68], their (harmonic) axial potential is generated by an extra chip wire that runs perpendicular to the central part of their z wire. This produces a deep axial harmonic potential which is independent of the trap roughness. This allows them to investigate the suppression of roughness of their trap, while maintaining adequate confinement of their condensate. They additionally use this setup to investigate the effect of reduced roughness on the damping rate of the condensate centre of mass oscillations. This leads to an interesting result where they see the damping rate significantly reduced at a particular frequency of their rf dressing field. It is pointed out that at this frequency the transverse aspect ratio of the trap ω_x/ω_y is approximately 1. They note this to be an interesting feature that should be investigated further. This is an area we have begun to investigate in our experiment. However, in our experiment the axial potential in which we trap and oscillate the condensate is shallow since it results directly from the edge

roughness of the z wires that are 100 μm away, rather than the larger scale layout of the chip wires. We currently find that increasing the frequency of the dressing field further towards this frequency of interest, the depth of the local minimum where the condensate sits is reduced below the chemical potential, allowing the condensate to spill out, exploring the wider trap potential.

Even when the rf frequency is a few tens of kHz below the splitting frequency, we see the oscillating condensate can explore a much wider region where the axial potential is no longer harmonic. This can be seen from the data in fig.6.6b and the function fitted to it. Firstly, the amplitude response in the dressed trap is between three and four times larger than that in the static trap. In both cases, oscillations were driven by applying a sinusoidally modulating field gradient with the same amplitude, with a frequency close to resonance, and over two cycles. We might expect a similar amount of energy to be absorbed by the cloud per cycle, and consequently an amplitude about twice as large for the rf dressed trap which has a frequency about half that of the static trap. The increased amplitude response we measure seems to be disproportionally large, and may be the result of the rf potential having a smaller curvature further out from its centre. More conclusively however, we found that a simple damped sine wave does not fit the measured centre of mass oscillation in fig.6.6b, slipping $2\pi/3$ out of phase with our data over three oscillations periods. For a trap that has smaller curvature at larger distances from its centre, the oscillation frequency would be smaller for larger amplitude oscillations. To model damped oscillations in such a trap we fit a damped sinusoidal function, but with a frequency that increased with time,

$$\Delta z(t) = Ae^{-t/\tau} \sin\left[(\omega_0 + mt)t + \phi\right]. \tag{6.21}$$

Here we have used a frequency that increases linearly with time, $\omega(t) = \omega_0 + mt$, as a first order approximation of $\omega(t)$, which is a reasonable approximation since we observed oscillations over a time approximately equal to their $1/e$ decay time. We found this model remained in phase over the entire data set in fig.6.6b, to which it was fit.

In conclusion, we see that the addition of the rf field provides great fexibility to adjust the frequencies of the trap, to control its roughness, and even to split it in

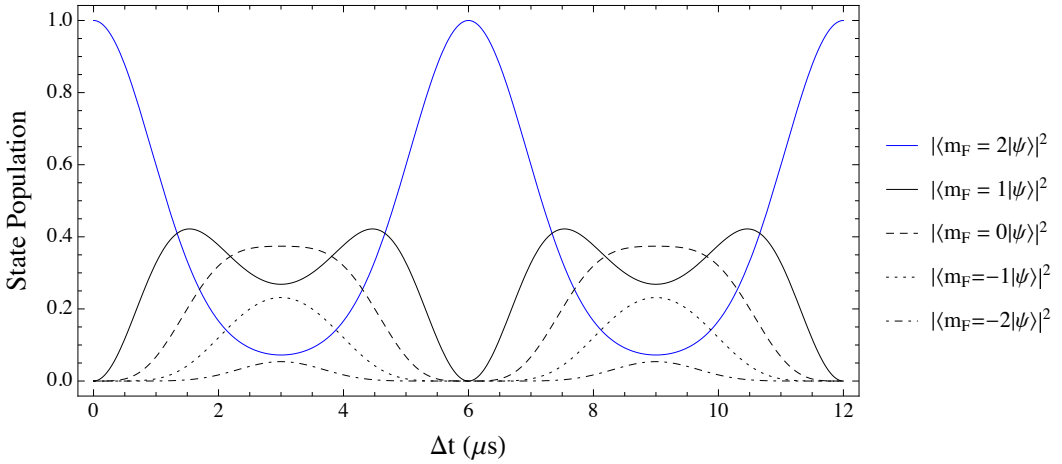

Figure 6.7: Simulation of Rabi oscillations calculated from eq.(6.24) with a detuning of 120 kHz and a Rabi frequency of 115 kHz. With these values, the period of a complete Rabi oscillation is 6 μs.

two, as we do for interferometry.

6.2 Coherent Evolution

We use the coherent evolution of the atoms in the rf field to calibrate the amplitude of the rf field, and to enable accurately controlled release of atoms from the trap. Calibration of Ω_0 is important for the precise application of the dressing field, particularly near the splitting point of the transverse potential. It is not reliable to calculate this from the rf current that enters the vacuum chamber heading to the chip wires, because the inductive and capacitive coupling to other conductors (and semi-conductors) is not well known. Instead, we calibrate Ω_0 directly by measuring the Rabi oscillations of the state populations $|\langle m_F|\psi(t)\rangle|^2$, following a square rf pulse of duration ΔT. Let

$$|\psi(t_0)\rangle = \sum_{m_F} c_{m_F}(t_0)\,|m_F\rangle\,, \tag{6.22}$$

be the state of each trapped atom at the time the pulse is switched on, t_0. While the rf is on, the state of the atom $|\tilde{\psi}(t)\rangle$ evolves in the Shrödinger picture as

$$|\tilde{\psi}(t)\rangle = \sum_{\tilde{m}_F} \langle \tilde{m}_F|\psi(t_0)\rangle\, e^{-i\tilde{m}_F\tilde{\Omega}(t-t_0)}\,|\tilde{m}_F\rangle\,, \tag{6.23}$$

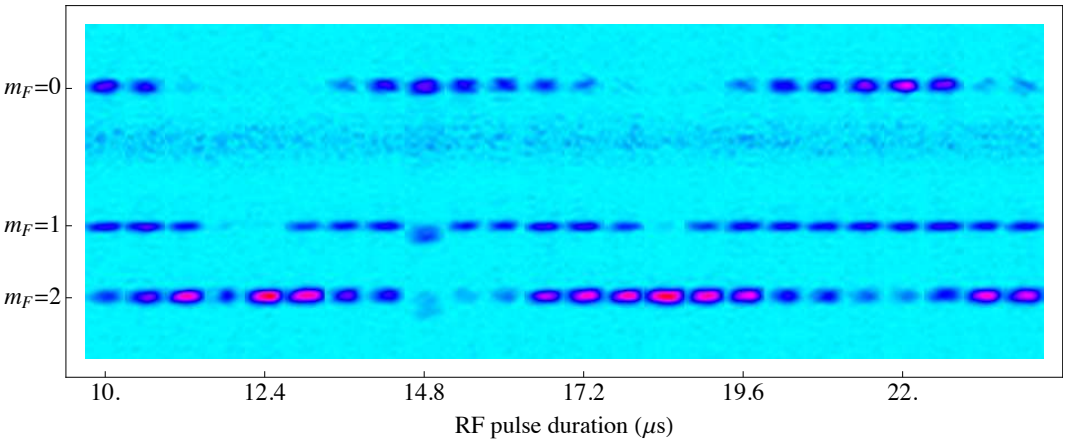

Figure 6.8: Sequence of absorption images of a condensate after Rabi pulses of different durations. Each image shows three clouds split from each other vertically. The Zeeman sub-level of these clouds is indicated on the left hand side. The figure consists of 24 images taken after Rabi pulses of different times. The difference in pulse length between consecutive images is 0.6 μs. The grainy horizontal line two thirds up each image is an artefact of our imaging system.

where $\tilde{\Omega}^2 = \Delta_0^2 + \Omega_0^2$, $|\tilde{m}_F\rangle$ are the dressed eigenstates, and Δ_0 and Ω_0 are the detuning and Rabi frequency at the trap bottom, where the atoms are located. Transforming back to the uncoupled basis, we have

$$\langle m'_F|\psi(t)\rangle = \sum_{\tilde{m}_F, m_F} \langle m'_F|\tilde{m}_F\rangle \langle \tilde{m}_F|m_F\rangle c_{m_F}(t_0) e^{-i\tilde{m}_F\tilde{\Omega}(t-t_0)}. \qquad (6.24)$$

where $\langle m_F|\tilde{m}_F\rangle = \langle \tilde{m}_F|m_F\rangle^*$ are the components of the dressed eigenstates in the uncoupled basis, which can be found from eq.(6.13). The square modulus of eq.(6.24) gives the probability of finding an atom in the state $|m'_F\rangle$ at time t after the rf was turned on. So, for example we expect an atom initially in the state $|m_F = 2\rangle$ to evolve into a superposition of the other four m_F states, returning to the state $|m_F = 2\rangle$ after one period, $2\pi/\tilde{\Omega}$. An example of just such Rabi oscillations are shown in fig.6.7 over two periods ($4\pi/\tilde{\Omega}$), with $\Delta_0 = 2\pi \times 120\,\text{kHz}$ and $\Omega_0 = 2\pi \times 115\,\text{kHz}$.

We observe Rabi oscillations like these in our experiment by applying an rf field for a time ΔT. We can find $\tilde{\Omega}$ by measuring the time taken for all atoms to return to the initial state $m_F = 2$. From this we can calculate Ω_0, where Δ_0 is known from rf spectroscopy of the trap bottom (see sec.4.2.1). We measure the state populations following a short Rabi pulse with ΔT of a few times the period $\frac{2\pi}{\tilde{\Omega}}$. This is done by turning the magnetic trap off and applying a magnetic field gradient to spatially

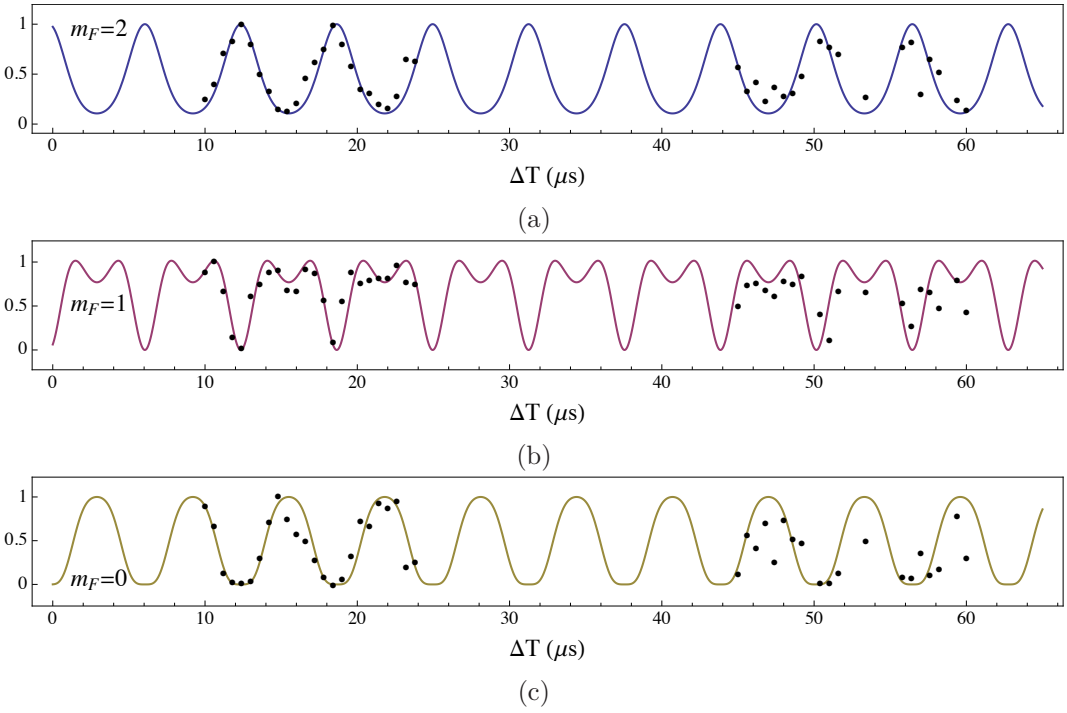

Figure 6.9: Figure 6.9 shows state populations oscillating in an rf field as a function of time ΔT. The data points show the measured populations derived from fig.6.8, and lines are the theory derived from eq.(6.24). Figure 6.9a shows the populations for $m_F = 2$, fig.6.9b for $m_F = 1$, and fig.6.9c for $m_F = 0$. All populations are shown normalised to their peak value - the relative populations are not known accurately because of noise in the absorption images for some of the clouds. The oscillation period $2\pi/\tilde{\Omega} = 6.2\,\mu$s, the detuning was measured to be 120 kHz, and the corresponding $\Omega_0 = 2\pi \times 105$ kHz.

split the atomic cloud by their spin state. The high field seeking states are rapidly lost before the trap is turned off. The remaining atoms, in the $m_F = 0,\ 1$ and 2 states, are spatially separated using the Stern-Gerlach effect. A magnetic field gradient, lasting for 2 ms, is applied by a current pulse in the Z wires 2 ms after the trap is turned off. The populations of these three states are then found from an absorption image as can be seen from fig.6.8. Here the three magnetic states appear, one above the other. A set of absorption images is shown for consecutive rf pulse durations ΔT with intervals of $0.6\mu s$. A small region of interest is selected around each of the separate clouds in each image. The total pixel counts in each region of interest gives a measure of the relative population of the relevant state at a given time. A sequence of images such as in fig.6.8 together describe the evolution of the state populations of the $m_F = 0,\ 1$ and 2 states.

Figure 6.9 shows the evolution of the relative populations of these states over 60 ms. The state evolution predicted by eq.(6.24) is also shown against the experi-

mental data. From this data the effective Rabi frequency $\tilde{\Omega}$ is measured. Together with the value of $\omega_{\rm rf}$ and rf spectroscopic measurement of ω_0, the Rabi frequency $\Omega = \sqrt{\tilde{\Omega}^2 - \Delta^2}$ is obtained. Operating our rf signal generator (the versatile frequency generator described in sec.2.2) at its maximum output power of 0 dBm, the Rabi frequency determined by this measurement is 105 kHz. This corresponds to an rf field amplitude of $B_{rf} = 0.3$ G, and an anticlockwise component of half this value.

6.2.1 Release of atoms using an rf pulse

We also use an rf pulse to release a fraction of the cloud from the magnetic trap in a well controlled manner [124, 125]. Before the pulse all atoms are in the state $|m_F = 2\rangle$. After the pulse, the atoms are in a coherent superposition of states $|m_F\rangle$. The state $|m_F = 0\rangle$ has no interaction with static magnetic fields, so this component is released from the trap by the pulse, and falls away under gravity. Components in the positive m_F states remain trapped, and components with negative m_F are rapidly accelerated out of the trap.

The released $m_F = 0$ cloud is then measured using absorption imaging. The fraction of atoms found in this state depends on Δ, Ω, and the pulse duration ΔT. This fraction is maximised for $\Delta = 0$ and $\Delta T = \pi/\Omega$, for which the fraction is $1/\sqrt{2}$.

The time scale over which an $m_F = 0$ cloud is released is on the order of $1/\Omega$. Since $\Omega \gg \omega_r$ the motion of atoms in the trap potential during the Rabi pulse is negligible. Once in the state $|m_F = 0\rangle$, the motion is unaffected by static or slowly varying ($\ll 1$ MHz) magnetic fields. This release process is highly repeatable since the length of the Rabi pulse can be precisely timed ($\lesssim$ 1ns), and is insensitive to magnetic field fluctuations which occur during our normal method of release, whereby the chip wire currents and other field coils are turned off.

We have used this technique to measure the transverse oscillations of our trapped condensate, which are at frequencies on the order of 1 kHz. These are excited by making a sharp 1% drop in the Z wire current giving a sudden height change in the trap, which defines the time $t = 0$. A fraction of the cloud is then released at later time t by a Rabi pulse of duration $\Delta T = \frac{3}{2}\frac{\pi}{\Omega}$ ($\Delta T \ll t$). The height of the $|m_F = 0\rangle$ cloud is then measured from an absorption image taken several ms after

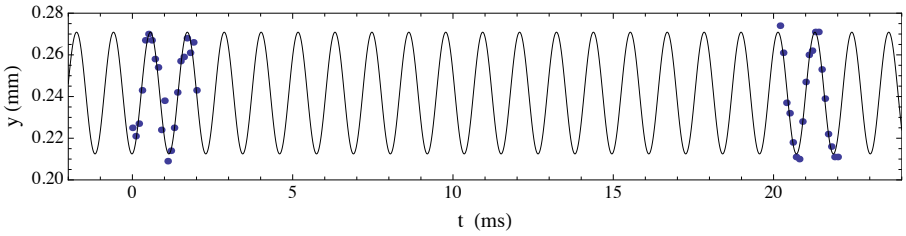

Figure 6.10: Measurement of transverse oscillations of the trapped condensate. The data points show the vertical centre of mass of the condensate after it was released from the trap. The black line shows a sine wave fitted to this data, from which we find a transverse oscillation frequency of 868.4 ± 0.8 Hz. The error is the standard error in the frequency of the sine wave we fit, assuming all data points have equal weighting.

the Rabi pulse. These images give the density profile in the y-z plane. Summing the pixel counts over the z direction gives the 1d density profile of the cloud $n(y)$, to which we can fit the Thomas Fermi profile of eq.(5.8). The fit picks out the centre of the cloud which we take as its height. This is repeated but for a range of times t. We see the height oscillates at frequency f, which corresponds to the transverse trap frequency $\omega_y/2\pi$. Figure 6.10 is an example of measurements of the transverse oscillations of the condensate. In this example we measured transverse oscillations with a frequency of 868.4 ± 0.8 Hz. Such measurements are difficult to make if the trap is turned off by turning off the trapping field rather than using a Rabi pulse to release atoms. This is because the trap field does not turn off fast enough, or with the required repeatability to resolve oscillations at this high frequency, due to the self-inductance in of the wires and coils which cause eddy currents when the current is varied rapidly. This technique allows us to make quick and accurate measurements of the transverse frequencies using the condensate. Furthermore, this technique could be used to measure the variation of the trap frequency as the trap is deformed by some other potential gradient, such as that from the Casimir-Polder interaction [96].

6.3 The RF Knife

An rf field is used to selectively remove the most energetic thermal atoms in our magnetic trap, cooling the remaining atoms to produce a Bose-Einstein condensate (see Ch.4 for details on evaporative cooling). Once a condensate is formed, this rf field is usually left on, limiting the depth of the trap so that any energetic thermal

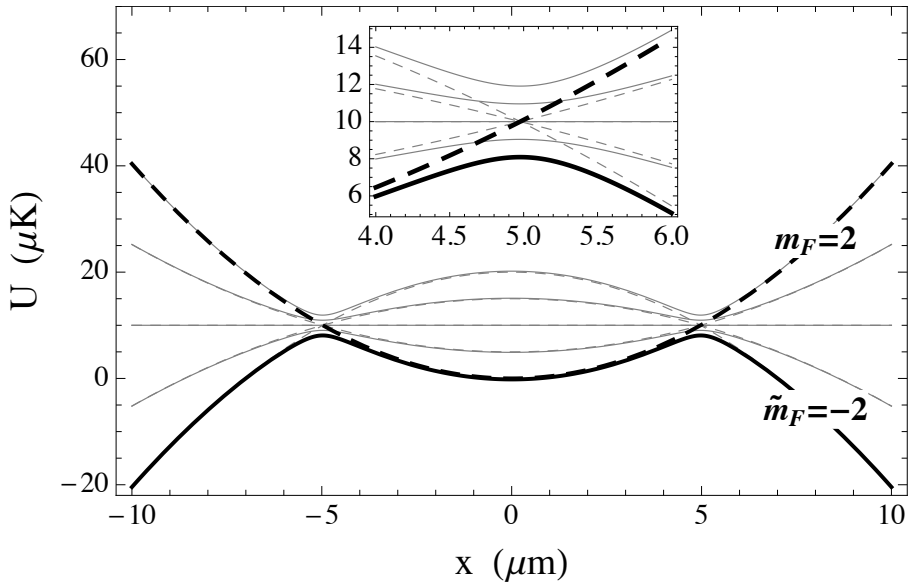

Figure 6.11: This figure shows the energies of the dressed (solid lines) and uncoupled states (dashed lines) of magnetically trapped atoms in the presence of an rf field. The black lines show the potential energy we trap atoms in with and without the rf field. The figure shows that the rf field turns over the trap potential at approximately $10\,\mu$K above the trap bottom, limiting the depth of the trap. The inset shows a zoomed in version of this anti-crossing. In calculating these lines we have used a harmonic trap with frequency $f_x = 1.4\,$kHz, a Rabi frequency of $20\,$kHz, and $\omega_{\rm rf} = \omega_0(0) + \eta k_{\rm B}T/2\hbar$ where $T = 1\,\mu$K and $\eta = 10$.

atoms that arise due to heating in the trap (see sec.4.2.3), are rapidly removed, with minimal disturbance to the condensate. This selective removal of energetic atoms can be viewed in a simple way, using the theory described in this chapter.

Once loaded, the magnetic trap contains a cloud of atoms at approximately $100\,\mu$K. For evaporation, we turn on the rf field at a frequency $\omega_{\rm rf} = \omega_0(0) + \eta k_{\rm B}T/2\hbar$, which is resonant only for atoms in a part of the potential that has energy close to $\eta k_{\rm B}T$ above the trap bottom, $\hbar\omega_0(0)$. We typically set $\eta = 10$, so most atoms are far from resonance. This rf field dresses the static field potential in the same way as described in sec.6.1. Figure 6.11 shows an example of the energies of the dressed states and the uncoupled states. For clarity, we have shown a trap with rf field resonance at an energy correspodning to $10\,\mu$K. The magnitude of the rf field is such that $\Omega = 2\pi \times 20\,$kHz, which is typical of our experiment. Since most atoms explore a region of the potential where they remain far from resonance, $\Delta = \omega_{\rm rf} - \omega_0(0) \gg \Omega$, the overlap $\langle -\tilde{m}_F | m_F \rangle \approx 1$. Hence when the rf field is turned on, almost all atoms are projected into the state $|\tilde{m}_F = -2\rangle$. From fig.6.11, we see that the atoms are now trapped in harmonic potential that turns over at an energy

$\eta k_{\rm B}T$ above the trap bottom. Thus the rf field, often referred to as an 'rf knife', sharply cuts the depth of the trap for $m_F = 2$ atoms to $\eta k_{\rm B}T$. Atoms that recoil from elastic collision with energy greater than $\eta k_{\rm B}T$ escape from the trap. For evaporative cooling, the depth of the trap is reduced by ramping down the rf frequency. For low temperatures of a few μK or less, we reduce the rf power such that Ω is small compared to the trap depth so the shape of the trap where most atoms are found is unaffected.

We briefly consider the efficiency with which energetic atoms are lost from this trap as they pass through the resonant shell where $\omega_0(\mathbf{r}) = \omega_{\rm rf}$. As discussed in Ch.4, energetic atoms reach this resonant shell on a time scale of half an oscillation period of their motion in the trap. [3] However, if these atoms are moving sufficiently fast they do not follow the dressed states adiabatically. In the extreme, they remain in the $m_F = 2$ state, where they continue to oscillate in a harmonic manner, later passing back through the resonant shell. The probability of them remaining in the $|m_F = 2\rangle$ depends on Ω and the rate at which their energy varies. For a narrow resonance, this rate is proportional to the velocity the atom passes through the resonance with.

For quantitative insight into this, we consider a simpler version of our trap, in which $F = \frac{1}{2}$ rather than 2. We consider the atom to be in an uncoupled state, $|\uparrow\rangle$, where it is trapped in the potential energy $E_\uparrow$. If it remains in this state after passing through the resonance, then it remains trapped. However, if the rf field flips the spin as it passes through it is accelerated out of the trap, and escapes forever. For an rf field with Rabi frequency Ω, and an atom moving through the resonance such that it experiences an uncoupled energy that varies with time at rate $\frac{{\rm d}E_\uparrow}{{\rm d}t}$, the probability that it remains in $|\uparrow\rangle$ is given by the well known Landau-Zener formula [124, 126],

$$P_{|\uparrow\rangle\rightarrow|\uparrow\rangle} = e^{-2\pi\Gamma} \quad \text{where } \Gamma = \left(\frac{\hbar\Omega}{2}\right)^2 \Big/ \left(\hbar\frac{\rm d}{{\rm d}t}|E_\uparrow - E_\downarrow|\right) . \tag{6.25}$$

[3] Except for the few atoms in an elliptical orbit of the trap which can remain at lower energies. Even for these, either the anharmonicity in our trap or elastic collisions prevent atoms remaining in such orbits for more than a few periods.

For this spin-half system model, we estimate that

$$\Gamma \approx \frac{\hbar\Omega^2}{2\sqrt{2\eta}\omega_r k_{\mathrm{B}} T}. \tag{6.26}$$

In this estimate, the trap is truncated at $\eta k_{\mathrm{B}} T$, and the energy levels are expanded linearly as a function of r about the point r_0 where $\eta k_{\mathrm{B}} T = \frac{1}{2} m\omega_r^2 r_0^2$. We then use the mean thermal velocity $\sqrt{k_{\mathrm{B}} T/m\omega_r^2}$ to calculate $\frac{\mathrm{d}}{\mathrm{d}t}|E_\uparrow - E_\downarrow|$. The Landau-Zener formula 6.25 estimates that atoms are highly likely to be ejected from the trap on their first pass through the resonance shell for temperatures of a few μK or lower, while for higher temperatures several passes may be required.

This result gives an indication of what is expected in a spin F. In fact, since an integer spin F system, $\mathscr{H}_F$, can be written as the symmetric terms in the tensor product space of $2F$ spin half systems, $\mathscr{H}_{1/2}^{\otimes F}$, we can write the state $|F = 2, m_F = 2\rangle$ as $|\uparrow\uparrow\uparrow\uparrow\rangle$. The other states of the $F = 2$ system can be written in a similar way. The probability for an atom initially in the state $|\uparrow\uparrow\uparrow\uparrow\rangle$ to remain in this state after passing through the resonance is approximately given by the fourth power of probability predicted by 6.25.

Chapter 7

Bose Einstein Condensates at Finite Temperature

In chapter 8 we will present and discuss data on the damping of centre of mass oscillations of our condensate due to the presence of a thermal cloud. In order to discuss the damping mechanism of the condensate by the thermal cloud we first introduce the analytical tools to describe such a system. This section extends the theory of a condensate at zero temperature given in Ch.5. The extended theory considers both the condensate, the thermal cloud, and the interactions between them in the second quantised limit.

7.1 Second Quantised Theory for a Bose Gas

At zero temperature each particle in the condensate is in the same single particle state - the ground state. The zero temperature N particle state is therefore the product of N identical single particle states and is symmetric under exchange of particles. At finite temperature however, higher energy states are also occupied, and the single product state of all the occupied single particle states is not correctly symmetrised. The symmetric many body state which describes the Bose gas is instead the superposition of product states with all possible permutations of particle orderings. For example the state for two particles, one in state $|\phi_1\rangle$, the other in $|\phi_2\rangle$ is given by $\left(|\phi_1\rangle\,|\phi_2\rangle + |\phi_2\rangle\,|\phi_1\rangle\right)/\sqrt{2}$. With more than just a few particles, the

many body states become complicated objects to describe using the notation of first quantisation. However, the second quantised approach to quantum theory offers a much simpler framework.[1]

7.1.1 Second Quantisation for Non-Relativistic Particles

In the second quantised theory one considers operators acting on states in Fock space, is the space of symmetric many particle states, constructed from the set of single particle states $\{|\nu_i\rangle\}$. In Fock space a multi-particle state $|\psi\rangle$ which has N_{ν_0} particles in the single particle state $|\nu_0\rangle$, N_{ν_1} in the state $|\nu_1\rangle$ ... etc., is represented by

$$|\psi\rangle = |N_{\nu_0}, N_{\nu_1}, \dots \ \dots, N_{\nu_i}, \dots\rangle\,. \tag{7.1}$$

The vacuum state $|0\rangle$ indicates the state where no single particle state is occupied.

The second quantised operators $\mathbf{a}^\dagger_{\nu_i}$ and $\mathbf{a}_{\nu_i}$, create and annihilate a particle in the single particle state $|\nu_i\rangle$, thus increasing or decreasing N_{ν_i} by 1:

$$\mathbf{a}^\dagger_{\nu_i}|N_{\nu_i}\rangle = \sqrt{N_{\nu_i}+1}\,|N_{\nu_i}+1\rangle\,, \qquad \mathbf{a}_{\nu_i}|N_{\nu_i}\rangle = \sqrt{N_{\nu_i}}\,|N_{\nu_i}-1\rangle\,. \tag{7.2}$$

The state $|N_{\nu_i}\rangle$ is therefore

$$|\dots, N_{\nu_i}, \dots\rangle = \prod_i \frac{(\mathbf{a}^\dagger_{\nu_i})^{N_{\nu_i}}}{\sqrt{N_{\nu_i}!}}\,|0\rangle\,. \tag{7.3}$$

To maintain the particle exchange symmetry of these states the creation and annihilation operators must obey the Bosonic commutator relations:

$$[\mathbf{a}^\dagger_{\nu_i}, \mathbf{a}^\dagger_{\nu_j}] = [\mathbf{a}_{\nu_i}, \mathbf{a}_{\nu_j}] = 0, \qquad [\mathbf{a}_{\nu_i}\mathbf{a}^\dagger_{\nu_j}] = \delta_{ij}. \tag{7.4}$$

The final relation ensures the correct symmetry for Bosons.[2] The number operator $\mathbf{a}^\dagger_{\nu_i}\mathbf{a}_{\nu_i}$ is defined such that

$$\mathbf{a}^\dagger_{\nu_i}\mathbf{a}_{\nu_i}|n_{\nu_i}\rangle = n_{\nu_i}|n_{\nu_i}\rangle\,. \tag{7.5}$$

[1] We review the second quantised approach to many-body quantum mechanics in the next section. A more extensive introduction can be found in many textbooks, for example [127]

[2] From it, one can show that the occupation number N_{ν_i} of any single particle state $|\nu_i\rangle$ may be arbitrarily large (for Bosons), and that $\mathbf{a}_{\nu_i}|0\rangle = 0$.

Equations (7.2) and eq.(7.3) can be derived from the commutator relations eq.(7.4) together with the definition eq.(7.5).

The creation operator transforms like the single particle state $|\nu_i\rangle$ under a change of single particle basis from $\{|\nu_i\rangle\}$ to $\{|\mu_j\rangle\}$, while the annihilation operator transforms like $\langle\nu_i|$;

$$\mathbf{a}^\dagger_{\mu_j} = \sum_i \langle\nu_i|\mu_j\rangle\, \mathbf{a}^\dagger_{\nu_i} \quad \text{and} \quad \mathbf{a}_{\mu_j} = \sum_i \langle\mu_j|\nu_i\rangle\, \mathbf{a}_{\nu_i}. \tag{7.6}$$

Transforming to the position representation, the creation and annihilation operators become the field operators $\mathbf{\Psi}(\mathbf{r})$ and $\mathbf{\Psi}^\dagger(\mathbf{r})$, where the label μ_i becomes the continuous variable $\mathbf{r}$ which labels the position states $|\mathbf{r}\rangle$. The operator $\mathbf{\Psi}^\dagger(\mathbf{r})$ creates a particle at position $\mathbf{r}$ in state $|\mathbf{r}\rangle$, and $\mathbf{\Psi}(\mathbf{r})$ destroys it. The useful transformations between $\{|\nu_i\rangle\}$ and $\{|\mathbf{r}\rangle\}$ are given by,

$$\mathbf{\Psi}(\mathbf{r}) = \sum_i \psi_{\nu_i}(\mathbf{r})\mathbf{a}_{\nu_i} \quad \text{and} \quad \mathbf{a}_{\nu_i} = \int \mathrm{d}\mathbf{r}\, \psi^*_{\nu_i}(\mathbf{r})\mathbf{\Psi}(\mathbf{r}) \tag{7.7}$$

where $\psi_{\nu_i}(\mathbf{r}) = \langle\mathbf{r}|\nu_i\rangle$ is the wavefunction of the state $|\nu_i\rangle$. The field operators obey the commutator relations

$$[\psi^\dagger(\mathbf{r}), \psi^\dagger(\mathbf{r}')] = [\psi(\mathbf{r}), \psi(\mathbf{r}')] = 0, \qquad [\psi(\mathbf{r}), \psi^\dagger(\mathbf{r}')] = \delta(\mathbf{r} - \mathbf{r}'), \tag{7.8}$$

where $\delta(\mathbf{r}-\mathbf{r}')$ is the Dirac-delta function. In the position representation, the number operator becomes the density operator $\mathbf{\Psi}^\dagger(\mathbf{r})\mathbf{\Psi}(\mathbf{r})$.

7.1.2 Hamiltonian of the Interacting Bose Gas

The Hamiltonian for a non-interacting Bose gas in the second quantised limit is given by

$$\mathbf{H}_0 = \int d\mathbf{r}\, \mathbf{\Psi}^\dagger(\mathbf{r}) \left(-\frac{\hbar^2\nabla^2}{2m} + V(\mathbf{r}) \right) \mathbf{\Psi}(\mathbf{r}) \tag{7.9}$$

where the first term measures the kinetic energy of the Bose gas, and the second term its energy due to the external potential $V(\mathbf{r})$. In addition to this we consider s-wave scattering interaction between pairs of atoms, which dominates over other interactions at low temperatures. For ^{87}Rb atoms trapped in the $F = 2$ ground

state by weak magnetic fields, this interaction is repulsive and at the temperatures associated with condensation is well described by the 'hard sphere' or 'contact' interaction considered in sec.**??**. In terms of the field operators this interaction is given by $\frac{g}{2}\int d\mathbf{r}\mathbf{\Psi}^\dagger(\mathbf{r})\mathbf{\Psi}^\dagger(\mathbf{r})\mathbf{\Psi}(\mathbf{r})\mathbf{\Psi}(\mathbf{r})$, hence describes an interaction where two colliding particles are annihilated at $\mathbf{r}$, followed by the creation of two scattered particles originating from the same point. The interaction strength is given by $g = 4\pi\hbar^2 a/m$ and a is the s-wave scattering length. Thus the Hamiltonian for an interacting Bose gas at low temperatures is

$$\mathbf{H} = \int \mathrm{d}\mathbf{r}\left(\mathbf{\Psi}^\dagger(\mathbf{r})\left(-\frac{\hbar^2\nabla^2}{2m} + V(\mathbf{r})\right)\mathbf{\Psi}(\mathbf{r}) + \frac{g}{2}\mathbf{\Psi}^\dagger(\mathbf{r})\mathbf{\Psi}^\dagger(\mathbf{r})\mathbf{\Psi}(\mathbf{r})\mathbf{\Psi}(\mathbf{r})\right). \qquad (7.10)$$

We wish to determine the form of the ground state, and the excitations of a Bose gas, from this Hamiltonian. At finite temperatures, the excited states are populated. The presence of the ground state strongly effects the form of the excited states. In addition, the effect of thermal excitations on the ground state can sometimes be significant.

We clarify the connection between the excitations we seek here, and those of the hydrodynamic and Bogoliubov theories at zero temperature as presented in Ch.5. The excitation of the Hamiltonian above, eq.(7.10), have a different nature depending on their energy. At low energies they are phonons - the quasiparticles associated with the propagation of sound. These are the same as the small amplitude wave-like excitations predicted by the hydrodynamic equations in the linearised limit, eq.(5.27). At high energies where the hydrodynamic theory breaks down, the excitations of eq.(7.10) are single particle like. They are similar but not identical to the single particle excitations of the harmonic potential.

In fact, the complete spectrum of eq.(7.10) at low temperatures ($k_\mathrm{B}T \ll \mu$) is very similar to the spectrum predicted by the zero temperature Bogoliubov theory. The main difference is the quantum fluctuations taken into account by the field operators here. Even at zero temperature these quantum fluctuations cause a small depletion ($< 1\%$) in the number of particles found in the condensate of a few percent [128, 11, 129]. For higher temperatures, eq.(7.10) also allows one to include the effect that large number of thermal excitations have on the ground state and excitations.

The second quantised Hamiltonian eq.(7.10) gives a more general description of the Bose gas than the theories in Ch.5. However, it is extremely difficult to work with directly due to the non-linear mixing of states in the interaction term. We therefore introduce two well known approximations which pertain to different aspects of the finite temperature Bose gas. The first, discussed in sec.7.2, is the Hartree Fock approximation from which a macroscopic description of the thermal and condensed fractions of the Bose gas can subsequently be made. We then use this to describe the density of the gas, which has a characteristic bimodal distribution that we fit our experimental data to. The second approximation, discussed in sec.7.4, is the Bogoliubov approximation in which the microscopic behaviour can be studied. The Bogoliubov approximation is then used in Ch.8 as the starting point to investigate the nature of damping of motion of our condensate that we measure experimentally.

For both approximations the starting point is the expansion of the Hamiltonian eq.(7.10) in terms of its action on the condensate and its action on excitations, which we demonstrate here. Using eq.(7.7), the field operators can be expanded in a single particle basis $\{|\psi_i\rangle\}$, where $|\psi_0\rangle$ corresponds to the single particle ground state of the gas,

$$\mathbf{\Psi}_0(\mathbf{r}) + \delta\mathbf{\Psi}(\mathbf{r}) = \psi_0(\mathbf{r})\mathbf{a}_{\psi_0} + \sum_{i>0} \psi_i(\mathbf{r})\mathbf{a}_{\psi_i}, \tag{7.11a}$$

$$\mathbf{\Psi}_0^\dagger(\mathbf{r}) + \delta\mathbf{\Psi}^\dagger(\mathbf{r}) = \psi_0^*(\mathbf{r})\mathbf{a}_{\psi_0}^\dagger + \sum_{i>0} \psi_i^*(\mathbf{r})\mathbf{a}_{\psi_i}^\dagger. \tag{7.11b}$$

The operators $\mathbf{\Psi}_0$ and $\mathbf{\Psi}_0^\dagger$ act on the condensate, annihilating and creating ground state particles at position $\mathbf{r}$ respectively. The 'fluctuation' operators $\delta\mathbf{\Psi}$ and $\delta\mathbf{\Psi}^\dagger$, annihilate and create excitations of the gas at $\mathbf{r}$. Since $n(\mathbf{r}) = \langle\mathbf{\Psi}^\dagger\mathbf{\Psi}(\mathbf{r})\rangle$ is the mean density of the Bose gas and $n_0(\mathbf{r}) = \langle\mathbf{\Psi}_0^\dagger(\mathbf{r})\mathbf{\Psi}_0(\mathbf{r})\rangle$ the mean density of condensed atoms, then $\langle\delta\mathbf{\Psi}^\dagger(\mathbf{r})\delta\mathbf{\Psi}(\mathbf{r})\rangle = n(\mathbf{r}) - n_0(\mathbf{r})$ must be the density of the non-condensed part of the gas.

Since we are working with operators, rather than the mean classical fields in Ch.5, one aspect that these fluctuations operators represent are quantum fluctuations of the ground state density about its mean value $\langle\mathbf{\Psi}_0^\dagger(\mathbf{r})\mathbf{\Psi}_0(\mathbf{r})\rangle$. In addition to quantum fluctuations, $\delta\mathbf{\Psi}$ and $\delta\mathbf{\Psi}^\dagger$ represent other fluctuations, for example those associated with the condensate dynamics when the trap potential is varied, or the

departure from the ground state due to thermal population of excited states at finite temperature. For the operator expansion in eq.(7.11) to be useful in simplifying the Hamiltonian eq.(7.10), the fluctuations associated with $\delta\Psi$ and $\delta\Psi^\dagger$ are assumed to be small. Thus the lowest order terms in these fluctuation operators are the most important. Higher order terms in $\delta\Psi$ and $\delta\Psi^\dagger$ can then be introduced as a small perturbation.

The Hamiltonian eq.(7.10) is expanded using eq.(7.11), and contains terms from zeroth to fourth order in the non-condensed operators $\delta\Psi$ and $\delta\Psi^\dagger$. In this expansion one finds Hermitian terms such as $\Psi_0^\dagger\Psi_0\delta\Psi^\dagger\delta\Psi$ (put in normal order), and non-hermitian terms such as $\Psi_0\Psi_0\delta\Psi^\dagger\delta\Psi^\dagger$. The hermitian terms have non-zero expectation value for a gas described by a Fock state, and correspond to real excitations of definite particle number.[3] The non-Hermitian terms have zero expectation value for Fock states, but non-zero mean squared value. These couple the energy states one finds in the Hermitian system, and can represent interactions with both real particles and virtual particles which correspond to quantum fluctuations in the gas.[4]

Retaining a selection of Hermitian and non-Hermitian terms, one finds the Bose gas is not described by a single Fock state but a superposition of different Fock states. This difference is more significant for low energy excitations, for which virtual excitations are longer lived and have larger effect. Far below the transition temperature to Bose Einstein condensation the Bose gas is no longer well described by a single Fock state.

7.2 Hartree Fock Approximation and Semi-Classical Description of the Thermal Cloud

The Hartree Fock approximation assumes that the Bose gas is well described by a Fock state. This approximation is good when $k_{\rm B}T$ is larger than the chemical potential μ, when the majority of thermally excited particles behave like free parti-

[3] They are energy conserving terms for which the particle propagators are 'on mass shell' (see [130] for example), maximising the probability amplitude of such events.

[4] The energy non-conserving terms give rise to virtual excitations. There are also energy conserving coupling terms which create and destroy real excitations.

cles rather than phonons in the condensed gas. Under this assumption the energy expectation value $\langle H \rangle$ has only contributions from the hermitian terms of the Hamiltonian:

$$\mathbf{H}_{\rm HF} = \int \mathrm{d}\mathbf{r} \left[-\mathbf{\Psi}_0^\dagger \frac{\hbar^2\nabla^2}{2m}\mathbf{\Psi}_0 - \delta\mathbf{\Psi}^\dagger \frac{\hbar^2\nabla^2}{2m}\delta\mathbf{\Psi} + V(\mathbf{r})\mathbf{\Psi}_0^\dagger\mathbf{\Psi}_0 + V(\mathbf{r})\delta\mathbf{\Psi}^\dagger\delta\mathbf{\Psi} \right.$$
$$\left. + \frac{g}{2}\mathbf{\Psi}_0^\dagger\mathbf{\Psi}_0^\dagger\mathbf{\Psi}_0\mathbf{\Psi}_0 + 2g\mathbf{\Psi}_0^\dagger\mathbf{\Psi}_0\delta\mathbf{\Psi}^\dagger\delta\mathbf{\Psi} + \frac{g}{2}\delta\mathbf{\Psi}^\dagger\delta\mathbf{\Psi}^\dagger\delta\mathbf{\Psi}\delta\mathbf{\Psi}. \right] \quad (7.12)$$

The expectation value can be evaluated term by term using the expansion of the field operators given in eq.(7.11). The ground state terms contain $\langle \mathbf{a}_{\psi_0}^\dagger \mathbf{a}_{\psi_0} \rangle = N_0$, and $\langle \mathbf{a}_{\psi_0}^\dagger \mathbf{a}_{\psi_0}^\dagger \mathbf{a}_{\psi_0}\mathbf{a}_{\psi_0} \rangle = N_0(N_0-1)$ which is approximated by N_0^2 since $N_0 \gg 1$. For the excited states,

$$\begin{aligned} \langle \delta\mathbf{\Psi}^\dagger\delta\mathbf{\Psi} \rangle &= \sum_{i,j>0} \psi_i^*\psi_j \langle \mathbf{a}_i^\dagger \mathbf{a}_j \rangle \\ &= \sum_{i>0} \psi_i^*\psi_i N_i, \qquad (7.13) \\ \langle \delta\mathbf{\Psi}^\dagger\delta\mathbf{\Psi}^\dagger\delta\mathbf{\Psi}\delta\mathbf{\Psi} \rangle &= \sum_{ijkl>0} \psi_i^*\psi_j^*\psi_k\psi_l \langle \mathbf{a}_i^\dagger\mathbf{a}_j^\dagger\mathbf{a}_k\mathbf{a}_l \rangle \\ &= \sum_{ij>0} |\psi_i|^2|\psi_j|^2 \left(2N_iN_j(1-\delta_{ij}) + \delta_{ij}N_i(N_i-1)\right) \qquad (7.14) \end{aligned}$$

Hence the energy expectation value is a functional of the mean fields $\sqrt{N_i}\psi_i(\mathbf{r})$,

$$E[\{\sqrt{N_i}\psi_i\}] = \int d\mathbf{r} \left[\frac{\hbar^2}{2m} \left(N_0 \nabla\psi_0^* \nabla\psi_0 + \sum_{i>0} N_i \nabla\psi_i^* \nabla\psi_i \right) + V(\mathbf{r}) \left(n_0(\mathbf{r}) + n_{\rm th}(\mathbf{r}) \right) \right.$$
$$\left. + \frac{g}{2} n_0(\mathbf{r})^2 + 2g n_0(\mathbf{r}) n_{\rm th}(\mathbf{r}) + g n_{\rm th}(\mathbf{r})^2 \right] \quad (7.15)$$

where the substitutions for the density of ground state particles and the density of excited particles,

$$n_{\rm th}(\mathbf{r}) = \sum_i |\psi_i|^2 N_i \quad \text{and} \quad n_0(\mathbf{r}) = |\psi_0|^2 N_0 \qquad (7.16)$$

have been made, and the term $\langle \delta\mathbf{\Psi}^\dagger\delta\mathbf{\Psi}^\dagger\delta\mathbf{\Psi}\delta\mathbf{\Psi} \rangle$ approximated by $g n_{\rm th}^2$. Comparing to the Gross Pitaevski energy functional eq.(B.9), this energy functional eq.(7.15) includes the kinetic, potential, and interaction energies of the excited particles in the Bose gas as well as the energy of the condensate. In addition to the mean

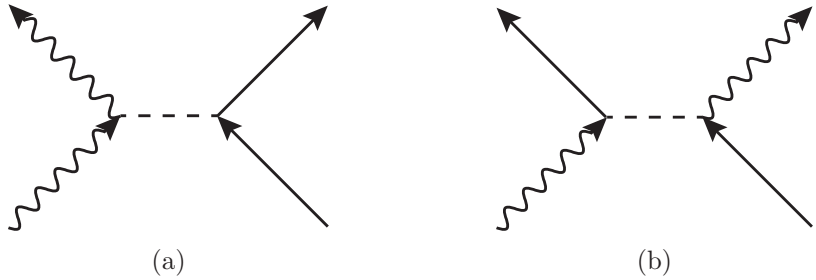

Figure 7.1: Feynman diagrams of the scattering interactions of eq.(7.12). Straight lines represent excited particles (or their propagators) and wavy lines ground state particles. The dashed line represents the mediation of the s-wave scattering interaction, which is presented in the text as a contact interaction so in fact has zero length. Figure 7.1a shows the interaction of the Hartree term $\frac{g}{2}\mathbf{\Psi}_0^\dagger\delta\mathbf{\Psi}^\dagger\mathbf{\Psi}_0\delta\mathbf{\Psi}$ where a condensed and excited particle propagate in the presence of each other. Figure 7.1b shows the interaction of the Fock exchange term $\frac{g}{2}\mathbf{\Psi}_0^\dagger\delta\mathbf{\Psi}^\dagger\delta\mathbf{\Psi}\mathbf{\Psi}_0$ where the condensed and excited particles are exchanged following the interaction.

field interaction term for excitations $gn_{\rm th}^2$, there are two further contributions to the interaction energy included through the $2gn_0n_{\rm th}$ term. One of these is Hartree mean field energy of an excitation propagating in the presence of condensed particles or vice versa. This is represented diagrammatically in fig.7.1a, and arises from $\frac{g}{2}\mathbf{\Psi}_0^\dagger\delta\mathbf{\Psi}^\dagger\mathbf{\Psi}_0\delta\mathbf{\Psi}$ and its Hermitian conjugate in the Hartree Fock Hamiltonian eq.(7.12) (where it has been put into normal order). The other contribution, represented in fig.7.1b is the Fock exchange energy, is due to the necessary symmetry of the state of the gas after an interaction. This arises from $\frac{g}{2}\mathbf{\Psi}_0^\dagger\delta\mathbf{\Psi}^\dagger\delta\mathbf{\Psi}\mathbf{\Psi}_0$ and its Hermitian conjugate in the Hartree Fock Hamiltonian eq.(7.12).

For a Bose gas in thermal equilibrium at temperature T, the single particle wave functions ψ_i and occupation numbers N_i are found by minimising the energy functional eq.(7.15) at constant entropy and constant number (see, for example [11]). It follows that the occupation numbers are given by the Bose Einstein distribution

$$N_i = \frac{1}{e^{(\epsilon_i-\mu)/k_BT}-1} \tag{7.17}$$

with single particle state energies ϵ_i and chemical potential μ. The condensate wave function ψ is given by

$$\left(-\frac{\hbar^2\nabla^2}{2m} + V(\mathbf{r}) + g\left(n_0(\mathbf{r}) + 2n_{\rm th}(\mathbf{r})\right)\right)\psi(\mathbf{r}) = \mu\psi(\mathbf{r}), \tag{7.18}$$

and the single particle wave functions of the excited states ($i > 0$) by

$$\left(-\frac{\hbar^2\nabla^2}{2m} + V(\mathbf{r}) + 2g\left(n_0(\mathbf{r}) + n_{\rm th}(\mathbf{r})\right)\right)\psi_i(\mathbf{r}) = \epsilon_i\psi_i(\mathbf{r}). \tag{7.19}$$

These three simultaneous equations (eq.(7.17), eq.(7.18) and eq.(7.19)) describe the finite temperature Bose gas under the Hartree Fock mean field approximation. Equation (7.18) and eq.(7.19) are a set of schrödinger equations that describe particles with kinetic energy $-\hbar^2\nabla^2\psi_i/2m$, trapped in non-linear effective potentials. Compared with the Gross Pitaevskii equation, the effective potential experienced by the ground state in equation eq.(7.18) has an additional non-linear term that represents the interactions between the ground state and thermal component of the Bose gas.

Like the Gross Pitaevskii equation, eq.(7.18) and eq.(7.19) are non-linear due to the density terms. In the $T = 0$ limit where $n_{\rm th}$ becomes zero, one recovers the Gross Pitaevskii equation exactly. At finite temperature, the presence of the thermal density $n_{\rm th}(\mathbf{r})$ in eq.(7.18), and the condensate density $n_0(\mathbf{r})$ in eq.(7.19), couple the ground state and excited state solutions. This coupling makes these equations difficult to work with analytically. However, in the next section, we use the semi-ideal approximation where one considers only the mean field repulsion of the condensate on the thermal cloud, ignoring the thermal mean fields effect on the condensate. Since the thermal density is typically an order of magnitude lower than that of the condensate, the condensate and thermal densities can be still accurately estimated. Furthermore, the significant simplification that the semi-ideal approximation provides allows us to find analytic expression for both n_0 and $n_{\rm th}$. This will be useful in analysing the density profiles that we measure experimentally in Ch.8.

7.2.1 Semi-Ideal Approximation

Figure 7.2 shows a false colour absorption image of a cloud after it has been released from the trap and allowed to expand for 2 ms. The brightest colours show the areas where the density is highest. The image shows a distinct central peak in the density where the condensate is located, and broader tails to the left and right from the non-condensed atoms. The axial density profile of the gas is shown below the

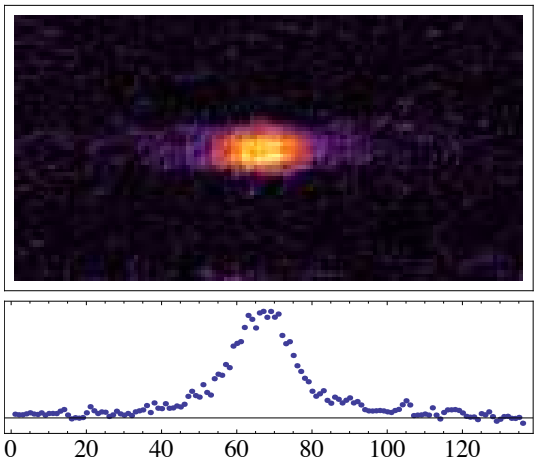

Figure 7.2: False colour absorption image of a partially condensed cloud. The brightest colors correspond to the highest density. The condensate is the yellow region, while the purple tails to the left and right are thermal atoms. Directly below the image is the density profile after integrating the image over the vertical direction. The horizontal axis is labelled by pixels. Each pixel is $3.45\,\mu$m and the magnification is 1:1.

image in fig.7.2 after summing over the pixels in the vertical ($\hat{\mathbf{y}}$) direction. We use the common technique of fitting a bimodal distribution to the axial density, with a component for the condensate density and another for the density of thermal atoms (or 'thermal cloud'[5]). This technique allows us to find useful parameters for the cloud including the condensed and thermal fractions, the condensate width, and estimates of the chemical potential and temperature of the gas. The bimodal distribution consists of the Thomas Fermi density for the condensate - proportional to $-V(\mathbf{r})$, and a gaussian distribution for the thermal cloud. This distribution was used in some of the first experiments in which a condensate was observed [5, 6]. In these experiments the condensate was allowed to expand for a time long enough such that the thermal density is a reflection of the gaussian momentum distribution, irrespective of the original distribution in the trap.

For experiments such as ours where the trap potential is harmonic, this bimodal distribution is

$$n_0(z) = a\left(1 - \left(\frac{z - z_0}{Z_0}\right)^2\right)^2 + b\exp\left(-\frac{(z - z_1)^2}{2\sigma^2}\right) \tag{7.20}$$

[5]In the Hartree Fock approximation it is a valid distinction to make between condensed and non-condensed atoms by referring to a condensate and a thermal cloud since the gas is assumed to be in a Fock state with a distinct ground state. However, as we will discuss later, this is no longer a good approximation to make at temperatures below μ/k_B.

where $a,\ b,\ z_0,\ z_1,\ Z_0$ and σ are fit parameters. However, we measure the cloud's density after a relatively short expansion time $\omega_z t \ll 1$. Although our trap potential is harmonic, it is not immediately clear how close the thermal density is to being gaussian, particularly in the central region where the condensate is present. We use a simple model based on the Hartree Fock approximation (eq.(7.17), eq.(7.18) and eq.(7.19)) to find a first order correction to the gaussian thermal density profile of an ideal gas due to its interaction with the condensate [131].

The particles in the thermal cloud experience an effective potential from eq.(7.19), $V_{\rm eff} = V(\mathbf{r}) + 2g(n_0(\mathbf{r}) + n_{\rm th}(\mathbf{r}))$. For an ideal gas this reduces to $V_{\rm eff} = V(\mathbf{r})$. For a 'semi ideal' gas in which thermal particles interact with the condensate but not other thermal particles, a first correction to the ideal gas is made by retaining the condensate density term as well. This term is typically much stronger than the mean field interaction of the thermal cloud with itself, which we neglect. The condensate density is taken to be the Thomas Fermi density

$$n_0(\mathbf{r}) = (\mu - V(\mathbf{r}))/g \quad \text{for } V(\mathbf{r}) < \mu. \tag{7.21}$$

In our anisotropic trap potential

$$V(\mathbf{r}) = \frac{1}{2}m\omega_r^2(\rho^2 + (z/\lambda)^2) \quad \text{where } \lambda = \frac{\omega_r}{\omega_z}, \tag{7.22}$$

given here in cylindrical coordinates (ρ, ϕ, z), and with trap frequencies ω_r and ω_z. The chemical potential is

$$\mu = \frac{1}{2}m\omega_r^2\left(\frac{Z_0}{\lambda}\right)^2 \tag{7.23}$$

in terms of the trap frequencies and condensate length $2Z_0$ which is taken here as a fit parameter. Thus, the effective potential shown in fig.7.3 experienced by the thermal cloud is given by

$$V_{\rm eff}(\rho, z) - \mu = \begin{cases} -a(\rho^2 - P_0^2(z)) & 0 < \rho < P_0(z),\ z < Z_0 \\ a(\rho^2 - P_0^2(z)) & \rho > P_0(z),\ z < Z_0 \\ a(\rho^2 - P_0^2(z)) & z > Z_0 \end{cases} \tag{7.24}$$

$$\text{where } P_0(z) = \frac{1}{\lambda}\sqrt{Z_0^2 - z^2} \quad \text{and } a = \frac{1}{2}m\omega^2. \tag{7.25}$$

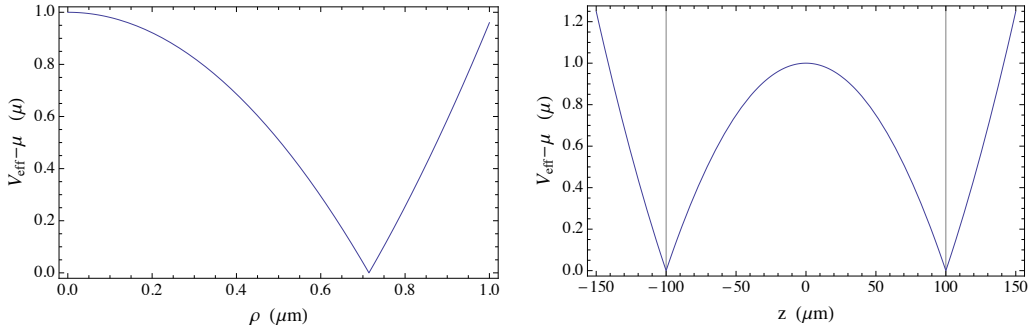

(a) (b)

Figure 7.3: The effective potential experienced by the thermal cloud in the semi ideal gas approximation eq.(7.24). Figure 7.3a shows the radial potential at $z = 0$, up to $1\,\mu$m. The effective potential is rescaled in units of the chemical potential μ. Figure 7.3b shows the axial potential. The two vertical lines indicate $\pm Z_0$, which we have set here at $\pm 100\,\mu$m.

A semi classical approximation of the thermal cloud can now be made in the energy of a thermal particle is taken to be $\epsilon = \mathbf{p}^2/2m + V_{\rm eff}(\mathbf{r})$, where $\mathbf{p}$ is the particle momentum [131, 132, 129]. Using the Bose Einstein distribution the phase space density of the thermal cloud is,

$$f(\mathbf{r},\mathbf{p}) = \left[\exp\left(\frac{q^2+p_z^2}{2mk_BT} + \frac{V_{\rm eff}(\rho,z)-\mu}{k_BT}\right) - 1\right]^{-1}, \tag{7.26}$$

where $q^2 = p_x^2 + p_y^2$. Equation (7.26) and eq.(7.21) together give a self consistent solution to the semi classical approximations of the Hartree Fock equations with the interaction strength between thermal particles set to zero.

In [131], the density distribution is found by first integrating over momentum space. Our work here differs from this since we wish to use this model to describe the axial density distribution after the cloud has been released from the trap. To do so we need to find the axial phase space distribution $f(p_z, z)$ by integrating over $p_x,\ p_y,\ \rho$ and ϕ. Our method of integration is given in appendix C, and yields the result

$$\frac{f(z,p_z)}{2\pi\sigma_r^2(h/\lambda_{\rm dB})^2} = \begin{cases} 2{\rm Li}_2\left(e^{-\frac{p_z^2}{2mk_BT}}\right) - {\rm Li}_2\left(e^{-\frac{p_z^2}{2mk_BT}}e^{\frac{1}{2\sigma_z^2}(z^2-Z_0^2)}\right) & |z| < Z_0 \\ {\rm Li}_2\left(e^{-\frac{p_z^2}{2mk_BT}}e^{-\frac{1}{2\sigma_z^2}(z^2-Z_0^2)}\right) & |z| > Z_0. \end{cases} \tag{7.27}$$

The polylogarithmic functions are defined as ${\rm Li}_n(x) = \sum_{k=1}^{\infty} x^k/k^n$, the thermal deBroglie wavelength is $\lambda_{\rm dB} = h/\sqrt{2\pi mk_BT}$, and the widths are $\sigma_r^2 = k_BT/m\omega_r^2$

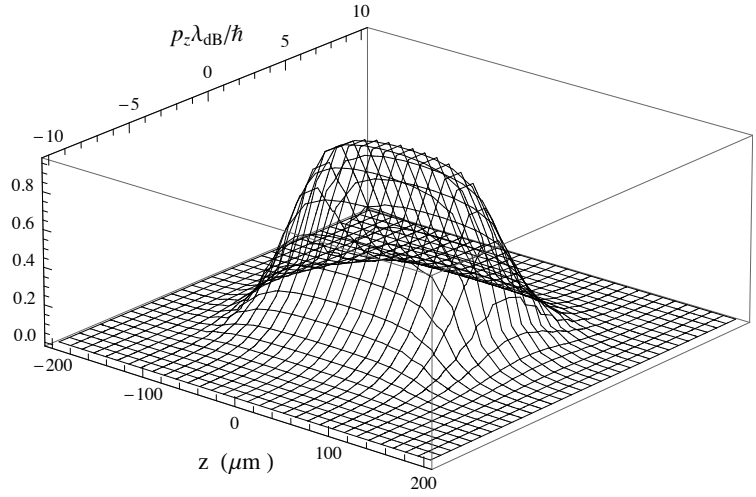

Figure 7.4: The axial phase space distribution of thermal cloud in the trap with the semi ideal gas approximation eq.(7.27). The axial position is shown in μm, and the axial momentum shown in dimensionless units of $p_z\lambda_{dB}/\hbar$. The axial phase space density is shown normalised to its peak value which occurs at $f(0,0)$. For the profile $f(z,p)$ shown, a temperature of 100 nK was used, and the length Z_0 of the condensate set to 100 μm. The sum in the poly-logarithms in eq.(7.27) where evaluated up to $k = 10$.

and $\sigma_z^2 = k_B T/m\omega_z^2$. The first order expansion (k=1) of the polylogarithms is equivalent to replacing the Bose Einstein distribution by the Maxwell Boltzmann distribution. In this case momentum and spatial parts of eq.(7.27) are separable. It is then clear that outside the condensate, $z > Z_0$, the thermal cloud has gaussian tails. Inside the condensed region, $z < Z_0$ the axial density is depleted from its value at $z = Z_0$ due to the presence of the condensate.

Figure 7.4 shows the axial phase space distribution $f(p_z, z)$ calculated from eq.(7.27) with $T = 100\,\text{nK}$, $Z_0 = 100\,\mu\text{m}$ and $\omega_z = 2\pi \times 10\,\text{Hz}$. It can be seen in this plot that at constant z, the function $f(p_z, z)$ is close to Gaussian in form. At constant p_z however, the shape of $f(p_z, z)$ is not gaussian. This is because of the anharmonic shape of the effective potential $V_{\text{eff}}(\mathbf{r})$, which takes into account the spatially dependent mean field repulsion of the condensate. However, for $z > Z_0$ it takes a gaussian form since here the effective potential is the same as the harmonic trap potential. The general shape of the distribution is in fact quite similar to that of a classical gas in the potential V_{eff}, as can be found by taking only the $k = 1$ term in the expansion of the poly-logarithms in eq.(7.27). The exact form of $f(z, p_z)$ is altered slightly by the higher order terms. However, the series expansion of the poly-logarithms in eq.(7.27) converge rapidly with respect to k. The function shown

in fig.7.4 was calculated up to the $k = 10$ term only. With $k = 15$ the difference in the function was found to be negligible, and for $k = 5$ only a small variation was observed of $\lesssim 1\%$.

Integrating eq.(7.27) over p_z gives

$$n_{\rm th}(z) = 2\pi\sigma_r^2 \left(\frac{h}{\lambda_{\rm dB}}\right)^3 \begin{cases} 2\,{\rm Li}_{5/2}\,(1) - {\rm Li}_{5/2}\left(e^{\frac{1}{2\sigma_z^2}(z^2-Z_0^2)}\right) & |z| < Z_0 \\ {\rm Li}_{5/2}\left(e^{-\frac{1}{2\sigma_z^2}(z^2-Z_0^2)}\right) & |z| \geq Z_0 \end{cases} \tag{7.28}$$

which is the the same axial density distribution described in [131, 132]. For the thermal and condensate densities to consistently satisfy the Hartree Fock equations in the semi ideal limit, the number of thermal and condensed atoms must satisfy

$$N_0 + N_{\rm th} = N, \tag{7.29}$$

for total atom number N. Integrating $n_{\rm th}(z)$ gives $N_{\rm th}$, while the number of condensed atoms is found by integrating the Thomas Fermi density eq.(7.21):

$$\begin{aligned} N_{\rm th} = (2\pi)^{3/2}\sigma_r^2\sigma_z \left(\frac{h}{\lambda_{\rm dB}}\right)^3 \sum_{k=1}^{\infty} \frac{1}{k^3} \Bigg[& 4Z_0 \frac{\sqrt{k}}{\sqrt{2\pi}\sigma_z} \\ & + e^{k\frac{Z_0^2}{2\sigma_z^2}} \left(1 - {\rm erf}\left(\frac{\sqrt{k}}{\sqrt{2\pi}\sigma_z} Z_0\right)\right) + e^{-k\frac{Z_0^2}{2\sigma_z^2}} {\rm erfi}\left(\frac{\sqrt{k}}{\sqrt{2\pi}\sigma_z} Z_0\right) \Bigg] \end{aligned} \tag{7.30a}$$

$$N_0 = \frac{a_{\rm ho}}{15a} \left(\frac{m\omega_r}{\hbar\lambda^{5/3}}\right)^{5/2} Z_0^5 \tag{7.30b}$$

Here ${\rm erf}(z) = \frac{1}{\sqrt{\pi}} \int_{-z}^{z} dt\, e^{-t^2}$ is the error function, ${\rm erfi}(z) = \frac{1}{\sqrt{\pi}} \int_{-z}^{z} dt\, e^{t^2}$, $a_{\rm ho} = \sqrt{\hbar/m\omega_{\rm ho}}$ is the geometric mean harmonic oscillator length and a the s-wave scattering length. The series for $N_{\rm th}$ converges rapidly and can be truncated after the first few terms to give an expression that is quick to calculate.

For a semi-ideal Bose gas in thermal equilibrium, eq.(7.29), eq.(7.30a) and eq.(7.30b) completely fix the relationship between N_0, $N_{\rm th}$, μ (or equivalently Z_0) and T for a given trap harmonic potential (ω_r and λ). Any two parameters can be chosen for a consistent solution of the total density, with all other parameters found through these equations. This may require the inversion of eq.(7.30a) depending which parameters are initially chosen, which can be done numerically (e.g. through an iterative process) in a short amount of time $< 1\,$s. Alternatively, an approximate relation for

N_0/N as function of T given in [131] can be used.

7.2.2 Expansion of Thermal Cloud after Release

While the in trap density distribution in a trap [131], and the expansion of a purely thermal cloud above T_c [133] have been discussed in the literature, we do not find an analytic description of the expansion of a partially condensed cloud for short times $\omega_z t \ll 1$ after release at $t = 0$.[6] An analytical expression for this expansion is derived here from the axial phase space distribution eq.(7.27) of the semi-ideal thermal component. In the semi-ideal case the condensate expands as described in [121] and sec.5.3.1. From this we assume that the condensate density decreases rapidly after release, and the mean field potential is sufficiently weak that it no longer influences the axial distribution of thermal atoms.[7] Hence we assume the atoms move along trajectories defined by the axial phase space distribution $f(p, z)$ in the trap at the instant of release, given by eq.(7.27). The relation eq.(7.29) and the equations (7.30a) and (7.30b) still hold after release, fixing the relation between $n_{\rm th}$ and n_0 as before.

To calculate how the axial density distribution evolves with time, we use the same method as given for the ballistic expansion of a classical gas in sec. 3.2.2, but start instead from the axial phase distribution 7.27. After expansion time t, an atom found at position z' which was initially at z, must have momentum $p = m(z' - z)/t$. To find the axial density of the expanding thermal cloud $n_{\rm th}(z', t)$, we make this substitution for p in the initial phase space distribution $f(p, z)$, then integrate over all possible initial positions, z. Thus,

$$n(z', t) = -\frac{m}{t} \int_{\infty}^{-\infty} \mathrm{d}z f(z, m\frac{z' - z}{t}) \tag{7.31}$$

The integrand, $f(z, m(z' - z)/t)$, takes on different forms in the regions $|z| > Z_0$

[6] As noted above, for longer expansion times $\omega_z t \gg 1$, the density distribution of the expanded cloud takes the same form as the initial momentum distribution, and the bimodal function eq.(7.20) provides a good description of the total density.

[7] The condensate itself follows a ballistic expansion once the mean field interaction energy is converted to kinetic energy. For our condensate the expansion is ballistic after at most a few hundred μs (see sec.5.3.1). Only during the initial few hundred μs does the mean field have significant effect, and for highly elongated traps this is almost exclusively in the radial direction where there is a high gradient in the condensate density.

Parameter	fig.7.5a	fig.7.5b	fig.7.5c
atom number	10^4	10^4	10^4
temperature (nK)	52.2	13.6	208.9
T/T_c	0.2	0.5	0.8
N_0	9724	7483	2687
Z_0 (μm)	73.0	69.3	56.5
$k_{\max}$	10	10	10
time of flight (ms)	2, 16, 32	2, 16, 32	2, 16, 32
peak density ($\mu\mathrm{m}^{-1}$)	126.7, 126.6, 126.2	116.9, 114.3, 110.1	86.9, 76.9, 65.4

Table 7.1: Table of parameters of the expanding semi-ideal Bose gases shown in fig.7.5.

and $|z| < Z_0$. Equation (7.31) is evaluated separately over these regions. Let $f\left(z', p(z,t)\right) = 2\pi\sigma_r^2(h/\lambda_{\mathrm{dB}})^2(f_+(z',z,t) + f_-(z',z,t))$ where

$$f_+(z',z,t) = \mathrm{Li}_2\left(e^{-\frac{(z'-z)^2}{2\sigma_z^2\tau^2}} e^{-\frac{z^2-Z_0^2}{2\sigma_z^2}}\right), \tag{7.32}$$

$$f_-(z',z,t) = \left[2\mathrm{Li}_2\left(e^{-\frac{(z'-z)^2}{2\sigma_z^2\tau^2}}\right) - \mathrm{Li}_2\left(e^{-\frac{(z'-z)^2}{2\sigma_z^2\tau^2}} e^{\frac{z^2-Z_0^2}{2\sigma_z^2}}\right)\right], \tag{7.33}$$

where $\tau = \omega_z t$. Then the thermal density after release is given by

$$\frac{n_{\mathrm{th}}(z',t)}{2\pi\sigma_r^2(h/\lambda_{\mathrm{dB}})^2} = \underbrace{\int_{-\infty}^{\infty} \mathrm{d}z f_+(z,z',t)}_{I_1} - \underbrace{\int_{-Z0}^{Z0} \mathrm{d}z f_+(z,z',t)}_{I_2} + \underbrace{\int_{-Z0}^{Z0} \mathrm{d}z f_-(z,z',t)}_{I_3} \tag{7.34}$$

The three integrals evaluate to

$$I_1 = \frac{h}{\lambda_{\mathrm{dB}}} \sum_{k=1}^{\infty} \frac{\alpha^{-1/2}}{k^{5/2}} e^{-k\frac{z'^2}{2\sigma_z^2\alpha}} e^{k\frac{Z_0^2}{2\sigma_z^2}}, \tag{7.35a}$$

$$I_2 = \frac{1}{2}\frac{h}{\lambda_{\mathrm{dB}}} \sum_{k=1}^{\infty} \frac{\alpha^{-1/2}}{(k)^{5/2}} e^{-k\frac{z'^2}{2\sigma_z^2\alpha}} e^{k\frac{Z_0^2}{2\sigma_z^2}} \times \left[\mathrm{erf}\left(\sqrt{\tfrac{k}{2\alpha}}\tfrac{\alpha Z_0 - z'}{\sigma_z\tau}\right) + \mathrm{erf}\left(\sqrt{\tfrac{k}{2\alpha}}\tfrac{\alpha Z_0 + z'}{\sigma_z\tau}\right)\right], \tag{7.35b}$$

$$I_3 = \frac{h}{\lambda_{\mathrm{dB}}} \sum_{k=1}^{\infty} \frac{1}{(k)^{5/2}} \left\{\mathrm{erf}\left(\sqrt{\tfrac{k}{2}}\tfrac{Z_0 - z'}{\sigma_z\tau}\right) + \mathrm{erf}\left(\sqrt{\tfrac{k}{2}}\tfrac{Z_0 + z'}{\sigma_z\tau}\right) - \frac{1}{2}\beta^{-1/2} e^{k\frac{z'^2}{2\sigma_z^2\beta}} e^{-k\frac{Z_0^2}{2\sigma_z^2}} \left[\mathrm{erf}\left(\sqrt{\tfrac{k}{2\beta}}\tfrac{\beta Z_0 - z'}{\sigma_z\tau}\right) + \mathrm{erf}\left(\sqrt{\tfrac{k}{2\beta}}\tfrac{\beta Z_0 + z'}{\sigma_z\tau}\right)\right]\right\}, \tag{7.35c}$$

where $\alpha = 1 + \tau^2$, $\beta = 1 - \tau^2$.

Figure 7.5 shows the theoretical prediction of the axial density $n(z,\tau)$ for 10^4 atoms after the trap potential is turned off. Figures 7.5a, 7.5b and 7.5c show the

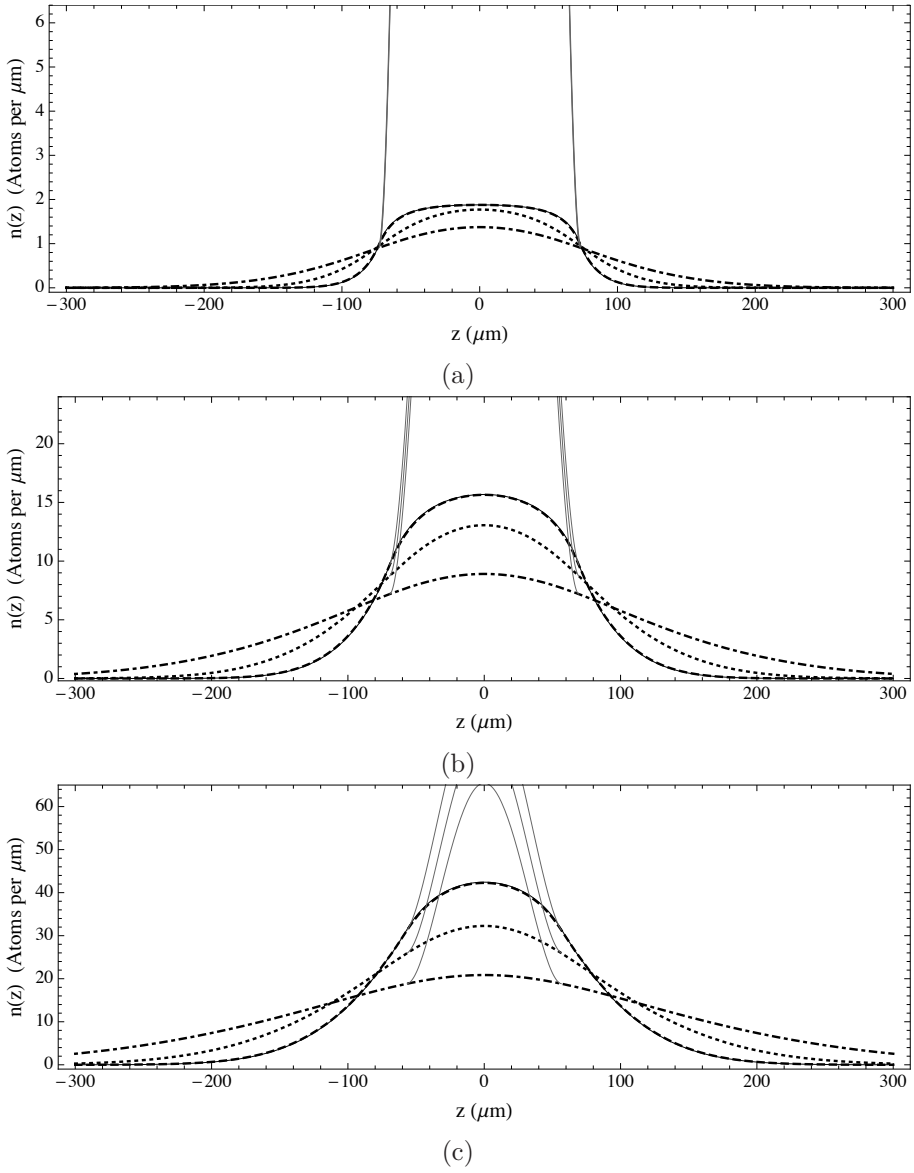

Figure 7.5: Total axial density $n(z)$, and thermal axial density $n_{\rm th}(z)$, after release from the magnetic trap as predicted by eq.(7.34). Figure 7.5a shows the densities for a cloud at temperature $T = 0.2T_c$. The solid lines show the thermal (thick line) and total density (thin lines) in trap. The dashed line shows the thermal density after 2 ms ($\tau = 1/8$) of expansion, the dotted line after 16 ms ($\tau = 1$), and the dot-dashed line after 32 ms ($\tau = 2$). Figure 7.5b shows the total and thermal densities for a cloud at $0.5T_c$, with solid, dashed, dotted and dot-dashed lines as before. In this image the variation in the total density in the condensed region ($z < Z_0$) can be resolved. The solid grey lines show the total density in this region for each time, and the solid black line shows the thermal density in trap. Figure 7.5c shows the total and thermal densities for a cloud at $0.8T_c$. Line styles are the same as fig.7.5b. All plots are for a gas of 10^4 atoms in the same trap with $\omega_z = 2\pi \times 10\,\text{Hz}$, and $\omega_\rho = 2\pi \times 1.4\,\text{kHz}$. The parameters for each figure are summarised in table 7.1.

density for clouds at three different temperatures $T/T_c = 0.2$, 0.5 and 0.8. A detailed set of parameters for the profiles shown in fig.7.5 are given in table 7.1. For each temperature, the density is shown at four different times: at the instant of release (solid lines), at $\tau = \frac{1}{8}$ (dashed lines), $\tau = 1$ (dotted lines) and at $\tau = 2$ (dot-dashed lines). In our experiment we typically take an image of the cloud 2 ms after it is released, which for our trap frequency, $\omega_z = 2\pi \times 10\,\mathrm{Hz}$, corresponds to $\tau = \frac{1}{8}$. Using the examples in fig.7.5, we will now discuss the behaviour of the density of the expanding cloud for $\tau \ll 1$ and for $\tau \gg 1$.

When τ is small compared to 1, the first integral I_1 almost completely describes the density for $|z| > Z_0$. Here the effective potential of the cloud when trapped is just the harmonic trap potential. At these short expansion times, few atoms from the central region reach this outer region, and hence the influences of I_2 and I_3 are small. To first order in k the density for $z > Z_0$ is gaussian, with width $\sigma_z\sqrt{1+\tau^2}$ which is the same width as for an ideal thermal gas (see 3.2.2 for example). The amplitude of the gaussian to which these tails belong is increased by factor $\exp\left(\frac{Z_0}{2\sigma_z^2}\right) = \exp\left(\frac{\mu}{k_\mathrm{B}T}\right)$ due to the repulsive effective potential in the central region $|z| < Z_0$. The density in the central region from I_1 alone would be incorrect, as it does not take into account the shape of the mean field potential. Therefore, the second integral I_2 is used to cancel the contribution to the density from I_1 that results from particles it assumed were in the central $|z| < Z_0$ at $\tau = 0$. The third integral I_3 then describes correctly the density of the expanding cloud due to particles initially in the central region, taking into account the mean field influence of the condensate. For temperatures close to T_c where the condensate is small as in fig.7.5c, the result of I_3 is close to the central region of the gaussian predicted by I_1. For low temperatures as in fig.7.5a, I_3 gives a flatter density profile over the central region close to the value $n(z = z_0)$.

For longer expansion times $\tau > 1$, the density distribution becomes less dependent on the initial density distribution, as can be seen from the dot-dashed lines in fig.7.5 for all the temperatures shown. As $\tau \to \infty$, the density distribution of the expanding cloud tends to the shape of its momentum distribution, which is a Bose enhanced gaussian with width $\sigma_p = \sqrt{m k_\mathrm{B} T}$. The width of this density distribution tends to $\sigma_p \frac{\tau}{m\omega_z} = \sqrt{\frac{k_\mathrm{B}T}{m}}t$.

In the next section, we compare the results of the semi-ideal Bose gas model to axial density profiles measured from our experiment. By fitting this model to the measured profiles we can accurately predict various parameters of the Bose gas such as its temperature or condensed fraction N_0/N. This technique is useful in the analysis of the data in Ch.8.

7.3 Measurement of Equilibrium Density Distribution

We now describe an experiment in which a partially condensed Bose gas is produced then held in the trap for a sufficient length of time to reach its thermal equilibrium. The Bose gas is then released and an image taken from which the axial density profile is found. This experiment is repeated at different temperatures, so density profiles with different thermal fractions are measured. Such density profiles are shown in fig.7.7. We then discuss the methods of fitting to the measured profiles the theoretical density profiles of the ideal model given by eq.(7.20), and of the semi-ideal model given by eq.(7.34) and eq.(7.35). The objective of this experiment is to test how well the semi-ideal gas model fits the measured density profiles of clouds at various temperatures compared to the ideal gas model.

7.3.1 Measurement of Equilibrium Axial Density Profile

In the experiment a Bose Einstein condensate emerges during the final stage of an 8.5 s evaporation ramp. In this stage the frequency of the rf knife is reduced from 1.67 MHz to 1.585 MHz over 1 s, where it is then held for 100 ms to increase the condensed fraction further. The frequency is then increased over the next 10 ms by 10 kHz, and held for a further 34 ms before switching the rf off.[8] The gas is then left in the trap to thermalise for at least 500 ms to reach its equilibrium density distribution.

After a few collisions and a few axial trap oscillations periods we expect the Bose gas to essentially be in thermal equilibrium. The calculated peak density in the

[8] In some experiments we perform, the rf knife is left on while the Bose gas remains trapped. This maintains a high condensate fraction despite the slow heating of the gas due to technical noise in the experiment (e.g. from noise in the chip wire currents).

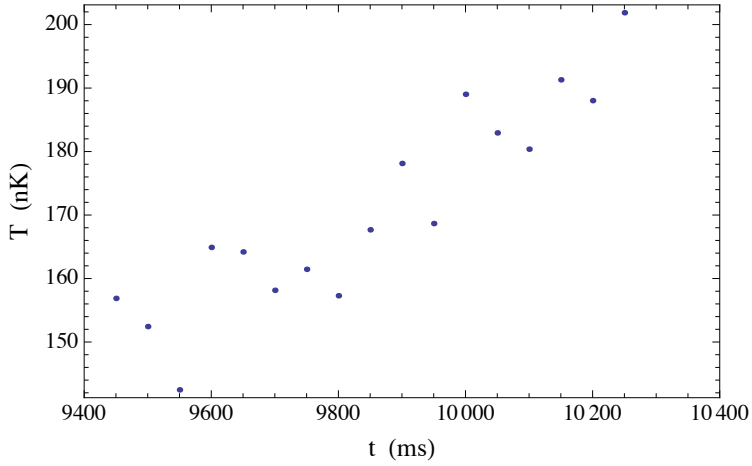

Figure 7.6: The temperature of the partially condensed Bose gas in the magnetic trap as a function of time. The temperature was estimated from the fraction of condensed atoms N_0/N using the semi-ideal gas model. From this data we estimate a heating rate of approximately $50\,\mathrm{nK\,s^{-1}}$.

thermal fraction, $n_0 = \zeta(\frac{3}{2})\lambda_{\mathrm{dB}}^{-3}$, suggests a collision rate of about 100 Hz for the cloud which has an equilibrium temperature of between 100 and 150 nK. The axial trap frequency is 10 Hz. We therefore expect that 500 ms is enough for thermal equilibrium to be approached.

Meanwhile the gas heats up slowly due to technical noise in the experiment. We view this slow heating as a quasi-static processes. The longer the gas is held in the trap, the hotter it becomes, and the higher the thermal fraction. By measuring the fraction of condensed atoms at time t we can estimate the temperature of the cloud as a function of time [9]. Figure 7.6 shows the temperature of clouds against the time they were held in the trap. The graph suggests a heating rate of approximately $50\,\mathrm{nK\,s^{-1}}$.

After the thermalisation period the trap is rapidly switched off by reducing the chip wire currents to zero which takes less than $100\,\mu$s. Once off only the uniform bias fields remain so the atoms are no longer trapped. The x-bias field is reduced from 35 G to 3 G over 1 ms, where it sets the quantisation axis for absorption imaging. After 2 ms of free fall and expansion, an absorption image of the gas is taken with a $100\,\mu$s pulse of the imaging beam. A background image is taken 200 ms later when the cloud is no longer present. The absorption image is processed to give a 2D array of the cloud's density distribution in terms of atoms detected per pixel. We find

[9] We explain how we measure this in the sections that follow

the axial density profile of the clouds from these images by summing over the pixels in the vertical direction ($\hat{\mathbf{y}}$). Three examples of these measured profiles for clouds at three different temperatures are shown by the data points in fig.7.7. However, before summing to find $n(z)$ we process the images further to reduce some of the noise in the images not related to the density of the clouds.

Small differences in the image beam intensity between the absorption and background images lead to a mean background offset in the counts per pixel of the processed image. This mean offset is measured over a region where no atoms are present, then subtracted from all pixels in the image. The remaining counts are summed over the region where the cloud is present to give an estimate of the atom number. In addition to a background offset, fringes appear in the processed image due to optical aberrations together with small differences in the imaging beam path between the two images. These are filtered using a notch filter on the Fourier transform of the processed image in which a distinct feature due to these fringes is visible. Finally a short but wide region is selected around the cloud image, and summed over the (short) $\hat{\mathbf{y}}$ direction to give the axial density profile, $n(z) = \int \mathrm{d}x\mathrm{d}y\, n(x, y, z)$. The region is kept short to minimise the distortion of the density profile due to artefacts elsewhere in the image, yet tall enough (a few times the clouds r.m.s. width) to effectively include all atoms. The density profile is in fact a discrete version $n(z)$, specifically $n(z_i)\Delta z$, where z_i is the axial coordinate of the i^{th} column of pixels, and $\Delta z = 3.45\,\mu$m is the pixel width.

Figures 7.7a, 7.7b and 7.7c show axial density profiles measured in this way for three different clouds with condensed fractions of 0.6, 0.6 and 0.3 respectively. The blue data points show the measured density profiles $n(z_i)$, shown normalised to a peak density of 1. We have fitted both the ideal gas model of eq.(7.20), and the semi-ideal gas model of eq.(7.34) and eq.(7.35) to these data points. The solid black lines show the fitted total denisty $n(z)$ from the semi-ideal model, and the dotted line its thermal part $n_{\text{th}}(z)$. The dot-dashed line shows the fitted Gaussian profile of the thermal density $n_{\text{th}}(z)$ in the ideal gas model. Testing how well the semi-ideal model fits the data, and comparing it to the commonly used ideal gas model is the focus of this experiment, which we discuss in sec.7.3.3 below. Before our discussion, we explain in next section, sec.7.3.2, how we fit these two different models to the

measured density profiles.

7.3.2 Fitting to the Axial Density Profile

The lines plotted against the data in fig.7.7 show a Thomas Fermi density profile for the condensate combined with that of either an ideal or semi ideal thermal cloud fitted to the measured axial density. The ideal gas model given in (7.20) for the expanding thermal cloud is often used in experiments with Bose Einstein condensates where a thermal cloud is visible. However, this model fails to take into account the influence the condensate has on the thermal density. Its accuracy in describing the thermal cloud in the vicinity of the condensate is not clear, especially for short expansion times $\tau \ll 1$. The semi ideal model of the expanding thermal cloud is that developed in here in sec.7.2.2, and is based on the in trap model of [131]. The density profiles are found from equations (7.29), (7.34) and (7.35). This model considers the first order effect of the condensate on the thermal cloud and should therefore provide a more accurate fit to the experimental data than the ideal model. We will compare the fits of the two models in sec.7.3.3. In this section we explain the methods of fitting the ideal and semi-ideal models to the data.

The dot-dashed lines in fig.7.7 show the ideal thermal gas model fitted to our data. To fit this model we first select data of the tails of the thermal cloud only, excluding the central region where condensed atoms are present. A Gaussian function is fitted by method of least squares to the thermal tails. [10] The fitted Gaussian is then used to represent the thermal component of the combined bimodal distribution. The full bimodal distribution of this Gaussian plus the Thomas Fermi density for the condensate are then fitted over the full range of the density profile. For the fit to converge reliably we find a good initial estimate of the condensate fit parameters is necessary. These initial estimates are found by fitting a pure Thomas Fermi profile to selected data in the centre of the profile where the condensate is present. This process is similar to that discussed in [110]. We find the fitted function can be sensitive to the size of the central region excluded when we initially fit to the thermal tails. In fig.7.7 the total bimodal density functions $n(z)$ from the ideal model are

[10] The fit is found in MATHEMATICA, which finds the parameter set that minimises the squared distance of data points to the fitted function. The method of numerical minimisation in parameter space is automatically chosen by mathematica.

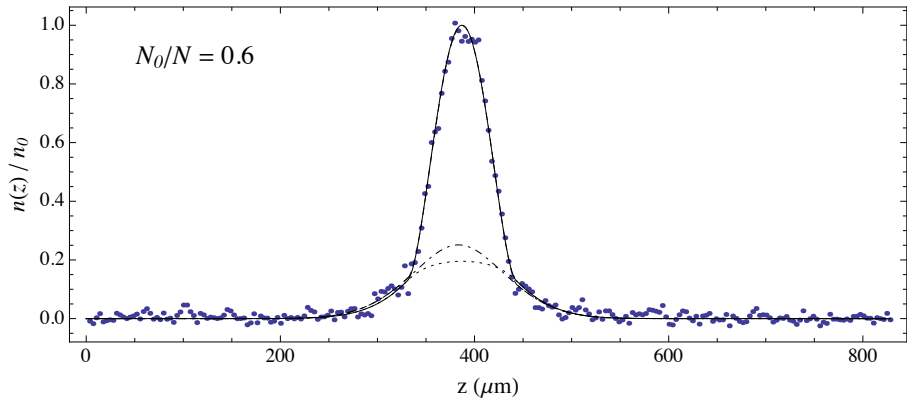

(a)

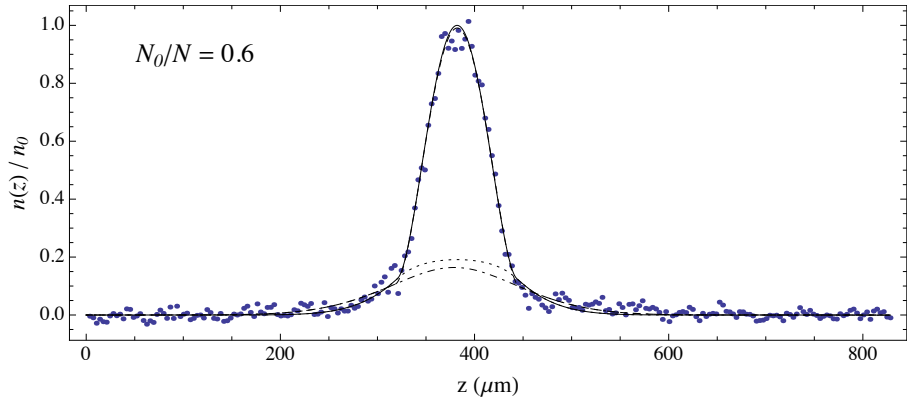

(b)

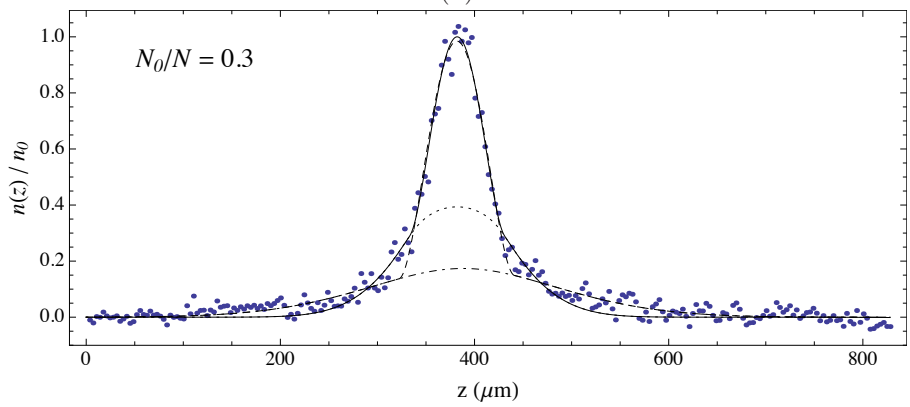

(c)

Figure 7.7: Measured and theoretical density profiles of three different partially condensed clouds. Figure 7.7a shows the density profile for a cloud with a condensed fraction of 0.6 and total atom number of 9.6×10^3. The density is shown normalised to a peak density of 1. The data points show the density found from absorption images of the cloud in our experiment. The solid black line shows the density of the semi-ideal model eq.(7.34) fitted to the data points. The dotted line shows the density of thermal atoms, $n_{\rm th}(z)$, predicted by this model. The dot-dashed line shows the Gaussian thermal density profile estimated from the ideal gas model fitted to the data points. Figure 7.7b shows the axial density of a cloud also with $N_0/N = 0.6$, but a higher atom number of 1.07×10^4, and therefore slightly higher absolute temperature. The solid, dotted and dot-dashed lines are the fitted profiles of the semi-ideal and ideal models as in fig.7.7a Figure 7.7c shows the axial density of a cloud with a lower condensed fraction of 0.3, and atom number of 8.5×10^3. The lines are indicated for fig.7.7a and fig.7.7b.

shown by the dashed line, and the ideal thermal component $n_{\rm th}(z)$ shown by the dot-dashed line.

The solid lines in fig.7.7 show the axial density $n(z)$ from the semi-ideal model fitted to the experimental data, and the dotted line the thermal part of this density $n_{\rm th}(z)$. To fit the semi ideal model to experimental profiles is actually more straight forward than for the ideal model because the entire function can be fit at once, and depends on just three fit parameters where thermal equilibrium is assumed. Two of these control the widths of the condensed and thermal components, and the third defines the centre of the distribution. From the model given by equations (7.29), (7.34) and (7.35), we generate a 3D interpolation function for the axial density $n(z, T/T_c, Z_0)$, as a function of z, the fractional temperature T/T_c and the condensate width Z_0. The translated function $n(z - z_c, T/T_c, Z_0)$, centred at z_c, is then fitted to the experimental data using the method of least squares. The three fit parameters are z_c, T/T_c and Z_0. In the density profiles of fig.7.7 the total density $n(z)$ for the semi ideal model is shown by the solid line, and the semi-ideal thermal component $n_{\rm th}(z)$ shown by the dotted line.

7.3.3 Discussion of Measured and Fitted Density Profiles

The main reason for fitting a model to the density distribution is to determine what component of the total density is due to the condensate and what component is due to the thermal cloud. Through determination of this, the thermal fraction N_{th}/N of the total atom number can be calculated. From this other parameters such as the fraction temperature T/T_c, the number of atoms in the condensate, and subsequently its chemical potential can all be determined. Therefore the accuracy with which a model of the density of a Bose gas fits to the profiles that are measured is important, and motivates our discussion in this section.

We fit the two theoretical models of the density profile to the density profiles we measure as explained in previous sections. The first is the ideal model, consisting of a Gaussian that describes the thermal component of the Bose gas, and a Thomas Fermi density profile that describes the condensed component. In this model the thermal cloud is considered independently of the condensate. The second model is

the semi-ideal model, which considers the influence of the condensate on the thermal cloud. The thermal component of the semi ideal model, eq.(7.34), is made up of three subcomponents given by I_1, I_2 and I_3 of (7.35). The semi-ideal model is a more accurate model of the Bose gas since it considers to first order the correction to the thermal density due to the presence of the condensate.

From a theoretical point of view, one would expect the Gaussian of the ideal model to closely match the Gaussian tail given by I_1 of the semi-ideal model.[11] Subsequently the ideal model would be expected to overestimate the thermal density in the central region - where the actual thermal density is depleted - and therefore overestimate the thermal fraction. However, experimentally we do not find this to be the case.

The measured density profiles in fig.7.7a and fig.7.7b are very similar. From the fitted semi-ideal model we find an almost identical condensed fractions of 0.37 and 0.39 respectively, and temperature of the cloud in fig.7.7b is only slightly higher than for the cloud in fig.7.7a. However, compared to the semi-ideal fit, the Gaussian of the ideal thermal cloud model fits the two profiles differently. In fig.7.7a it closely follows the semi-ideal density profile outside the condensed region, and overestimates its density in the central region. In fig.7.7b the ideal model estimates a higher density in the outer region with a wider Gaussian profile than in fig.7.7a, but consequently underestimates the thermal density in the central region. The wider Gaussian in fig.7.7b is due to a marginally higher proportion of atoms in the thermal tails of the distribution. We chose the profiles in fig.7.7a and fig.7.7a to illustrate how sensitive the bimodal model is to slight variations in the cloud temperature. In fig.7.7c, where the condensed fraction $N_0/N = 0.3$ and temperature higher than the clouds in fig.7.7a and fig.7.7a, the Gaussian is even wider when compared with the semi-ideal model, and it greatly underestimates the thermal density in the central region.

If our trap was a perfectly harmonic potential, one would expect the Gaussian of the ideal model to be very similar to the thermal tails of the semi-ideal model, regardless of the temperature. We would therefore not expect such variation of

[11] In the experiment discussed in this section the cloud is allowed to expand for only a short time $\tau \ll 1$ after it is released from the trap, hence the expanding tails deviate little from the I_1.

the fitted models as the temperature increases. However our trap is not a perfect harmonic trap, as the shape depends on the small transverse currents in the central wires of our atom chip as explained in sec.4.3. The gradual widening of the fitted Gaussian away from that predicted by the semi-ideal model as the temperature rises is due to the effects of anharmonicity and roughness in the trap potential.

Firstly, anharmonicity of the local minimum where the gas is trapped, means the potential widens slightly more than expected for a harmonic potential, thereby widening the tails of the density distribution. Secondly, roughness in the trap potential leads to small peaks in the density away from the centre of the cloud. Neither model explicitly considers these two effects which tend to widen the tails of the thermal cloud. However, the Gaussian of the ideal model is fitted only to the tails of the measured density, and is not constrained in any way by the density profile in the central region, around the condensate. This model is therefore strongly influenced by anharmonicity and roughness in the trap. In contrast, the semi-ideal model fits directly to the entire profile, and gives a better description of the measured density over the $200\,\mu$m wide central region, where almost all of the atoms are found. The three plots shown in 7.7 are specific cases, but the overall effect can be observed over many more profiles.

Two quantify our assertion that the ideal model fits better to the tails of the measured distributions, and the semi-ideal model fits better to the central region, we look at the fit residuals for the two models, and ratio of their χ^2 values over the central and outer region of the measured profiles. We first fit the two models to 34 individual density profiles measured in the same method given in sec.7.3.1. The condensate fraction and temperature were varied between different measurements by holding the gas in the trap for longer, allowing it to heat up at a rate of $50\,\mathrm{nK\,s^{-1}}$. In addition, small variations of about 10 kHz in the energy of the trap bottom altered the final trap depth set by the rf knife.

The first plot in fig.7.8a shows an example of one of these profiles, together with the ideal and semi-ideal model fits. The error bars on the data points are calculated from the shot noise in the CCD counts. A pixel in the absorption (background) image with A (B) counts has uncertainty $\sqrt{A}$ ($\sqrt{B}$). This leads to an uncertainty of $\sqrt{1/A + 1/B}$ in the processed pixel of the absorption. To find the axial density

profiles from the processed absorption images, we sum over the pixels in the vertical direction, and therefore add these pixel uncertainties in quadrature to give the error bars as shown in fig.7.8a.

We then calculate the normalised residuals $R_i = [n(z_i) - n_{\rm fit}(z_i)]/\sigma_i$, for these profiles for the ideal and semi-ideal fitted models, where $n(z_i)$ is the measured value of the density, $n_{\rm fit}(z_i)$ its value from the fit, σ_i the uncertainty, and i the pixel index which runs over the number of pixels in the axial direciton (see, for example [134]). The lower middle and bottom plots in fig.7.8a show these residuals for the fitted ideal model and fitted semi-ideal model respectively.

To verify our assertion above, we compare the values of $\chi^2 = \sum_j R_j^2$ for the two models, calculated over two regions. The first region is the inner region $300 < z < 480\,\mu$m, where we expect the thermal density to be strongly effected by the mean field repulsion of the condensate. The second region is the outer region where $z < 300\,\mu$m or $z > 480\,\mu$m. In this region, the axial potential differs from the 10 Hz harmonic potential we expect at the centre of the trap. The data points in fig.7.8 shows the ratios $\chi^2_{\rm SI}/\chi^2_{\rm I}$, calculated over the inner region (blue round data points), and the outer region (purple square data points). $\chi^2_{\rm SI}$ is the chi-squared value for the semi-ideal fitted model over the indicated region, and $\chi^2_{\rm I}$ the value for the ideal fitted model. For the inner region, the (blue) data points all lie in the region $\chi^2_{\rm SI}/\chi^2_{\rm I} < 1$, where the semi-ideal model provides a better fit to the measured density profiles. For the outer region, the (purple square) data points lie in the region $\chi^2_{\rm SI}/\chi^2_{\rm I} > 1$, where the ideal model provides a better fit. This is because the gaussian part of the ideal model is not constrained by what is expected for the density in the central region, and is therefore able to reach a closer agreement with the thermal density in this outer region where the axial potential is weaker than the 10 Hz harmonic potential found at the centre of the trap. We see in fig.7.8 that the ratio $\chi^2_{\rm SI}/\chi^2_{\rm I}$ in the outer region decreases as the condensed fraction N_0/N increases. This is explained by the reduced population in the thermal tails as N_0/N increases, or equivalently as the temperature of the Bose gas decreases. Thus the axial width of the thermal tails is reduced, and a higher fraction of thermal atoms are found closer to the centre of the trap where it is closer the 10 Hz harmonic axial potential used in the semi-ideal model.

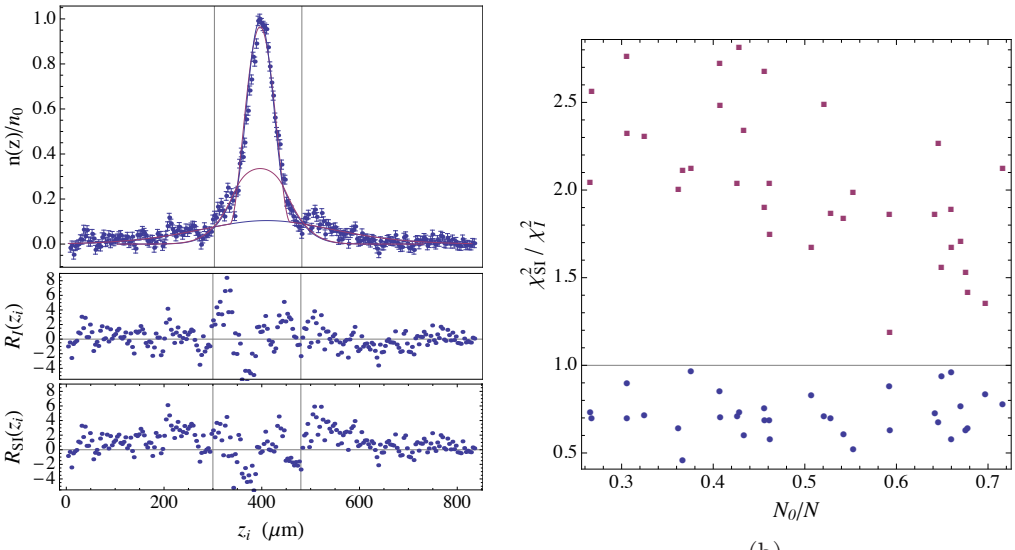

(a) (b)

Figure 7.8: Comparison of fit residuals of the semi-ideal and ideal fitted models. Figure 7.8a shows an example of a measured axial density profiles, together with the ideal and semi-ideal fitted model and their fit residuals. The the upper plot, the data points are found from summing over columns of pixels in a processed absorption image, and the error bars are derived from the uncertainty due to shot noise in the raw absorption and background images. The blue line shows the ideal model fitted to the data, and the purple line the semi-ideal model. The middle plot shows the fit residual for the ideal model, and lower plot shows the fit residuals from the semi-ideal model. The region in between the vertical gridlines is defined as the 'inner' region, and outside these lines the 'outer' region is defined. Figure 7.8b shows the ratios of the chi-squared value found for each model in the inner and outer regions. These ratios were found for 34 different absorption images, from which the density profiles such as that shown in fig.7.8a were determined. Each image was of a cloud with a slightly different condensed fraction, as indicated by the horizontal scale. The blue round data points show the ratio $\chi^2_{\rm SI}/\chi^2_{\rm I}$ in the central region for each cloud, and the purple square data points show the ratio $\chi^2_{\rm SI}/\chi^2_{\rm I}$ in the outer region for each cloud. For the profile in fig.7.8a, $N_0/N = 0.41$, and $\chi^2_{\rm SI}/\chi^2_{\rm I}$ is 0.6 in the central region, and 1.8 in the outer region.

For estimating the thermal fraction, an accurate estimate of the thermal density in the central region, is much more important than that of the tails for two reasons. Firstly, it is only in this central region that the thermal density cannot be measured directly from absorption images, since in this region it must be separated from the condensate density. Secondly, this is where the thermal density is highest, so incorrect estimation in this region will can lead to a larger error in the number of thermal atoms. The semi-ideal model provides not only a more accurate theoretical description of the thermal density in this region, but also provides a better fit to the experimental data, as shown by our analysis above. We are therefore confident that the number of thermal atoms estimated by the semi-ideal model fit in this region is

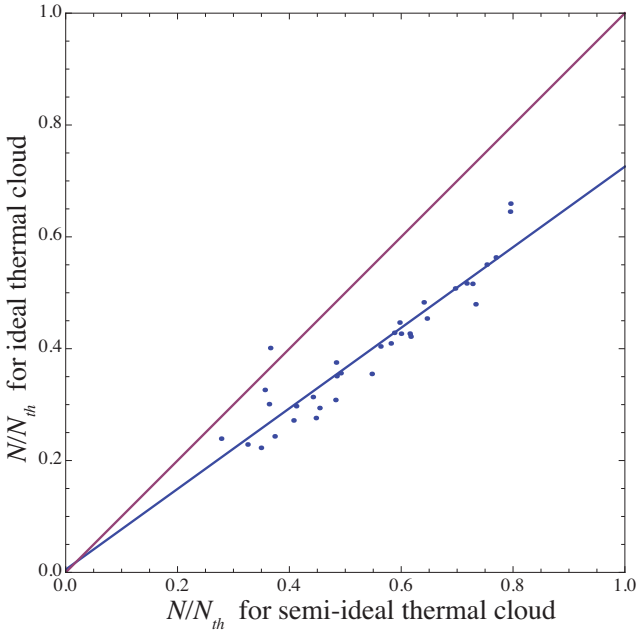

Figure 7.9: Thermal fraction estimated from the semi-ideal model versus the estimate from the ideal model. Data point show the estimates for the two models for each of the 34 measured density profiles we fit to. The blue line is a linear fit to the data points. Its gradient indicates that the ideal-model underestimates the thermal fraction quite consistently by 30%. The purple line shows where data points with a 1:1 relation of the thermal fraction from the two models would lie.

a more accurate estimate than given by the ideal model. In the remainder of this thesis we use the semi-ideal model as the correct model for estimating the thermal density in this central region.

Finally, we show in fig.7.9 the thermal fraction estimated from the ideal model plotted against the thermal fraction estimated from the semi-ideal model. There is a strong correlation between the two estimates, and a straight line is fit to this data. The slope of the line is less than 1, and indicates that the ideal model systematically underestimates the thermal fraction by approximately 30%. The line also passes through the origin where the thermal fraction is zero and the two models become identical Thomas Fermi density profiles.

7.4 Low temperature excitations of the gas

We now return to the full Hamiltonian eq.(7.10) for the interacting Bose gas, and introduce the Bogoliubov approximation in the second quantised limit. This approx-

imation is central to the microscopic theory of the Bose gas, which will be used in the following chapter in the discussion of damping of the motion of the condensate. In contrast to the Hatree-Fock approximation, the second order non-Hermitian terms of $\delta\mathbf{\Psi}$ and $\delta\mathbf{\Psi}^\dagger$ are retained in the Bogoliubov approximation. As discussed in sec.7.2, these terms couple the single particle states expected from a Hermitian theory of the gas (such as Hartree Fock theory). As a result, the excitations of the gas are no longer single Fock states, but superposition states more like the coherent states found in quantum electrodynamics. The Bogoliubov theory serves as the starting point for investigating processes third order in $\delta\mathbf{\Psi}$ or $\delta\mathbf{\Psi}^\dagger$, which are used to explain the damping of collective oscillations of the condensate in Ch.8.

7.4.1 Bogoliubov Approximation

The Hamiltonian $\mathbf{H}_{\rm B}$ consisting of all terms up to second order in $\delta\mathbf{\Psi}$ or $\delta\mathbf{\Psi}^\dagger$ is given by,

$$\mathbf{H}_{\rm B} = \int {\rm d}\mathbf{r} \left[-\mathbf{\Psi}_0^\dagger \frac{\hbar^2\nabla^2}{2m}\mathbf{\Psi}_0 - \delta\mathbf{\Psi}^\dagger \frac{\hbar^2\nabla^2}{2m}\delta\mathbf{\Psi} + V(\mathbf{r})\mathbf{\Psi}_0^\dagger\mathbf{\Psi}_0 + V(\mathbf{r})\delta\mathbf{\Psi}^\dagger\delta\mathbf{\Psi} + \frac{g}{2}\mathbf{\Psi}_0^\dagger\mathbf{\Psi}_0^\dagger\mathbf{\Psi}_0\mathbf{\Psi}_0 \right.$$
$$\left. +2g\mathbf{\Psi}_0^\dagger\mathbf{\Psi}_0\delta\mathbf{\Psi}^\dagger\delta\mathbf{\Psi} + \frac{g}{2}\left(\mathbf{\Psi}_0^\dagger\mathbf{\Psi}_0^\dagger\delta\mathbf{\Psi}\delta\mathbf{\Psi} + \delta\mathbf{\Psi}^\dagger\delta\mathbf{\Psi}^\dagger\mathbf{\Psi}_0\mathbf{\Psi}_0\right)\right]. \quad (7.36)$$

In the Bogoliubov theory, the operators $\delta\mathbf{\Psi}$ and $\delta\mathbf{\Psi}^\dagger$ are thought of as producing small fluctuations in the gas about the ground state. In this context they are commonly referred to as the fluctuation operators. The final two terms of $\mathbf{H}_{\rm B}$ are the non-hermitian terms, and the third to last term is the Hartree Fock exchange term. The fourth order term $\frac{g}{2}\delta\mathbf{\Psi}^\dagger\delta\mathbf{\Psi}^\dagger\delta\mathbf{\Psi}\delta\mathbf{\Psi}$, which accounts for collisions between excited particles, is not included in the initial development of this theory. The Hamiltonian $\mathbf{H}_{\rm B}$ can be diagonalised through a method of transformation named after Bogoliubov. The Bogoliubov method transforms the system into one of independent bosonic quasiparticles, in the presence of the ground state mean field and external potential.

The Bogoliubov transformation is a canonical transformation of the creation and annihilation operators $\mathbf{a}_i^\dagger$ and $\mathbf{a}_i$ to a new pair of operators

$$\alpha_i = u_i\mathbf{a}_i + v\mathbf{a}_i^\dagger, \qquad \alpha_i^\dagger = u_i\mathbf{a}_i^\dagger + v_i\mathbf{a}_i. \quad (7.37)$$

where u and v are a pair of complex valued coefficients. The single particle basis of the creation and annihilation operators in eq.(7.37) is completely arbitrary. Using eq.(7.11) to work in the position basis instead, the operators α_i and $\alpha_i^\dagger$ can be written in terms of the field operators $\delta\mathbf{\Psi}(\mathbf{r})$ and $\delta\mathbf{\Psi}^\dagger(\mathbf{r})$. For $i > 0$,

$$\alpha_i = \int \mathrm{d}\mathbf{r} \left(u_i(\mathbf{r})^* \delta\mathbf{\Psi}(\mathbf{r}) + v_i(\mathbf{r}) \delta\mathbf{\Psi}^\dagger(\mathbf{r}) \right), \qquad \alpha_i^\dagger = \int \mathrm{d}\mathbf{r} \left(u_i(\mathbf{r}) \delta\mathbf{\Psi}^\dagger(\mathbf{r}) + v_i^*(\mathbf{r}) \delta\mathbf{\Psi}(\mathbf{r}) \right), \tag{7.38}$$

where the coefficients u and v have become functions of $\mathbf{r}$. One requires that these transformation be canonical, preserving the bosonic commutator relations such that

$$[\alpha_i^\dagger, \alpha_j^\dagger] = [\alpha_i, \alpha_j] = 0, \qquad [\alpha_i, \alpha_j^\dagger] = \delta_{ij}. \tag{7.39}$$

These commutator relations subsequently lead to the following orthogonality relation between $u_i(\mathbf{r})$ and $v_j(\mathbf{r})$, found on substitution of eq.(7.38),

$$\int \mathrm{d}\mathbf{r} \left(u_i^*(\mathbf{r}) u_j(\mathbf{r}) - v_i(\mathbf{r}) v_j^*(\mathbf{r}) \right) = \delta_{ij}. \tag{7.40}$$

This fixes the relation between the sets of functions $\{u_i(\mathbf{r})\}$ and $\{v_i(\mathbf{r})\}$.

The transformations are easily inverted to give

$$\delta\mathbf{\Psi} = \sum_i u_i(\mathbf{r}) \alpha_i - v_i^*(\mathbf{r}) \alpha_i^\dagger, \qquad \delta\mathbf{\Psi}^\dagger = \sum_i u_i^*(\mathbf{r}) \alpha_i^\dagger - v_i(\mathbf{r}) \alpha_i. \tag{7.41}$$

The inverse transformations are used to re-write the Hamiltonian in terms of the operators α_i and $\alpha_i^\dagger$. The resulting expression for the hamiltonian consists of 'diagonal' terms like $\alpha_i^\dagger \alpha_i$ and 'off diagonal' terms like $\alpha_i^\dagger \alpha_i^\dagger$. The coefficients $u_i(\mathbf{r})$ and $v_j(\mathbf{r})$, which so far only have the one constraint eq.(7.40), can be chosen such that the off diagonal terms of the Hamiltonian are equal to zero. In its diagonal form the Hamiltonian describes a system of Bosons with no interaction between them. Thus by making the Bogoliubov transformation we have found the eigenbasis of Hamiltonian $\mathbf{H}_\mathrm{B}$ of eq.(7.36). Unlike the original basis, it is not complicated by coupling between modes. In the next section we give an example of the Bogoliubov transformation for a uniform Bose gas which clearly demonstrates the point we have made here.

To take into account changes in particle number one usually works with the grand canonical Hamiltonian $\mathbf{K} = \mathbf{H}_{\mathrm{B}} - \mu\mathbf{N}$ instead of $\mathbf{H}_{\mathrm{B}}$.[11] For the chosen functions $u_i(\mathbf{r})$ and $v_i(\mathbf{r})$ to diagonalise $\mathbf{K}$, they must satisfy the Bogoliubov equations,

$$\left(-\frac{\hbar^2\nabla^2}{2m} + V(\mathbf{r}) + 2gn_0(\mathbf{r}) - \mu\right) u_i(\mathbf{r}) - g\psi^2 v_i(\mathbf{r}) = \epsilon_i u_i(\mathbf{r}), \qquad (7.42a)$$

$$\left(-\frac{\hbar^2\nabla^2}{2m} + V(\mathbf{r}) + 2gn_0(\mathbf{r}) - \mu\right) v_i(\mathbf{r}) - g\psi^{*2} u_i(\mathbf{r}) = -\epsilon_i v_i(\mathbf{r}). \qquad (7.42b)$$

These coupled equations define the set of normal modes of the hamiltonian $\mathbf{K}$ in terms of the eigenfunctions $u_i(\mathbf{r})$ and $v_i(\mathbf{r})$, with energy eigenvalue ϵ_i. The operators that create and destroy excitations in these normal modes are $\alpha_i^\dagger$ and α_i; a single excitation in the i^{th} mode written as $\alpha_i^\dagger |0\rangle$ and has energy ϵ_i.

7.4.2 Bogoliubov Excitations in a Box

It is not a trivial task to find the Bogoliubov modes of a trapped Bose gas from eq.(7.42). These simultaneous equations can be solved numerically at zero temperature as outlined in [15], and the related equations at finite temperatures outlined in [128], where the modes are populated according the Bose-Einstein distribution. Once solutions are found, working with them is not necessarily straight forward due to their complicated form. An alternative is to approximate the trap potential by a box of dimensions L_x, L_y and L_z and volume V. Inside the box the Bose gas is homogenous, and the Bogoliubov modes can be found in terms of plane waves $e^{i\mathbf{k}\cdot\mathbf{r}}/\sqrt{V}$. Working in this simplified system, it is easier to form an intuitive explanation of various processes, for which some analytic results can be found. We summarise the key components of the homogenous theory here, so that they can be used in the next chapter in the discussion of Landau damping.

In the momentum representation the single particle eigenfunctions in the box are plane waves $e^{i\mathbf{k}\cdot\mathbf{r}}/\sqrt{V}$, with wavevector $\mathbf{k} = (\frac{n\pi}{L_x}, \frac{n\pi}{L_y}, \frac{n\pi}{L_z})$, where the integers n_i run from $-\infty$ to ∞. Using eq.(7.7) the field operators can be expanded in the momentum representation as

$$\mathbf{\Psi}(\mathbf{r}) = \sum_k \frac{e^{i\mathbf{k}\cdot\mathbf{r}}}{\sqrt{V}}\mathbf{a}_{\mathbf{k}}, \qquad \mathbf{\Psi}^\dagger(\mathbf{r}) = \sum_k \frac{e^{-i\mathbf{k}\cdot\mathbf{r}}}{\sqrt{V}}\mathbf{a}_{\mathbf{k}}^\dagger. \qquad (7.43)$$

which are used to expand the Bogoliubov Hamiltonian eq.(7.36). In addition to this the ground state operators are replaced by their expectation value $\sqrt{n_0} = \sqrt{N_0/V}$, where n_0 is the ground state density. The integral in eq.(7.36) with respect to $\mathbf{r}$ over the plane waves lead to Kronecker delta symbols, e.g.

$$\delta_{ij} = \frac{1}{V}\int d\mathbf{r}\, e^{i(\mathbf{k}_i - \mathbf{k}_j)\cdot\mathbf{r}} \tag{7.44}$$

which ensure conservation of momentum. Subtracting $\mu\mathbf{N}$ from the result, one finds after some simple algebra

$$\mathbf{H}_{\mathrm{B}} - \mu\mathbf{N} = -\frac{g}{2}Vn_0^2 + \sum_{i>0}\left[\left(\frac{\hbar^2k^2}{2m} + gn_0\right)\left(\mathbf{a}_{\mathbf{k}}^\dagger\mathbf{a}_{\mathbf{k}} + \mathbf{a}_{-\mathbf{k}}^\dagger\mathbf{a}_{-\mathbf{k}}\right) + gn_0\left(\mathbf{a}_{\mathbf{k}}^\dagger\mathbf{a}_{-\mathbf{k}}^\dagger + \mathbf{a}_{\mathbf{k}}\mathbf{a}_{-\mathbf{k}}\right)\right]. \tag{7.45}$$

The first term under the summation is the hermitian diagonal term, but the second term is non-hermitian, creating or annihilating pairs of momentum states $|\pm\mathbf{k}\rangle$. To find the diagonal form, the creation and annihilation operators $\mathbf{a}_{\mathbf{k}}^\dagger$ and $\mathbf{a}_{\mathbf{k}}$ are transformed under the Bogoliubov transformation

$$\boldsymbol{\alpha}_{\mathbf{k}} = u_k\mathbf{a}_{\mathbf{k}} + v_k\mathbf{a}_{-\mathbf{k}}^\dagger \qquad \boldsymbol{\alpha}_{\mathbf{k}}^\dagger = u_k\mathbf{a}_{\mathbf{k}}^\dagger + v_k\mathbf{a}_{-\mathbf{k}} \tag{7.46}$$

where the amplitudes u_k and v_k are real and positive and depend on the magnitude of $\mathbf{k}$. As described in sec.7.4.1 for the general approach, the new operators $\boldsymbol{\alpha}$ and $\boldsymbol{\alpha}^\dagger$ must satisfy the bosonic commutator relations eq.(7.39). For the operators to satisfy $\left[\boldsymbol{\alpha}, \boldsymbol{\alpha}^\dagger\right] = 1$, the coefficients must satisfy the orthogonality relation

$$u_k^2 - v_k^2 = 1. \tag{7.47}$$

This relation is used to find the inverse transformations,

$$\boldsymbol{a}_{\mathbf{k}} = u_k\boldsymbol{\alpha}_{\mathbf{k}} - v_k\boldsymbol{\alpha}_{-\mathbf{k}}^\dagger, \qquad \boldsymbol{a}_{\mathbf{k}}^\dagger = u_k\boldsymbol{\alpha}_{\mathbf{k}}^\dagger - v_k\boldsymbol{\alpha}_{-\mathbf{k}}. \tag{7.48}$$

Using these to expand eq.(7.45), gives

$$\begin{aligned}\mathbf{H}_{\rm B}-\mu\mathbf{N} = &-\frac{g}{2}Vn_0^2+2c_kv_k^2-2\mu u_kv_k\\ &+\sum_{k>0}\Big[\left(c_k(u_k^2+v_k^2)-2\mu u_kv_k\right)\left(\boldsymbol{\alpha}_{\mathbf{k}}^\dagger\boldsymbol{\alpha}_{\mathbf{k}}+\boldsymbol{\alpha}_{-\mathbf{k}}^\dagger\boldsymbol{\alpha}_{-\mathbf{k}}\right)\\ &\quad+\left(\mu(u_k^2+v_k^2)-2c_ku_kv_k\right)\left(\boldsymbol{\alpha}_{\mathbf{k}}^\dagger\boldsymbol{\alpha}_{-\mathbf{k}}^\dagger+\boldsymbol{\alpha}_{\mathbf{k}}\boldsymbol{\alpha}_{-\mathbf{k}}\right)\Big]\end{aligned} \tag{7.49}$$

where $c_k=\frac{\hbar^2k^2}{2m}+\mu$, and the chemical potential $\mu=gn_0$. This equation takes diagonal form if

$$\mu(u_k^2+v_k^2)-2c_ku_kv_k=0, \tag{7.50}$$

which is the Bogoliubov equation for the homogeneous system, equivalent to the set of simultaneous equations eq.(7.42), in the trapped system. Equation (7.50) is solved together with the orthogonality relation eq.(7.47) to give the amplitudes of the Bogoliubov modes,

$$u_k^2=\frac{1}{2}\left(\frac{c_k}{\epsilon_k}+1\right),\qquad v_k^2=\frac{1}{2}\left(\frac{c_k}{\epsilon_k}-1\right) \tag{7.51}$$

together with the energy eigenvalues

$$\epsilon_k=\left[\left(\frac{\hbar^2k^2}{2m}+gn_0\right)^2-(gn_0)^2\right]^{1/2}. \tag{7.52}$$

This equation is the well known Bogoliubov dispersion relation for excitations in a homogeneous gas. In the low momentum limit these are phonons propagating with sound velocity $c=d\epsilon_k/d(\hbar k)=\sqrt{gn_0/m}$.

Now in diagonal form, eq.(7.45) is given by

$$\mathbf{H}_{\rm B}-\mu\mathbf{N}=-\frac{g}{2}Vn_0^2+\sum_{k>0}\left[\epsilon_k-\left(\frac{\hbar^2k^2}{2m}+gn_0\right)+\epsilon_k\left(\boldsymbol{\alpha}_{\mathbf{k}}^\dagger\boldsymbol{\alpha}_{\mathbf{k}}+\boldsymbol{\alpha}_{-\mathbf{k}}^\dagger\boldsymbol{\alpha}_{-\mathbf{k}}\right)\right]. \tag{7.53}$$

This describes the excitations of the gas as a system of non-interacting bosons, created and annihilated by $\boldsymbol{\alpha}_{\mathbf{k}}^\dagger$ and $\boldsymbol{\alpha}_{\mathbf{k}}$, in the presence of the ground state which has wavefunction $\sqrt{n_0}$. The field operators $\delta\boldsymbol{\Psi}$ and $\delta\boldsymbol{\Psi}^\dagger$, defined in eq.(7.11), can be

rewritten in terms of these modes using eq.(7.43) and eq.(7.48), which gives

$$\delta\mathbf{\Psi}(\mathbf{r}) = \sum_{\mathbf{k}\neq 0}\left(u_{\mathbf{k}}(\mathbf{r})\boldsymbol{\alpha}_{\mathbf{k}} - v^*_{\mathbf{k}}(\mathbf{r})\boldsymbol{\alpha}^\dagger_{-\mathbf{k}}\right), \qquad \delta\mathbf{\Psi}^\dagger(\mathbf{r}) = \sum_{\mathbf{k}\neq 0}\left(u^*_{\mathbf{k}}(\mathbf{r})\boldsymbol{\alpha}^\dagger_{\mathbf{k}} - v_{\mathbf{k}}(\mathbf{r})\boldsymbol{\alpha}_{-\mathbf{k}}\right) \tag{7.54}$$

where

$$u_{\mathbf{k}}(\mathbf{r}) = u_k\frac{e^{i\mathbf{k}\cdot\mathbf{r}}}{\sqrt{V}} \quad \text{and} \quad v^*_{\mathbf{k}}(\mathbf{r}) = v_k\frac{e^{i\mathbf{k}\cdot\mathbf{r}}}{\sqrt{V}}. \tag{7.55}$$

Thus the field operator $\delta\mathbf{\Psi}^\dagger$ acting on the ground state $|N_0\rangle$ creates a particle-like excitation with amplitude u_k and momentum $\mathbf{k}$, together with a hole-like excitation with amplitude v_k and opposite momentum $-\mathbf{k}$. In thermal equilibrium these modes are thermally excited; the average occupation number of the mode with momentum $\mathbf{k}$ is given by the Bose Einstein distribution $f(\epsilon_k) = (e^{(\epsilon_k-\mu)/k_\mathrm{B}T} - 1)^{-1}$, where ϵ_k is given by the dispersion relation eq.(7.52).

Equation (7.53) provides the starting point for investigating higher order interactions in the gas. Using the expansion eq.(7.54) for the operators $\delta\mathbf{\Psi}$ and $\delta\mathbf{\Psi}^\dagger$, which in the Bogoliubov theory represent small fluctuations from the ground state, one can include the terms of third order in $\delta\mathbf{\Psi}$ or $\delta\mathbf{\Psi}^\dagger$ as a small perturbation to eq.(7.53). Such terms represent processes where two excitations collide to form a ground state particle and a different excitation, or vice versa. This method is used in Ch.8 to study the the damping of a collective excitation caused by collisions with thermal excitations.

The mean field effect of the fourth order terms $\frac{g}{2}\delta\mathbf{\Psi}^\dagger\delta\mathbf{\Psi}^\dagger\delta\mathbf{\Psi}\delta\mathbf{\Psi}$ can also be included under Popov approximation [135, 136]. In this approximation it is assumed that the field operators in this term can be replaced by their mean field values in the original (un-transformed) Fock basis. In thermodynamic equilibrium the mean field values are given by the occupation numbers found from the Bose Einstein distribution. The other terms are treated as above in the Bogoliubov approximation.[12] For the homogenous gas, making the Popov approximation does not change the form of the Bogoliubov modes $u_k(\mathbf{r})$ and $v_k(\mathbf{r})$, only adding a constant energy term of $-2gn_0N_\mathrm{th} - gN^2_\mathrm{th}/V$ to the Hamiltonian (see for example chap. 8 in [11]).

[12] Formally, one starts with in the Hartree Fock approximation and assumes the quantum fluctuations due to the non-hermitian second order terms are small, hence the state of the gas is approximately a Fock state. The non-hermitian second order terms are then added to the Hartree Fock Hamiltonian and the Bogoliubov transformation is made.

Chapter 8

Damping of Centre of Mass Oscillation

In this chapter we present and discuss measurements we have made on the damping of centre of mass oscillations of the condensate, trapped in the presence of a stationary thermal cloud. The Bose gas sits in a local minimum of the rough axial potential, which is several hundred nano-Kelvin deep. At the lowest energies, where the condensate sits, this potential is approximately harmonic with a frequency of 10 Hz. We drive simple harmonic motion in the condensate centre of mass. This motion is damped as the condensate moves through the stationary thermal cloud that surrounds it. We measure how the amplitude of the oscillations decay, and how this changes for thermal clouds at different temperatures.

The damping is due to collisions between condensed particles and particles in the thermal cloud. It is therefore expected that changing the population of the thermally excited states will change the damping rate of condensate oscillations. We use the depth of the local minimum of the trap to control the fraction and energy of atoms that are in the thermal cloud. This depth is set by the frequency difference Δf between the rf knife and the bottom of the local minimum, and is held at a constant value while the condensate oscillates.

We repeat the experiment but with Δf held at a different constant value, and therefore with a different thermal fraction. We measure the damping rate for clouds

with different thermal fractions and observe the damping rate to be reduced for smaller thermal fractions.

In sec.8.1 we describe how the oscillations of the condensate are produced. Section 8.2 explains how we extract information about the oscillations and the thermal fraction of the gas. We present our damping measurements versus the thermal fraction and temperature in sec.8.3, and discuss our observations. Using the analytical tools developed in ch.7, we then give a detailed description of Landau damping in sec.8.4, which we believe to be the mechanism for the temperature-dependent damping rate we observe. We derive the well known model of Landau damping for a uniform Bose gas in sec.8.4.1, but show in sec.8.4.2 that this gives a significantly higher damping rate than we observe. In sec.8.4.3 we make a modification to this model to take into account the discrete spectrum of our trap, then show in sec.8.4.4 that it describes well the damping behaviour that we observe.

8.1 Experimental Method

A condensate is produced at the end of the rf evaporation ramp as described in sec.7.3.1. The final frequency of the rf evaporation ramp is approximately 10 kHz above the trap bottom. The rf knife remains here for 100 ms before being raised over 350 ms to sit at Δf above the trap bottom.

The position of the trap centre is then varied in the axial direction to drive axial centre of mass oscillations. To shift the trap centre, a small magnetic field gradient of less than $100\,\mathrm{mG\,cm^{-1}}$ is applied to the magnetic trap. This field is produced by making a small change to the current running through one of the end wires of the atom chip. Since the length of the region where the trapped cloud sits is small compared to its distance from the end wire, the field gradient experienced by the cloud is constant to a good approximation. This shifts the position of the local minimum of the trap potential in the axial direction by up to $10\,\mu$m. The shift in the transverse position is negligible (less then 1 nm), due to the tight transverse confinement of the trap.

The end-wire current is varied sinusoidally for two complete cycles, with an am-

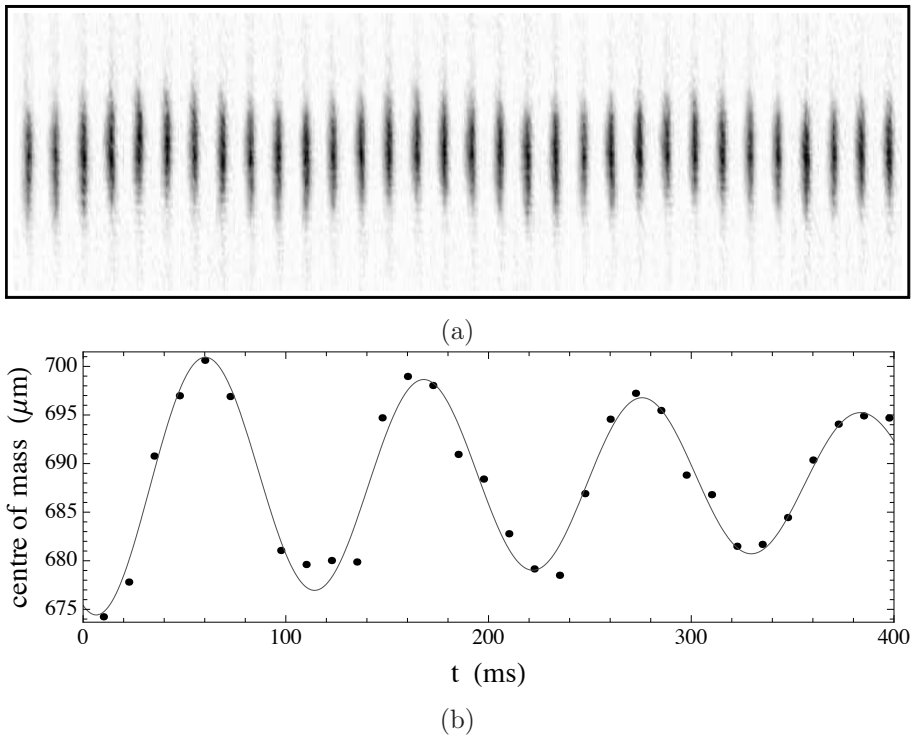

Figure 8.1: Damped oscillation of condensate centre of mass. Figure 8.1a shows a movie of the centre of mass oscillations of the condensate, comprising of 32 absorption images of different condensates, taken over a series of evenly spaced times from 10 to 400 ms. The images in fig.8.1a are orientated such that the long (z) axis of the trap is vertical on this page. The height of the box corresponds to 30 μm. Figure 8.1b shows the centre of mass of the condensate after we start it oscillating. Data points show measurements of the condensate centre of mass. The fitted line is the function eq.(8.1), from which we determine the damping rate γ (see sec.8.2 for details).

plitude of 50 mA a frequency ω to match the axial trap frequency of $\omega_z = 2\pi \times 10\,\mathrm{Hz}$ at the bottom of the local minimum, thus driving axial oscillation in the condensate centre of mass. During this time the energy of the trap bottom also oscillates, so the rf field is temporarily turned off to prevent any unwanted trap loss. Once the driving sequence is finished the rf field is turned back on at the same frequency, Δf above the trap bottom. The axial potential experienced by the thermal cloud is anharmonic and has weaker confinement than a 10 Hz harmonic potential. The thermal cloud therefore oscillates at a different frequency to the condensate, and has negligible responce to this 10 Hz driving force.

The condensate is left to oscillate in the trap for a time t between 10 ms and 400 ms. After this time the magnetic trap is turned off and the cloud is allowed to expand freely for 2 ms before an absorption image is taken. The condensate centre of mass and the fraction of thermal atoms in the cloud are measured from

the absorption image. We build up a movie of the centre of mass oscillations for a given value of Δf by running this sequence 32 times, allowing the condensate to oscillate for a different length of time $10 < t < 400$ ms in each run. An example given in fig.8.1. Figure 8.1a shows a series of 32 of these images which make a movie of the motion of the condensate over 400 ms. The condensate centre of mass is plotted in fig.8.1b as a function of time, showing the damped oscillations. In general, the measured oscillations have an initial amplitude of typically 10 to 15 μm, and a period of about 10.5 Hz. The amplitude decays exponentially with a typical $1/e$ time between 125 ms and 630 ms.

A single set of data takes approximately 30 mins to acquire. We take several data sets at each of six different values of Δf; 10, 20, 50, 100, 200 and 300 kHz. Changing Δf changes the temperature of the thermal cloud by adjusting the depth of the trap. This in turn alters the thermal fraction, because the condensate is roughly in thermal equilibrium with it. Since collisions between the condensate and thermal atoms are a cause of damping, we expect the damping rate to change depending on the size of the thermal fraction. By changing Δf in this way, we are able to measure how the damping rate of the centre of mass oscillations varies with the thermal fraction.

8.2 Measuring the Condensate Centre of Mass and the Thermal Fraction

The information about the condensate centre of mass, atom number, thermal fraction and subsequently temperature of the gas, is all found from the absorption images. Once processed, the absorption images (see sec.2.1.8) are a direct measurement of the column density at each pixel. We image the cloud with the imaging beam directed along the x-axis, so each pixel gives a count of the optical density integrated over the pixel ares, $\sigma\, n(y_i, z_j)A$, where y_i, z_j are the pixel coordinates, $A = 3.45^2\ \mu\text{m}^2$ is the pixel area, and σ is the scattering cross section for the optical transition $|F = 2\rangle \rightarrow |F' = 3\rangle$ (see sec.2.1.8). An example of a processed absorption image of a cloud is shown in fig.8.2a.

In all our images we observe diagonal fringes such as those visible in fig.8.2a.

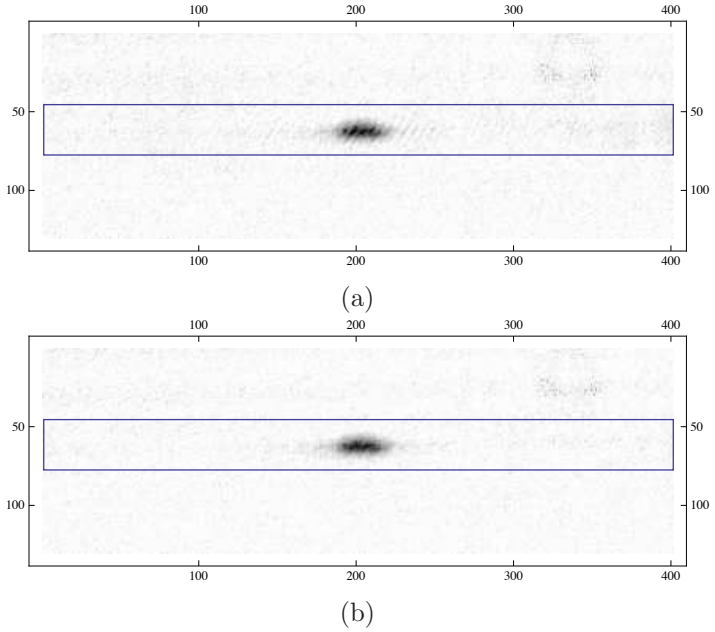

Figure 8.2: Processed absorption images of a cloud in free expansion after release from trap in which it was oscillating. The box indicates the region of interest selected. Figure 8.2a shows the unfiltered image, in which diagonal fringes can be seen which are due to interference fringes in the background and raw absorption images. Figure 8.2b shows the same image after applying a notch filter to its Fourier transform as explained in the text.

These are caused by interference fringes in the intensity profile of the imaging beam, and are not due to density fluctuations of the cloud. In the raw images of the shadow of the cloud and the background image these diagonal fringes are highly visible. In principle the fringe should be removed by subtracting images with and without atoms. However, small movements of the interference pattern between the two images being taken, prevent these fringes from being completely cancelled when the images are processed. We therefore filter out these fringes after subtraction. To do this we Fourier transform the subtracted absorption image and remove the points of transformed image at the frequency of the fringes using a narrow notch filter. The inverse Fourier transform is then applied to recover the absorption image. Figure 8.2b shows the absorption image of fig.8.2a after filtering.

Following this, a small region is selected around the cloud of 30×400 pixels. The pixel counts are summed over this region in the vertical direction, to obtain the axial density profile. To find the centre of mass of the condensate we fit to the density profile the bimodal model of eq.(7.20), which has a thermal component treated as a non-interacting (ideal) gas. Importantly, this model allows the centre of mass of the condensate to be determined independently from that of the thermal cloud centre

of mass. We take the fit parameter z_0 as the centre of mass of the condensate.

An example of the centre of mass measurements taken over an entire oscillation data set is shown in fig.8.1b. In each dataset we measure approximately four oscillations, to which we fit the function for weakly damped simple harmonic motion,

$$z_0(t) = A\, e^{-\gamma t} \sin(\omega t + \phi) + B, \tag{8.1}$$

where $A,\ B,\ \gamma,\ \omega$ and ϕ are used as fit parameters. We remove any outlying data points where either the atom number or thermal fraction lies outside two standard deviations from the mean values for the dataset, since significant fluctuations in either are likely to significantly change the damping rate for the individual data point [21, 22]. Such data points represent oscillating clouds that are likely to be damped at an appreciably different rate, which would potentially skew the dataset. Typically 95% of all data points are retained, as expected for a normal distribution.

In each data set we also looked at the thermal cloud centre of mass, also found through the fitted ideal model. We do not see any sign that the thermal cloud oscillates with the condensate. Thus we observe a condensate oscillating in the presence of a stationary thermal cloud. The fraction of atoms in the thermal cloud N_{th}/N, is varied for different datasets.

To estimate the thermal fraction N_{th}/N from the measured density profile we compare the integral of the total density profile to that of the thermal density. The integral of the total density is found directly by summing over all pixel counts and gives the total atom number N. To extract the thermal density profile we use a combination of direct summation in the thermal tails, and an estimate using a fitted model in the vicinity of the condensate. As discussed in sec.7.3, the ideal thermal gas model does not give an accurate prediction of the density of the thermal component in the vicinity of the condensate. We therefore estimate the thermal component in this region from a fit of the semi-ideal model of sec.7.2.1 to the total density profile (see sec.7.3.2 for how we fit this model). From the fitted semi-ideal model we determine the density of the thermal component as explained in sec.7.2.1.

In contrast to the experiment in sec.7.3, the gas is not necessarily in thermal equilibrium once it starts to oscillate. Despite this, the semi-ideal model still provides

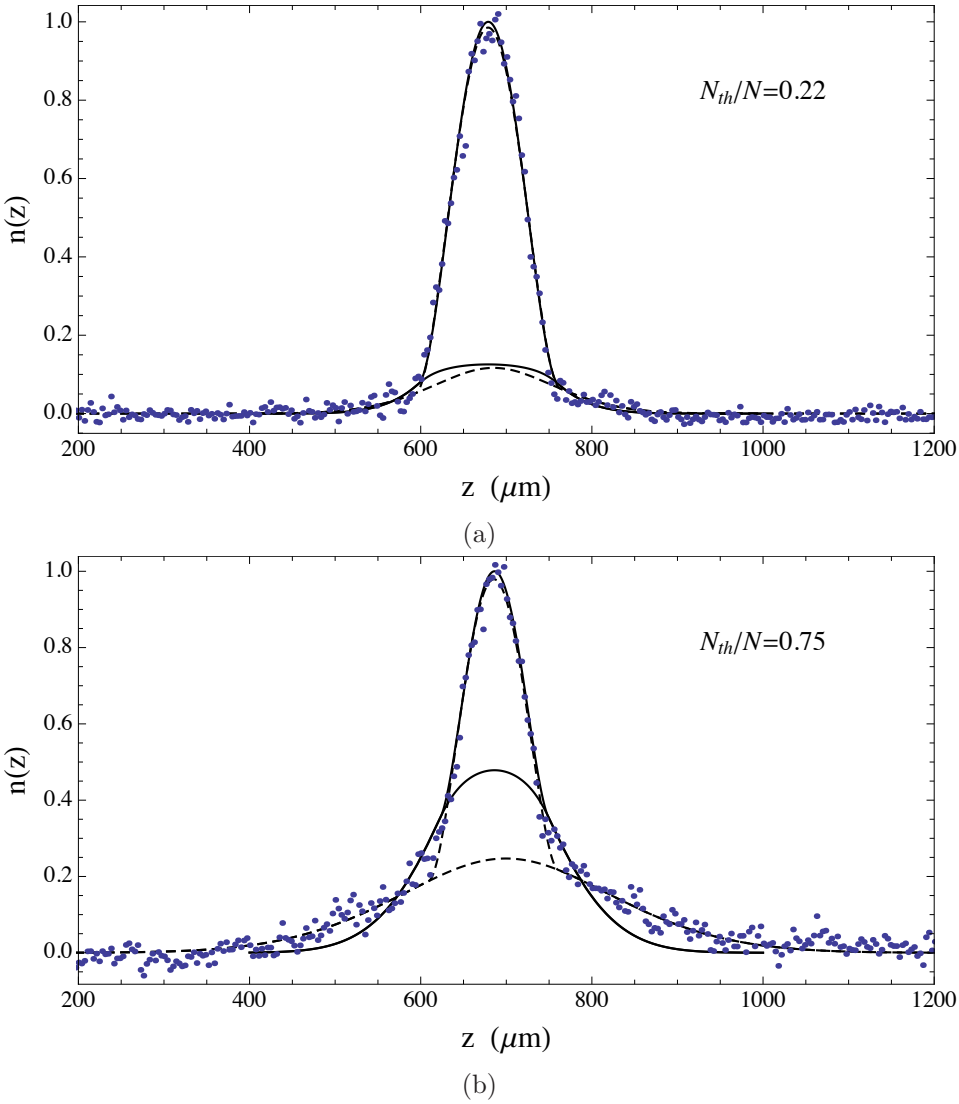

Figure 8.3: Measured axial density profiles for two different temperature clouds, with ideal and semi-ideal models fitted to them. Figure 8.3a shows the density profile for a cloud with small thermal fraction (0.22), for which the rf knife was held at frequency $\Delta f = 10\,\mathrm{kHz}$ above the trap bottom. The data points are the density from absorption images after summation over the transverse direction. The solid lines show the fitted functions for total axial density $n(z)$ and thermal axial density $n_{th}(z)$ from the semi-ideal model. The dotted lines show $n(z)$ and $n_{th}(z)$ from the bimodal model. Figure 8.3b shows the density profile of a cloud with larger thermal fraction (0.75), for which $\Delta f = 300\,\mathrm{kHz}$. Solid lines show fitted functions for $n(z)$ and $n_{th}(z)$ from the semi-ideal gas model, and the dashed lines show $n(z)$ and $n_{th}(z)$ from the bimodal model. While the semi-ideal model provides a good fit over the condensed region in both figures, it underestimates the tails of the thermal cloud density at higher temperatures . This is due to due to the anharmonicity of the trap which is not included in the trap potential in the semi-ideal gas model.

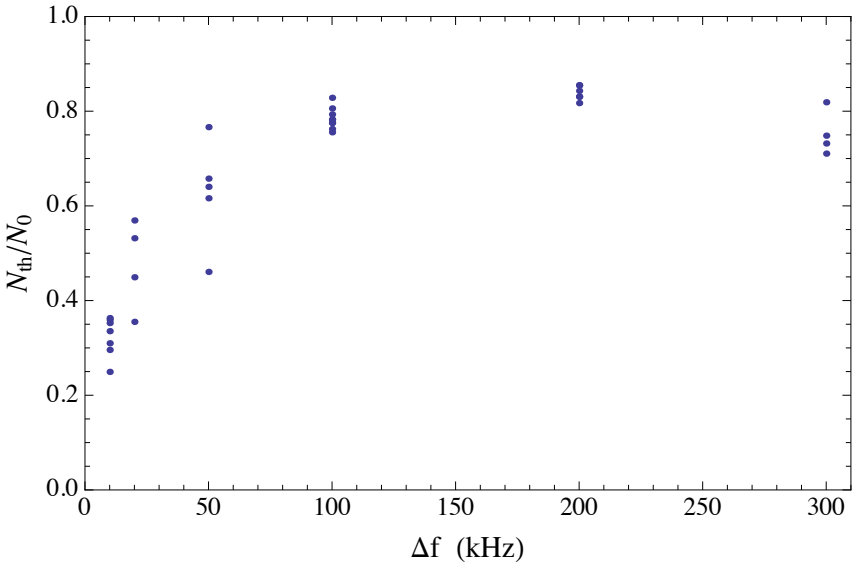

Figure 8.4: Estimated thermal fraction against Δf - the frequency difference between the rf knife and the trap bottom.

a good fit close to the condensate. We explain why the cloud remains close to thermal equilibrium in sec.8.4.1 below. Farther from the condensate the semi-ideal gas model gives a poorer fit, particularly at higher temperatures, due the effect of trap anharmonicity as was discussed in sec.7.3.3. This same effect is illustrated for this experiment in fig.8.3 which shows two examples of measured axial density profiles with the semi-ideal models fitted to each. The profile in fig.8.3a shows a low temperature cloud which gives the 235 ms data point in fig.8.1b. The profile in fig.8.3b is for a hotter cloud with a high thermal fraction. In both cases the semi-ideal model is a close fit to the measured density profile in the vicinity of the condensate. For the colder cloud (fig.8.3a) the fitted semi-ideal model closely follows the measured density profile over the whole region. For the hotter cloud (fig.8.3b) the measured density is higher than that of the fitted semi-ideal gas model for for $z < 580\,\mu$m and $z > 800\,\mu$m. In our analysis of this experiment this effect is accounted for by measuring the thermal density directly in the outer region $|z - z_0| < Z_0$, where we know there is no condensate.

Figure 8.4 shows the mean value of the thermal fraction measured over each data set, and plotted against the value of Δf used. In our experiment we find that the efficiency of our evaporation slowly drifts over several hours. This also affects the temperature of the cloud. Over a single dataset the variation of the thermal fraction is small, with a typical standard deviation of 0.06. However, repeating the

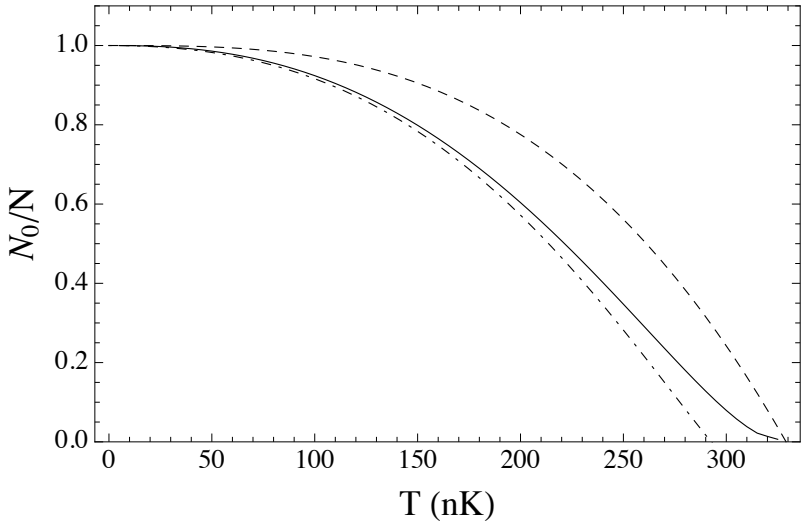

Figure 8.5: Condensate fraction versus temperature for $N = 2 \times 10^4$ atoms. The solid line shows the condensed fraction calculated for the semi-ideal model using eq.(7.30a) and eq.(7.30b). The dashed line is given by the ideal gas equation eq.(8.2) with $\alpha = 3$. The dot-dashed line is the approximate analytic result eq.(8.3) for the semi-ideal gas.

experiment several hours or days later gives a slightly different thermal fraction for the same value of Δf. This is illustrated in fig.8.4 by the spread in thermal fraction for a given Δf. We take advantage of this to measure the damping of centre of mass oscillations for a large set of values of the thermal fraction.

We also use the semi-ideal model to estimate the fractional temperature T/T_c of the measured cloud, which is a fit parameter of this model. However this value does not take into account the slightly higher number of atoms in the tails of the thermal clouds at higher temperature. A better estimate of T/T_c can be made from the measurement of $N_0/N = 1 - N_{th}/N$ we described above.

In the absence of any interactions, the fractional temperature can be found from N_0/N by inverting the well known equation for the ideal Bose gas,

$$\frac{N_0}{N} = 1 - \left(\frac{T}{T_c}\right)^{\alpha} \tag{8.2}$$

where for a harmonic trap $\alpha = 3$. The behaviour in eq.(8.2) has been compared with the behaviour of the semi-ideal gas in [131]. In fig.8.5 we make the same comparison for our typical parameters ($N = 2 \times 10^4$, $f_r = 1.4\,\mathrm{kHz}$ and $f_z = 10\,\mathrm{Hz}$). The dashed line shows eq.(8.2), while the solid line shows the condensed fraction calculated from eq.(7.30a) and eq.(7.30b) as a function of T/T_c with the total number $N_0 + N_{th}$ kept

fixed.[1] The analytic approximation for the semi-ideal gas model from [131],

$$\frac{N_0}{N} = 1 - \left(\frac{T}{T_c}\right)^3 - \frac{\mu}{k_{\mathrm{B}}T}\frac{\zeta(2)}{\zeta(3)}\left(\frac{T}{T_c}\right)^2\left[1-\left(\frac{T}{T_c}\right)^3\right]^{2/5} \tag{8.3}$$

is also shown in fig.8.5 by the dot-dashed line. The critical temperature T_c is the same for both ideal and semi-ideal models because it is defined as the temperature at which $N_0 \to 0$ as $\mu \to \epsilon_0$. Since N_0 vanishes at this point so does the condensate mean field, and the two models are identical. Figure 8.5 shows that the ideal gas expression eq.(8.2) gives an appreciable overestimate of N_0/N. The approximation eq.(8.3) is also insufficient when the condensed fraction is low. We therefore calculate T/T_c using the full expressions eq.(7.30a) and eq.(7.30b) of the semi-ideal model, together with the values of N_{th}/N and N - and subsequently N_0 and N_{th}- that we measure. From N_0 we find the condensate size Z_0 using eq.(7.30b) with $f_r = 1.4\,\mathrm{kHz}$ and $f_z = 10\,\mathrm{Hz}$. We can then solve eq.(7.30a) numerically for our measured value of N_{th} to find T.

8.3 Effect of thermal fraction on the decay rate of centre of mass oscillations

Figure 8.6 shows the damping rate of oscillations measured in each dataset, plotted against the mean thermal fraction of the clouds in the dataset. The damping rate is given by the fit parameter γ of eq.(8.1) when fitted to an oscillation dataset by method of least squares, with equal weightings for each datapoint.[2] All datasets span a time interval of 400 ms, have a similar oscillation period close to 10 Hz, and are therefore over a similar number of cycles. The vertical error bars show the standard error in the fit parameter γ calculated to a 1σ confidence level.[3] This error is larger for higher damping rates where the oscillations decay to an amplitudes lower than the $1 - 2\,\mu$m of noise in the measured condensate centre. The value of

[1] If Z_0 in eq.(7.30a) is not known from the outset, then eq.(7.30a) is an implicit function for N_0. In producing the line in fig.8.5, T and N are known, but $Z_0(N_0)$ is not. We therefore use a simple trial and error algorithm to search for the correct value of N_0 that yields the specified N. N is found from the sum of N_0 and N_{th} from eq.(7.30a) and eq.(7.30b) at a given temperature T. From this we get the value of N_0/N at temperature T.

[2] We use the function 'NonlineaModelFit' in Mathematic, which automatically chooses an algorithm to search for the set of parameters that minimise the χ^2 of the fit.

[3] We use the same Mathematica function to find these errors.

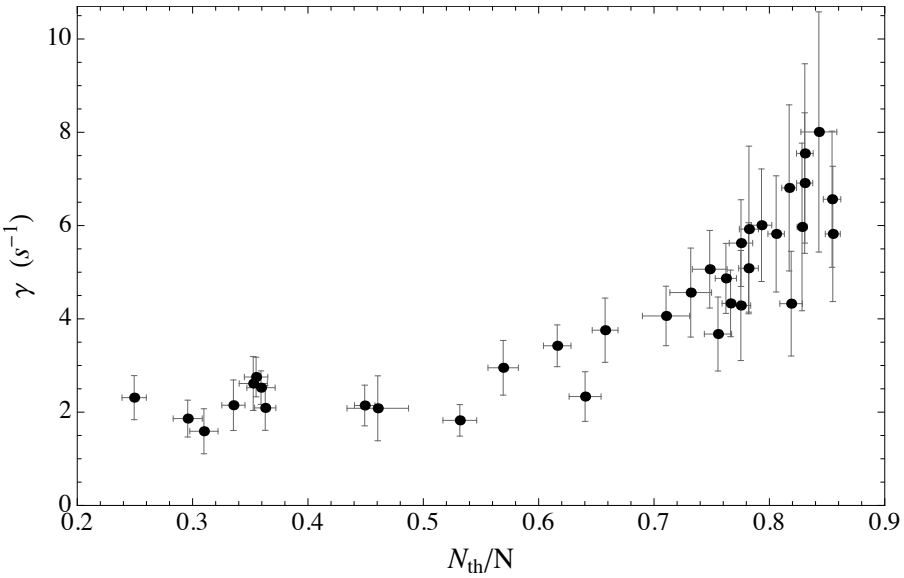

Figure 8.6: Damping rate of oscillations plotted against the thermal fraction. Each data point represents the damping rate obtained by fitting eq.(8.1) to a single data set. The thermal fraction is the mean value taken over all points in the dataset. The error bars indicate the standard error in the fit parameter γ, and the standard error of $\langle N_{\rm th}/N \rangle$.

N_{th}/N for each data point in fig.8.6 is the mean value of over all the images in the dataset. For each individual image N_{th}/N was measured using a combination of direct summation and the fitted semi-ideal model as described in the section sec.8.2. Small variations in the evaporation efficiency cause a small spread in the individual values of N_{th}/N in a dataset. To indicate this, the standard error in the mean value N_{th}/N for each dataset is given by the horizontal error bars of the data points in fig.8.6.

We next discuss our observations of how the damping rate γ varies with N_{th}/N (or equivalently T) in fig.8.6. Starting at low values of N_{th}/N we observe the damping rate has an almost constant value of about $2\,\mathrm{s}^{-1}$ up to about $N_{th}/N = 0.5$. Once N_{th}/N reaches 0.5 this behaviour then changes relatively quickly. For $N_{th}/N > 0.5$ we see a clear temperature dependence of γ which rises steadily as the thermal fraction increases. One would expect this temperature dependent behaviour when the damping of the condensate motion is caused by collisions between the condensate and atoms of the thermal cloud. As the thermal cloud becomes more populated at higher temperatures, the rate of such collisions increases and the condensate motion is damped faster. This temperature dependent behaviour is typical of Landau damping [21, 22, 26].

Landau damping, however, does not explain the constant damping rate we observe for $N_{th}/N < 0.5$. It is well understood that the damping rate from the Landau mechanism should disappear as the temperature approaches zero, since at zero temperature there are no longer any thermally excited atoms for the condensate to collide with. It is therefore reasonable to suggest that the damping rate we have measured comprises two components: A temperature dependent rate $\gamma(T)$ due to the Landau mechanism, and a constant background rate γ_0 due to some other mechanism(s). We take the value $\gamma_0 = 2.2\,\mathrm{s}^{-1}$ which is the mean damping rate of data points below $N_{th}/N = 0.5$ in fig.8.6. These have standard deviation of $0.35\,\mathrm{s}^{-1}$. We define the temperature dependent rate $\gamma(T) = \gamma_{tot} - \gamma_0$ where γ_{tot} is the total damping rate as plotted in fig.8.6.

Our data is suited well to the study of the temperature dependent rate $\gamma(T)$ since we see a clear variation of the damping rate with T (or N_{th}/N). In the remaining sections of this chapter we look at the Landau mechanism and the corresponding damping rate in more detail. We will show in sec.8.4.4 that a simple theoretical model of our gas predicts damping rates which are in good agreement with the temperature dependent rate $\gamma(T)$ that we observe.

We have not understood the origin of the constant rate γ_0, however it is worth speculating here about the two most likely causes of the background rate. These are Beliaev damping [137, 19], and damping of the condensate motion due to roughness in the axial trap potential [68]. Beliaev damping is caused by quanta of collective excitation of the condensate decaying to two excitations of lower energy.[4] In a homogenous Bose gas, Beliaev predicted the decay rate for low energy excitations is

$$\Gamma_B = \frac{3\,q^5}{640\pi\hbar^3 m n_0} \tag{8.4}$$

where the wavenumber $q = \epsilon_q/(\hbar c)$, with sound velocity $c = \sqrt{g n_0/m}$ [137]. With density $n \sim 10^{20}\,\mathrm{m}^{-3}$ and energy $\epsilon_q \sim m\omega_z^2 Z_0^2$ of our experiment the Beliaev decay rate is on the negligible order of $10^{-2}\,\mathrm{s}^{-1}$ or lower, and only becomes of order 1 for condensate densities one or two orders of magnitude lower. However, eq.(8.4) is for a homogenous gas where the density is uniform. In our case the condensate density

[4] A similar but higher order (and smaller amplitude) process is the Beliaev decay to three excitations of lower energy.

tends to zero near its surface. It is plausible that Beliaev decay could occur at an appreciable rate at the surface of the condensate and could account for the damping rate γ_0.

The second possible mechanism for γ_0 is excitations caused by the motion of the condensate over bumps in the axial potential created by anomalous transverse currents in the chip wires (see sec.4.3). Landau described an equivalent process in a homogenous gas, moving past an obstacle at velocity $\mathbf{v}$. Landau found that for particles to be excited out of the condensate into a mode with energy ϵ and momentum $\mathbf{p}$, the velocity must be higher than a critical value [3]. This critical value is the phase velocity of the excitation $\epsilon/\mathbf{p}$. The lowest energy excitations are phonons whose phase velocity is the sound velocity $c = \sqrt{gn_0/m}$. Thus the neccesary condition for exciting a particle out the condensate is for its velocity to be greater than c. This process is excluded over the bulk of the condensate where the sound velocity is close to $3\,\mathrm{mm\,s^{-1}}$ for our condensate, which is an order of magnitude higher than the velocities typical of our condensate. Even for the maximum amplitude oscillations we observe (15 μm), the peak velocity of the centre of mass oscillations is less than $1\,\mathrm{mm\,s^{-1}}$. However, like Beliaev decay, as the density tends to zero at the condensate surface so does the sound velocity, and this process may occur. Surface excitations created as the condensate runs over the rough potential may therefore also account for γ_0.

Finally, it is useful to show our data for the damping rate versus T rather N_{th}/N where its temperature dependence can be studied explicitly. The temperature of each oscillation dataset is taken as the mean value over the dataset. For each image in the dataset the temperature is calculated from the thermal fraction N_{th}/N and the total atom number using eq.(7.30a) and eq.(7.30b) as described in sec.8.2. Figure 8.7 shows the temperature dependence of the damping rate, $\gamma(T)$, after the background damping rate γ_0 has been subtracted. The horizontal error bars show the standard error of the mean temperature, which has a small spread due to the fluctuations in evaporation efficiency.

The behaviour of γ with T is similar to that of γ with N_{th}/N since the two parameters are so closely related. In fig.8.7 we observe the same sharp change in the behaviour, where γ begins to rise when the temperature exceeds 200 nK as

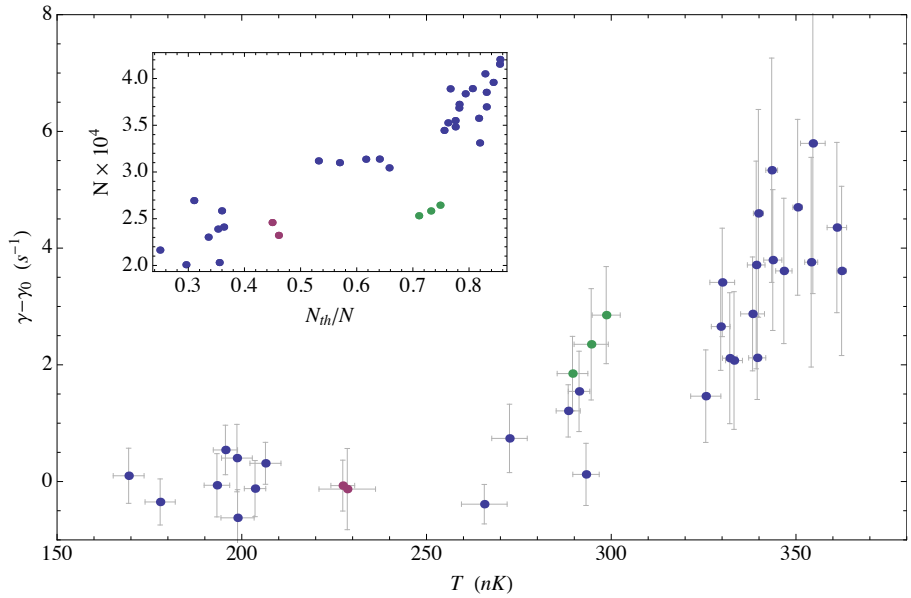

Figure 8.7: Damping rate of oscillations plotted against temperature. Each data point represents the damping rate obtained by fitting eq.(8.1) to a single data set. The temperature is calculated from the measured thermal fraction and atom number using eq.(7.30a) and eq.(7.30b). Compared to fig.8.6, sum of the data points appear more closely bunched together in their temperatures. This can be attributed to a lower atom number for the three data points highlighted in green, and the two in purple. The lower atom number than for other surrounding data points with which these had a similar thermal fraction means that the value of the critical and absolute temperatures are reduced. This is illustrated in the inset, which shows the mean atom number for each dataset plotted against the thermal fraction. The same five data points have been highlighted, and have a visibly lower atom number compared to the trend set by the surrounding data points.

was found for $N_{th}/N > 0.5$ in fig.8.6. In fig.8.7 however, the data points in the range $250 - 300\,\mathrm{nK}$ appear bunched together, where in fig.8.6 these datapoints are spread out much more evenly. This is a manifestation of the different mean atom numbers for each dataset. By inverting the approximate relation eq.(8.2) to give $T = (N_{th}/N)^{1/3} T_c$, and using the critical temperature $T_c = (\hbar/k_B)(\omega_r^2 \omega_z/\zeta(3))^{1/3} N^{1/3}$, it can be seen that for a given thermal fraction N_{th}/N, the absolute temperature depends approximately on the cube root of N. The mean atom number N is shown against N_{th}/N in the inset in fig.8.7. The lower atom number of the two groups of highlighted data points corresponds to lower values of the absolute temperature. This can be seen in the main plot where the corresponding data points are coloured accordingly. The reduced temperature of these two groups of data points is why the data points from $250 - 300\,\mathrm{nK}$ appear bunched together. In the next section we give a more detailed introduction to the Landau damping mechanism and derive the corresponding damping rate. We then compare the damping data presented in

fig.8.7 with the theoretical predictions.

8.4 Landau Damping

Landau damping is caused by collisions between thermal excitations and particles in the moving condensate [138, 26]. These collisions can be divided into two types; those that result in a thermal excitation of higher energy than the initial thermal excitation, thus removing energy from the moving condensate, and those that result in an excitation of lower energy, increasing the energy of the moving condensate. Normally there are more of the first type of collisions, so there is a net loss in energy associated with the motion of the condensate, and the motion is damped.

This damping mechanism was first proposed by Landau to explain the damping of electromagnetic waves in a plasma [138]. More recently, it was proposed by Liu and Schieve [139] that this mechanism could explain the temperature dependent damping of shape oscillations in a dilute atomic vapour found experimentally [21, 22]. A general method for calculating the Landau damping rate in a dilute atomic vapour was first presented by Pitaevskii and Stringari [26]. They additionally give a special case of their method applied to a homogeneous Bose gas, where the equations are simplified greatly, and analytical results can be derived. We compare those results with the damping rate in our experiment, and find that they give a significant overestimate. However, when we adapt the theory to suit our specific case, we obtain a model that fits our observations well.

Pitaevskii and Stringari [26] consider a condensate undergoing a classical oscillation with single particle energy ϵ_q and momentum $\mathbf{q}$. The oscillation is classical in the sense that many particles participate, as in the oscillation experiment (see sec.5.2.3). The condensate is assumed to be moving independently of the thermal cloud, which is also the case in our experiment. Finally, the thermal cloud is populated according to the equilibrium distribution. In this regard, the experimental situation requires further thought.

In thermal equilibrium, the thermal fraction is a function of the temperature, and for an ideal gas $N_{\mathrm{th}}/N = (T/T_c)^3$. We observe only a small spread in the measured

thermal fraction over the 400 ms interval of an oscillation dataset, as indicated by the horizontal error bars in fig.6.10. In the discussion of density profiles in sec.7.3, we argued that a time interval of this duration is completely adequate for the gas to reach its equilibrium distribution, based on the peak thermal density $\zeta(3/2)/\lambda_{\rm dB}^3$, and the tightness of effective potential *eq.*(7.24). In those experiments, we saw no significant variation in thermal fraction (as measured from the density distribution), indicating that the cloud was indeed close to equilibrium the entire time interval. In this experiment however, we must also consider (i) the energy absorbed by the thermal cloud as a result of Landau damping, and (ii) the effect of the rf knife.

In the case of (i), Landau damping converts the kinetic energy of the oscillating condensate into an increase of the thermal energy of the thermal cloud. An upper limit for this is found by assuming that the amplitude of the condensate oscillations decays from an initial amplitude of Z_0, to zero. Since the amplitude of oscillations is small ($Z_0 \approx 10\,\mu$m), this corresponds to negligible temperature increase of 10 nK or less.

In the case of (ii), the rf knife limits the trap depth, causing the hottest atoms to evaporate from the trap. This leads to a redistribution of the remaining energy in the thermal cloud through elastic collisions, lowering its temperature. Once the cloud is cooled by this process sufficiently, it is found to be in a quasi-equilibrium state where further evaporation becomes negligible. In our discussion of evaporative cooling (see Ch.4), we found the time taken to reach the quasi-equilibrium state is on the order of $2\pi/\omega_z$, which is 100 ms in our trap. Furthermore, this time is reduced for when a condensate is present since the curvature of the axial potential is increased. We therefore expect the 400 ms over which oscillations are observed to be a sufficiently long length of time that the cloud remains roughly in thermal equilibrium. Regarding both (i) and (ii), the constancy of the thermal fraction that we measure seems to confirm that the gas is indeed close to equilibrium over the entire time we observe oscillations.

Following this justification, let us recall the method of Landau damping by Pitaevskii and Stringari, which gives the damping rate due to the lowest order coupling between excitations [26]. They treat the condensate and its collective motion as a coherent superposition of N_0 particles in the ground state $|0\rangle$, and N_q particles

in the excited state $|q\rangle$ which has energy $\epsilon_q = \hbar\omega_q$. The total energy associated with the motion of the condensate is therefore $E_q = N_q\hbar\omega_q$. Transitions between $|0\rangle$ and $|q\rangle$ change the populations N_0 and N_q, and subsequently the energy E_q. These transitions are caused by collisions between condensed particles and particles in the thermal cloud. The rate of change of E_q is given by

$$\frac{\mathrm{d}E_q}{\mathrm{d}t} = -\hbar\omega\left(W^{(a)} - W^{(e)}\right). \tag{8.5}$$

Here, $W^{(a)}$ is the rate of the transitions $|q\rangle \to |0\rangle$, whereby one quantum of energy $\hbar\omega_q$ is lost by the condensate and gained by the thermal cloud. $W^{(e)}$ is the reverse process $|0\rangle \to |q\rangle$, whereby the condensate gains a quantum of energy $\hbar\omega_q$ from the thermal cloud. These transition rates are found by considering the collisions in the Bose gas at a microscopic level. These collisions can be studied by adding a small perturbation to the Hamiltonian in the Popov approximation which we discuss next.

The Popov approximation (introduced in sec.7.4.2 for a homogeneous gas) gives a microscopic description of the Bose gas together with its spectrum of thermally populated elementary excitations, which are given by a set of non-interacting quasiparticles [135, 140, 11]. In the Popov approximation these quasiparticle states are thermally populated in accordance with the Bose-Einstein distribution, and we refer to them as 'thermal excitations' here. The second quantised field operators $\mathbf{\Psi}$ and $\mathbf{\Psi}^\dagger$ are separated into operators $\mathbf{\Psi}_0$ and $\mathbf{\Psi}_0^\dagger$, which annihilate and create condensed particles, and the fluctuation operators $\delta\mathbf{\Psi}$ and $\delta\mathbf{\Psi}^\dagger$, which create and annihilate thermal excitations.

In general for a Bose gas with a pairwise contact interaction between particles the Hamiltonian in second quantised form is

$$H = H_0 + \frac{g}{2}\int \mathrm{d}\mathbf{r}\mathbf{\Psi}^\dagger\mathbf{\Psi}^\dagger\mathbf{\Psi}\mathbf{\Psi} \tag{8.6}$$

where H_0 is given by eq.(7.9) and the second term on the right represents the pairwise interaction. The coupling strength is taken as $g = 4\pi\hbar^2 a/m$ and $a = 5.4\,\mathrm{nm}$ is the s-wave scattering length for ^{87}Rb. In the Popov approximation, only the terms of the pairwise interaction that are zeroth ($\mathbf{\Psi}_0^\dagger\mathbf{\Psi}_0^\dagger\mathbf{\Psi}_0\mathbf{\Psi}_0$), second (e.g. $\mathbf{\Psi}_0^\dagger\delta\mathbf{\Psi}^\dagger\delta\mathbf{\Psi}\mathbf{\Psi}_0$) and fourth ($\delta\mathbf{\Psi}^\dagger\delta\mathbf{\Psi}^\dagger\delta\mathbf{\Psi}\delta\mathbf{\Psi}$) order in the fluctuation operators are included. The fourth

order terms are replaced by their expectation (mean field) values which are found from the Bose Einstein distribution at temperature T. On making this replacement, the difference between the Popov Hamiltonian and that of the Bogoliubov theory eq.(7.36), is just a shift in the mean field energy. The Popov Hamitonian can thus be diagonalised by making the Bogoliubov transformation to give a spectrum of non-interacting quasiparticles. These quasi-particle modes take the same form as the Bogoliubov modes (sec.7.4), and are populated according to the Bose Einstein distribution. The Popov approximation thus gives a description of the condensate and thermal excitations of the Bose gas at finite temperature. However, the collisions between condensed particles and thermal excitations that we require for an explanation of damping are not yet included.

To calculate the absorption rate and emission rates $W^{(a)}$ and $W^{(e)}$, the interaction terms third order in the fluctuation field operators

$$V = \frac{g}{2}\int \mathrm{d}\mathbf{r}\left(\boldsymbol{\Psi}_0^\dagger \delta\boldsymbol{\Psi}^\dagger \delta\boldsymbol{\Psi}\delta\boldsymbol{\Psi} + \delta\boldsymbol{\Psi}^\dagger \boldsymbol{\Psi}_0^\dagger \delta\boldsymbol{\Psi}\delta\boldsymbol{\Psi} + \delta\boldsymbol{\Psi}^\dagger \delta\boldsymbol{\Psi}^\dagger \boldsymbol{\Psi}_0 \delta\boldsymbol{\Psi} + \delta\boldsymbol{\Psi}^\dagger \delta\boldsymbol{\Psi}^\dagger \delta\boldsymbol{\Psi}\boldsymbol{\Psi}_0\right), \quad (8.7)$$

are included as a small perturbation to the Popov theory. The rates are calculated, as we will show below, from the first order perturbation. The fluctuation operators can be expanded in terms of the Bogoliubov modes $u_j(\mathbf{r})$ and $v_j(\mathbf{r})$ using eq.(7.41) which we repeat here,

$$\delta\boldsymbol{\Psi} = \sum_j u_j(\mathbf{r})\alpha_j - v_j^*(\mathbf{r})\alpha_j^\dagger, \qquad \delta\boldsymbol{\Psi}^\dagger = \sum_j u_j^*(\mathbf{r})\alpha_j^\dagger - v_j(\mathbf{r})\alpha_j. \quad (8.8)$$

We can then describe the state of the Bose gas in terms of the populations of the single (quasi) particle states $|j\rangle = \alpha_j^\dagger|0\rangle$. These modes have energy ϵ_j relative to the ground state energy ϵ_0 which is taken to be zero.

Following the method of Pitaevskii and Stringari, we assume that the collective excitation of the condensate is described by N_q quanta in the single-particle state $|q\rangle$, which has energy $\hbar\omega_q$. In the case of Landau damping, a quantum of energy $\hbar\omega_q$ is transferred from the collective excitation to the thermal cloud through a collision between a particle in state $|q\rangle$ and a thermal excitation in state $|i\rangle$ with energy ϵ_i. This results in a new thermal excitation in state $|k\rangle$ with energy $\epsilon_k = \epsilon_i + \hbar\omega_q$, and a

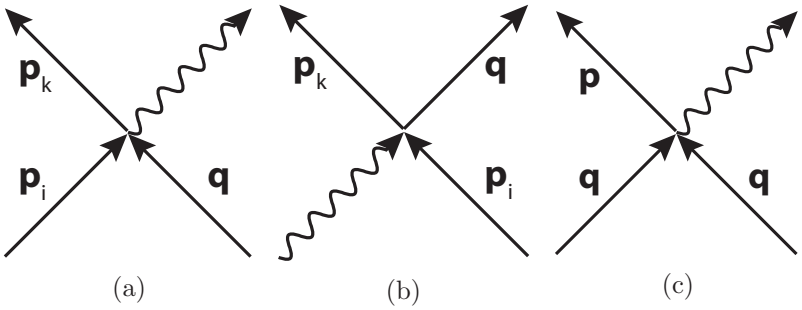

Figure 8.8: Feynman diagrams of third order interactions. These involve a single ground state particle shown by the wave arrows, and three excitations. Figure 8.8a shows the process of absorption of energy by the thermal cloud in Landau damping. In this process a thermal excitation ($\mathbf{p}_i$) and a particle of the collective mode ($\mathbf{q}$) collide and result in a different thermal excitation ($\mathbf{p}_k$) and a particle in the condensate ground state. Figure 8.8b shows the reverse process where the collective mode gains energy from the thermal cloud. Figure 8.8c shows a collision that results in Beliaev decay through two particles in the collective mode colliding to give a different excitation and a ground state particle.

particle in the ground state (condensate) $|0\rangle$.[5] A collision of this type is represented diagrammatically in fig.8.8a. The rate $W^{(a)}$ is the rate at which all the possible transitions $|q,i\rangle \rightarrow |0,k\rangle$ occur. The possible transitions are those where matrix elements of the perturbation V are non-zero, and (to first order in this perturbation) are resonant with energy $\hbar\omega_q$.

From first order time-dependent perturbation theory the absorption rate is

$$W^{(a)} = \sum_{ik} \frac{2\pi}{\hbar} |V_{ik}|^2 N_q N_i \delta(\epsilon_k - \epsilon_i - \hbar\omega_q), \tag{8.9}$$

$$\text{where} \qquad V_{ik} = \langle q,i| \, V \, |0,k\rangle \tag{8.10}$$

is the transition matrix element of the perturbation V given by eq.(8.7). Using eq.(8.8) to expand V, it is straightforward to show that the matrix element eq.(8.10) is

$$V_{ik} = 2g \int \mathrm{d}\mathbf{r}\, \psi_0 \left[\left(u_k^* v_i + v_k^* v_i + u_k^* u_i\right) u_q + \left(v_k^* u_i + v_k^* v_i + u_k^* u_i\right) v_q \right], \tag{8.11}$$

where the Bogoliubov amplitudes u_j and v_j are all functions of $\mathbf{r}$. The Dirac-delta function $\delta(\epsilon_k - \epsilon_i - \hbar\omega_q)$ in eq.(8.9) indicates that according to first order perturbation theory the absorption of energy by the thermal cloud is a resonant

[5] In keeping with the notation of Pitaevskii and Stringari in [26], we call the thermally excited modes i and k. Particles in the collective excitation of the condensate are in mode q. Where necessary we use the letter j to denote a general Bogoliubov mode not constricted to be any particular one of the modes i, k or q.

process; the energy-conserving collisions that contribute to $W^{(a)}$ are centred around those where the incoming and outgoing modes $|i\rangle$ and $|j\rangle$ are separated by energy $\hbar\omega_q$. Contributions from other modes are negligible.

The population N_i in eq.(8.9) of the thermally populated mode i is found from the Bose Einstein distribution,

$$\begin{aligned} f(\epsilon_j) &= N_j \\ &= 1/(e^{\beta(\epsilon_j-\mu)}-1). \end{aligned} \tag{8.12}$$

Degenerate energy levels are treated here by including all degenerate modes in the sum over i,k (instead of a degeneracy factor in the Bose-Einstein distribution).

The rate $W^{(e)}$ involves the reverse process $|k,0\rangle \rightarrow |i,q\rangle$, as shown diagrammatically in fig.8.8b. $W^{(b)}$ is given by

$$W^{(e)} = \sum_{ik} \frac{2\pi}{\hbar}|V_{ik}|^2(N_q-1)N_k\delta(\epsilon_k-\epsilon_i-\hbar\omega_q), \tag{8.13}$$

where $N_k = f(\epsilon_k)$ is the population of the thermally excited state $|k\rangle$. We also assume $N_q \gg 1$, as is the case for our experiment, and approximate $N_q - 1 \approx N_q$.

The rate of energy loss, eq.(8.5), can now be written with the explicit expressions eq.(8.9) and eq.(8.13) for $W^{(a)}$ and $W^{(e)}$,

$$\frac{\mathrm{d}E_q}{\mathrm{d}t} = -2\pi\omega_q \sum_{ik}|V_{ik}|^2\delta(\epsilon_k-\epsilon_i-\hbar\omega_q)N_q\left(f(\epsilon_i)-f(\epsilon_k)\right). \tag{8.14}$$

The damping rate is defined as

$$\frac{\mathrm{d}E_q}{\mathrm{d}t} = -2E_q\gamma = -2N\hbar\omega_q\gamma, \tag{8.15}$$

and from eq.(8.14) is given by

$$\gamma = \pi\omega_q \sum_{ik}|V_{ik}|^2\delta(\epsilon_k-\epsilon_i-\hbar\omega_q)\frac{f(\epsilon_i)-f(\epsilon_k)}{\hbar\omega_q}. \tag{8.16}$$

This equation is the starting point for calculating the damping rate over a discrete spectrum of the excited states of the gas. This equation remains completely gen-

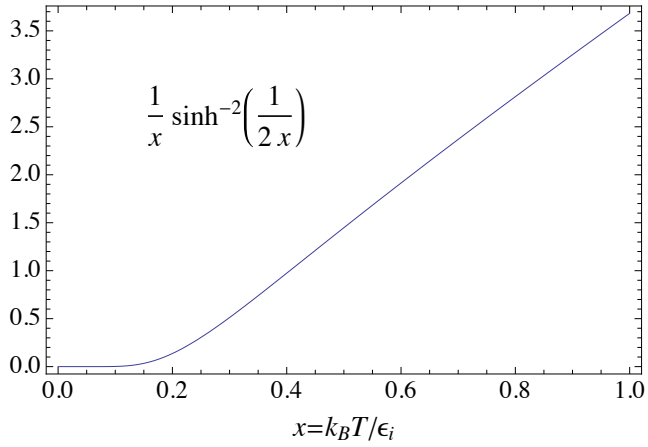

Figure 8.9: Temperature dependence of contribution to the damping rate from modes with energy ϵ_i. This originates from the differential of the Bose-Einstein distribution $\partial f/\partial\epsilon_i \propto x^{-1}\sinh^{-2}(x^{-1}/2)$ with $x = k_{\rm B}T/\epsilon_i$.

eral for a Bose gas, with no assumptions made about the trap geometry and the corresponding excitation spectrum of Bogoliubov modes.

In eq.(8.16), the temperature dependence of the damping rate enters through the thermal populations f_i and f_k. Furthermore, in [26] they assume that $\hbar\omega_q/k_{\rm B}T \ll 1$, which is also true for our experiment where $\hbar\omega_q/k_{\rm B}T \sim 10^{-2}$. This allows them to approximate the difference $(f_k - f_i)/\hbar\omega_q$ by the differential $\left.\frac{\partial f(\epsilon)}{\partial\epsilon}\right|_{\epsilon_i}$:

$$\gamma = \pi\omega_q \sum_{ik} |V_{ik}|^2 \delta(\epsilon_k - \epsilon_i - \hbar\omega_q) \left.\frac{\partial f(\epsilon)}{\partial\epsilon}\right|_{\epsilon_i}. \tag{8.17}$$

Figure 8.9 shows the function for the Bose-Einstein distribution (eq.(8.12)),

$$\left.\frac{\partial f(\epsilon)}{\partial\epsilon}\right|_{\epsilon_i} \propto \frac{1}{x}\sinh^{-2}\left(\frac{1}{2x}\right), \qquad \text{where } x = k_{\rm B}T/\epsilon_i. \tag{8.18}$$

As illustrated in fig.8.9, this function increases with temperature, and therefore so does the Landau damping rate for the transition $|q,i\rangle \to |0,k\rangle$. Figure 8.9 shows that $\frac{\partial f}{\partial\epsilon}|_{\epsilon_i}$ is small for small x, then increases almost linearly when $x > 1/4$, i.e. when $\epsilon_i < 4k_{\rm B}T$.

The exact functional form of $\gamma(T)$ depends on what modes in the sum over i and k are permitted, and on the amplitude of V_{ik}. These mode are restricted by two conditions. Firstly, the they must satisfy energy conservation during collisions, as stipulated by the resonance condition $\delta(\epsilon_k - \epsilon_i - \hbar\omega_q)$ in eq.(8.16) and eq.(8.17).

Secondly, not all modes $|i\rangle$ and $|k\rangle$ are coupled by V (eq.(8.7)).Often a condition may be found for which the matrix elements $V_{ik} \neq 0$. For example, in a homogeneous gas the Bogoliubov modes are plane waves, and the condition that $V_{ik} \neq 0$ is the condition that momentum be conserved, i.e. $\mathbf{k}_k = \mathbf{k}_i + \mathbf{k}_q$. This arises naturally from the orthogonality of plane waves.

The simple form of the modes, and the straightforward condition of momentum conservation make the homogenous gas an appealing system for an initial study of Landau damping. Two variations of homogeneous gas models form the basis of the following sections, and when compared with our experimental observations, offer considerable insight into the damping that occurs in our experiment.

Having introduced the microscopic mechanism of Landau damping, it is a convenient place to note that Landau damping is not the only damping mechanism caused by the annihilation of quanta of the collective motion of the condensate. Beliaev decay, illustrated in fig.8.8c, is another such process [137, 26, 27].A Beliaev decay of a quasiparticle in state $|q\rangle$ results in three particles in lower energy states. For the third order interaction term eq.(8.7), one of the resultant particles is in the ground state, while the other two are in excited states of $|i\rangle$ and $|k\rangle$ with energy such that $\epsilon_i + \epsilon_k = \hbar\omega_q$. This process is shown in fig.8.8c. For particles in a collective mode $|q\rangle$ which has a low single particle energy in a discrete spectrum, very few final states are accessible. The Beliaev damping which results is therefore naturally small compared to Landau damping for which many more resonant transitions can be found. For Beliaev decay of a quanta $|q\rangle$ into three lower energy excitations the damping rate is likely to be smaller still. Furthermore, Beliaev damping depends on the population of the collective excitation N_q, but not that of thermally excited modes, and is therefore not explicitly temperature dependent. We observe a strong temperature dependence in the damping rates that we have measured, and therefore do not consider Beliaev damping in an explanation of the temperature dependent damping. However, it may explain the constant background damping rate.

8.4.1 Landau damping for a homogeneous gas in free space

We now describe the specific case of Landau damping in a 3D homogeneous Bose gas, which is a good starting point for discussing the Landau damping in our experiment. Analytic expressions (eq.(8.30) and eq.(8.29) below) for the Landau damping rate of a homogeneous gas in free space were first derived in [141] and [142]. Of particular interest is the temperature dependence of γ that these results predict. More recently the same results were derived in the work [26] by Pitaevskii and Stringari as an example of a specific case of their general formulation. We follow their derivation of these results in the first part of this section, and then we compare the analytic results to the data from our experiment. Although both theory and experiment show an increase in γ with T, we find that the calculated damping rate is significantly larger than the rate we measure. However, a simple adaptation of the theory, described below in sec.8.4.3, provides a much better description of our trapped gas and gives values for $\gamma(T)$ in close agreement with our measurements.

For a homogeneous gas with periodic boundary conditions defined by the lengths $L_x,\ L_y$ and $L_z,\ |\psi(x,y,z)\rangle = |\psi(x+n_xL_x, y+n_yL_y, z+n_zL_z)\rangle$ (n_x, n_y, n_z being integers), and the Bogoliubov modes take on the particularly simple form of plane waves with momentum

$$\mathbf{k} = \left(\frac{2\pi n_x}{L_x}, \frac{2\pi n_y}{L_y}, \frac{2\pi n_z}{L_z}\right). \tag{8.19}$$

In the example presented by Pitaevskii and Stringari [26], they begin by working with the discrete set of modes by keeping $L_x,\ L_y$ and L_z finite, then later take the continuum limit at constant density, and thus describe a 3D homogeneous Bose gas in the thermodynamic limit. The discrete modes were introduced in eq.(7.51) and eq.(7.55) of sec.7.4.2, and follow the dispersion relation eq.(7.52). For the collective mode $|q\rangle$ which has low energy compared to μ, we use the phonon approximation

$$\epsilon(k_q) = c\hbar k_q \qquad \text{where } c = \sqrt{gn_0/m}, \tag{8.20}$$

is the velocity of sound. For the thermal excitations we use the single particle energy

$$\epsilon(k) = \frac{\hbar^2 k^2}{2m}. \tag{8.21}$$

These are good approximations for the energies in our experiment.

The matrix element V_{ik} is found using eq.(7.51) and eq.(7.55) in eq.(8.11),

$$V_{ik} = \frac{2g\sqrt{n_0}}{V^{3/2}} \int_V \mathrm{d}\mathbf{r}\, C_{kiq}\, e^{i(\mathbf{k}_i+\mathbf{k}_q-\mathbf{k}_k)\cdot\mathbf{r}}, \tag{8.22}$$

$$\text{where} \quad C_{kiq} = (u_k v_i + u_k u_i + v_k v_i)u_q + (v_k u_i + u_k u_i + v_k v_i)v_q. \tag{8.23}$$

The tensor components C_{kiq} are constant, and for finite volume where the wave-vector takes the discrete values of eq.(8.19), the integral evaluates to the Kronecker delta product

$$\frac{1}{V}\int_V \mathrm{d}\mathbf{r}\, e^{i(\mathbf{k}_i+\mathbf{k}_q-\mathbf{k}_k)\cdot\mathbf{r}} = \delta_{n_{x_i} n_{x_k}} \delta_{n_{y_i} n_{y_k}} \delta_{(n_{z_i}+n_q) n_{z_k}} \tag{8.24}$$

where n_{x_i} is the integer of the x-component of the wave-vector $\mathbf{k}$. The right hand side of eq.(8.24) is equal to one only when momentum is conserved. Consequently, given $\mathbf{k}_i$ and $\mathbf{k}_q$, $\mathbf{k}_k$ is fixed and the sum in eq.(8.16) over all modes k for a given mode i can be dropped:

$$\gamma = \pi\omega_q \frac{4g^2 n_0}{V} \sum_i C_{kiq}^2 \delta(\epsilon_k - \epsilon_i - \hbar\omega_q)\, \frac{\partial f(\epsilon)}{\partial \epsilon}\bigg|_{\epsilon_i} \tag{8.25}$$

The continuum limit can be taken at this point, replacing $\sum_i \to \frac{V}{(2\pi)^3}\int \mathrm{d}\mathbf{k}_i$,

$$\gamma = 4\pi\omega_q g^2 n_0 \int \frac{\mathrm{d}\mathbf{k}_i}{(2\pi)^3} C^2(\epsilon_i, \epsilon_k, \epsilon_q)\delta(\epsilon_k - \epsilon_i - \hbar\omega_q)\, \frac{\partial f(\epsilon)}{\partial \epsilon}\bigg|_{\epsilon_i} \tag{8.26}$$

where following [26] we work from the variant eq.(8.17) of eq.(8.16) with $[f(\epsilon_k) - f(\epsilon_i)]/\hbar\omega_q \approx \frac{\partial f}{\partial \epsilon}$.

The next step is to turn the condition of energy conservation into a region in k-space to integrate over. First consider the condition $\mathbf{k}_k = \mathbf{k}_i + \mathbf{k}_q$, shown diagrammatically in fig.8.10a. The unit vector $\hat{\mathbf{z}}$ is oriented along the direction of the collective motion of the condensate such that $\mathbf{k}_q = k_q\hat{\mathbf{z}}$. Switching to spherical polar coordinates, the angle θ of the vector $\mathbf{k}_i$ is the angle between $\mathbf{k}_q$ and $\mathbf{k}_i$. Momentum conservation requires $k_{\perp_i} = k_{\perp_k}$ with their azimuthal angles ϕ equal, and the distance between the heads of the vectors $\mathbf{k}_i$ and $\mathbf{k}_k$ is k_q. As θ is varied the vector $\mathbf{k}_k$ sketches out the curve labelled $k_k(\theta)$ in fig.8.10a, while $\mathbf{k}_i$ sketches out a circular

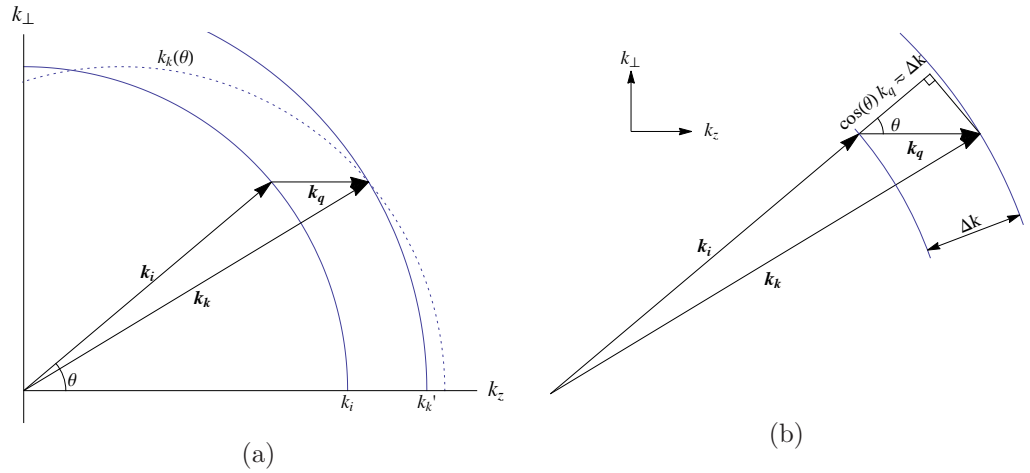

Figure 8.10: Conditions for energy and momentum conservation for Landau damping. The vectors $\mathbf{k}_i$, $\mathbf{k}_k$ and $\mathbf{k}_q$ are represented by the arrows as labelled, and the direction $\hat{\mathbf{z}}$ is taken such that $\mathbf{k}_q = k_q\hat{\mathbf{z}}$. θ is the angle between $\mathbf{k}_q$ and $\mathbf{k}_i$. Figure 8.10a shows graphical solution of θ that conserves both energy and momentum. From momentum conservation $\mathbf{k}_k$ must fall along the dotted curve $k_k(\theta)$. Energy conservation requires $\mathbf{k}_k$ to fall on the circular arc of radius $k_i + \Delta k$. The solution of θ is where the curve and arc cross. Figure 8.10b illustrates the approximation of Δk used to define θ in eq.(8.27). The separation of the arcs is the true value of arc Δk.

arc of radius k_i. However, energy conservation requires that $\mathbf{k}_k$ takes value k_k' such that $\epsilon(k_k') = \epsilon(k_i) + \hbar\omega_q$. Where the curve $k_k(\theta)$ and the arc of radius k_k' intersect, energy and momentum are both conserved.

In [26] this condition for θ is found from the approximate relation $\epsilon_k - \epsilon_i \approx \frac{\partial\epsilon}{\partial k}\Delta k$. $\Delta k = |k_k - k_i|$ and is itself approximated by $k_q \cos\theta$ as shown in fig.8.10b. Furthermore, the momentum k_q is found from the energy $\hbar\omega_q$, using the low energy dispersion relation eq.(8.20). Thus the integral over θ in eq.(8.26) only has non-zero contribution for θ such that

$$\epsilon_k - \epsilon_i = \frac{\hbar\omega_q}{c} v_g(\epsilon_i)\cos\theta. \tag{8.27}$$

where $v_g = \partial\epsilon/\partial\hbar k\big|_{\epsilon_i}$ is the group velocity of mode i, and c is the phonon velocity $\sqrt{gn_0/m}$. After integrating eq.(8.26) over θ we find

$$\gamma = \frac{c}{4\pi\hbar} 4g^2 n_0 \int_0^\infty \frac{k_i^2 \mathrm{d}k_i}{v_g(\epsilon_i)} C^2(\epsilon_i, \epsilon_q) \left.\frac{\partial f(\epsilon)}{\partial\epsilon}\right|_{\epsilon_i} \tag{8.28}$$

where $C(\epsilon_i, \epsilon_q)$ is given by eq.(8.23) with u_k and v_k evaluated at energy $\epsilon_i + \hbar\omega_q$. This is the main result for the Landau damping rate in a free space homogeneous

gas, and is equivalent to equation (14) in [26][6].

8.4.2 Discussion of behaviour of $\gamma(T)$ in the homogenous free space theory

We can find the damping rate $\gamma(T)$ from eq.(8.28) by evaluating the integral numerically. We take the upper integration limit of k to be $10^8\,\mathrm{m}^{-1}$, by which point the integrand is essentially zero due to the term $\frac{\partial f}{\partial \epsilon}$ at the relevant temperatures. To evaluate eq.(8.28) we must also choose an appropriate energy ϵ_q of the collective mode in our simple model. The harmonically trapped oscillating condensate in our experiment is described by a coherent superposition of the low energy (axial) Bogoliubov modes, similar to the coherent state that describes centre of mass oscillations for an ideal Bose gas. A thorough comparison between the superposition that describes the collective oscillation in a harmonic trap, and the equivalent collective excitation for a uniform gas is a subject for future work, but a straightforward estimate of the size of ϵ_q is made here. For the harmonically trapped gas, we know the average energy per particle in this superposition must be $\frac{1}{2}m\omega_z^2 Z_0^2$, where ω_z is the axial trap frequency and Z_0 the amplitude of the centre of mass oscillations. By analogy of the coherent state for an ideal gas in a harmonic trap, on average, particles are to be found in the excited state with this mean energy.[7] Thus, in our uniform gas model, we take the mode with energy $\epsilon_q = \frac{1}{2}m\omega_z^2 Z_0^2$ to represent the collective oscillation.

Figure 8.11a shows the Landau damping rate γ calculated from eq.(8.28) as a function of T up to $5 \times 10^{-7}\,\mathrm{K}$. The condensate density was taken to be $n_0 = 3 \times 10^{20}\,\mathrm{m}^{-3}$, which is typical of our experiment, and $\epsilon_q = \frac{1}{2}m\omega_z^2 Z_0^2$ with $\omega_z = 2\pi \times 10\,\mathrm{Hz}$ and $Z_0 = 10^{-5}\,\mathrm{m}$. At $T = 0$ where there are no thermal excitations the damping rate is zero. There is barely any increase in the damping rate up to $T = 10^{-8}\,\mathrm{K}$ as can

[6] It is not clear how they arrived at their approximation in their equation (15) for the term $C(\epsilon)$ in their equation (14), but the factor $\sqrt{2g}$ appears to be incorrectly stated. However, our result eq.(8.28) agrees with the low and high temperature approximations when evaluated (see fig.8.11), and agrees with their dimensionless version of their equation (14) - for comparison see the theoretical lines on our fig.8.11a and their figure (1). For these reasons we are confident that our eq.(8.28) is correct.

[7] The energy spectrum, $n\hbar\omega_0$, for a harmonic trap of frequency ω_0 is actually remarkably similar to the spectrum of low energy Bogoliubov modes, $\hbar\omega_z\sqrt{n(n+3)/4}$, which quickly approaches $\hbar\omega_z n/2$ [143].

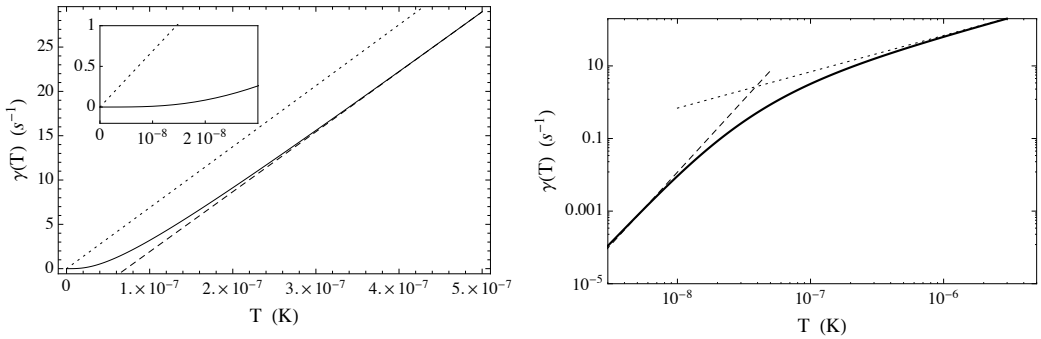

Figure 8.11: Landau damping rate calculated from eq.(8.28) with $\epsilon_q = m\omega_z^2 z^2/2$ and $n_0 = 3 \times 10^{20}\,\mathrm{m}^{-3}$. Figure 8.11a shows the variation of γ with T calculated by numerical integration of eq.(8.28) and plotted on a linear scale (solid line). At higher temperatures the temperature dependence of γ is almost linear. The dotted line shows the high temperature approximation eq.(8.29) for $\gamma(T)$, which has a similar gradient to the solid line for $T \gtrsim 2.5 \times 10^{-7}\,\mathrm{K}$ but overestimates γ. The dashed line has the same gradient as the high temperature approximation but is shifted down to match the solid line. Figure 8.11b shows the same exact function of γ (solid line) on a logarithmic scale, where the change in its dependence on T can be seen clearly. At low temperature it scales approximately as T^4, similar to the low temperature approximation eq.(8.30) (dashed line). The high temperature linear approximation is shown by the dotted line.

be seen from the inset in fig.8.11a. Between $10^{-8}\,\mathrm{K}$ and approximately $2 \times 10^{-7}\,\mathrm{K}$ the damping rate increases more and more rapidly as the gradient $\partial\gamma/\partial T$ increases. As the temperature increases further, the damping rate reaches a linear regime. The linear approximation, shown by the dashed straight line in fig.8.11a, is barely different from the exact result above $3 \times 10^{-7}\,\mathrm{K}$.

In fact, the Landau damping rate can be approximated in high and low temperature regimes by eq.(8.29) and eq.(8.30) given below. In the high temperature regime, $k_\mathrm{B}T \gg gn_0$, the damping rate scales linearly with temperature,

$$\gamma = \frac{3\pi}{8}\frac{k_\mathrm{B}Taq}{\hbar^2}, \tag{8.29}$$

where $a = 5.4\,\mathrm{nm}$ is the s-wave scattering length [102], and q is the quasi-particle wavenumber. This can be be derived from eq.(8.28) by approximating $f(\epsilon_i)$ in the Rayleigh-Jeans limit [26], but was originally studied by a different method in [141]. This high temperature approximation is shown by the dotted line in fig.8.11a which matches the gradient of the dashed line but has an offset leading to an over estimate of the damping rate. In the low temperature regime $k_\mathrm{B}T \ll gn_0$ the damping rate

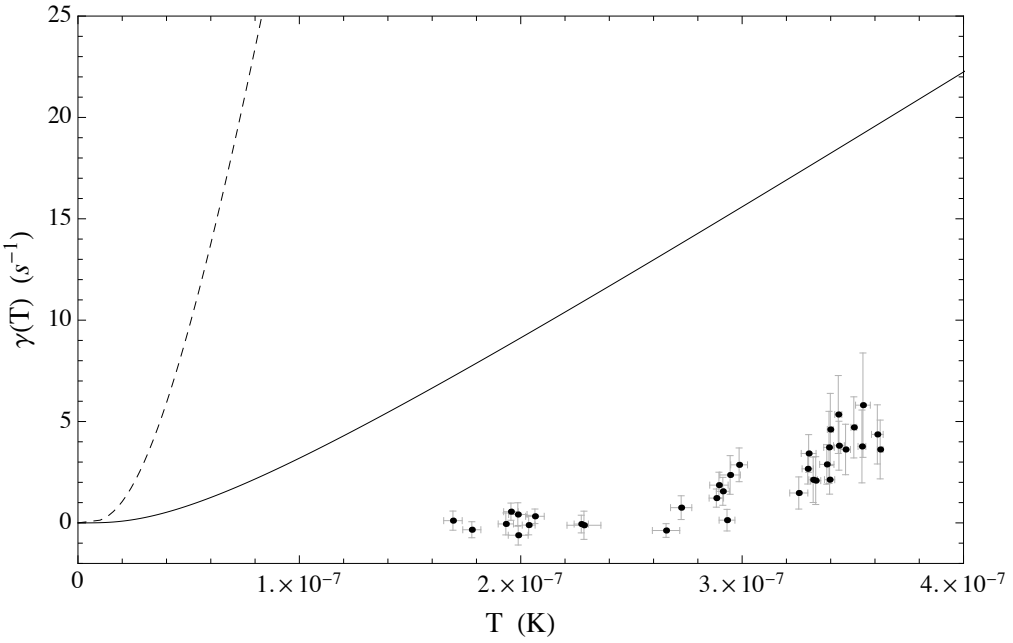

Figure 8.12: Comparison of measured damping rate to homogenous gas model eq.(8.28). Data points show the experimental measurements just as shown in fig.8.7. The solid line is the damping rate calculated from eq.(8.28) with the lower estimated of the collective mode single particle energy $\epsilon_q = m\omega_z^2 Z_0^2/2$, and the dashed line is with the higher estimate $\epsilon_q = 5m\omega_z^2 Z_0^2$.

scales like T^4,

$$\gamma = \frac{27\pi}{16}\frac{\omega\rho_n}{\rho} \approx \frac{27\pi}{16}\frac{\omega}{mn_0}\frac{2\pi^2(k_{\rm B}T)^4}{45\hbar^3c^5}, \tag{8.30}$$

where $\rho_n = 2\pi^2(k_{\rm B}T)^4/(45\hbar^3c^5)$ is the normal part density of the phonon gas ([144] section 22). This result was first found by Hohenberg and Martin [142], but can also be found from eq.(**??**).

In fig.8.11a the low and high temperature regimes are in the regions where $T < 10^{-8}\,\mathrm{K}$ and $T > 3\times10^{-7}\,\mathrm{K}$ respectively. However, this is best seen in the log plot fig.8.11b, where the solid line shows the exact result from eq.(8.28). The dashed line shows the low temperature approximation eq.(8.30), and the dotted line the high temperature approximation eq.(8.29). For $T < 10^{-8}\,\mathrm{K}$ the predicted damping rate is very small ($\gamma < 10^{-2}\,\mathrm{s}^{-1}$) and closely follows the dashed line of the low temperature approximation. The behaviour of the damping rate then smoothly varies until it follows the dotted line above a few $10^{-7}\,\mathrm{K}$, where it varies linearly with T.

We now compare this Landau damping rate for the homogeneous gas, given by eq.(8.28), with the measurements made in our experiment discussed in sec.8.3 above. Figure 8.12 shows the temperature dependent part of the measured damping rate

$(\gamma - \gamma_0)$ plotted alongside the theoretical value of $\gamma(T)$ from eq.(8.28). The solid line shows the theoretical value with $n_0 = 3 \times 10^{20}\,\mathrm{m}^{-3}$ and energy of the collective mode given by $\epsilon_q = m\omega_z^2 Z_0^2/2$. Most obviously, the theory significantly overestimates the damping rate that we measure, even for the lower estimate of ϵ_q. However, the overall form of the temperature dependence does resemble that of our measurements, even though the scale is incorrect. In particular, both show a negligible increase in γ at lower temperatures, then around $2.6 \times 10^{-7}\,\mathrm{K}$ in our experiment and around $10^{-8}\,\mathrm{K}$ in the theory, the damping rate starts to increase. The theory then becomes linear at higher temperatures, and above $3 \times 10^{-7}\,\mathrm{K}$ the measured damping rate appears to rise quite steadily with a similar gradient.

It is insightful for the comparison between the data and theory to ask why this change in behaviour from a low temperature regime to a high temperature regime occurs. As suggested above in the discussion of eq.(8.17), eq.(8.18) and fig.8.9, the temperature dependence originates from the population difference $f(\epsilon_i) - f(\epsilon_k)$ between the incident and scattered thermal excitations $\mathbf{k}_i$ and $\mathbf{k}_k$. For damping of a collective mode with low energy $\epsilon_q \ll k_\mathrm{B}T$, this difference is $\partial_\epsilon f(\epsilon_i)\,\epsilon_q \approx (1/4k_\mathrm{B}T)\sinh^{-2}(\epsilon_i/2k_\mathrm{B}T)$. We can therefore write the general expression eq.(8.17) for the Landau damping rate as the weighted sum of temperature dependent functions $g_i(T)$ over all modes k_i indexed by i,

$$\gamma(T) = \sum_i W_i g_i(T). \tag{8.31}$$

The temperature dependent functions are given by

$$g_i(T) = \frac{\epsilon_i}{k_\mathrm{B}T}\sinh^{-2}\left(\frac{\epsilon_i}{2k_\mathrm{B}T}\right), \tag{8.32}$$

which are shown in fig.8.13a for three different values of $\mathbf{k}_i$. For smaller values of k_i the functions $g_i(T)$ start to rise above zero to reach the linear regime at lower temperatures. For example for $k_i = 5 \times 10^6\,\mathrm{m}^{-1}$ the function $g_i(T)$ starts to turn up at a temperature of about $10^{-8}\,\mathrm{K}$, while for $k_i = 2 \times 10^7\,\mathrm{m}^{-1}$ it does not start to turn up until about $2 \times 10^{-7}\,\mathrm{K}$.

In the homogenous gas theory given in this section the spectrum of states k_i is a continuum. The corresponding weight factor is proportional to $k_i^2 C_{kiq}^2/(\epsilon_i v_g(\epsilon_i))$,

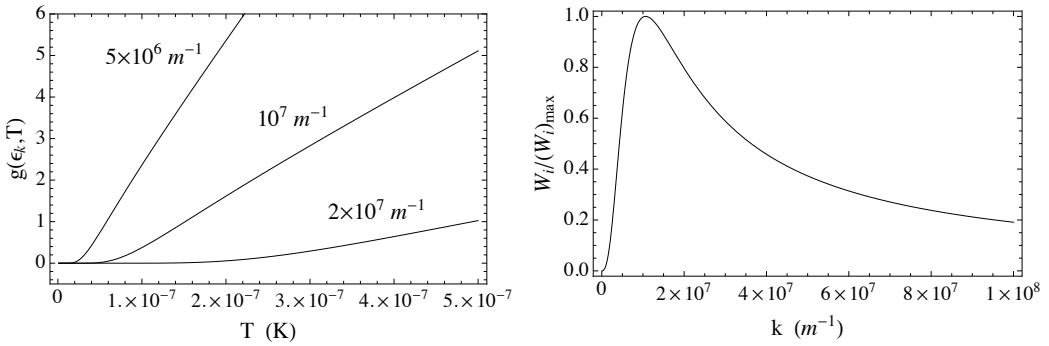

(a) (b)

Figure 8.13: The temperature dependence of Landau damping comes from the weighted sum eq.(8.31), over the temperature dependent functions such as those in fig.8.13a, with a weight factor such as that shown in fig.8.13b. Figure 8.13a shows the temperature dependence of the function eq.(8.32) for three values of the wavenumber, $k = 2 \times 10^7,\ 10^7, 5 \times 10^6\,\mathrm{m}^{-1}$. Figure 8.13b shows the weight factor as a function of k, found from the temperature independent part of the integrand in eq.(8.28) and normalised to 1.

and is shown normalised to 1 in fig.8.13b against the value of k_i. In this continuum theory the weighted sum becomes an integral over all $k_i > 0$. The weight factor shows that there is an appreciable contribution to γ from functions over a large range of k_i which extends down to k_i close to zero. It is the low energy contributions which cause the damping rate to start to turn up above zero at the relatively low temperature of about 10^{-8} K in the continuum theory.

However, in our experiment the trapped gas has a discrete spectrum. The tight transverse confinement of our trap means that the energy spacing of transverse modes is particularly large - on the order of $k_{\mathrm{B}}T$. Incorporating a similar discrete spectrum into the simpler model of a homogeneous gas will change the damping rate significantly, since the weighted sum will be over fewer, and higher energy modes. Subsequently, we hypothesise that such a discrete spectrum will have two main effects on the Landau damping rate: (i) at a given temperature the damping rate will be reduced, and (ii) the point at which the damping rate starts to rise will be raised to higher temperatures. If our hypotheses are correct, the damping rate predicted by a homogenous gas model with a discrete spectrum will be in closer agreement to the damping rates we observe in our experiment. To test our hypotheses, we derive a version of Landau damping with a discrete spectrum in the next section.

8.4.3 Landau damping in a highly elongated trap

We will show that by taking into account the discrete spectrum of our trap, we are able to obtain a much closer description of the damping rate we observe in our experiment. In deriving the Landau damping rate for the free space homogenous gas, which had a continuous spectrum, we initially started with a discrete spectrum of states with mode volume V. We then took the continuum limit in deriving eq.(8.26) from eq.(8.25), by taking $V \to \infty$. Here, we continue from the homogenous gas damping rate eq.(8.25) (repeated below), without taking the continuum limit.

$$\gamma = \pi\omega_q \frac{4g^2 n_0}{V} \sum_i C_{kiq}^2 \delta(\epsilon_k - \epsilon_i - \hbar\omega_q) \left.\frac{\partial f(\epsilon)}{\partial \epsilon}\right|_{\epsilon_i} \tag{8.33}$$

The discrete spectrum of modes is defined by the periodic boundary conditions $\psi(x, y, z) = \psi(x + m_x W, y + m_y W, z + m_z L)$, and hence the wave vector of each mode is given by

$$\mathbf{k}_j = \left(\frac{2\pi n_{j_x}}{W}, \frac{2\pi n_{j_y}}{W}, \frac{2\pi n_{j_z}}{L}\right). \tag{8.34}$$

In this theory, W and L are now the characteristic (transverse) width and (axial) length of the trapped Bose gas in our experiment.

We now re-examine the constraints on energy and momentum when the spectrum is discrete. As previously shown, momentum conservation is required for a non-zero matrix element of a Landau damping collision. We recall that these collision are between a thermal excitation of momentum $\mathbf{k}_i$ and a particle of the collective excitation with momentum $\mathbf{k}_q$, resulting in a new thermal excitation with momentum $\mathbf{k}_k$ and a ground state particle with zero momentum.

Energy conservation is enforced by the narrow function $\delta(\epsilon_k - \epsilon_i - \hbar\omega_q)$. With a continuous spectrum, we took this function to be the Dirac-delta. Since the spectrum was continuous we could always find modes that satisfied the stringent condition that ϵ_k must be exactly equal to $\epsilon_i + \hbar\omega_q$. In the discrete spectrum theory this is not the case. This can be seen by examining fig.8.14, which is an illustration of the conditions of energy and momentum conservation for the discrete spectrum. The arrows show a set of wave vectors $\mathbf{k}_i$, $\mathbf{k}_k$ and $\mathbf{k}_q$, which obey momentum conservation. For an incident thermal excitation of momentum $\mathbf{k}_i$ lying on the arc of radius $k(\epsilon_i)$, energy

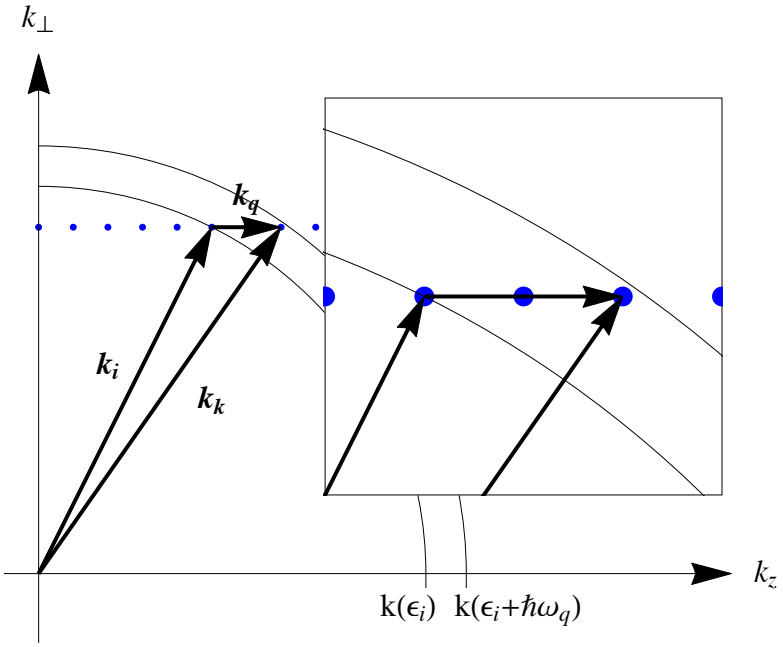

Figure 8.14: Conditions for energy and momentum conservation when the spectrum is discrete. The arrows show the momenta of the incident thermal excitation $|i\rangle$, the collective mode $|q\rangle$, and the scattered thermal excitation $|k\rangle$. The blue dots are the Bogoliubov modes permitted by a set of periodic boundary condition, which form a discrete spectrum. For the clarity of this illustration we have not used the exact values of momenta and the boundary conditions that correspond to our experiment. In this illustration these are shown for the lowest non-zero radial component. The circular arcs show the condition for energy to be conserved: For $\mathbf{k}_i$ falling on the inner arc, $\mathbf{k}_k$ must fall on the outer arc for which its energy is $\epsilon(k_k) = \epsilon_i + \epsilon_q$. The inset shows how this criterion is not generally satisfied when the spectrum is discrete.

conservation requires the head of $\mathbf{k}_k$ to lie on the arc of radius $k(\epsilon_i + \hbar\omega_q)$. In a discrete spectrum, we additionally required that the value of momentum is one of these given by eq.(8.34). The allowed values of momentum are represented by dots in fig.8.15, and the arrows shown are the valid momenta that obey momentum conservation. Evidently, it is not usually possible to find modes that satisfy the conditions of energy and momentum conservation simultaneously.[8]

However, in a more realistic model of our trapped gas, $\delta(\epsilon_k - \epsilon_i - \hbar\omega_q)$ actually has finite width, due to the limited coherence time of the interaction. From first order time-dependent perturbation theory, the probability of a transition from state i to state k in time interval τ is given by

$$P_{ik}(\tau) = (2\pi)^2 |V_{ik}|^2 \delta(\Delta\epsilon)^2 \qquad \text{where } \delta(\Delta\epsilon) = \frac{\tau}{2\pi\hbar}\text{sinc}\left(\frac{\tau}{2\hbar}\Delta\epsilon\right). \tag{8.35}$$

[8] In fact, a resonance can only occur for specific combinations of ϵ_i and ϵ_q and the length parameter L.

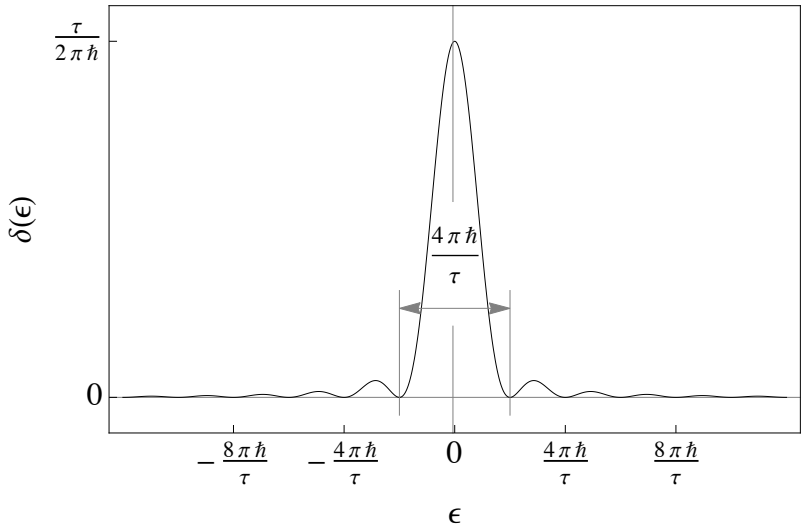

Figure 8.15: Energy resonance for Landau collisions as given by eq.(8.36). There is only one scale, set by the interaction time τ ($\sim 1/\gamma_{\rm el}$), which determines the height and width of this function. We take the width $4\pi\hbar/\tau$ to be the energy difference between the principal roots of this function, as illustrated.

This means that the function $\delta(\epsilon_k - \epsilon_i - \epsilon_q)$, first introduced in the absorption and emission rates in eq.(8.9) and eq.(8.13), should be replaced by

$$\delta(\epsilon_k - \epsilon_i - \hbar\omega_q) = \frac{\tau}{2\pi\hbar}\mathrm{sinc}^2\left(\frac{\tau}{2\hbar}(\epsilon_k - \epsilon_i - \hbar\omega_q)\right). \tag{8.36}$$

The function eq.(8.36) is shown in fig.8.15 and has width on the order of $4\pi\hbar/\tau$. Consider a thermal excitation in state $|\mathbf{k}_i\rangle$ which has finite probability of being transformed into state $|\mathbf{k}_k\rangle$ through the Landau interaction V_{ik}. The excitation $|\mathbf{k}_i\rangle$, created at time t_0 by some interaction of third or fourth order in the fluctuation operators $\delta\mathbf{\Psi}$ and $\delta\mathbf{\Psi}^\dagger$, can decay at time $t_0 + \tau$ into a different excitation through a third or fourth order interaction other than the Landau interaction. The time interval τ, during which a Landau interaction can take place, is therefore limited by the lifetime of the thermal excitation $|\mathbf{k}_i\rangle$ due to other interactions.

In the free space homogeneous theory considered in the previous section we ignored any other third or fourth order interactions. Consequently, we took the lifetime to be infinite and the function $\delta(\epsilon_k - \epsilon_i - \hbar\omega_q)$ to be the Dirac-delta. In our experiment however, we know that the lifetime is at the very least limited by elastic collisions between thermal excitations, which are the fourth order interaction in the fluctuation operators, and are necessary for us to perform evaporative cooling. From

the semi-ideal gas model of the partially condensed Bose gas, elastic collisions occur at a peak rate of

$$\gamma_{\rm el} = \frac{\zeta(3/2)}{\lambda_{dB}^3}\langle v_{\rm rel}\rangle\sigma \qquad \text{where } \sigma = 8\pi a^2\left[1+\left(\frac{2\pi a}{\lambda_{dB}}\right)^2\right]^{-1}. \tag{8.37}$$

and we take the interaction time τ to be on the order of $1/\gamma_{\rm el}$.

Taking into consideration the finite width of the delta function eq.(8.36), the Landau damping rate eq.(8.33) in the homogeneous discrete spectrum theory is now given by

$$\gamma(T) = \pi\omega_q\frac{g^2 n_0}{W^2 L}\sum_i C_{kiq}^2\frac{\tau}{2\pi\hbar}\mathrm{sinc}^2\left(\frac{\tau}{2\hbar}(\epsilon_k-\epsilon_i-\hbar\omega_q)\right)\left.\frac{\partial f(\epsilon)}{\partial\epsilon}\right|_{\epsilon_i} \tag{8.38}$$

This is the general result for the Landau damping rate of a homogenous gas with a discrete spectrum given by the periodic boundary conditions. In deriving this we have taken the two transverse widths to be equal, $L_x = L_y = W$, but an equivalent expression with different widths is also valid. We next look at how we evaluate this expression for the parameters W and L of orders of magnitude that suit our trap. For our typical parameters W and L, the sum is over a large number of modes and therefore time consuming to evaluate for one specific temperature T alone. However, we show below the problem can be simplified to significantly reduce the number of terms in the sum.

The sum in eq.(8.38) is over all excited modes eq.(8.34), as permitted by the boundary conditions specified by W and L. The sum over i can thus be split into consecutive sums over n_x, n_y and n_z.

$$\sum_i \to \sum_{n_x=-\infty}^{\infty}\sum_{n_y=-\infty}^{\infty}\sum_{n_z=-\infty}^{\infty} \tag{8.39}$$

To use eq.(8.38) to estimate the damping rate in our trapped Bose gas we choose the width W and length L to match our condensate. The width of our highly elongated condensate is on the order of the radial harmonic oscillator length $\sqrt{\hbar/m\omega_\rho} \approx 3\times10^{-7}$ m and its length approximately 200 μm. To calculate the damping rate $\gamma(T)$ up to a few hundred nano-Kelvin the sum over transverse modes can be truncated once $n_x, n_y \gtrsim 10$, above which $\epsilon \gg k_{\rm B}T$. The sum over axial modes can be truncated

so that it covers an energy range of a few times the width $4\pi\hbar/\tau$ of the function $\delta(\epsilon_i - \epsilon_k - \hbar\omega_q)$ of eq.(8.36) which describes the energy resonance between the incident and scattered modes. Beyond this range the function $\delta(\epsilon_k - \epsilon_i - \hbar\omega_q)$ is close to zero. To define this range we must find the k-space value k_{z_0}, and the interval Δk_z, which corresponds to the centre and width of this resonance.

Given a transverse mode $k_{i_\perp}$, this region is centred about the value of k_{i_z}, which satisfies

$$\epsilon(k_i) + \hbar\omega_q = \epsilon(k_k) \quad \text{with } k_i^2 = k_{i_\perp}^2 + k_{i_z}^2, \quad k_k^2 = k_{i_\perp}^2 + (k_{i_z} + k_q)^2 \tag{8.40}$$

where k_k^2 follows from momentum conservation. This can be solved for k_{i_z} analytically using the Bogoliubov dispersion relation eq.(7.52), but yields a lengthy expression which is difficult to work with. Instead, using the high temperature approximation eq.(8.21) of the dispersion relation for the thermal excitations and the low energy approximation for the collective mode, we find the energy difference from resonance is given by[9]

$$\begin{aligned} \Delta\epsilon &= \epsilon(k_k) - \epsilon(k_i) - \hbar\omega_q \\ &\approx \frac{\hbar^2 k_q^2}{2m} - c\hbar k_q + \frac{\hbar^2}{m} k_q k_z \qquad \text{for } g^2 n_0^2 \ll \left(\frac{\hbar^2 k_i^2}{2m}\right)^2. \end{aligned} \tag{8.41}$$

In deriving this we have used the momentum conservation relations for the components of $\mathbf{k}_i$ and $\mathbf{k}_k$. Setting this equal to zero we find the value of k_{i_z} at resonance which we define as

$$k_{z_0} = \frac{mc}{\hbar} - \frac{1}{2} k_q. \tag{8.42}$$

To find the width Δk_z we substitute the expression eq.(8.41) for $\Delta\epsilon$ into the argument of the sinc function in eq.(8.36). From this we have an explicit relation between $\mathbf{k}_{i_z}$ and the value of $\delta(\epsilon_k - \epsilon_i - \epsilon_q)$ which takes the form of the function $\mathrm{sinc}^2\mathrm{x}$. It reaches its first zero values when k_{i_z} is a distance $(2\pi/\tau)(mc/\epsilon_q)$ either side of the resonance at k_{z_0}. Its width with respect to k_{i_z} is thus

$$\Delta k_z = \frac{4\pi}{\tau} \frac{mc}{\epsilon_q}. \tag{8.43}$$

[9]The approximation shown in fig.8.10b could also be used, and is not dependent on the condition $g^2 n_0^2/(\hbar^2 k_i^2/2m)^2 \ll 1$. We have instead chosen to use the simpler expression here.

For $L \approx 10^{-4}\,\mathrm{m}$ the k-width of the resonance Δk_z is about 10^3 times larger than the spacing $2\pi/L$ between axial modes. Since $\delta(\epsilon_k - \epsilon_i - \epsilon_q)$ is the function in eq.(8.38) which varies most rapidly with respect to k_{i_z}, the sum over axial modes can thus be approximated by the integral $\frac{L}{2\pi}\int \mathrm{d}k_z$.

$$\gamma(T) = \frac{1}{2}\omega_q \frac{g^2 n_0}{W^2} \sum_{n_x}\sum_{n_y} \int \mathrm{d}k_{i_z} C_{kiq}^2 \frac{\tau}{2\pi\hbar} \mathrm{sinc}^2\left(\frac{\tau}{2\hbar}\Delta\epsilon(k_{i_z})\right) \left.\frac{\partial f(\epsilon)}{\partial \epsilon}\right|_{\epsilon_i} \tag{8.44}$$

In doing this, the factor L from the axial mode density cancels with the factor $1/L$ which arises from the matrix elements. Hence, the dependence of Landau damping on L is eliminated provided the mode spacing $2\pi/L$ is sufficiently small for this approximation to be made.[10]

In our experiment the energy spacing between axial modes is on the order of $\hbar\omega_z$ with an axial frequency of 10 Hz, and the radial mode spacing is on the order of $\hbar\omega_r$ with a radial frequency of 1.4 kHz. The width delta function, $4\pi\hbar/\tau$, can be estimated from eq.(8.37). For $T \approx 10^{-7}\,\mathrm{K}$ the collision rate is approximately 100 Hz. This means the width of delta function eq.(8.36) is approximately 10 times greater than the energy spacing between axial modes in our trap, but 10 time smaller than the spacing between transverse modes.[11] Hence our replacement of the sum over k_z by an integral is justified, while the transverse modes must still be summed over.

To calculate the damping rate from eq.(8.44) we evaluate the integral over k_{i_z} numerically over a finite range several times the width of the resonance Δk. This can be evaluated much more rapidly than the sum it approximates, which is over a large number of modes. This integral is evaluated for each term in the double sum over the transverse modes. We also use the symmetry of the transverse modes to replace the double sum $\sum_{n_x}\sum_{n_y}$ by a single sum $\sum_\rho g_{n_\rho}$ which includes an additional degeneracy factor. We typically evaluate these sum up to n_x or $n_y = 100$, by which point the value of γ has converged.[12]

We summarise the resultant expression for calculating the Landau damping rate

[10] This approximation becomes exact in the continuum limit of axial modes.

[11] In fact, for τ on this order, its exact value is not of great importance provided that C_{kiq} and $\partial f/\partial\epsilon$ vary slowly compared compared to $4\pi\hbar/\tau$. This can be seen from the integral $\int_0^\infty \mathrm{d}\epsilon f(\epsilon)(\tau/2\pi\hbar)\mathrm{sinc}^2((\epsilon-\epsilon_0)\tau/2\hbar)$, which for slowly varying $f(\epsilon)$ is approximately equal to $f(\epsilon_0)$.

[12] These performance enhancements have allowed us to reduce the triple sum in eq.(8.38) over about 10^5 modes to a single sum over just a few tens of terms, each involving a single integral which is evaluated numerically.

in a highly elongated trap such as ours, which has a discrete spectrum. The Landau damping rate $\gamma(T)$ is given by

$$\gamma(T) = \pi\omega_q \frac{g^2 n_0}{W^2} \sum_{n_\rho \in S} g_{n_\rho} F_{n_\rho}(T) \tag{8.45}$$

where S is the non-degenerate set of sums of pairs of squares , $S = \{1, 2, 4, 5, 8, 9 \dots\}$ and g_{n_ρ} their corresponding degeneracy, $2, 1, 2, 2, 1, 2 \dots$ respectively. The function $F_{n_\rho}(T)$ is given by

$$F_{n_\rho}(T) = \int_{k_{z_0}-\Delta k}^{k_{z_0}+\Delta k} \frac{\mathrm{dk_z}}{2\pi} C_{kiq}^2 \frac{\tau}{2\pi\hbar} \mathrm{sinc}^2\left(\frac{\tau}{2\hbar}\frac{\hbar^2 k_q}{m}(k_z - k_{z_0})\right) \frac{1}{k_\mathrm{B}T} \sinh^{-2}\left(\frac{\epsilon_i}{2k_\mathrm{B}T}\right) \tag{8.46}$$

where the integration limits are set by the resonant axial wavenumber k_{z_0} defined in eq.(8.42), and resonance width Δk_z defined in eq.(8.43). Equation (8.46) is valid provided the integrand varies slowly with respect to k_{i_z} on the scale $2\pi/L$ - otherwise the integral must be replaced by its corresponding sum.[13] In eq.(8.46) the energy ϵ_i is given by

$$\epsilon_i = \frac{\hbar^2}{2m}\left(\left(\frac{2\pi}{W}\right)^2 n_\rho + k_{i_z}^2\right), \tag{8.47}$$

and the coefficients C_{kiq} (eq.(8.23)) of the matrix element $\langle k| V_{\mathrm{int}} |i\rangle$ depend on this energy through the Bogoliubov amplitudes u_j and v_j given in eq.(7.55).

8.4.4 Effect of Discrete Spectrum on Landau Damping Rate

Figure 8.16 shows the damping rate predicted by eq.(8.45), plotted for three different values of W, 3×10^{-7}, 5×10^{-7} and 10^{-6} m. The lowest value corresponds to the radial harmonic oscillator length of our trap, $a_\perp = \sqrt{\hbar/m\omega_r}$, with a radial frequency of 1.4 kHz. In addition, the dashed line shows the damping rate in the continuum limit calculated from eq.(8.28). All the lines shown in fig.8.16 have similar functional form as a result of the functions $(1/k_\mathrm{B}T)\sinh^{-2}(\epsilon_i/2k_\mathrm{B}T)$ which are found in both

[13] Writing γ in this way with $F_{n_\rho}(T)$ also shows that a further approximation can be made. If C_{kiq}^2 and $\partial f/\partial\epsilon$ vary slowly over width Δk_z then the function $(\tau/2\pi\hbar)\mathrm{sinc}^2(\tau\Delta(\epsilon)/2\hbar)$ can be replaced by the Dirac-delta function, for which the integral can be evaluated analytically. It should then be possible to use high and low temperature approximations of the Bose-Einstein distribution, and the approximation of C_{kiq}^2 used in [26] to make high and low temperature approximations for $\gamma(T)$ in the discrete spectrum theory. In the present work we are most interested in the behaviour of $\gamma(T)$ in the intermediate temperature range, so we shall leave the derivation of such approximations and their limits of validity for future work.

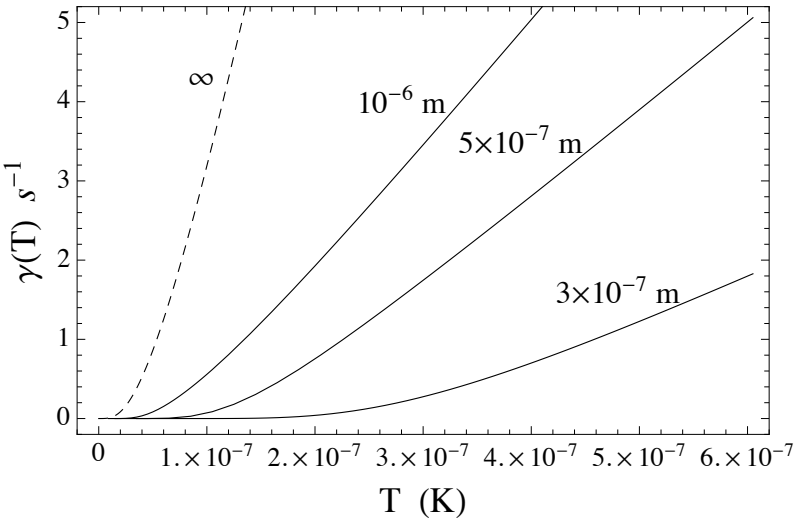

Figure 8.16: Effect of trap width W on the Landau damping rate for a homogenous gas with discrete spectrum. The solid lines show the temperature dependent damping rate calculed from the discrete spectrum result eq.(8.45), for three different widths, $W = 3 \times 10^{-7},\ 5 \times 10^{-7},\ 10^{-6}\,\mathrm{m}$. The dotted line shows the case $W \to \infty$ given by eq.(8.28). All lines were calculated using the estimate $\epsilon_q = m\omega_z^2 Z_0^2/2$ with $Z_0 = 10^{-5}\,\mathrm{m}$. For the discrete spectrum theory, the maximum value of the index n_ρ of the sum in eq.(8.45) was 10^2. For larger widths, calculation over a larger number of radial modes is required.

eq.(8.28) and eq.(8.45) and carry the temperature dependence. However, the exact behaviour of $\gamma(T)$ clearly depends on W. Figure 8.16 shows that decreasing the value of W has two effects on the damping rate: (i) the damping rate decreases as W decreases at fixed temperature, and (ii) the 'turning point' where $\gamma(T)$ starts to rise is shifted to higher temperatures as W decreases. The two effects of the discrete spectrum width W are exactly the two effects we desired to show by introducing the discrete spectrum theory.

The discrete spectrum theory is also a more realistic model for damping of the trapped Bose gas in our experiment, which also has a discrete spectrum. We compare the Landau damping rate from the discrete spectrum theory to the measurements from our experiment in fig.8.17 (for details on these measurements see sec.8.2). The solid lines in fig.8.17 show the damping rate given by our discrete spectrum theory using eq.(8.45) with three different widths, $W = a_\perp,\ 2a_\perp$ and $4a_\perp$, where $a_\perp = 2.9 \times 10^{-7}\,\mathrm{m}$. Since W defines the energy spacing of the excitations in the presence of the condensate, an appropriate value is somewhere between the full width half maximum of the condensate (radial) density and the Thomas Fermi (radial) width of the condensate. From the numerical solutions of the Gross Pitaevskii

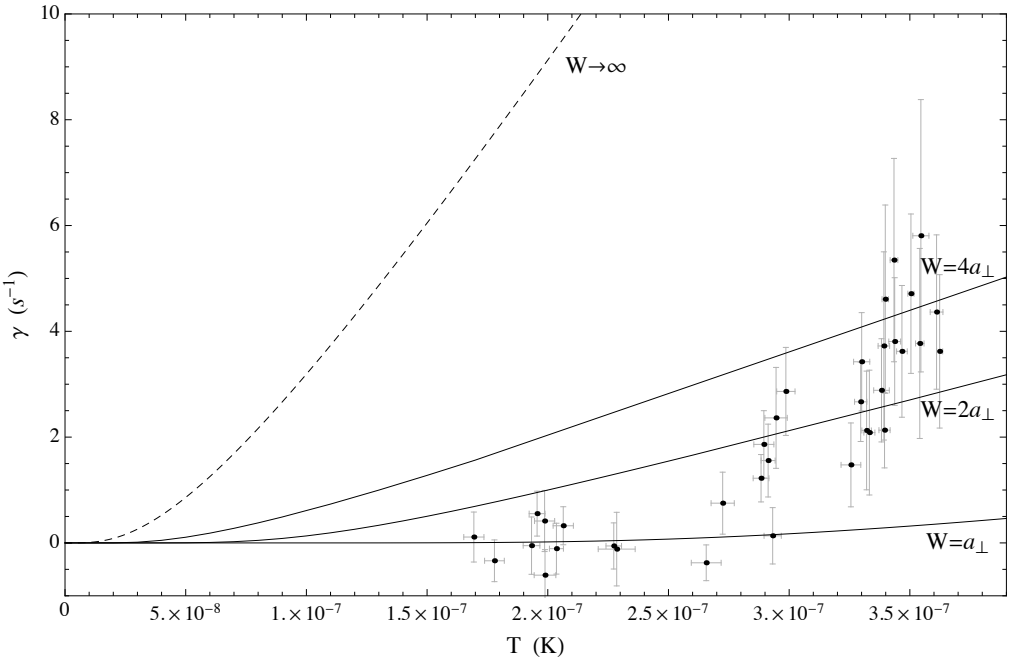

Figure 8.17: Measured damping rate and theoretical Landau damping rates from discrete spectrum and continuum spectrum homogenous gas theories. The data points show our measurements of $\gamma(T)$ exactly as shown in fig.8.7. The solid lines show the Landau damping rate from the discrete spectrum result eq.(8.45), with width equal to the harmonic oscillator width of our trap $W = 3 \times 10^{-7}\,\mathrm{m}$. For comparison, the dashed line shows the damping rate in the continuum limit calculated by numerical integration of eq.(8.28). The energy $\epsilon_q = \frac{1}{2}m\omega_z^2 Z_0^2$ was used in the theoretical damping rates, where $Z_0 = 10^{-5}\,\mathrm{m}$, $\omega_z = 2\pi \times 10\,\mathrm{Hz}$, and m is the mass of a ^{87}Rb atom.

equation presented in fig.5.2a, this gives a range for W between about $2a_\perp$ and $4a_\perp$, where the harmonic oscillator length $a_\perp = 2.9 \times 10^{-7}\,\mathrm{m}$. The energy $\epsilon_q = \frac{1}{2}m\omega_z^2 Z_0^2$ which is approximately $4\hbar\omega_z$. The data points in fig.8.17 show the measurements from our experiment. We have also plotted the predictions of the continuum theory from eq.(8.28) using the same two values of ϵ_q.

Figure 8.17 show that the discrete spectrum theory gives values of the Landau damping rate that are in much better agreement with our experimental observations than those of the continuum theory. At and above $3\times10^{-7}\,\mathrm{K}$, the range of γ given by the discrete spectrum theory with a sensible choice of W (between $2a_\perp$ and $4a_\perp$), is well within the range of γ that we observe experimentally. The characteristic temperature at which γ starts to rise is also higher for the discrete spectrum theory than for the continuum limit. Compared to our data in which γ starts to rise at about $2.5 \times 10^{-7}\,\mathrm{K}$, the characteristic temperature for $W = a_\perp$ line is closest, while the $W = 4a_\perp$ starts to rise at about half this temperature.

Although our simple analytic model of a homogeneous gas does not take into account the full characteristics of our harmonically trapped Bose gas, it clearly shows that the discrete spectrum of our trap plays an important role in the microscopic dynamics of the gas which cause Landau damping. The essence of our argument can be understood from a simple example of Newton's cradle. Consider a cradle of five balls, four of which are in motion at any time. The cradle restricts the motion of all balls to a single dimension which we label **z**. As a result, the motion is passed coherently between the first four balls and the last four balls, each collision transferring exactly one unit of momentum along **z** to the stationary ball. Now suppose the four balls are once again set into motion, but the fifth (initially stationary) ball is suspended from a single string so it may move in two dimensions. On impact with the fifth ball, the slightest imperfection in the transverse alignment will cause this ball to recoil at an angle to **z**, but with less than one unit of momentum along **z**. After a few cycles, the coherent motion between the 5 balls is completely destroyed. In a Bose gas the four balls in motion represent the collective oscillation, and the fifth, imperfectly aligned ball, a thermal excitation. The imperfect alignment of the 'fifth ball' is caused by transverse thermal motion of this thermal excitation. For a continuum spectrum the thermal excitation can have a transverse component of motion at low energy, so damping occurs even at low temperatures when thermal excitations typically have low energy according to the Bose-Einstein distribution. For a highly elongated Bose gas with tight transverse confinement such as ours, at low temperatures this transverse thermal motion is frozen out for all but a few thermal excitations with the highest energies. Consequently the momentum transfer between quanta of the collective motion and the majority of thermal excitation is coherent, just as for the standard version of Newton's cradle.[14]

In further support of this explanation of our experimental observations we comment of the results of experiments at JILA [21] and MIT [22]. Both experiments measure the temperature dependence of the damping rate of the low energy $m = 0$

[14]This coherent collision is actually given by the Fock exchange interaction which is second order in the fluctuation operators. Third order interactions of this type are not permitted. As with the standard Newton's cradle, one quantum of the collective motion and one quantum of the motionless (perfectly aligned) ground state are destroyed (balls 1 and 5), then a new quantum of the collective motion and a new quantum of the groundstate are created (balls 5 and 1). This is included in both the Hartree-Fock approximation and the Bogoliubov approximation without the need for including third or higher order processes.

and $m = 2$ collective modes of the condensate in harmonic traps [12, 13]. However, the condensates they produce are 3D in character with relatively low trap frequencies compared to the high radial frequency of our trap. This makes the continuum spectrum homogenous gas model a more adequate model for estimating the Landau damping rate in their experiments than it is for ours. For the temperatures and trap frequencies of their experiments, excitations in the radial and transverse directions are both easily accessible, giving the motion of particles in the thermal cloud a 3D character. For example, in [21] they have radial and axial trap frequencies of $f_r = 129\,\mathrm{Hz}$ and $f_z = 365\,\mathrm{Hz}$ and at the lowest temperatures they measure ($T \approx 125\,\mathrm{nK}$), they have $k_\mathrm{B}T/(2\pi\hbar f_z) \approx 10$. In [22], $f_r = 17\,\mathrm{Hz}$ and $f_z = 230\,\mathrm{Hz}$, and for their lowest accurately measured temperatures ($T \approx 500\,\mathrm{nK}$), they have $k_\mathrm{B}T/(2\pi\hbar f_r) \approx 50$. For comparison, in our trap we have $k_\mathrm{B}T/(2\pi\hbar f_r) \sim 1$, while axially we have $k_\mathrm{B}T/(2\pi\hbar f_z) \sim 100$. Even though their trapped gases will have a discrete spectrum, the 3D character of the motion of thermal particles in their traps is more accurately modelled by the continuum homogenous gas theory than by the discrete spectrum model for highly elongated traps in which the transverse motion is frozen out. Additionally, their lower trap frequencies mean the mode spacing in their experiments is much closer to the width of the energy resonance $\delta(\epsilon_k - \epsilon_i - \epsilon_q)$ than it is in ours. Comparing their results to our own, we note that the damping rates they measure are higher than ours, and we see that the damping rate clearly rises with temperature over the entire range of measured temperatures. In our experiment we found little temperature dependence of the damping rate at temperatures comparable to their lower temperature measurements. Furthermore, we have found the damping rate estimated by eq.(8.28) of the continuous spectrum theory give functions $\gamma(T)$ that agree well in both functional form and magnitude to damping rate measurements in these two experiments.

Further support of the argument presented here could be made with our apparatus by measuring the damping rate as a function of the transverse trap frequency at a given temperature. By varying the magnitude of the magnetic field B_0 along the axis of the trap we are able to vary the radial trap frequency ($f_r \propto B_0^{-1/2}$) as given by eq.(3.29) in sec.3.3.2. With our current apparatus, we are able to vary f_r from about 500 Hz to about 4 kHz. The data shown here was taken in the middle of this range at $f_r = 1.4\,\mathrm{kHz}$. The transverse width of the condensate varies as $f_r^{-1/2}$

in the 1D regime and $f_r^{-3/5}$ in the 3D Thomas-Fermi regime. As shown by fig.8.16, reducing the condensate width by a factor of two should give an appreciable change in the damping rate of 1 or $2\,\mathrm{s}^{-1}$ for a cloud at about 300 nK.

We briefly comment on the extension of the discrete spectrum homogenous gas theory to that for a harmonically trapped gas. The reduced damping rate in the homogenous theory is a result of the reduced number of modes over a given energy range that are permitted for Landau damping collisions. The permissible modes of the discrete spectrum are those that obey energy conservation and have non-zero interaction matrix element, and for a homogenous gas, the later condition can be interpreted as momentum conservation during collisions. In the discrete spectrum theory a consequence of these conditions is that Landau collisions are prohibited at low energies where a radial component cannot be excited. Thus, at temperatures where $k_{\mathrm{B}}T$ is small compared to the lowest radial excited state, very few Landau collisions will occur, resulting in a much lower damping rate than what would be expected for a continuum spectrum.

After some initial investigation of the low energy modes of Bose gas trapped in a highly elongated harmonic trap, it seems that the same effect occurs, and the damping rate should be reduced in a similar way.[15] Only at higher energies where thermal excitations may have a radial component can modes be found that cause Landau damping; the radial component introduces an extra degree of freedom into the energy of the thermal modes, which allows modes to be found which are much closer to resonant. Furthermore, for collisions involving modes at higher energies,

[15] From the theory in [14] as applied in [145], the low energy modes are axial modes labelled by quantum number j.These have energy $\sqrt{j(j+3)/4}$ and wave function proportional to $\sqrt{1-z^2}P_j^{(1,1)}(z)$, where $P_j^{(1,1)}(z)$ are Jacobi polynomials. For these low energy modes the coherence time τ is likely to be long, being limited by Beliaev lifetime ($\gtrsim 10^2$ s). Thus Landau collisions must be very close to resonance indeed. Exact energy conservation is given by the diophantine equation

$$\sqrt{i(i+3)/4}+\sqrt{q(q+3)/4}=\sqrt{k(k+3)/4} \tag{8.48}$$

where i, q and k correspond to the modes of the incident thermal excitation, collective oscillation, and scattered thermal excitation respectively. This equation appears to have just one solution, $i=q=2$, $k=5$. Collisions between these modes are prohibited by the interaction matrix element, which for a set of low lying modes is proportional to

$$\int_{-1}^{1}\mathrm{d}z(1-z^2)^2P_i^{(1,1)}(z)P_q^{(1,1)}(z)P_k^{(1,1)}(z). \tag{8.49}$$

Little leniency in the condition eq.(8.48) is gained for axial modes of higher energy than this, even though the width of the resonance is larger. This is because the minimum difference between the lhs and rhs of eq.(8.48) tends to 1/2 for higher energy axial modes.

the width of the delta function that defines the resonance is likely to be larger, allowing a wider range of collisions to occur.

We finally return to the subject of the background damping rate $\gamma_0 = 2.2\,\mathrm{s}^{-1}$ that we identified in sec.8.3. We hypothesised in sec.8.3 that this rate was not due to Landau damping, and the observed damping rate could be separated into two parts, a constant temperature independent part γ_0, and a temperature dependent part. The ability of our theoretical model to predict a similar function $\gamma(T)$ to the temperature dependent part of the observed damping rate supports this hypothesis.

An interesting comparison between our experiment and the damping experiment presented in [68] sheds some light on the background rate γ_0. They measure the damping of centre of mass oscillations in highly elongated trap similar to ours ($f_r = 880\,\mathrm{Hz},\ f_z = 48.5\,\mathrm{Hz}$). Their trap is also created by a z-wire on an atom chip, and similar to ours, their trap exhibits roughness in the axial magnetic potential (see sec.4.3 for details of roughness in our trap). They do not give the exact temperature of their gas, but the depth of their trap (1 μK), and their observation that the condensate is "almost pure", together with the atom number (3×10^4) suggest a temperature of about $10^{-7}\,\mathrm{K}$. In this trap they observe a damping rate of $2\,\mathrm{s}^{-1}$ (obtained from their figure 5a) which is almost the same as ours. They show that this rate can be reduced by smoothing out the roughness of the axial potential of their trap. They do this by using an rf field to reduce the coupling strength between the magnetic potential of an atom and the axial magnetic field (see sec.6.1 for such a scheme in our trap). As the rf frequency is increased the coupling strength is reduced and hence the trap smoothed out further. This supports the idea that the background rate γ_0 in our trap can be associated with the roughness of the axial potential.

A secondary effect of the rf field is that it breaks the cylindrical symmetry of the trap such that the transverse trap frequencies ω_x and ω_y are different. In figure 5c of [68], they show an unexplained resonance where the damping rate is reduced by an order of magnitude. This happens to occur where ω_x and ω_y are almost equal. This effect may be due to the different modes that are permitted by the energy spectrum and the interaction matrix elements of either Landau or Beliaev decay for an asymmetric gas. With further development, the discrete spectrum theory

presented here may be able to shed some light on this phenomenon.

8.5 Chapter Summary

In this chapter we have presented data from our experiment that demonstrates the temperature dependence of the damping rate of centre of mass oscillations of a condensate, as it moves through the thermal cloud. We have explained the microscopic mechanism which causes this temperature dependent damping, known as Landau damping. We then compared our results to a simple theoretical model of Landau damping in a homogenous gas, but found that this overestimated the damping rate and its temperature dependence. We suggested that by incorporating the discrete nature of excitations in our trapped Bose gas into this simple model, it would give a damping rate in much better agreement with our measurements. We subsequently derived such a model and showed that this was the case. This opens up the interesting prospect that by changing the confinement of a quasi-1D Bose gas such as ours, one can alter the dynamics of the gas significantly.

Chapter 9

Conclusion

Producing a Bose Einstein condensate is a particularly challenging endeavour. Chapters 2, 3 and 4 of this thesis describe this process, and offer various insights into the stages we found crucial in attaining a Bose Einstein condensate: the efficient loading of the UMOT (sec.3.1), efficient transfer from the UMOT to the magnetic trap (sec.3.4), and evaporative cooling in our highly elongated trap (Ch.4). As I found the work of [56] and [99] gave particularly useful guidance along this path, I hope these chapters will offer some assistance to students in the future.

With an instrument that can routinely create a Bose Einstein condensate this is an exciting time in our laboratory, where a wide range of experiments can now be performed. Some of these we have not even touched on in this thesis - in particular, its use as a matter wave interferometer, [76, 56, 123]. In this respect, our instrument has already proved to be an incredibly sensitive energy gradiometer [69], and has the potential to make sensitive measurements a few microns from a surface with which the atoms interact. This is currently the focus of the current PhD student Iain Barr, to whom I wish much success.

In chapters 5, 6 and 7 we present and discuss several techniques for manipulating the condensate, as well as analytical tools for understanding its character and behaviour. We draw attention to the semi-ideal gas model [131], which we have extended in sec.7.2. This model gives an accurate analytic description of the density and phase space density distributions of the Bose gas at finite temperature $T < T_c$.

In its use, this model provides a better description of the gas than the crude bimodal model eq.(7.20), which is commonly used to fit measured density profiles. The semi-ideal gas model in sec.7.2 is easier to fit to measured profiles. This fit yields more accurate values for the parameters that characterise the gas, such as its condensed fraction.

The final focus of this thesis is on the dynamics of our condensate at finite temperature, for which our findings were presented in ch.8. A trapped Bose gas at finite temperature has many similarities to the electromagnetic field in a cavity, where the role of the vacuum is played by the condensate in the Bogoliubov approximation sec.7.4.1. Furthermore, by varying the confinement of the gas, one can change its dynamics dramatically. Like other quantum systems in reduced dimensions, the quasi-1D regime of a Bose gas is interesting to study. We have demonstrated that the Landau damping rate of centre of mass oscillations of our condensate by the thermal part of the Bose gas is significantly reduced in the quasi-1D regime, compared to that expected in the 3D limit. Our theoretical model of this also suggests that the damping rate is particularly sensitive to the width of the trap in this regime.

Our investigations of ch.8 highlight the potential for further study in this area. The principles of the theoretical model of a homogenous Bose gas with discrete spectrum which provided a simple description of our experiment, are also applicable to a harmonic model. Development of such a model would enable us to make more accurate predictions of the Landau damping of a condensate like ours. We have also begun to collaborate with the group of Professor Mark Fromhold[1], who are modelling our experiment numerically. Finally, we suggest an extension of our damping experiment, in which the damping rate of centre of mass oscillations is measured in traps of different widths at a fixed temperature. Our current theoretical understanding of this suggests for example, that at a temperature of approximately 200 nK, increasing our current transverse trap frequency of 1.4 kHz by a factor of three would increase the Landau damping rate from (essentially) zero to several Hz. Together with the data presented in sec.8.3, such an experiment would demonstrate how the dynamics of a superfluid can be significantly varied just by changing the shape of the container in which it is confined.

[1] University of Nottingham.

Appendix A

Bias Field Coils

Table A.1 gives the specifications for the five pairs of coils that generate uniform bias fields in the $\hat{\mathbf{x}}$, $\hat{\mathbf{y}}$ and $\hat{\mathbf{z}}$. Figure **??** shows the labelled coils. Coils X_1, Y_1, & Z_1, are used in conjunction with the chip wires to form and shift the position of UMOT field and magnetic trap, and shift the position of the mMOT field. Coils Y_2 & Z_2 are used to rotate the magnetic trap towards the chip, and to boost the magnetic trap z bias field, reducing the radial trap frequencies respectively.

Coils	C-C sep.* (mm)	Diameter (mm)	Strength ($\mathrm{G\,A^{-1}}$)	Uniformity (%)
X	146	300×230	3.5	0.090
Y_1	100	230	5.4	0.20
Y_2	100	220	12.6	0.15
Z_1	270	90	1.0	2.6
Z_2	340	180	0.8	1.2

Table A.1: Table shows specifications of bias coils. *Coil centre to centre separation. The X bias coils are rectangular. Uniformity calculated as maximum variation of field 10 mm from chip centre.

Appendix B

Derivation of the Gross Pitaevskii Equation

The Gross Pitaevskii equation is derived in this appendix. In section B.1 we begin with a description of the many particle state, then introduce the Hamiltonian of trapped interacting bosons in this state, before deriving the time independent Gross Pitaevskii equation for the condensate wave function. The time dependant version is then derived in section **??**, which is put into the form of a pair of hydrodynamic equations.

B.1 Time Independant Gross Pitaevskii Equation

The time independent Gross Pitaevskii equation describes the ground state of N trapped bosons. It is assumed that the number of particles is much greater than one, and all particles are in the same single particle particle state $|\psi_0\rangle$. In general the state of N bosons is a tensor product state of N single particle states, symmetric under interchange of particles. To incorporate this symmetry the product state is summed over all possible orderings. In the Hartree approximation one neglects the symmetrising sum. However, when all particles are assumed to be in the same quantum state all orderings are identical. Symmetry under particle interchange is satisfied automatically, and the Hartree approximation a valid one. The many

particle state can be written in terms of the single particle states,

$$|\psi_N\rangle = |\psi\rangle_1 |\psi\rangle_2 \dots \quad \dots |\psi\rangle_N . \tag{B.1}$$

The subscripts on the right hand side label the single particle state spaces, and not the single particle states. The subscript on the left indicates the state is the N particle state.

The position representation of $|\psi_N\rangle$ is obtained by acting on each single particle space with the the identity operator $\int d\mathbf{r}_i |\mathbf{r}_i\rangle \langle \mathbf{r}_i|$, where $\{|\mathbf{r}_i\rangle\}$ is the position basis and $\mathbf{r}_i$ the spatial coordinate of the i^{th} subspace. The complex coefficients in these bases give the many body wavefunction

$$\psi_N(r_1, r_2 \dots \ \dots r_N) = \psi(r_1)\psi(r_2) \dots \ \dots \psi(r_N). \tag{B.2}$$

Remarkably, the nature of the ground state of a trapped atomic vapour of bosons is often well characterised by only the diagonal terms of B.2, $\psi(r_i = r)$. This follows from the short range nature of the atom-atom interactions when compared to the mean inter-particle spacing at low density $n^{1/3} \ll a$, with s wave scattering length a. Thus the many-body wave function can be reduced to a single 'classical' field of just a single coordinate $\psi_0(\mathbf{r}) \propto \psi_N(r_i = r)$, and is commonly referred to as the 'wave function' of the condensate. A convenient normalisation is chosen,

$$N = \int d\mathbf{r} |\psi_0(\mathbf{r})|, \tag{B.3}$$

such that the square amplitude of $\psi_0(\mathbf{r})$ gives the density of the the condensate

$$n(\mathbf{r}) = |\psi_0(\mathbf{r})|. \tag{B.4}$$

The field $\psi_0(\mathbf{r})$ emerges naturally from the many body wave function $\psi_N(\{r_i\})$ for the hamiltonian considered below.

The energy of the multi particle state is lowest when all particles are in the ground state $\psi_(\mathbf{r})/N^{1/2N}$. To find the form of $\psi_0(\mathbf{r})$, the energy is written as a functional of $\psi_0(\mathbf{r})$ and minimised. This results in time independent Gross Pitaevskii equation, which is the necessary condition for ψ_0 to minimise the energy.

In the absence of interactions, the energy of i^{th} particle of the many particle state B.1 in the position representation is found from the Hamiltonian

$$H_0(\mathbf{r}_i) = \frac{\mathbf{p}_i^2}{2m} + V(\mathbf{r}_i). \tag{B.5}$$

The interaction potential between particles also contributes to the energy of the system. For atoms at low temperature and density the interaction is considered as s-wave scattering between pairs of particles. The scattering potential is replaced by a contact interaction between pairs of particles

$$V_{\text{int}}(\mathbf{r}_i - \mathbf{r}_j) = g\delta(\mathbf{r}_i - \mathbf{r}_j) \qquad \text{where } g = \frac{4\pi\hbar^2}{m}. \tag{B.6}$$

This leads to the many body Hamiltonian

$$H = \sum_i \frac{\mathbf{p}_i^2}{2m} + V(\mathbf{r}_i) + \sum_{i<j} g\delta(\mathbf{r}_i - \mathbf{r}_j) \tag{B.7}$$

where the second sum is over distinct particle pairs. Taking the expectation value $\langle\psi\{\mathbf{r}_i\}|\, H\, |\psi\{\mathbf{r}_i\}\rangle$ gives the energy functional $E[\psi_0(\mathbf{r})]$ which is to be minimised.

$$\begin{aligned} E[\psi_0(\mathbf{r})] = &\sum_i \left(\prod_{j\neq i} \int d\mathbf{r}_j |\psi(\mathbf{r}_j)|^2 \int d\mathbf{r}_i \frac{\hbar^2}{2m} \nabla\psi^*(\mathbf{r}_i)\nabla\psi(\mathbf{r}_i) + V(\mathbf{r}_i)|\psi(\mathbf{r}_i)|^2 \right) \qquad \text{(B.8)} \\ &+ \sum_{i<j} \left(\prod_{k\neq i,j} \int d\mathbf{r}_k |\psi(\mathbf{r}_k)|^2 \int d\mathbf{r}_i \mathbf{r}_j g\psi^*(\mathbf{r}_i)\psi^*(\mathbf{r}_j)\delta(\mathbf{r}_i - \mathbf{r}_j)\psi(\mathbf{r}_i)\psi(\mathbf{r}_j) \right) \\ = &\int d\mathbf{r} \left(\frac{\hbar^2}{2m} \nabla\psi_0^*(\mathbf{r})\nabla\psi_0(\mathbf{r}) + V(\mathbf{r})|\psi_0(\mathbf{r})|^2 + \frac{g}{2}|\psi_0(\mathbf{r})|^4 \right) \qquad \text{(B.9)} \end{aligned}$$

In the first line ψ and ψ^* are put on equal footing by integrating $\psi^*\nabla^2\psi$ by parts with the assumption that ψ and ψ^* vanish in the limit $\mathbf{r} \to \infty$. [1] In the second equality the index i can be dropped after integrating over the coordinates $\mathbf{r}_j$ and $\mathbf{r}_k$. The first sum then gives a factor N and the second sum $N(N-1)/2$, which is usually approximated by $N \approx N-1$ for $N \gg 1$. The result follows from substitution of $\psi_0 = \sqrt{N}\psi$. The contributions are the kinetic energy, external potential energy, and the pairwise interaction energy of a particle in the mean field of $N-1$ other

[1] This assumption is valid for any bound state. On the contrary, spatial derivatives of the ground state vanish for the uniform Bose gas for which the potential $V = 0$.

particles.

The energy functional $E[\psi, \psi*]$ must be minimised whilst maintaining the normalisation condition B.3. This can be done by the Lagrange multiplier method. By defining

$$L[\psi, \psi*, \mu] = E[\psi, \psi*] - \mu \left(\int \mathbf{r} |\psi_0|^2 - N \right), \tag{B.10}$$

with lagrange multiplier μ. Setting the partial derivative $\partial L/\partial \mu$ requires the correct normalisation of ψ_0. Setting to zero the functional derivatives $\delta L/\delta \psi$, $\delta L/\delta \psi^*$ gives the following equation and it's complex conjugate,

$$\int d\mathbf{r} \left(-\frac{\hbar^2}{2m} \nabla\psi\nabla\phi + \psi V \phi + g|\psi|^2 \psi\phi - \mu\psi\phi \right) = 0 \tag{B.11}$$

where $\phi(\mathbf{r})$ is an arbitrary function by which $\psi_0(\mathbf{r})$ varies in between the end points $r \to \pm\infty$ where $\phi \to 0$. The integrand is factorized by ϕ after integrating $\nabla\psi\nabla\phi$ by parts. Since $\phi(\mathbf{r})$ is arbitrary the necessary condition for the integral to vanish, and therefore the energy functional B.9 to be minimised, is

$$-\frac{\hbar^2}{2m} \nabla^2 \psi_0(\mathbf{r}) + V(\mathbf{r})\psi(\mathbf{r}) + g|\psi(\mathbf{r})|^2 \psi_0(\mathbf{r}) = \mu\psi(\mathbf{r}) \tag{B.12}$$

together with the normalisation condition B.3. This is the Gross Pitaevskii equation which has the condensate wave function as its solution. It takes the form of a schrödinger equation for ψ_0 with a nonlinear term given by the mean field atom-atom interaction. Its action on the mean field ψ_0 is equivalent to the action of the many body Hamiltonian B.7 on the multi-particle state $|\psi\{\mathbf{r}_i\}\rangle$. The ground state energy of the mean field is given by the chemical potential μ.

Appendix C

Axial Phase Space Distribution in Semi-Ideal Model

We find the axial phase space distribution by first integrating eq.(7.26) over the radial momentum coordinate q, then integrate over the radial spatial coordinate ρ. For the transverse momentum integral, the exponential of momenta q, $\exp(q^2/2mk_BT)$, is separated from the other exponents, written in short as $\exp(A(\rho, z, p_z))$. The momentum integral gives,

$$f(\mathbf{r}, p_z) = 2\pi \int_0^\infty \mathrm{d}q\, q f(,r\mathbf{p}) \tag{C.1}$$

$$= \frac{2\pi}{Z_\mathbf{r} Z_\mathbf{p}} \int_0^\infty \mathrm{d}q\, q \left(e^{q^2/(2mk_BT)} e^A - 1 \right)^{-1} \tag{C.2}$$

$$= \frac{(2\pi)(2mk_BT)}{Z_\mathbf{r} Z_\mathbf{p}} \left(-\frac{1}{2} \right) \ln\left(1 - \frac{1}{A} \right), \tag{C.3}$$

$$\text{where } A = \exp\left(\frac{p_z^2}{2mk_BT} + \frac{V_{\text{eff}} - \mu}{k_BT} \right). \tag{C.4}$$

The function $A(\rho, z, p_z)$ takes two forms due to the U_{eff}, one form where $\rho^2 + z^2 < R_0^2$, and the other where $\rho^2 + z^2 > R_0^2$. To do the spatial integral we therefore break

A into two parts,

$$A = \begin{cases} B_- \exp\left(-\frac{a\rho^2}{k_B T}\right) & \rho^2 + z^2 < R_0^2, \\ B_+ \exp\left(-\frac{a\rho^2}{k_B T}\right) & \rho^2 + z^2 > R_0^2, \end{cases} \tag{C.5}$$

$$\text{where} \quad B_- = \exp(\frac{p_z^2}{2mk_BT}) \exp(\frac{aP_0^2}{k_BT}) \tag{C.6}$$

$$\text{and} \quad B+ = \exp(\frac{p_z^2}{2mk_BT}) \exp(\frac{-aP_0^2}{k_BT}) \tag{C.7}$$

To evaluate the radial spatial integral

$$f(z,p_z)Z_{\mathbf{r}}Z_{\mathbf{p}} = (2\pi)^2(2mk_BT)(-1/2)\int_0^\infty \mathrm{d}\rho\, \rho \ln\left(1 - \frac{1}{A}\right), \tag{C.8}$$

it is separated into three regions of the ρ-z plane. These regions are shown in fig. **??** and are labelled as region 1 where $\rho < P_0,\ z < R_0$, region 2 where $\rho > P_0,\ z < R_0$ and region 3 where $z > R_0$. The integral is then separated into the following three parts,

$$\frac{f(z,p_z)Z_{\mathbf{r}}Z_{\mathbf{p}}}{(2\pi)^2(2mk_BT)(1/2)} = \begin{cases} -\int_0^{P_0} \mathrm{d}\rho\ \rho \ln\left(1 - \frac{1}{A}\right) - \int_{P_0}^\infty \mathrm{d}\rho\ \rho \ln\left(1 - \frac{1}{A}\right) & z < R_0 \\ -\int_0^\infty \mathrm{d}\rho\ \rho \ln\left(1 - \frac{1}{A}\right) & z > R_0. \end{cases} \tag{C.9}$$

, where the appropriate substitution must be made in place of A as defined by eq. C.5.

To evaluate these integrals we first note that since $A > 1$, the logarithm in C.3 has the analytic expansion

$$-\ln\left(1 - \frac{1}{A}\right) = \sum_{k=0}^\infty \frac{A^{-(k+1)}}{k+1} \tag{C.10}$$

Now integrating over region 1,

$$-\int_0^{P_0} \mathrm{d}\rho\ \rho \ln\left(1 - \frac{1}{A}\right) = \sum_{k=0}^\infty \frac{B_-^{-(k+1)}}{k+1} \int_0^{P_0} \mathrm{d}\rho\ \rho \exp((k+1)\frac{a\rho^2}{k_BT}) \tag{C.11}$$

$$= \sum_{k=0}^\infty \frac{B_-^{-(k+1)}}{(k+1^2)} \frac{k_BT}{a} \int_0^{U_0} \mathrm{d}u\ \exp(u^2) \tag{C.12}$$

$$= \frac{k_BT}{2a} \sum_{k=0}^\infty \frac{B_-^{-(k+1)}}{(k+1)^2} \left(\exp((k+1)\frac{aP_0^2}{k_BT} - 1)\right), \tag{C.13}$$

In the second line the substitution $u^2 = (k+1)a\rho^2/(k_BT)$ is made. The series in this results can be written concisely as a polylogarithm, $\mathrm{Li_n}(x)$, defined as

$$\mathrm{Li_n}(x) = \sum_{k=0}^{\infty} \frac{x^{(k+1)}}{(k+1)^n} \qquad \text{for } x < 1. \tag{C.14}$$

Expanding B_-, cancelling common terms and using C.14, we find

$$-\int_0^{P_0} \mathrm{d}\rho\ \rho \ln\left(1-\frac{1}{A}\right) = \frac{k_BT}{m\omega^2}\left[\mathrm{Li}_2\left(e^{-\frac{p_z^2}{2mk_BT}}\right) - \mathrm{Li}_2\left(e^{-\frac{p_z^2}{2mk_BT}} e^{\frac{a}{k_BT}(z^2-R_0^2)}\right)\right]. \tag{C.15}$$

Integrating over region 2 by the same method gives,

$$-\int_{P_0}^{\infty} \mathrm{d}\rho\ \rho \ln\left(1-\frac{1}{A}\right) = \frac{k_BT}{m\omega^2}\mathrm{Li}_2\left(B_+^{-1} e^{-\frac{m\omega^2 P_0^2}{k_BT}}\right) \tag{C.16}$$

$$= \frac{k_BT}{m\omega^2}\mathrm{Li}_2\left(e^{-\frac{p_z^2}{2mk_BT}}\right) \tag{C.17}$$

The result of the integral over region 3 is found by setting the lower limit to zero in eq. C.16, giving,

$$-\int_0^{\infty} \mathrm{d}\rho\ \rho \ln\left(1-\frac{1}{A}\right) = \frac{k_BT}{m\omega^2}\mathrm{Li}_2\left(B_+^{-1}\right) \tag{C.18}$$

$$= \frac{k_BT}{m\omega^2}\mathrm{Li}_2\left(e^{-\frac{p_z^2}{2mk_BT}} e^{-\frac{m\omega^2}{2k_BT}(z^2-R_0^2)}\right) \tag{C.19}$$

The axial phase space distribution is now found by substituting the results eq. C.15, eq. C.17 and eq. C.19 into eq. C.9;

$$\frac{f(z,p_z)Z_{\mathbf{r}}Z_{\mathbf{p}}}{(2\pi)(2mk_BT)\frac{k_BT}{m\omega^2}} = \begin{cases} \mathrm{Li}_2\left(e^{-\frac{p_z^2}{2mk_BT}}\right) - \frac{1}{2}\mathrm{Li}_2\left(e^{-\frac{p_z^2}{2mk_BT}} e^{\frac{m\omega^2}{2k_BT}(z^2-R_0^2)}\right) & |z| < R_0 \\ \frac{1}{2}\mathrm{Li}_2\left(e^{-\frac{p_z^2}{2mk_BT}} e^{-\frac{m\omega^2}{2k_BT}(z^2-R_0^2)}\right) & |z| > R_0. \end{cases} \tag{C.20}$$

Bibliography

[1] F London. The-phenomenon of liquid helium and the bose-einstein degeneracy. *Nature*, 141(3571):643–644, 1938.

[2] JF Allen and AD Misener. Flow of liquid helium ii. *Nature*, 141(3558):75, 1938.

[3] LD Landau. Two-fluid model of liquid helium ii. *J. Phys. USSR*, 5:71, 1941.

[4] Richard P Feynman. Application of quantum mechanics to liquid helium. *Progress in low temperature physics*, 1:17–53, 1955.

[5] Mike H Anderson, Jason R Ensher, Michael R Matthews, Carl E Wieman, and Eric A Cornell. Observation of bose-einstein condensation in a dilute atomic vapor. *science*, 269(5221):198–201, 1995.

[6] K. B. Davis, M. O. Mewes, M. R. Andrews, N. J. van Druten, D. S. Durfee, D. M. Kurn, and W. Ketterle. Bose-einstein condensation in a gas of sodium atoms. *Phys. Rev. Lett.*, 75:3969–3973, Nov 1995.

[7] C. C. Bradley, C. A. Sackett, J. J. Tollett, and R. G. Hulet. Evidence of bose-einstein condensation in an atomic gas with attractive interactions. *Phys. Rev. Lett.*, 75:1687–1690, Aug 1995.

[8] EP Gross. *Nuovo Cimento*, 20:454, 1961.

[9] Eugene P. Gross. Hydrodynamics of a superfluid condensate. *Journal of Mathematical Physics*, 4(2):195–207, 1963.

[10] LP Pitaevskii. Vortex lines in an imperfect bose gas. *Sov. Phys. JETP*, 13(2):451–454, 1961.

[11] C. Pethick and H. Smith. *Bose-Einstein Condensation in Dilute Gases*. Cambridge University Press, 2002.

[12] D. S. Jin, J. R. Ensher, M. R. Matthews, C. E. Wieman, and E. A. Cornell. Collective excitations of a bose-einstein condensate in a dilute gas. *Phys. Rev. Lett.*, 77:420–423, Jul 1996.

[13] M.-O. Mewes, M. R. Andrews, N. J. van Druten, D. M. Kurn, D. S. Durfee, C. G. Townsend, and W. Ketterle. Collective excitations of a bose-einstein condensate in a magnetic trap. *Phys. Rev. Lett.*, 77:988–991, Aug 1996.

[14] S. Stringari. Collective excitations of a trapped bose-condensed gas. *Phys. Rev. Lett.*, 77:2360–2363, Sep 1996.

[15] Mark Edwards, P. A. Ruprecht, K. Burnett, R. J. Dodd, and Charles W. Clark. Collective excitations of atomic bose-einstein condensates. *Phys. Rev. Lett.*, 77:1671–1674, Aug 1996.

[16] M. R. Andrews, D. M. Kurn, H.-J. Miesner, D. S. Durfee, C. G. Townsend, S. Inouye, and W. Ketterle. Propagation of sound in a bose-einstein condensate. *Phys. Rev. Lett.*, 79:553–556, Jul 1997.

[17] C Fort, M Prevedelli, F Minardi, FS Cataliotti, L Ricci, GM Tino, and M Inguscio. Collective excitations of a 87rb bose condensate in the thomas-fermi regime. *EPL (Europhysics Letters)*, 49(1):8, 2000.

[18] R. Onofrio, D. S. Durfee, C. Raman, M. Köhl, C. E. Kuklewicz, and W. Ketterle. Surface excitations of a bose-einstein condensate. *Phys. Rev. Lett.*, 84:810–813, Jan 2000.

[19] O. M. Maragò, S. A. Hopkins, J. Arlt, E. Hodby, G. Hechenblaikner, and C. J. Foot. Observation of the scissors mode and evidence for superfluidity of a trapped bose-einstein condensed gas. *Phys. Rev. Lett.*, 84:2056–2059, Mar 2000.

[20] D. Guéry-Odelin and S. Stringari. Scissors mode and superfluidity of a trapped bose-einstein condensed gas. *Phys. Rev. Lett.*, 83:4452–4455, Nov 1999.

[21] D. S. Jin, M. R. Matthews, J. R. Ensher, C. E. Wieman, and E. A. Cornell. Temperature-dependent damping and frequency shifts in collective excitations of a dilute bose-einstein condensate. *Phys. Rev. Lett.*, 78:764–767, Feb 1997.

[22] D. M. Stamper-Kurn, H.-J. Miesner, S. Inouye, M. R. Andrews, and W. Ketterle. Collisionless and hydrodynamic excitations of a bose-einstein condensate. *Phys. Rev. Lett.*, 81:500–503, Jul 1998.

[23] Onofrio Maragò, Gerald Hechenblaikner, Eleanor Hodby, and Christopher Foot. Temperature dependence of damping and frequency shifts of the scissors mode of a trapped bose-einstein condensate. *Phys. Rev. Lett.*, 86:3938–3941, Apr 2001.

[24] F. Chevy, V. Bretin, P. Rosenbusch, K. W. Madison, and J. Dalibard. Transverse breathing mode of an elongated bose-einstein condensate. *Phys. Rev. Lett.*, 88:250402, Jun 2002.

[25] B. Jackson and E. Zaremba. Quadrupole collective modes in trapped finite-temperature bose-einstein condensates. *Phys. Rev. Lett.*, 88:180402, Apr 2002.

[26] L.P. Pitaevskii and S. Stringari. Landau damping in dilute bose gases. *Physics Letters A*, 235(4):398 – 402, 1997.

[27] S. Giorgini. Damping in dilute bose gases: A mean-field approach. *Phys. Rev. A*, 57:2949–2957, Apr 1998.

[28] J. M. Vogels, K. Xu, C. Raman, J. R. Abo-Shaeer, and W. Ketterle. Experimental observation of the bogoliubov transformation for a bose-einstein condensed gas. *Phys. Rev. Lett.*, 88:060402, Jan 2002.

[29] J. Steinhauer, R. Ozeri, N. Katz, and N. Davidson. Excitation spectrum of a bose-einstein condensate. *Phys. Rev. Lett.*, 88:120407, Mar 2002.

[30] J. Steinhauer, N. Katz, R. Ozeri, N. Davidson, C. Tozzo, and F. Dalfovo. Bragg spectroscopy of the multibranch bogoliubov spectrum of elongated bose-einstein condensates. *Phys. Rev. Lett.*, 90:060404, Feb 2003.

[31] E. E. Rowen, N. Bar-Gill, R. Pugatch, and N. Davidson. Energy-dependent damping of excitations over an elongated bose-einstein condensate. *Phys. Rev. A*, 77:033602, Mar 2008.

[32] D. M. Stamper-Kurn, A. P. Chikkatur, A. Görlitz, S. Inouye, S. Gupta, D. E. Pritchard, and W. Ketterle. Excitation of phonons in a bose-einstein condensate by light scattering. *Phys. Rev. Lett.*, 83:2876–2879, Oct 1999.

[33] Belén Paredes, Artur Widera, Valentin Murg, Olaf Mandel, Simon Fölling, Ignacio Cirac, Gora V Shlyapnikov, Theodor W Hänsch, and Immanuel Bloch. Tonks–girardeau gas of ultracold atoms in an optical lattice. *Nature*, 429(6989):277–281, 2004.

[34] Toshiya Kinoshita, Trevor Wenger, and David S. Weiss. Observation of a one-dimensional tonks-girardeau gas. *Science*, 305(5687):1125–1128, 2004.

[35] Henning Moritz, Thilo Stöferle, Michael Köhl, and Tilman Esslinger. Exciting collective oscillations in a trapped 1d gas. *Phys. Rev. Lett.*, 91:250402, Dec 2003.

[36] M. Kottke, T. Schulte, L. Cacciapuoti, D. Hellweg, S. Drenkelforth, W. Ertmer, and J. J. Arlt. Collective excitation of bose-einstein condensates in the transition region between three and one dimensions. *Phys. Rev. A*, 72:053631, Nov 2005.

[37] Toshiya Kinoshita, Trevor Wenger, and David S Weiss. A quantum newton's cradle. *Nature*, 440(7086):900–903, 2006.

[38] S Hofferberth, I Lesanovsky, B Fischer, T Schumm, and J Schmiedmayer. Non-equilibrium coherence dynamics in one-dimensional bose gases. *Nature*, 449(7160):324–327, 2007.

[39] A. H. van Amerongen, J. J. P. van Es, P. Wicke, K. V. Kheruntsyan, and N. J. van Druten. Yang-yang thermodynamics on an atom chip. *Phys. Rev. Lett.*, 100:090402, Mar 2008.

[40] József Fortágh and Claus Zimmermann. Magnetic microtraps for ultracold atoms. *Rev. Mod. Phys.*, 79:235–289, Feb 2007.

[41] Jakob Reichel and Vladan Vuletic. *Atom Chips*. John Wiley & Sons, 2010.

[42] J. Reichel, W. Hänsel, and T. W. Hänsch. Atomic micromanipulation with magnetic surface traps. *Phys. Rev. Lett.*, 83:3398–3401, Oct 1999.

[43] H.J. Metcalf and P. Van der Straten. *Laser cooling and trapping*. Graduate Texts in Contemporary Physics Series. Springer-Verlag GmbH, 1999.

[44] C.J. Foot. *Atomic physics*. Oxford master series in physics. Oxford University Press, 2005.

[45] Jocelyn Anna Retter. *Cold Atom Microtraps above a Videotape Surface*. PhD thesis, University of Sussex, 2002.

[46] D Steck. Rubidium 87 d line data, December 2010.

[47] U Volz and H Schmoranzer. Precision lifetime measurements on alkali atoms and on helium by beam–gas–laser spectroscopy. *Physica Scripta*, 1996(T65):48, 1996.

[48] H. M. J. M. Boesten, C. C. Tsai, J. R. Gardner, D. J. Heinzen, and B. J. Verhaar. Observation of a shape resonance in the collision of two cold ^{87}Rb atoms. *Phys. Rev. A*, 55:636–640, Jan 1997.

[49] R. F. Gutterres, C. Amiot, A. Fioretti, C. Gabbanini, M. Mazzoni, and O. Dulieu. Determination of the ^{87}Rb $5p$ state dipole matrix element and radiative lifetime from the photoassociation spectroscopy of the Rb_2 $0_g^-(P_{3/2})$ long-range state. *Phys. Rev. A*, 66:024502, Aug 2002.

[50] Jun Ye, Steve Swartz, Peter Jungner, and John L. Hall. Hyperfine structure and absolute frequency of the 87rb 5p3/2 state. *Opt. Lett.*, 21(16):1280–1282, Aug 1996.

[51] E. L. Raab, M. Prentiss, Alex Cable, Steven Chu, and D. E. Pritchard. Trapping of neutral sodium atoms with radiation pressure. *Phys. Rev. Lett.*, 59:2631–2634, Dec 1987.

[52] C. G. Townsend, N. H. Edwards, C. J. Cooper, K. P. Zetie, C. J. Foot, A. M. Steane, P. Szriftgiser, H. Perrin, and J. Dalibard. Phase-space density in the magneto-optical trap. *Phys. Rev. A*, 52:1423–1440, Aug 1995.

[53] Thad Walker, David Sesko, and Carl Wieman. Collective behavior of optically trapped neutral atoms. *Phys. Rev. Lett.*, 64:408–411, Jan 1990.

[54] Z. T. Lu, K. L. Corwin, M. J. Renn, M. H. Anderson, E. A. Cornell, and C. E. Wieman. Low-velocity intense source of atoms from a magneto-optical trap. *Phys. Rev. Lett.*, 77:3331–3334, Oct 1996.

[55] C. D. J. Sinclair. *Bose-Einstein Condensation in Microtraps on Videotape*. PhD thesis, Imperial College London, 2005.

[56] R Sewell. *Matter Wave Interference on an Atom Chip*. PhD thesis, Imperial College London, 2009.

[57] Ettore Majorana. Atomi orientati in campo magnetico variabile. *Il Nuovo Cimento*, 9(2):43–50, 1932.

[58] Alan L. Migdall, John V. Prodan, William D. Phillips, Thomas H. Bergeman, and Harold J. Metcalf. First observation of magnetically trapped neutral atoms. *Phys. Rev. Lett.*, 54:2596–2599, Jun 1985.

[59] W. Ketterle and N. J. van Druten. Evaporative cooling of atoms. *Advances in Atomic, Molecular, and Optical Physics*, 37:181–236, 1996.

[60] J Fortágh, H Ott, S Kraft, A Günther, and C Zimmermann. Surface effects in magnetic microtraps. *Physical Review A*, 66(4):041604, 2002.

[61] MPA Jones, CJ Vale, D Sahagun, BV Hall, CC Eberlein, BE Sauer, K Furusawa, D Richardson, and EA Hinds. Cold atoms probe the magnetic field near a wire. *Journal of Physics B: Atomic, Molecular and Optical Physics*, 37(2):L15, 2004.

[62] Jérôme Estève, Christine Aussibal, Thorsten Schumm, Cristina Figl, Dominique Mailly, Isabelle Bouchoule, Christoph I Westbrook, and Alain Aspect. Role of wire imperfections in micromagnetic traps for atoms. *Physical Review A*, 70(4):043629, 2004.

[63] AE Leanhardt, Y Shin, AP Chikkatur, David Kielpinski, W Ketterle, and DE Pritchard. Bose-einstein condensates near a microfabricated surface. *Physical review letters*, 90(10):100404, 2003.

[64] Z. Moktadir, B. Darqui, M. Kraft, and E. A. Hinds. The effect of self-affine fractal roughness of wires on atom chips. *Journal of Modern Optics*, 54(13-15):2149–2160, 2007.

[65] O. Zobay and B. M. Garraway. Two-dimensional atom trapping in field-induced adiabatic potentials. *Phys. Rev. Lett.*, 86:1195–1198, Feb 2001.

[66] I. Lesanovsky, S. Hofferberth, J. Schmiedmayer, and P. Schmelcher. Manipulation of ultracold atoms in dressed adiabatic radio-frequency potentials. *Phys. Rev. A*, 74:033619, Sep 2006.

[67] S Hofferberth, I Lesanovsky, B Fischer, J Verdu, and J Schmiedmayer. Radiofrequency-dressed-state potentials for neutral atoms. *Nature Physics*, 2(10):710–716, 2006.

[68] J. J. P. van Es, S. Whitlock, T. Fernholz, A. H. van Amerongen, and N. J. van Druten. Longitudinal character of atom-chip-based rf-dressed potentials. *Phys. Rev. A*, 77:063623, Jun 2008.

[69] Florian Baumgärtner, R. J. Sewell, S. Eriksson, I. Llorente-Garcia, Jos Dingjan, J. P. Cotter, and E. A. Hinds. Measuring energy differences by bec interferometry on a chip. *Phys. Rev. Lett.*, 105:243003, Dec 2010.

[70] Baumg artner F. *Measuring the Acceleration of Free Fall with an Atom Chip BEC Interferometer*. PhD thesis, Imperial College London, 2011.

[71] *AVT Pike Technical Manual V5.1.2*.

[72] Kai Dieckmann. *Bose-Einstein Condensation with High Atom Number in a Deep Magnetic Trap*. PhD thesis, University of Amsterdam, 2001.

[73] Myung Sim Jun, Chang Yong Park, and D Cho. Low velocity intense source of rubidium atoms. *Journal-Korean Physical Society*, 33:260–264, 1998.

[74] L. Cacciapuoti, A. Castrillo, M. de Angelis, and G.M. Tino. A continuous cold atomic beam from a magneto-optical trap. *The European Physical Journal D - Atomic, Molecular, Optical and Plasma Physics*, 15(2):245–249, 2001.

[75] Yuri B Ovchinnikov. Compact magneto-optical sources of slow atoms. *Optics communications*, 249(4):473–481, 2005.

[76] R J Sewell, J Dingjan, F Baumgrtner, I Llorente-Garca, S Eriksson, E A Hinds, G Lewis, P Srinivasan, Z Moktadir, C O Gollasch, and M Kraft. Atom chip for bec interferometry. *Journal of Physics B: Atomic, Molecular and Optical Physics*, 43(5):051003, 2010.

[77] E. Koukharenko, Z. Moktadir, M. Kraft, M.E. Abdelsalam, D.M. Bagnall, C. Vale, M.P.A. Jones, and E.A. Hinds. Microfabrication of gold wires for atom guides. *Sensors and Actuators A: Physical*, 115(23):600 – 607, 2004. ¡ce:title¿The 17th European Conference on Solid-State Transducers¡/ce:title¿.

[78] S Kraft, A Gnther, H Ott, D Wharam, C Zimmermann, and J Fortgh. Anomalous longitudinal magnetic field near the surface of copper conductors. *Journal of Physics B: Atomic, Molecular and Optical Physics*, 35(21):L469, 2002.

[79] P. Krüger, L. M. Andersson, S. Wildermuth, S. Hofferberth, E. Haller, S. Aigner, S. Groth, I. Bar-Joseph, and J. Schmiedmayer. Potential roughness near lithographically fabricated atom chips. *Phys. Rev. A*, 76:063621, Dec 2007.

[80] A. S. Arnold, J. S. Wilson, and M. G. Boshier. A simple extended-cavity diode laser. *Review of Scientific Instruments*, 69(3):1236–1239, 1998.

[81] C. Wieman and T. W. Hänsch. Doppler-free laser polarization spectroscopy. *Phys. Rev. Lett.*, 36:1170–1173, May 1976.

[82] M. L. Harris, C. S. Adams, S. L. Cornish, I. C. McLeod, E. Tarleton, and I. G. Hughes. Polarization spectroscopy in rubidium and cesium. *Phys. Rev. A*, 73:062509, Jun 2006.

[83] C P Pearman, C S Adams, S G Cox, P F Griffin, D A Smith, and I G Hughes. Polarization spectroscopy of a closed atomic transition: applications to laser frequency locking. *Journal of Physics B: Atomic, Molecular and Optical Physics*, 35(24):5141, 2002.

[84] M.P.A Jones. *Bose-Einstein Condensation on an Atom Chip*. PhD thesis, University of Sussex, 2002.

[85] Coherent. *Coherent MBR-110 Service Manual*, 26 edition, 08 2002.

[86] G. Ritt, G. Cennini, C. Geckeler, and M. Weitz. Laser frequency offset locking using a side of filter technique. *Applied Physics B*, 79:363–365, 2004.

[87] Succo M. *An Integrated Optical-Waveguide Chip for Measurement of Cold-Atom Clouds*. PhD thesis, Imperial College London, 2011.

[88] A. M. Steane, M. Chowdhury, and C. J. Foot. Radiation force in the magneto-optical trap. *J. Opt. Soc. Am. B*, 9(12):2142–2158, Dec 1992.

[89] D. M. Brink and C. V. Sukumar. Majorana spin-flip transitions in a magnetic trap. *Phys. Rev. A*, 74:035401, Sep 2006.

[90] C. V. Sukumar and D. M. Brink. Spin-flip transitions in a magnetic trap. *Phys. Rev. A*, 56:2451–2454, Sep 1997.

[91] Wolfgang Petrich, Michael H. Anderson, Jason R. Ensher, and Eric A. Cornell. Stable, tightly confining magnetic trap for evaporative cooling of neutral atoms. *Phys. Rev. Lett.*, 74:3352–3355, Apr 1995.

[92] P. K. Rekdal, S. Scheel, P. L. Knight, and E. A. Hinds. Thermal spin flips in atom chips. *Phys. Rev. A*, 70:013811, Jul 2004.

[93] M. P. A. Jones, C. J. Vale, D. Sahagun, B. V. Hall, and E. A. Hinds. Spin coupling between cold atoms and the thermal fluctuations of a metal surface. *Phys. Rev. Lett.*, 91:080401, Aug 2003.

[94] S. Scheel, P. K. Rekdal, P. L. Knight, and E. A. Hinds. Atomic spin decoherence near conducting and superconducting films. *Phys. Rev. A*, 72:042901, Oct 2005.

[95] C. I. Sukenik, M. G. Boshier, D. Cho, V. Sandoghdar, and E. A. Hinds. Measurement of the casimir-polder force. *Phys. Rev. Lett.*, 70:560–563, Feb 1993.

[96] D. M. Harber, J. M. Obrecht, J. M. McGuirk, and E. A. Cornell. Measurement of the casimir-polder force through center-of-mass oscillations of a bose-einstein condensate. *Phys. Rev. A*, 72:033610, Sep 2005.

[97] O. J. Luiten, M. W. Reynolds, and J. T. M. Walraven. Kinetic theory of the evaporative cooling of a trapped gas. *Phys. Rev. A*, 53:381–389, Jan 1996.

[98] Isabel Llorente-Garcia. *Advances in the design and operation of atom chips*. PhD thesis, Imperial College London, 2008.

[99] Aidan Arnold. *Preparation and Manipulation of an Rb Bose-Einstein Condensate*. PhD thesis, University of Sussex, 1999.

[100] D. W. Snoke and J. P. Wolfe. Population dynamics of a bose gas near saturation. *Phys. Rev. B*, 39:4030–4037, Mar 1989.

[101] K.B. Davis, M.-O. Mewes, and W. Ketterle. An analytical model for evaporative cooling of atoms. *Applied Physics B*, 60:155–159, 1995.

[102] N. R. Newbury, C. J. Myatt, and C. E. Wieman. s-wave elastic collisions between cold ground-state ^{87}Rb atoms. *Phys. Rev. A*, 51:R2680–R2683, Apr 1995.

[103] A. G. Martin, K. Helmerson, V. S. Bagnato, G. P. Lafyatis, and D. E. Pritchard. rf spectroscopy of trapped neutral atoms. *Phys. Rev. Lett.*, 61:2431–2434, Nov 1988.

[104] Kristian Helmerson∗, Alex Martin, and David E. Pritchard. Laser and rf spectroscopy of magnetically trapped neutral atoms. *J. Opt. Soc. Am. B*, 9(4):483–492, Apr 1992.

[105] J. Soding, D. Guery-Odelin, P. Desbiolles, F. Chevy, H. Inamori, and J. Dalibard. Three-body decay of a rubidium bose-einstein condensate. *Applied Physics B*, 69(4):257–261, 1999.

[106] C. A. Sackett, C. C. Bradley, and R. G. Hulet. Optimization of evaporative cooling. *Phys. Rev. A*, 55:3797–3801, May 1997.

[107] S. Groth, P. Kruger, S. Wildermuth, R. Folman, T. Fernholz, J. Schmiedmayer, D. Mahalu, and I. Bar-Joseph. Atom chips: Fabrication and thermal properties. *Applied Physics Letters*, 85(14):2980–2982, 2004.

[108] Daw-Wei Wang, Mikhail D. Lukin, and Eugene Demler. Disordered bose-einstein condensates in quasi-one-dimensional magnetic microtraps. *Phys. Rev. Lett.*, 92:076802, Feb 2004.

[109] D. M. Stamper-Kurn, H.-J. Miesner, A. P. Chikkatur, S. Inouye, J. Stenger, and W. Ketterle. Reversible formation of a bose-einstein condensate. *Phys. Rev. Lett.*, 81:2194–2197, Sep 1998.

[110] J. Szczepkowski, R. Gartman, M. Witkowski, L. Tracewski, M. Zawada, and W. Gawlik. Analysis and calibration of absorptive images of boseeinstein condensate at nonzero temperatures. *Review of Scientific Instruments*, 80(5):–, 2009.

[111] E.P. Gross. Structure of a quantized vortex in boson systems. *Il Nuovo Cimento Series 10*, 20(3):454–477, 1961.

[112] Eugene P Gross. Hydrodynamics of a superfluid condensate. *Journal of Mathematical Physics*, 4:195, 1963.

[113] L. P. Pitaevskii. Vortex lines in an imperfect bose gas. *Sov. Phys. JETP*, 13:451, 1961.

[114] Gordon Baym and C. J. Pethick. Ground-state properties of magnetically trapped bose-condensed rubidium gas. *Phys. Rev. Lett.*, 76:6–9, Jan 1996.

[115] Mark Edwards and K. Burnett. Numerical solution of the nonlinear schrödinger equation for small samples of trapped neutral atoms. *Phys. Rev. A*, 51:1382–1386, Feb 1995.

[116] Mark Edwards, R. J. Dodd, C. W. Clark, P. A. Ruprecht, and K. Burnett. Properties of a bose-einstein condensate in an anisotropic harmonic potential. *Phys. Rev. A*, 53:R1950–R1953, Apr 1996.

[117] F. Dalfovo and S. Stringari. Bosons in anisotropic traps: Ground state and vortices. *Phys. Rev. A*, 53:2477–2485, Apr 1996.

[118] Franco Dalfovo, Stefano Giorgini, Lev P. Pitaevskii, and Sandro Stringari. Theory of bose-einstein condensation in trapped gases. *Rev. Mod. Phys.*, 71:463–512, Apr 1999.

[119] N Bogolubov. On the theory of superfluidity. *J. Phys*, 11(1):23, 1947.

[120] Chiara Menotti and Sandro Stringari. Collective oscillations of a one-dimensional trapped bose-einstein gas. *Phys. Rev. A*, 66:043610, Oct 2002.

[121] Y. Castin and R. Dum. Bose-einstein condensates in time dependent traps. *Phys. Rev. Lett.*, 77:5315–5319, Dec 1996.

[122] Alan Robert Edmonds. *Angular momentum in quantum mechanics*. Princeton University Press, 1996.

[123] T Schumm, S Hofferberth, L Mauritz Andersson, S Wildermuth, S Groth, I Bar-Joseph, J Schmiedmayer, and P Krüger. Matter-wave interferometry in a double well on an atom chip. *Nature Physics*, 1(1):57–62, 2005.

[124] M.-O. Mewes, M. R. Andrews, D. M. Kurn, D. S. Durfee, C. G. Townsend, and W. Ketterle. Output coupler for bose-einstein condensed atoms. *Phys. Rev. Lett.*, 78:582–585, Jan 1997.

[125] R. J. Ballagh, K. Burnett, and T. F. Scott. Theory of an output coupler for bose-einstein condensed atoms. *Phys. Rev. Lett.*, 78:1607–1611, Mar 1997.

[126] Jan R. Rubbmark, Michael M. Kash, Michael G. Littman, and Daniel Kleppner. Dynamical effects at avoided level crossings: A study of the landau-zener effect using rydberg atoms. *Phys. Rev. A*, 23:3107–3117, Jun 1981.

[127] Henrik Bruus and Karsten Flensberg. *Many-body quantum theory in condensed matter physics: an introduction*. Oxford University Press, 2004.

[128] D. A. W. Hutchinson, E. Zaremba, and A. Griffin. Finite temperature excitations of a trapped bose gas. *Phys. Rev. Lett.*, 78:1842–1845, Mar 1997.

[129] Lev P Pitaevskii and Sandro Stringari. *Bose-einstein condensation*. Number 116 in International Series of Monographs on Physics. Oxford University Press, 2003.

[130] Anthony Zee. *Quantum field theory in a nutshell*. Princeton university press, 2010.

[131] M. Naraschewski and D. M. Stamper-Kurn. Analytical description of a trapped semi-ideal bose gas at finite temperature. *Phys. Rev. A*, 58:2423–2426, Sep 1998.

[132] D. M. Stamper-Kurn. *Peeking and Poking at a new quantum fluid: Studies of gaseous Bose-Einstein condensate in magnetic and optical traps*. PhD thesis, Massachusetts Institute of Technology, 2000.

[133] P. Pedri, D. Guéry-Odelin, and S. Stringari. Dynamics of a classical gas including dissipative and mean-field effects. *Phys. Rev. A*, 68:043608, Oct 2003.

[134] Ifan Hughes and Thomas Hase. *Measurements and their uncertainties: a practical guide to modern error analysis*. Oxford University Press, 2010.

[135] VN Popov. Green functions and thermodynamic functions of a non-ideal bose gas. *Sov. Phys. JETP*, 20(1185):23, 1965.

[136] VN Popov. Functional integrals and collective modes. *NY: Cambridge Univ*, 1987. chap. 6.

[137] ST Beliaev. Energy spectrum of a non-ideal bose gas. *Sov. Phys.-JETP*, 7:299–307, 1958.

[138] Lev Davidovich Landau and Dirk Ter Haar. *Collected papers of LD Landau*. Pergamon Press Oxford, 1965.

[139] William C. Schieve W. Vincent Liu. Comment on "collective excitations of a bose-einstein condensate in a magnetic trap". http://arxiv.org/abs/cond-mat/9702122.

[140] A. Griffin. Conserving and gapless approximations for an inhomogeneous bose gas at finite temperatures. *Phys. Rev. B*, 53:9341–9347, Apr 1996.

[141] P Szepfalusy and I Kondor. On the dynamics of continuous phase transitions. *Annals of Physics*, 82(1):1 – 53, 1974.

[142] P.C Hohenberg and P.C Martin. Microscopic theory of superfluid helium. *Annals of Physics*, 34(2):291 – 359, 1965.

[143] S. Stringari. Dynamics of bose-einstein condensed gases in highly deformed traps. *Phys. Rev. A*, 58:2385–2388, Sep 1998.

[144] EM Lifshitz and LP Pitaevskii. Statistical physics part 2, landau and lifshitz course of theoretical physics vol. 9, 1980.

[145] D. S. Petrov, G. V. Shlyapnikov, and J. T. M. Walraven. Phase-fluctuating 3d bose-einstein condensates in elongated traps. *Phys. Rev. Lett.*, 87:050404, Jul 2001.